

PHYSIK-DEPARTMENT



Dissertation

**Photon Reconstruction and
Partial-Wave Analysis of
Three-Body Final States with
Neutral Particles at COMPASS**

Sebastian Uhl



TECHNISCHE UNIVERSITÄT MÜNCHEN

TECHNISCHE UNIVERSITÄT MÜNCHEN

Physik-Department

Photon Reconstruction and Partial-Wave Analysis of
Three-Body Final States with Neutral Particles at
COMPASS

Sebastian Uhl

Vollständiger Abdruck der von der Fakultät für Physik der Technischen Universität München zur Erlangung des akademischen Grades eines

Doktors der Naturwissenschaften (Dr. rer. nat.)

genehmigten Dissertation.

Vorsitzende: Univ.-Prof. Dr. Nora Brambilla

Prüfer der Dissertation: 1. Univ.-Prof. Dr. Stephan Paul

2. Univ.-Prof. Dr. Laura Fabbietti

Die Dissertation wurde am 09.05.2016 bei der Technischen Universität München eingereicht und durch die Fakultät für Physik am 19.07.2016 angenommen.

Abstract

The study of the light-meson spectrum is one of the major goals of the physics program of the COMPASS experiment at CERN. The mesons are produced in diffractive reactions of a high-energy pion beam with a liquid-hydrogen target. In 2008 and 2009 an unprecedented number of these reactions were recorded. In this thesis, the $\pi^-\pi^0\pi^0$ and $\pi^-\eta\eta$ final states are studied. The reconstruction of neutral hadrons, like π^0 and η , from their decays into two photons has been improved by developing a new algorithm to identify photon signals from the information provided by the electromagnetic calorimeters. This method improves the π^0 mass resolution by 25%. A partial-wave analysis is applied to the two aforementioned three-body final states. From the $\pi^-\pi^0\pi^0$ final state the well-known resonances are extracted with Breit-Wigner parameters that are in good agreement with the PDG. In addition, the hybrid-meson candidate $\pi_1(1600)$ is observed in a spin-exotic wave with $J^{PC} = 1^{-+}$ quantum numbers that are forbidden for quark-antiquark states. The novel $a_1(1420)$ signal, which is observed in the $\pi^-\pi^-\pi^+$ final state, is confirmed in the $\pi^-\pi^0\pi^0$ final state. In the $\pi^-\eta\eta$ final state, a new method to construct a wave set is applied. The results are in agreement with previous experiments, and lay the foundation to study also higher-mass states.

Zusammenfassung

Die Untersuchung des Spektrums leichter Mesonen ist eines der Hauptziele des COMPASS Experiments am CERN. Die Mesonen werden in diffraktiven Reaktionen eines hochenergetischen Pionenstrahls mit einem Flüssigwasserstofftarget erzeugt. In 2008 und 2009 wurde eine bislang unübertroffene Anzahl dieser Reaktionen aufgezeichnet. In dieser Arbeit werden die $\pi^-\pi^0\pi^0$ and $\pi^-\eta\eta$ Endzustände untersucht. Die Rekonstruktion neutraler Hadronen, wie etwa π^0 oder η , aus ihren Zwei-Photonen-Zerfällen wurde durch die Entwicklung eines neuen Algorithmus zur Identifizierung von Photonsignalen in den Daten der elektromagnetischen Kalorimeter verbessert. Mit der neuen Method wird eine um 25 % bessere π^0 -Massenauflösung erzielt. Eine Partialwellenanalyse der beiden oben genannten Dreikörperendzustände wurde durchgeführt. Die für den $\pi^-\pi^0\pi^0$ Endzustand bestimmten Breit-Wigner-Parameter bekannter Resonanzen sind in guter Übereinstimmung mit dem PDG. Darüber hinaus wird ein Kandidat für ein Hybridmeson, das $\pi_1(1600)$, in einer für Quark-Antiquark-Zustände verbotenen Welle mit $J^{PC} = 1^{-+}$ Quantenzahlen beobachtet. Das neuartige $a_1(1420)$ -Signal, das zuvor im $\pi^-\pi^-\pi^+$ Endzustand beobachtet wurde, wird auch im $\pi^-\pi^0\pi^0$ Endzustand bestätigt. Für die Analyse des $\pi^-\eta\eta$ Endzustandes wurde eine neue Methode zum Abschneiden der Partialwellenentwicklung angewendet. Die hierbei erzielten Ergebnisse stimmen mit vorangegangenen Experimenten überein und legen den Grundstein für die Untersuchung von Zuständen mit höheren Massen.

Contents

1	Introduction	1
1.1	The COMPASS Experiment	4
2	Electromagnetic Calorimeters	7
2.1	ECAL1	7
2.2	ECAL2	9
2.3	Reconstruction	10
2.3.1	Shower Fitting in ECAL2	11
2.3.2	Correction of Shower Parameters	14
2.4	Performance on Real Data	16
2.4.1	Stability	16
2.4.2	Time Resolution	18
2.4.3	Two-Photon Mass Resolution	18
2.5	Simulation	19
2.5.1	Single-Photon Acceptance	20
2.5.2	Two-Photon Mass Resolution	23
3	Event Selection	27
3.1	Preselection	27
3.1.1	DT0 Trigger	27
3.1.2	Primary Vertex	29
3.1.3	Photons	29
3.1.4	RPD Reconstruction	29
3.2	Calorimeter Information	29
3.2.1	Energy Thresholds for Photons	29
3.2.2	Time Information	30
3.3	Selection of Neutral Particles	31
3.4	Kinematic Selection	31
3.4.1	Vertex Position	31
3.4.2	Beam Momentum	31
3.4.3	Momentum Conservation	34
3.4.4	Reduced Squared Four-Momentum Transfer t'	36
3.4.5	Mass Ranges for Partial-Wave Analysis	37
3.5	Simulation	40
3.5.1	$\pi^- \pi^0 \pi^0$ Final State	40
3.5.2	$\pi^- \eta \eta$ Final State	43

4	Partial-Wave Analysis Method	51
4.1	Cross Section	51
4.2	Decay Amplitudes	53
4.3	Total Partial-Wave Intensity	56
4.4	Mass-independent Partial-Wave Analysis	57
4.5	Spin-density matrix	60
5	Partial-Wave Analysis of the $\pi^- \pi^0 \pi^0$ Final State	63
5.1	Fit Model	63
5.1.1	Masses and Parameterisations	64
5.1.2	Wave Set	69
5.2	Verification of Fit Quality	69
5.3	Total Intensities and Spin Totals	76
5.4	Individual Partial-Wave Intensities	81
5.5	Phases	81
5.6	Resonance-Model Fit	81
5.7	The $J^{PC} = 1^{++}$ Sector	89
5.8	The $J^{PC} = 2^{++}$ Sector	93
5.9	The $J^{PC} = 2^{-+}$ Sector	97
5.10	The $J^{PC} = 0^{-+}$ Sector	104
5.11	The $J^{PC} = 4^{++}$ Sector	106
5.12	The $a_1(1420)$	108
5.13	The $\pi_1(1600)$	112
5.14	Some Systematics of the Resonance-Model Fit	115
5.15	Comparison with the $\pi^- \pi^- \pi^+$ Final State	118
6	Partial-Wave Analysis of the $\pi^- \eta \eta$ Final State	125
6.1	Partial-Wave Analysis using the Wave Set by E852	125
6.2	Biggest-Conceivable-Model Method	126
7	Conclusions and Outlook	135
7.1	Electromagnetic Calorimetry	135
7.2	Partial-Wave Analysis of the $\pi^- \pi^0 \pi^0$ Final State	135
7.3	Partial-Wave Analysis of the $\pi^- \eta \eta$ Final State	137
	List of Figures	139
	List of Tables	143
	Bibliography	145
	Own contributions	153
	Acknowledgements	155

Chapter 1

Introduction

In the standard model of particle physics, the strong interaction between the color charges of point-like quarks is described by Quantum Chromodynamics (QCD). This interaction is mediated by gluons, which carry color charges themselves. This implies that gluons interact with each other and leads to the non-Abelian character of QCD. The self-interaction of gluons has far reaching consequences. It eventually leads to the confinement of quarks and gluons into color-neutral hadrons. The phenomenon of confinement is responsible for 95% of the mass of the visible universe [67]. Its quantitative understanding is still one of the open questions in particle physics.

Hadrons, the bound states of the strong interaction, exist with integer and half-integer spin, and are called mesons and baryons, respectively. Due to its running coupling constant [65], QCD can be treated in a perturbative way only at high energies. At the energy scales of hadrons, the coupling constant is so large, that the perturbative expansion does not converge anymore. Currently, the only way to calculate the hadron excitation spectrum from first principle is lattice QCD [42]. A prediction of masses for states with several quantum numbers J^{PC} is shown in fig. 1.1. For computational reasons, these calculations cannot yet be performed at physical quark masses, and the results need to be extrapolated to the physical point. Decays of the states can in general not be calculated, in the light-meson sector only the ρ has been studied for its dynamic properties [41]. Therefore, further models are required to understand the light-meson spectrum.

In the constituent quark model [47], mesons are systems of a quark and an antiquark ($q\bar{q}$) bound by the strong interaction. Quarks are fermions with spin $\frac{1}{2}$, so that the spins of the quark and the antiquark can couple to a total intrinsic spin S of either 0 or 1. The relative orbital momentum L between the quark and the anti-quark couples with the intrinsic spin S to the total spin J of the meson. The parity P of such a state is given by the intrinsic parities of the quark and the antiquark, and the parity of the spatial wave function defined by the orbital angular momentum L . As the intrinsic parities of quarks and antiquarks have opposite sign, the overall parity of a meson is given by

$$P = (-1)(-1)^L = (-1)^{L+1} \quad (1.1)$$

To fulfill Fermi statistics, the wave function of the $q\bar{q}$ system has to be antisymmetric under the exchange of quark and antiquark. Therefore the wave functions

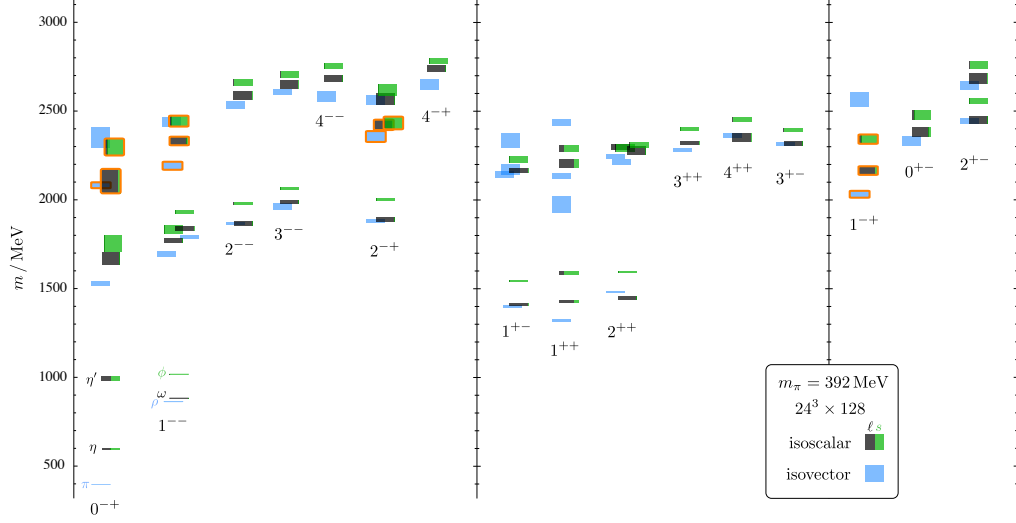


Figure 1.1: Meson spectrum predicted by lattice QCD for states separated by the quantum numbers isospin I and J^{PC} (figure taken from [42]). The height of the boxes indicates the statistical uncertainty on the mass determination.

has to change sign when the coordinates, the spins and the charge variables are exchanged. The exchange of coordinates is equivalent to the parity operation, which has an eigenvalue of $(-1)^L$. The exchange of spins gives a factor of $(-1)^{S+1}$, so that

$$(-1) = (-1)^L (-1)^{S+1} C \quad \text{which yields} \quad C = (-1)^{L+S} \quad (1.2)$$

The C -parity is a good quantum number only for neutral mesons. By convention, the C -parity of the neutral isospin partner is also assigned to charged mesons. Alternatively, the G -parity is introduced. It is defined as the charge conjugation followed by a rotation around the y -axis in isospin space, flipping the sign of the isospin z -component I_z and with it the charge of the meson

$$G = C e^{i\pi I_y} = C (-1)^I = (-1)^{L+S+I} \quad (1.3)$$

Following these rules, some J^{PC} combinations are forbidden in the constituent quark model, these are

$$J^{PC} = 0^{--}, 0^{+-}, 1^{-+}, 2^{+-}, 3^{-+}, 4^{+-}, \dots \quad (1.4)$$

These combinations of J^{PC} are called spin-exotic quantum numbers. Accordingly, states with these quantum numbers are often called “spin exotics” or “spin-exotic mesons”.

Models and lattice QCD predict states that contain not only $q\bar{q}$, but additional gluonic degrees of freedom (“hybrid mesons”, $q\bar{q}g$), or that are even pure gluonic

bound states (“glueballs”, gg). In fig. 1.1 such states are indicated by orange boxes [42]. Some of these states have spin-exotic quantum numbers. Finding such a state would be unambiguous proof for bound states beyond the constituent quark model and would be an important confirmation of QCD.

A number of experiments have claimed evidence for states with spin-exotic quantum numbers $I^G J^{PC} = 1^- 1^{-+}$. The first observations were based on $\eta\pi^-$ and $\eta'\pi^-$ final-states produced in diffractive scattering of high-energy pion beams off nuclear targets. The $\pi_1(1400)$ was claimed by the “Joint IHEP and CERN experiment” as a narrow state with a mass of $1406 \text{ MeV}/c^2$ and a width of $180 \text{ MeV}/c^2$ [12]. The VES experiment observed intensity in the spin-exotic waves for both $\eta\pi^-$ and $\eta'\pi^-$ final states [22]. Most of the intensity in the $\eta\pi^-$ final state was found below $1400 \text{ MeV}/c^2$. In the $\eta'\pi^-$ a bump around $1600 \text{ MeV}/c^2$ was observed. Later, this bump was described by a Breit-Wigner for the $\pi_1(1600)$ with a mass of $1570 \text{ MeV}/c^2$ and a width of $550 \text{ MeV}/c^2$ [80]. The E852 experiment at BNL found the $\pi_1(1400)$ in the $\eta\pi^-$ final state at a mass of $1370 \text{ MeV}/c^2$ and with a width of $385 \text{ MeV}/c^2$ [31]. A $\pi_1(1600)$ was found in the $\eta'\pi^-$ final state at a mass of $1643 \text{ MeV}/c^2$ and with a width of $392 \text{ MeV}/c^2$ [4]. E852 also claimed a $\pi_1(1600)$ in the $(3\pi)^-$ final states with a mass of $1593 \text{ MeV}/c^2$ and a width of $168 \text{ MeV}/c^2$ [32], but a later publication using an extended data set explained this signal with leakage from the $\pi_2(1670)$ [44]. Also the COMPASS collaboration claimed a $\pi_1(1600)$ with a mass of $1660 \text{ MeV}/c^2$ and a width of $269 \text{ MeV}/c^2$ in the $\pi^-\pi^-\pi^+$ final state produced in diffractive scattering of a pion beam off a lead target [13]. COMPASS also found signals compatible with the $\pi_1(1400)$ in the $\eta\pi^-$ and with the $\pi_1(1600)$ in the $\eta'\pi^-$ final states when scattering a pion beam off a liquid-hydrogen target [10]. However, despite the more precise data set, resonance parameters could not be extracted reliably. For both states, the $\pi_1(1400)$ and the $\pi_1(1600)$, the resonance parameters vary widely. In particular the widths are only poorly known. For both signals the resonance interpretation is discussed controversially, it is also not clear that those states can be mapped to a hybrid meson [63].

But also the knowledge about states with ordinary quantum numbers is limited, in particular for excited states, like e.g. the $a_2(1700)$ or the $\pi_2(2005)$. A new axial-vector meson, the $a_1(1420)$, has been observed for the first time in COMPASS in the $\pi^-\pi^-\pi^+$ final state when scattering a pion beam off a liquid-hydrogen target [50, 11, 9]. Its interpretation is still unclear. Various resonant and non-resonant explanations have been proposed, but so far none of these describes all features of the data [9].

Apart from the huge $\pi^-\pi^-\pi^+$ data set, COMPASS has also collected data for the $\pi^-\pi^0\pi^0$ final state. The analysis of this final state is complementary to the one of the $\pi^-\pi^-\pi^+$ final state. The two channels contain the same resonances, but the isospin z -component I_z of the final-state particles is different. As a π^0 immediately decays to two photons which are detected in electromagnetic calorimeters, the two final states probe different detector systems of an experiment. For the $\pi^-\pi^0\pi^0$ final state the photon detection efficiency is crucial, while only a single charge

track has to be reconstructed. For the analysis of the $\pi^-\pi^-\pi^+$ final state the electromagnetic calorimeters are not used at all, but three charged tracks have to be reconstructed. The two channels are therefore affected by completely different experimental challenges and different systematic effects, and one channel can be used to confirm findings in the other.

The resonance parameters extracted by a resonance-model fit of the partial-wave decomposition of the $\pi^-\pi^0\pi^0$ final state need to be in agreement with previous experiments to make the complete analysis trustworthy. This is in particular true for the $a_2(1260)$, the $\pi_2(1670)$, and the $\pi(1800)$ resonances, which have well-known parameters for their mass and width [65]. Once the quality of the data has been established, it can be studied for the less-known and controversial states. The search for the $a_1(1420)$ previously observed in the $\pi^-\pi^-\pi^+$ final state is of major interest, a confirmation in the $\pi^-\pi^0\pi^0$ final state would be a first step to establish this state. Given the long history of the $\pi_1(1600)$, a final answer on the existence and resonance nature of this state is improbable. A comparison of the result in the $\pi^-\pi^0\pi^0$ final state with the one from the $\pi^-\pi^-\pi^+$ final state, can provide further insights into this state.

To improve the reconstruction efficiency for neutral hadrons, in particular for π^0 and η , a shower fit for the electromagnetic calorimeters was implemented. Its performance is discussed in chapter 2. The event selection for the $\pi^-\pi^0\pi^0$ and $\pi^-\eta\eta$ final state from data recorded with a pion beam scattering off a liquid-hydrogen target is shown in chapter 3. The partial-wave analysis method is introduced in chapter 4, results for the $\pi^-\pi^0\pi^0$ final state are shown in chapter 5. This partial-wave analysis was performed in the same way as for the $\pi^-\pi^-\pi^+$ final state. In chapter 6 a partial-wave analysis of the $\pi^-\eta\eta$ final state is presented as an starting point to study the spectrum of light hadrons also at higher masses.

1.1 The COMPASS Experiment

The COMPASS experiment (fig. 1.2) is a versatile two-stage fixed-target spectrometer located in the North Area of CERN. The primary 400 GeV/c proton beam from the SPS is extracted onto a Beryllium production target where secondary hadrons are produced [17]. Depending on the requirements of the physics program, the secondary hadrons, pions, kaons and (anti-)protons, are either directly guided to the experiment, or the hadrons are removed from the beam by hadron absorbers keeping only the muons from the pions and kaons that decay between the production target and the absorbers in the beam. While the particles are guided to the experiment their momentum is selected via deflection in magnets. The data used in this thesis have been recorded in 2008 using a negative hadron beam with a momentum of 190 GeV/c. The negative hadron beam consists mostly of pions (97%) with a small admixture of kaons (2.4%) and anti-protons (0.8%). The set-up of the spectrometer is extensively discussed in [1, 2]. Here, only a brief overview of the set-up used in 2008 is given.

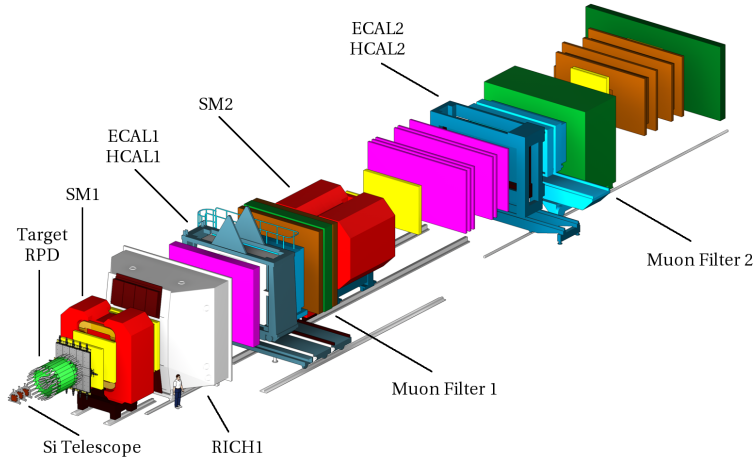


Figure 1.2: Artistic view of the COMPASS set-up in 2008 and 2009 (figure taken from [2]). The beam enters the experiment from the bottom left corner. Different colors indicate different spectrometer components.

Position and direction of the beam particles are measured by one scintillating fibre detector and three silicon stations in front of the target. The magnitude of the momentum of the individual beam particles is not measured for the hadron beam, the momentum spread is about 1% around the nominal momentum.

The beam then enters the 40 cm long liquid-hydrogen target. The target is surrounded by a recoil-proton detector (RPD). It consists of two cylindrical layers of scintillator slabs. A signal in both layers is used to identify protons leaving the target. This coincidence is used to trigger the recording of an event. The protons need to have a minimal momentum of $270 \text{ MeV}/c$ to reach the outer slab.

The position of the interaction vertex is precisely reconstructed by measuring the position and direction of charged particles leaving the target with two silicon stations directly downstream of the target. Momenta of the charged particles are measured in a two-stage magnetic spectrometer. Photons are detected in two electromagnetic calorimeters, one in each spectrometer stage.

The first stage is built around the first spectrometer magnet (SM1) with a bending power of 1.0 Tm [1]. This stage measures particles that have an angle between roughly 30 mrad and 300 mrad with respect to the beam axis viewed from the target. It also features the first electromagnetic calorimeter (ECAL1, section 2.1). The ring-imaging Cherenkov (RICH1) detector in this spectrometer stage is not used in this thesis, but its light-gas pipe is important for the photon acceptance (section 2.5.1).

Particles with angles smaller than 30 mrad are measured by the second spectrometer stage built around the second spectrometer magnet (SM2) with a bending power of 5.5 Tm [1]. Charged particles with a momentum above $15 \text{ GeV}/c$

are able to enter the second stage [2]. This stage also features an electromagnetic calorimeter (ECAL2, section 2.2).

Events containing particles with angles larger than the acceptance of the first spectrometer stage are vetoed by a sandwich detector [73, 72]. This ensures that all final-state particles can be detected, so that an exclusive measurement can be performed. Photons in the final state are detected in either of the two electromagnetic calorimeters.

For the tracking of charged particles a variety of detectors featuring different detection principles is used. These detectors provide a measurement of the position perpendicular to the beam axis. To measure particles close to the beam axis, detectors with a high-rate capability are required. Scintillating fiber detectors [1] and PixelGEM detectors [2] with an active area of about $10 \times 10 \text{ cm}^2$ fulfill this requirement. The scintillating fiber detectors achieve this with a temporal resolution of around 400 ps, the PixelGEM detectors with a pixelised readout structure that reduces the maximal rate per pixel to 100 kHz. Micromegas and GEM detectors with active areas of $40 \times 40 \text{ cm}^2$ and $30 \times 30 \text{ cm}^2$ [1], respectively, are used for the tracking of particles with a small angle with respect to the beam axis. An inactive area with a diameter of 5 cm in the center of each detector ensures that the detectors are not blinded by the high rates of the beam. Further outside the position information is provided by drift chambers, straw-tube chambers, and multi-wire proportional chambers covering areas up to several square meters [1, 2]. These detectors have inactive centers with a diameter larger than 20 cm to keep the rates below an absolute limit of 250 kHz per channel.

The position measurements are used in a Kalman filter to reconstruct tracks and measure the momenta of charged particles via the deflection in the magnetic fields in the two spectrometer magnets [1, 2].

Chapter 2

Electromagnetic Calorimeters

The COMPASS set-up of 2008 and 2009 comprises two electromagnetic calorimeters, one in each spectrometer stage [2]. They are designed to measure the energy and incident position of electrons and photons. As (electrically) neutral particles do not leave hits in tracking detectors, the calorimeters are the only detectors able to measure photons.

2.1 ECAL1

The electromagnetic calorimeter in the first spectrometer stage of COMPASS is called ECAL1. It is located roughly 14.5 m downstream of the target and covers an angular acceptance of 37 mrad to 136 mrad in the horizontal and 21 mrad to 98 mrad in the vertical direction as viewed from the target center [2]. Photons that are emitted under an angle smaller than the lower bounds of the angular acceptance of ECAL1 can still be detected in the calorimeter in the second spectrometer stage (section 2.2), a central hole ensures that the calorimeter does not affect particles at this small angles. ECAL1 consists of 1500 lead-glass blocks of three different types (fig. 2.1).

The inner-most part is equipped with 608 blocks with a transverse dimension of $3.83 \times 3.83 \text{ cm}^2$ (GAMS [25]). They are arranged in a matrix of 44 columns times 24 rows with the inner 28×16 blocks left empty. The high-voltage of the photomultipliers is adjusted to give a dynamic range up to 60 GeV [2].

On top of and below the GAMS blocks are matrices of 22×13 blocks of $7.5 \times 7.5 \text{ cm}^2$ (Mainz). To accommodate for the difference in size compared to the GAMS blocks in horizontal direction there are vertical gaps of 1.6 mm between the blocks (fig. 2.2). The two rows left and right of the ECAL1 center are positioned without a gap, and the two gaps on each side of the center are filled with iron sheets to ensure that particles perpendicular to the calorimeter surface have to traverse enough material such that photons create electromagnetic showers. For the gaps further away from the center this is not necessary as photons from the target have a sufficiently large angle so that they cannot pass through the gap. The high-voltage of the photomultipliers of the Mainz-type blocks is adjusted to give a dynamic range up to 30 GeV [2].

The very outer part of ECAL1 is covered by a matrix of 8×20 blocks with a transverse size of $14.1 \times 14.1 \text{ cm}^2$ (OLGA [16]) on either side of the calorimeter.

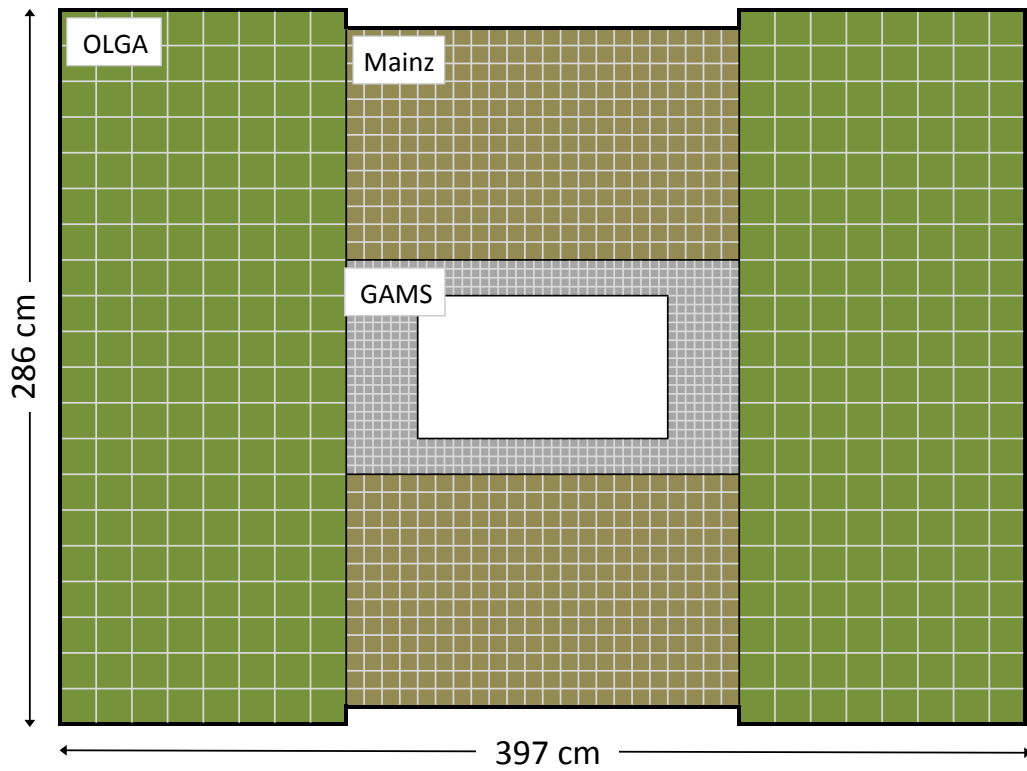


Figure 2.1: Schematic view of ECAL1 showing the areas equipped with the three different block types (figure taken from [2]).

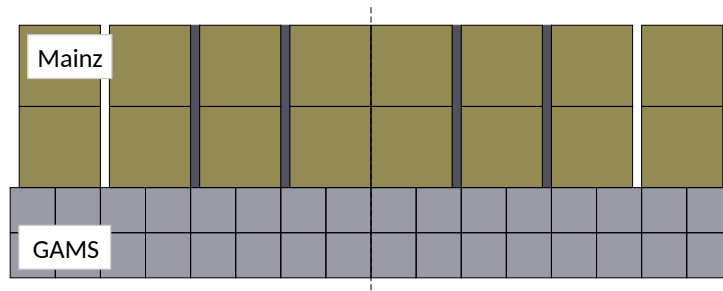


Figure 2.2: Schematic view of ECAL1 showing the details of the gaps in the center of ECAL1. In the center the two columns of Mainz-type blocks are directly adjacent. The next two gaps between columns of Mainz blocks to either side are filled with iron sheets, the other gaps are filled with air.

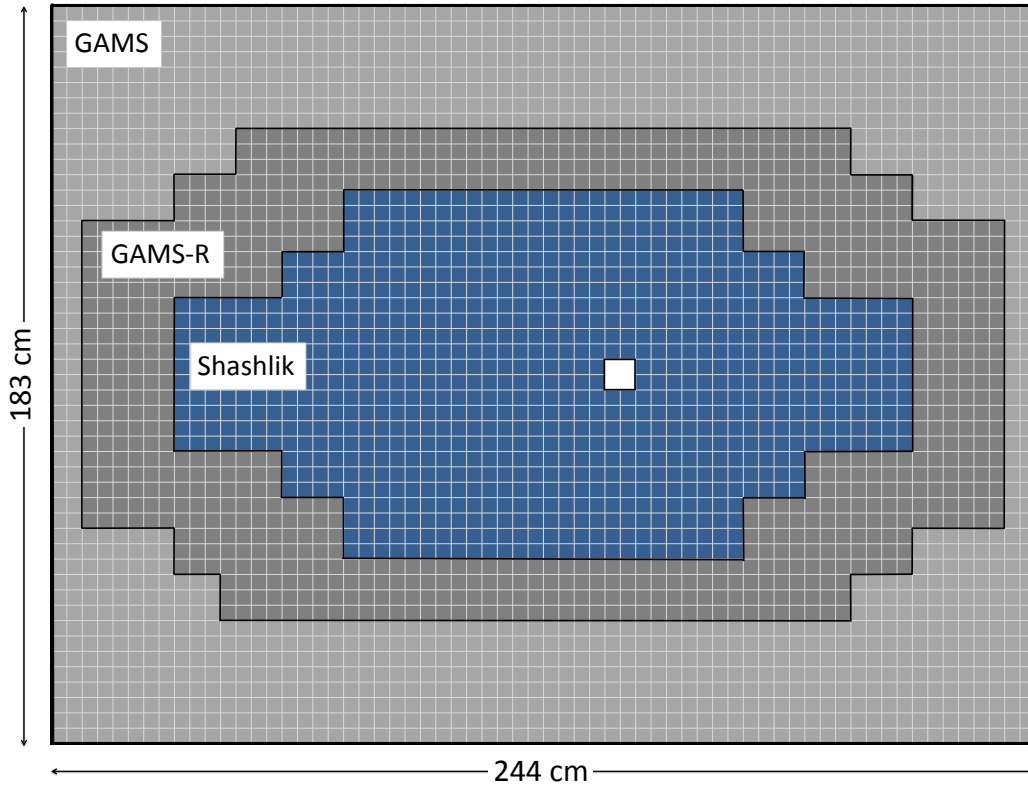


Figure 2.3: Schematic view of ECAL2 showing the areas equipped with the three different block types (figure taken from [2]).

The high-voltage of the photomultipliers is adjusted to give a dynamic range up to 20 GeV [2].

The Cherenkov photons emitted by the charged particles in the electromagnetic showers are detected with one photomultiplier per block. The signals of these photomultipliers are digitized by a sampling analog-to-digital converter (SADC) with a frequency of 80 MHz and a dynamic range of 10 bits [62]. For each event 32 samples of the signal waveform are recorded.

2.2 ECAL2

The electromagnetic calorimeter in the second spectrometer stage of COMPASS is called ECAL2. It is located roughly 33.5 m downstream of the target and covers the angular acceptance up to 39 mrad in the horizontal and up to 29 mrad in the vertical direction. The blocks are arranged in a matrix of 64×48 with a transverse size of $3.83 \times 3.83 \text{ cm}^2$ per block. A hole of 2×2 blocks is removed at the position of the non-interacting beam. Three different block types are used according to the required radiation hardness (fig. 2.3).

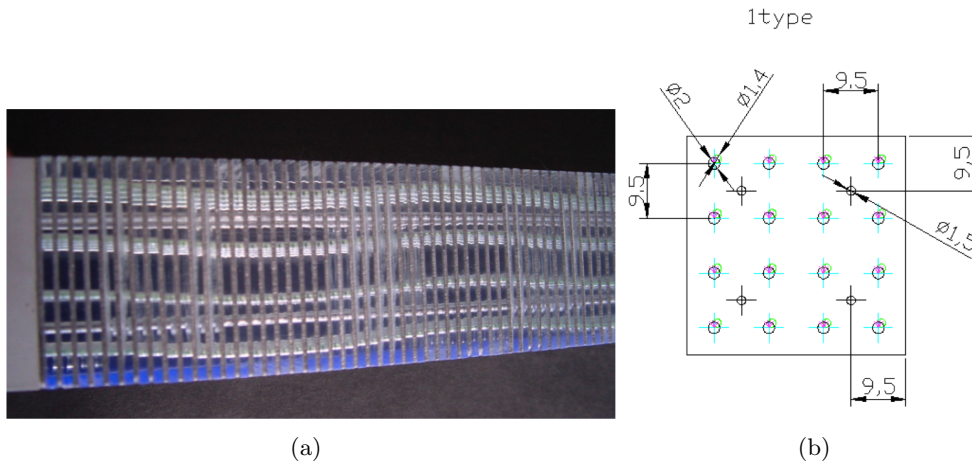


Figure 2.4: (a) Detail of a Shashlyk block, showing the layers of scintillator and absorber material. The straight steel rods, and the spiraling wavelength-shifting fibers are also visible. (b) Sketch of the holes for the wavelength-shifting fibers and the steel rods (figures taken from [69]).

The innermost part of ECAL2 consists of so-called Shashlyk blocks (fig. 2.4). They consist of 155 double layers of 0.8 mm lead and 1.5 mm scintillator. The scintillation light is collected in 16 wavelength-shifting fibers and guided to a photomultiplier. The layers are stacked onto four steel rods.

The intermediate part of ECAL2 is build from radiation-hard lead-glass blocks (GAMS-R), the outermost part is made from the same lead-glass blocks already used in ECAL1 (GAMS). For these lead-glass blocks the Cherenkov photons emitted by the charged particles in the electromagnetic showers are detected by photomultipliers.

The high-voltage of the photomultipliers for ECAL2 is adjusted to be able to detect showers up to 200 GeV for the inner 16×16 blocks, the rest of the central 48×48 blocks covers energies up to 150 GeV. Two stripes of 8×48 blocks on each side of the central part cover up to 60 GeV. The signals of the photomultipliers are digitized by a sampling analog-to-digital converter (MSADC) with a frequency of 80 MHz and a dynamic range of 12 bits [62]. For each event 32 samples of the signal waveform are recorded.

2.3 Reconstruction

The first steps of the reconstruction are the same for both electromagnetic calorimeters. From the 32 signal samples the signal amplitude and time are extracted. A parabola is defined using the maximal sample and its two neighbors. The signal amplitude is the maximum of the parabola. The time is given by the position

of the maximum within the 12.5 ns sampling bin. The extracted signal time is shifted by a block-specific calibration constant t_0 to accommodate for different cable lengths between the photomultipliers and the read-out electronics.

To convert the signal amplitude into an energy deposit several calibration factors are applied. The first is a coefficient to convert ADC channels into units of energy. This coefficient is obtained by shooting an electron beam of known energy onto the calorimeters and observing their response. This calibration procedure is typically performed once per year. To correct for fluctuations due to, e.g., changes in the response of the photomultipliers with the ambient temperature, the response of the calorimeters is monitored by illuminating the calorimeter blocks with a well known light pulse from a laser for ECAL1 and an LED for ECAL2. Data for this LED/laser correction are permanently recorded in the off-spill time, when no other signals are present. These data give one correction factor per block and spill.

The next level of correction is based on the measurement of the π^0 mass [48]. As the electron calibration is performed only for a single energy and with a limited amount of data, an energy-dependent correction is calculated in an iterative procedure for each block to bring the π^0 mass peak to the correct position.

Finally, to correct for rate effects in the 200 most central blocks of ECAL2, a correction of the energy depending on the time-in-spill is performed. Again this calibration is obtained from the π^0 mass peak [48].

After all calibrations are applied, the clustering is performed. Adjacent blocks with a signal are grouped into clusters. Blocks are assigned to the same cluster, if they are direct or diagonal neighbors.

For ECAL1 one cluster corresponds to one shower produced by one particle. The position of this shower is calculated from the 3×3 blocks around the most energetic one. The shower time is defined by the block with the highest energy.

2.3.1 Shower Fitting in ECAL2

To improve the spatial resolution and to separate overlapping showers from particles hitting the calorimeter close to each other, a shower separation is performed for ECAL2. The algorithm is based on cumulative shower profiles [60]. If a shower is projected onto any axis in its transverse plane, the ratio of the energy deposited up to a position x along this axis w.r.t. the total energy in the shower is parameterized by (fig. 2.5(a))

$$F(x) = \frac{\int_{-\infty}^x dx' \rho_E(x')}{\int_{-\infty}^{\infty} dx' \rho_E(x')} = \frac{1}{2} + \frac{1}{\pi} \sum_i a_i \arctan \frac{x}{b_i} \quad (2.1)$$

Here $\rho_E(x)$ is the energy density along the axis the shower is projected onto. The coefficient a_i gives the relative contribution of the term with index i , the sum of all a_i is equal to one ($\sum_i a_i = 1$). The parameter b_i determines the width of the contribution i .

The parameters for the lead-glass blocks are determined from the electron calibration data [61]. Those for the Shashlyk blocks are determined from events with

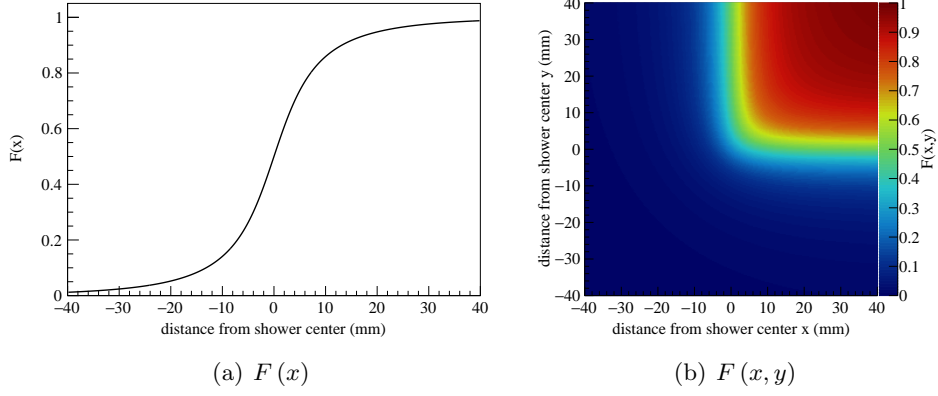


Figure 2.5: Cumulative shower profiles (a) in one and (b) in two transverse dimensions.

a single high-energetic photon [59]. These data sets evenly illuminated the surface of a subset of blocks. In case of the lead-glass blocks of ECAL2 the sum in eq. (2.1) has two components, for the Shashlyk blocks there are three.

The shower profiles can be extended to the two dimensions x and y in the transverse plane of the shower parallel to the edges of the calorimeter blocks (fig. 2.5(b), [60])

$$\begin{aligned}
 F(x, y) &= \frac{\int_{-\infty}^x dx' \int_{-\infty}^y dy' \rho_E(x', y')}{\int_{-\infty}^{\infty} dx' \int_{-\infty}^{\infty} dy' \rho_E(x', y')} \quad (2.2) \\
 &= \frac{1}{4} + \frac{1}{2\pi} \sum_i a_i \left(\arctan \frac{x}{b_i} + \arctan \frac{y}{b_i} + \arctan \frac{xy}{b_i \sqrt{b_i^2 + x^2 + y^2}} \right) \quad (2.3)
 \end{aligned}$$

There is one term describing the behavior along each dimension, and a third term to account for the asymmetry along the diagonal. The parameters a_i and b_i are the same as in eq. (2.1). The function $F(x, y)$ is used to calculate the ratio of the energy deposited in an area up to the position (x, y) w.r.t. the total shower energy. Setting one coordinate to infinity, one again obtains the one-dimensional function of eq. (2.1) $F(x, y \rightarrow \infty) = F(x)$.

The two-dimensional function is used to determine the ratio of the energy deposited in a block w.r.t. the total energy of a shower (fig. 2.6)

$$\begin{aligned}
 G_j(x, y) &= F(u_j + \Delta, v_j + \Delta) - F(u_j + \Delta, v_j - \Delta) \\
 &\quad - F(u_j - \Delta, v_j + \Delta) + F(u_j - \Delta, v_j - \Delta) \quad (2.4)
 \end{aligned}$$

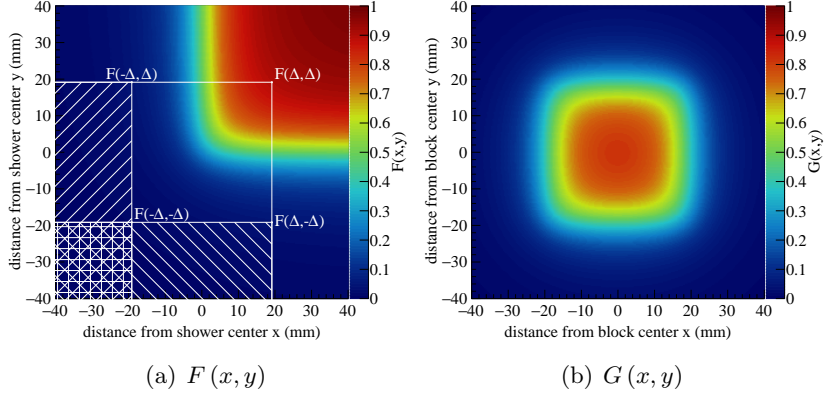


Figure 2.6: (a) Sketch of eq. (2.4) if the shower center and the block center are at the same position. (b) Ratio of the energy deposited within a block at position $(0, 0)$ w.r.t. the total energy of a shower for a shower centered at position (x, y) .

Here j denotes the block, (x, y) is the position of the shower, $u_j = X_j - x$ and $v_j = Y_j - y$ are coordinates relative to the centre (X_j, Y_j) of each block, and Δ is half the transverse size of the block.

To extract the shower energy e , position x and y and the time t , a fit of the shower profiles to the previously created clusters is performed. The energy deposited by a shower i in block j is predicted to be

$$E_{j,i}^{\text{pred}} = e_i \cdot G_j(x_i, y_i) \quad (2.5)$$

Several overlapping showers can be fitted into a single cluster, and accordingly the total energy predicted for one block is the sum over all showers in the current cluster

$$E_j^{\text{pred}} = \sum_i^{\text{showers}} E_{j,i}^{\text{pred}} = \sum_i^{\text{showers}} e_i \cdot G_j(x_i, y_i) \quad (2.6)$$

Timing of the showers is extracted from the signal time of each block. The predicted time in a block is the average time over all showers weighted by the energy

$$T_j^{\text{pred}} = \frac{\sum_i^{\text{showers}} e_i \cdot G_j(x_i, y_i) \cdot t_i}{\sum_i^{\text{showers}} e_i \cdot G_j(x_i, y_i)} \quad (2.7)$$

The shower parameters are obtained by minimizing the differences between the predicted and measured energies and times in all blocks belonging to one cluster

$$-\ln L = \frac{1}{2} \sum_j^{\text{blocks}} \left[\frac{(E_j^{\text{meas}} - E_j^{\text{pred}})^2}{\sigma_{j,E}^2} + \frac{(T_j^{\text{meas}} - T_j^{\text{pred}})^2}{\sigma_{j,T}^2} \right] \quad (2.8)$$

The Minuit2 fitter from the ROOT package [29] is used for the fit. The errors on the measured energies $\sigma_{j,E}$ and times $\sigma_{j,T}$ are taken from parameterizations of the results from a previous analysis of the calorimeter performance [48].

2.3.2 Correction of Shower Parameters

With the refined resolution from the shower-profile fit, it is possible to resolve the internal structure of the Shashlyk blocks (fig. 2.7). Selecting electron tracks and looking at the ratio of the track momentum over the calorimeter energy, the four rods are clearly visible as spots where a portion of the electron energy is not detected in the calorimeter. Similarly, the 16 locations of the wavelength-shifting fibers are seen as places where a surplus of energy is detected in the calorimeter. The magnitude of these deviations depends on the energy. The deviations are corrected with a position-dependent energy correction in four energy bins. Exploiting the symmetry of the Shashlyk blocks the deviations over the whole block are folded into the upper right quadrant for each energy bin, and a map for the $1.915 \times 1.915 \text{ cm}^2$ area is calculated with a resolution of 25×25 bins. The resulting corrections are smaller than 5%.

Also the position information of showers can be corrected. The difference between the position of a shower and the extrapolated incident position of electron tracks follows a sine-like curve (fig. 2.8): it is zero at the block borders and at the block center, but reaches deviations of up to 10 mm in between, in particular for low energies. Two ways have been tried to perform a position-dependent position correction.

The simpler method is to fit a third-order polynomial to the mean difference between shower and track position in three energy bins. During the reconstruction, the polynomial in the appropriate energy bin is used to correct the shower position depending on its position. This method has the disadvantage that unless the polynomials are forced to have the same value at the upper and lower edge of the block, showers might be shifted out of the current block and into a neighboring one. Also the binning in the energy leads to inconsistencies at the bin borders.

For the more advanced method, the difference is fit with $\alpha \sin + \beta \sin^3$ in energy bins of 2 GeV width. The argument of the sine is scaled such that one period corresponds to one block size. The parameters α and β are obtained for each narrow energy slice individually, and then described by the sum of two arctan functions and a constant offset. This method provides a smooth and consistent correction across the whole range.

The position-dependent energy correction and the simpler position-dependent position correction combined improve the π^0 mass resolution from 5.7 MeV to

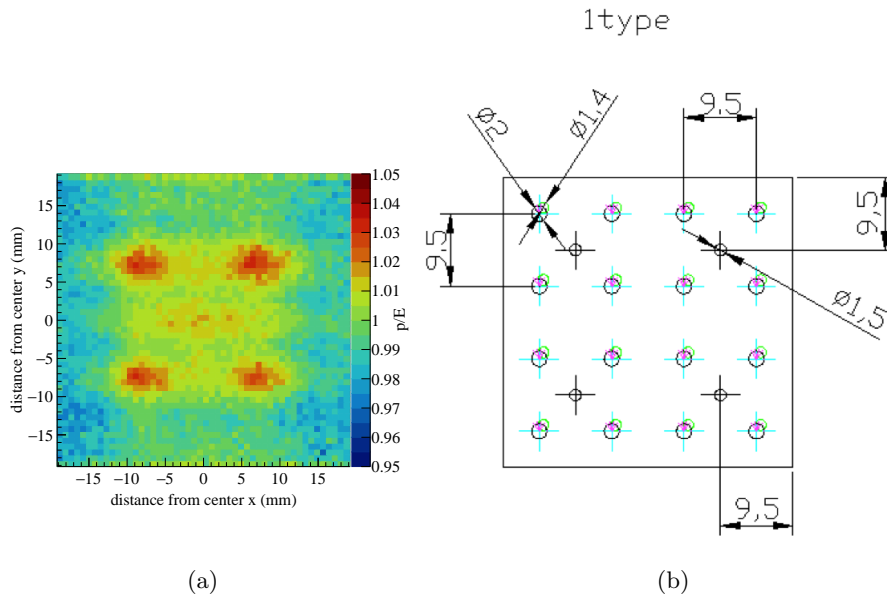


Figure 2.7: (a) Ratio of track momentum over calorimeter energy for electrons with an energy larger than 60 GeV as a function of the impact position on the Shashlyk blocks projected onto a single block. (b) For comparison the sketch of the internal structure of the Shashlyk blocks is shown again (fig. 2.4(b)).

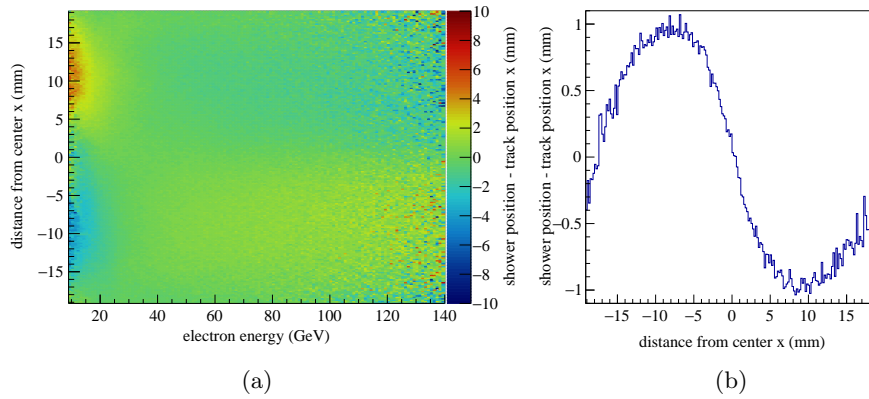


Figure 2.8: Shower position minus electron track position as a function of the transverse distance to the cell center (a) versus the electron energy, and (b) projected for an energy range from 60 GeV to 120 GeV.

4.0 MeV for high-energetic π^0 from Primakoff reactions of a π^- beam impinging on a nickel target producing a $\pi^-\pi^0$ final state [46]. For the analysis presented below, the position-dependent position correction does not have a sizable effect on the π^0 mass resolution, it is therefore not applied.

2.4 Performance on Real Data

The performance of the two electromagnetic calorimeters has been studied in terms of time resolution, and π^0 as well as η mass resolution. To select the data for the performance studies, the same cuts as for the physics analysis presented in chapter 3 are applied. This ensures a clean sample of photons from a known source.

2.4.1 Stability

The stability of the electromagnetic calorimeters was checked by looking at the π^0 signal over time. To separate effects from the two different calorimeters, only π^0 with both photons detected in the same calorimeter were used. For each run, the π^0 mass peak was fitted by a Gaussian plus a third order polynomial (as for the analysis of the mass resolution in section 2.4.3).

In principle the LED/laser corrections (section 2.3) should correct fluctuations that happen with time. For ECAL1, the position of the π^0 mass peak versus run number is indeed stable within 1% (fig. 2.9(a)), but is offset from the nominal π^0 mass despite the π^0 calibration being applied (section 2.3). For ECAL2, the position is also offset, but in addition there is an inexplicable rise around run number 70600 (fig. 2.9(b)). Neither the experimental setup nor the beam intensity were changed at that time. In addition, the width of the π^0 mass peak (fig. 2.10) does not change with time. This suggests that the rise is not the effect of a few bad blocks in ECAL2, but probably either a shift of the calorimeter response as a whole, or that it is not caused by the calorimeter itself. Also the jump around run number 70400 is an artifact of this rise. The whole data set was recorded in three periods, for each period an independent π^0 calibration was prepared. For the last period starting with run number 70450, the calibration was based on runs taken after the rise. Runs taken before the rise accordingly observe a too small π^0 mass introducing the discontinuity between the second and third period.

To correct the shift in the position of the π^0 mass peak, and also the offset with respect to the nominal π^0 mass position, one correction factor for the shower energy was determined per calorimeter and run in an iterative procedure.

However, this does not get rid of all artifacts observed in the calorimeters. Even after this correction the position of the π^0 mass peak in the case of one photon in ECAL1 and the other in ECAL2 is too high by about $1.5 \text{ MeV}/c^2$. Also the position of the η mass peak is found to be approximately $5 \text{ MeV}/c^2$ too low if both photons are detected in the same electromagnetic calorimeter. These effects are not corrected.

2.4 Performance on Real Data

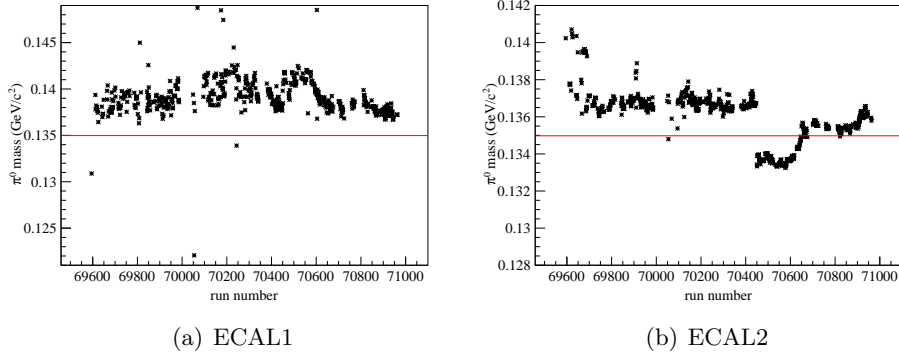


Figure 2.9: Position of the π^0 mass peak versus the run number in (a) ECAL1, and (b) ECAL2. The red line indicates the nominal π^0 mass.

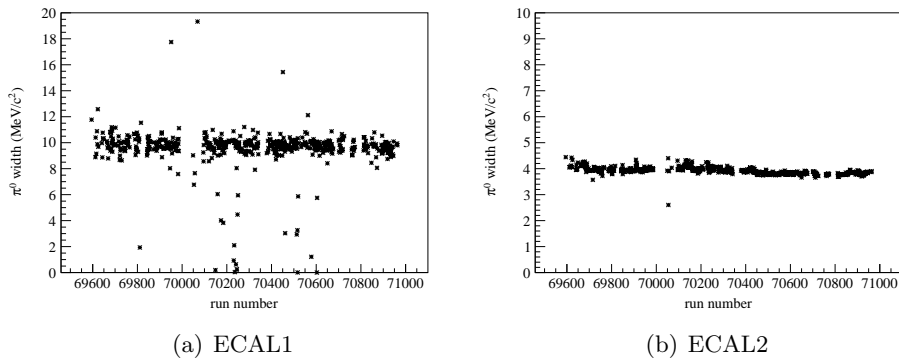


Figure 2.10: Width of the π^0 mass peak versus the run number in (a) ECAL1, and (b) ECAL2. Due to the small amount of π^0 in ECAL1 the fit is bad for some runs.

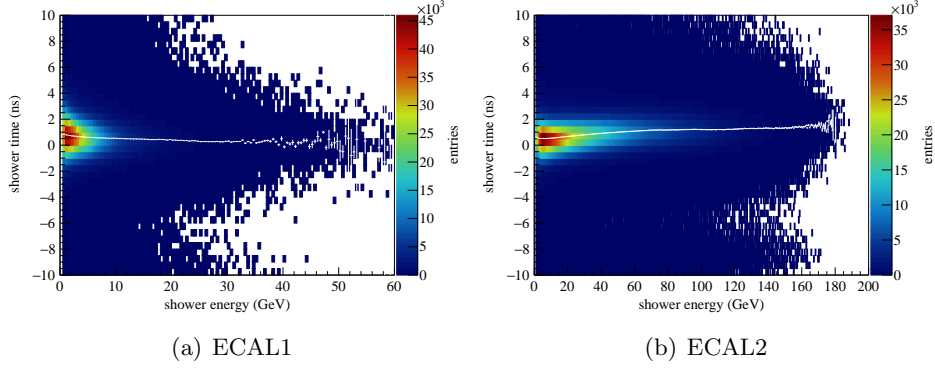


Figure 2.11: Shower time versus shower energy for (a) ECAL1, and (b) ECAL2. The white markers show the mean shower time in each energy slice obtained by fitting a Gaussian.

2.4.2 Time Resolution

The time information provided by the calorimeters is important to suppress noise and off-time particles. Except for a wider cut on the shower times, the same cuts as in chapter 3 are applied. In fig. 2.11 the time of a shower versus its energy is shown. A Gaussian fit was performed in energy slices of 0.5 GeV width. The Gaussians are not centered around zero, this is corrected in the following by parameterizing the offset and shifting the shower times accordingly.

The width of the Gaussians is used to obtain the time resolution (fig. 2.12). The energy dependence of the time resolution is empirically parameterized as the quadratic sum of a constant term and one term falling off with one over the energy. For ECAL1

$$\sigma_t(E) = 1.06 \oplus \frac{0.81}{E} \quad (2.9)$$

and for ECAL2

$$\sigma_t(E) = 0.95 \oplus \frac{1.18}{E} \quad (2.10)$$

For both calorimeters the time resolution for energies above 5 GeV is around 1 ns.

2.4.3 Two-Photon Mass Resolution

The mass resolution for the π^0 is determined from π^0 from the $\pi^-\pi^0\pi^0$ ($\pi^-4\gamma$) channel, the mass resolution of the η from the $\pi^-\eta$ ($\pi^-2\gamma$) channel. To select these final states the selection from chapter 3 is applied. For the $\pi^-\pi^0\pi^0$ final state exactly four ECAL clusters have to survive the cuts, for the $\pi^-\eta$ case exactly two clusters need to pass the cuts.

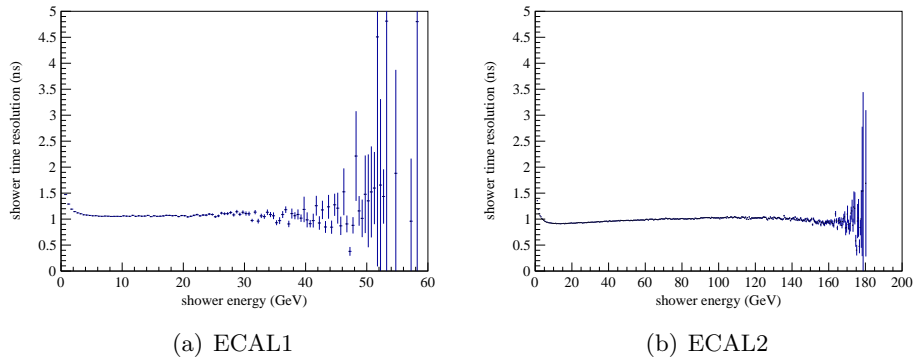


Figure 2.12: Shower time resolution versus shower energy for (a) ECAL1, and (b) ECAL2.

	π^0	η
both photons in ECAL1	8.85 MeV/c ²	24.5 MeV/c ²
both photons in ECAL2	3.88 MeV/c ²	11.6 MeV/c ²
one in ECAL1, one in ECAL2	8.32 MeV/c ²	21.9 MeV/c ²
overall	4.21 MeV/c ²	12.4 MeV/c ²

Table 2.1: Mass resolutions for π^0 and η . The resolutions are extracted from the fits show in fig. 2.14 (π^0) and fig. 2.15 (η).

Figure 2.13 shows the invariant masses of the two photon pairs in $\pi^-4\gamma$ final states versus each other. Dominantly the $\pi^-\pi^0\pi^0$ final state is visible, but there is also a small bump associated to $\pi^-\eta\eta$ final states. With the reconstruction for ECAL2 described above (section 2.3.1) this bump is visible without any further cuts to select η for the first time in COMPASS.

The mass resolutions of the two electromagnetic calorimeters differ mainly due to the different energy ranges, but also due to the different incident angles and reconstruction algorithms. Therefore the mass resolutions for π^0 and η are determined separately for three cases: the π^0 (respectively η) is build from two photons in ECAL1, two photons in ECAL2, or one photon in each electromagnetic calorimeter (see fig. 2.14 for π^0 and fig. 2.15 for η). A fit of a Gaussian plus a third order polynomial to the data is performed, and the width of the Gaussian is taken as the resolution (table 2.1).

2.5 Simulation

As the shower shapes found in real data are not reproduced by the GEANT3 simulation of COMPASS, the calorimeters are specifically calibrated for Monte

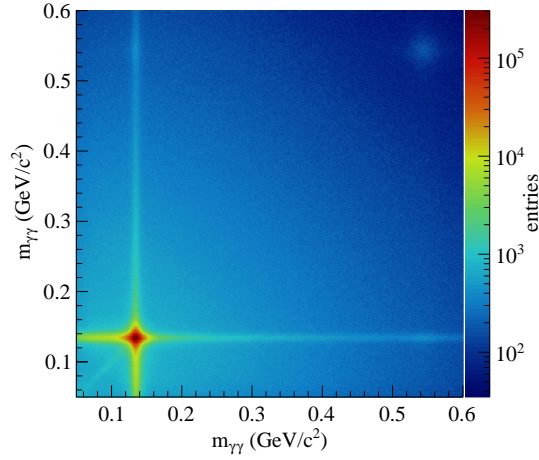


Figure 2.13: Invariant mass of one $\gamma\gamma$ pair versus the mass of the other $\gamma\gamma$ pair for events with four photons (three possible combinations per event). A clear indication of final states with two π^0 is visible, but also smaller contributions of final states with two η can be seen. Note the logarithmic color scale.

Carlo data. For ECAL1 the calibration only comprises the π^0 calibration.

For ECAL2, shower profiles are extracted in the same way as for real data by simulating electron-beam data for both types of GAMS blocks, and Primakoff events for the Shashlyk blocks. Also the π^0 calibration is performed in the same way as for real data. It corrects mostly for losses at high energies due to the limited length of the calorimeter blocks in the very center of the calorimeters.

2.5.1 Single-Photon Acceptance

The acceptance of the studied final states is mostly determined by the reconstruction efficiency of the photons from the decays of π^0 or η . Figure 2.16(a) shows that the single-photon acceptance is rather uniform in the photon energy with a value between 55% and 60% for photon energies above approximately 5 GeV and smaller than 140 GeV. However, the acceptance strongly depends on the direction of the photon (fig. 2.16(b)). The acceptance for photons with the direction $(\Delta x/\Delta z, \Delta y/\Delta z) \approx (0.005, 0)$ drops due to the hole in ECAL2 for the non-interacting beam. The circular shape intersecting with this hole can be attributed to photons that are absorbed in the light gas pipe of the ring-imaging Cherenkov detector (RICH1) in the first spectrometer stage. Further outwards, at $\Delta y/\Delta z \approx \pm 0.02$ the shadows of HCAL1 and SM2 on ECAL2 are visible as a horizontal line, while the vertical lines at $\Delta x/\Delta z \approx \pm 0.04$ stem from a non-perfect overlap of ECAL1 and ECAL2. A general trend of lower acceptance towards the

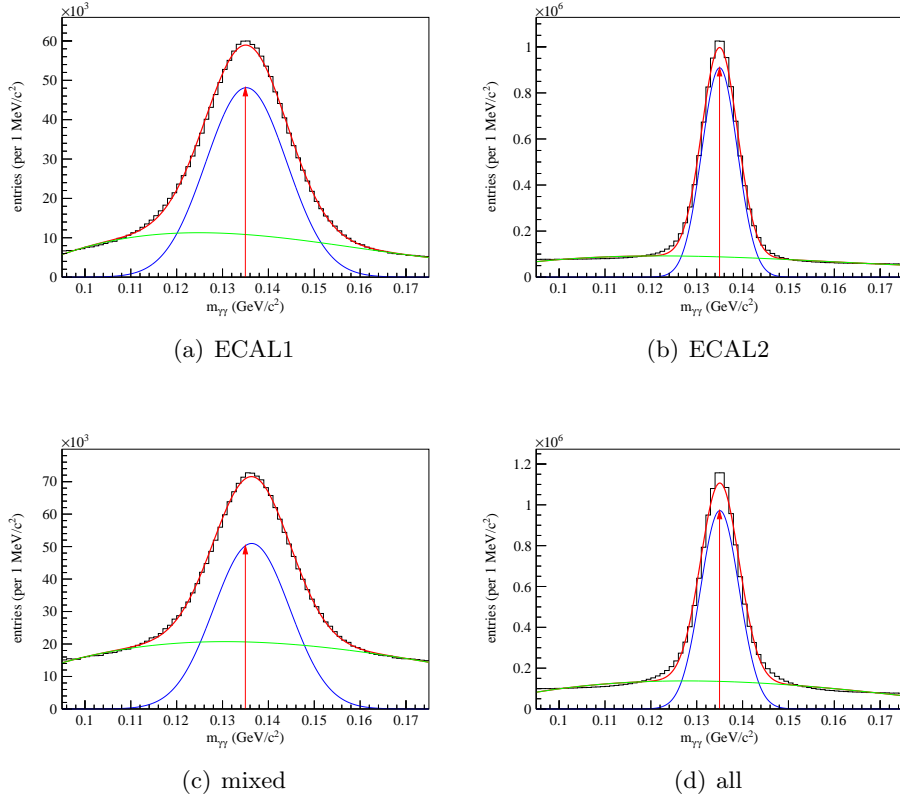


Figure 2.14: Two-photon invariant mass spectra for $\pi^-4\gamma$ final states for cases with (a) both photons detected in ECAL1, (b) both photons detected in ECAL2, and (c) for the mixed case with one photon in ECAL1, and the other in ECAL2. (d) shows the sum of these three cases. The mass spectra are zoomed to the π^0 mass region, the components of the fit are shown in different colors: the Gaussian of the π^0 signal in blue, the polynomial background in green, and the sum of the two in red. The nominal π^0 mass is indicated by the red arrows.

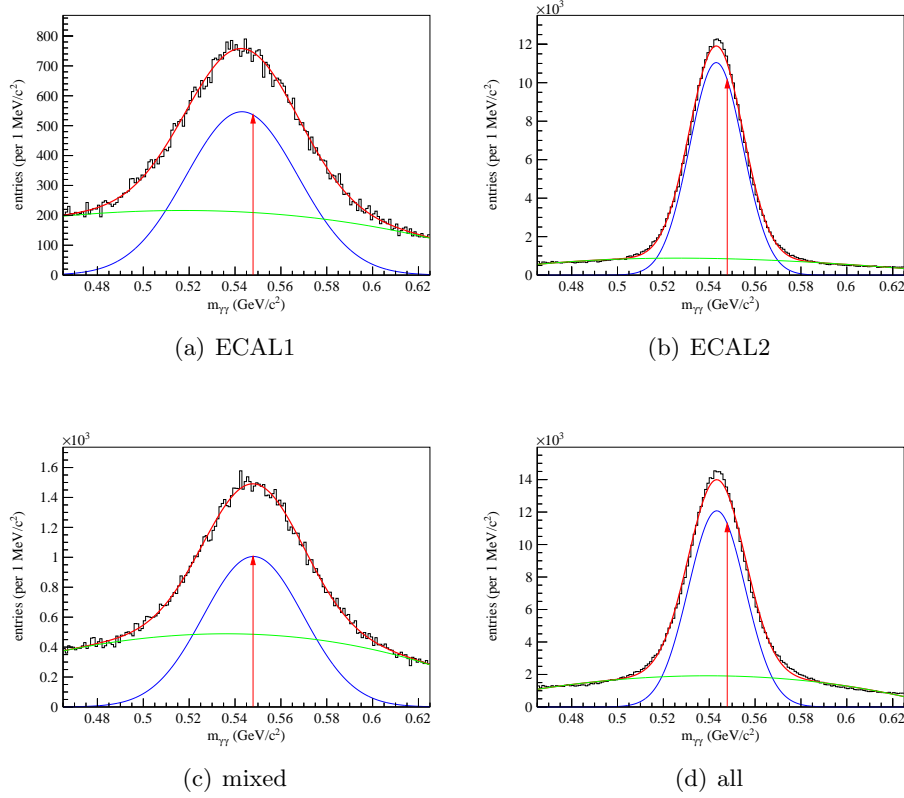


Figure 2.15: Two-photon invariant mass spectra for $\pi^-2\gamma$ final states for cases with (a) both photons detected in ECAL1, (b) both photons detected in ECAL2, and (c) for the mixed case with one photon in ECAL1, and the other in ECAL2. (d) shows the sum of these three cases. The mass spectra are zoomed to the η mass region, the components of the fit are shown in different colors: the Gaussian fit to the η signal in blue, the polynomial background in green, and the sum in red. The nominal η mass is indicated by the red arrows.

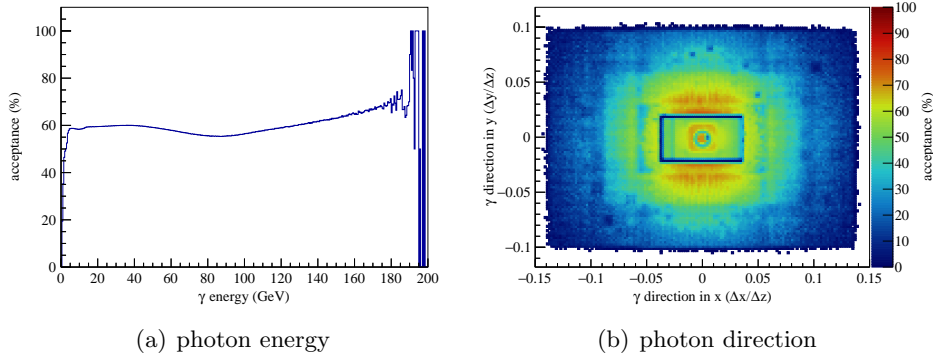


Figure 2.16: Single-photon acceptance depending on (a) the photon energy and (b) the direction of the photon in the laboratory system.

outer regions is also visible. Figure 2.17 shows the same information for four different energy ranges. For energies above the thresholds applied in the analysis (0.6 GeV for ECAL1 and 1.2 GeV for ECAL2), the acceptance for single photons appears to be rather uniform across the calorimeter surface (with the exception of the aforementioned holes, and, presumably, some detector frames showing up in ECAL1). Hence the lower acceptance towards the outer regions is caused by the loss of photons with an energy below the ECAL1 threshold. This is confirmed by fig. 2.17(c) and fig. 2.17(d) indicating that the circular area illuminated by photons of a certain energy becomes larger with lower photon energies. The lower acceptance in the outer regions can therefore simply be explained by the large fraction of undetectable photons below threshold that go into this region.

2.5.2 Two-Photon Mass Resolution

The π^0 mass resolution in Monte Carlo data is compared to the mass resolution in real data in fig. 2.18 after all cuts of the event selection (chapter 3) are applied. A comparatively good agreement is found if both photons are detected in ECAL2. In Monte Carlo data the π^0 seems to sit on a lower background, but the width agrees. As soon as one (or more) photon is detected in ECAL1 the mass distributions differ significantly. The resolution in real data is about a factor of 1.5 worse than it is for Monte Carlo data. While for the mixed case the π^0 peak is shifted up by about $1.5 \text{ MeV}/c^2$ for real data, such a shift is not visible in the Monte Carlo case.

The comparison of the η signal in the calorimeters (fig. 2.19) reveals more differences than seen in the π^0 case. While in real data the position of the η peak is shifted down by almost $5 \text{ MeV}/c^2$ for ECAL2, it is closer to the PDG mass in Monte Carlo. Also the width for Monte Carlo is smaller than for real data, and the η is sitting on a lower background. The comparison for ECAL1 is even worse. The η are reconstructed with an about $2 \text{ MeV}/c^2$ too high mass in Monte Carlo,

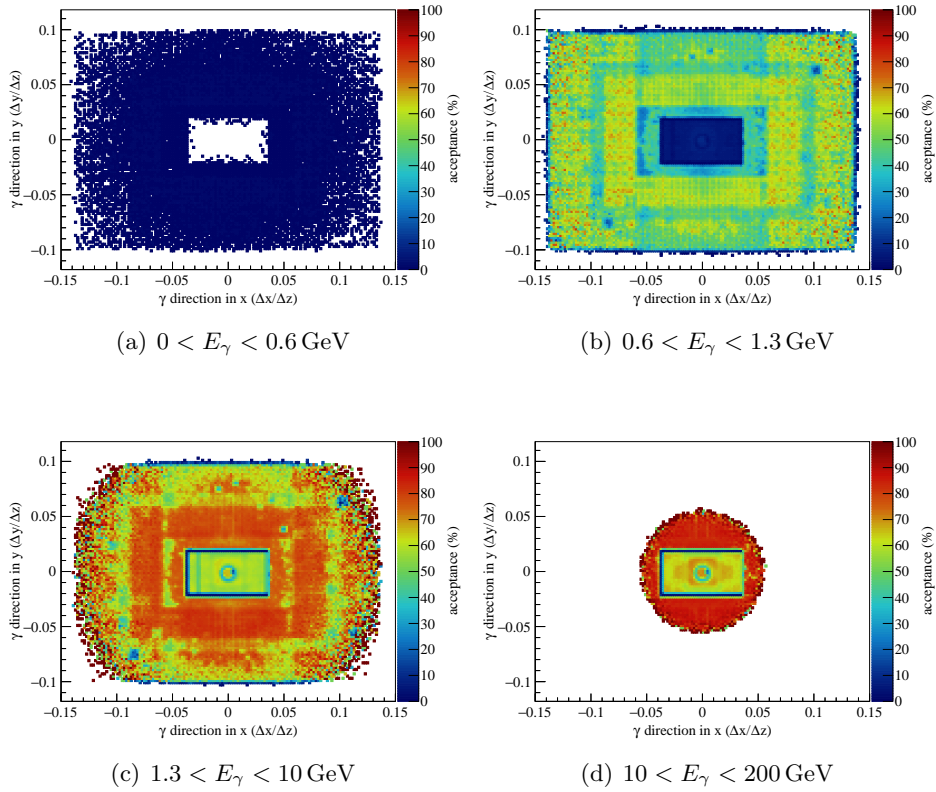


Figure 2.17: Single-photon acceptance depending on the direction of the photon in the laboratory system for four different energy regions.

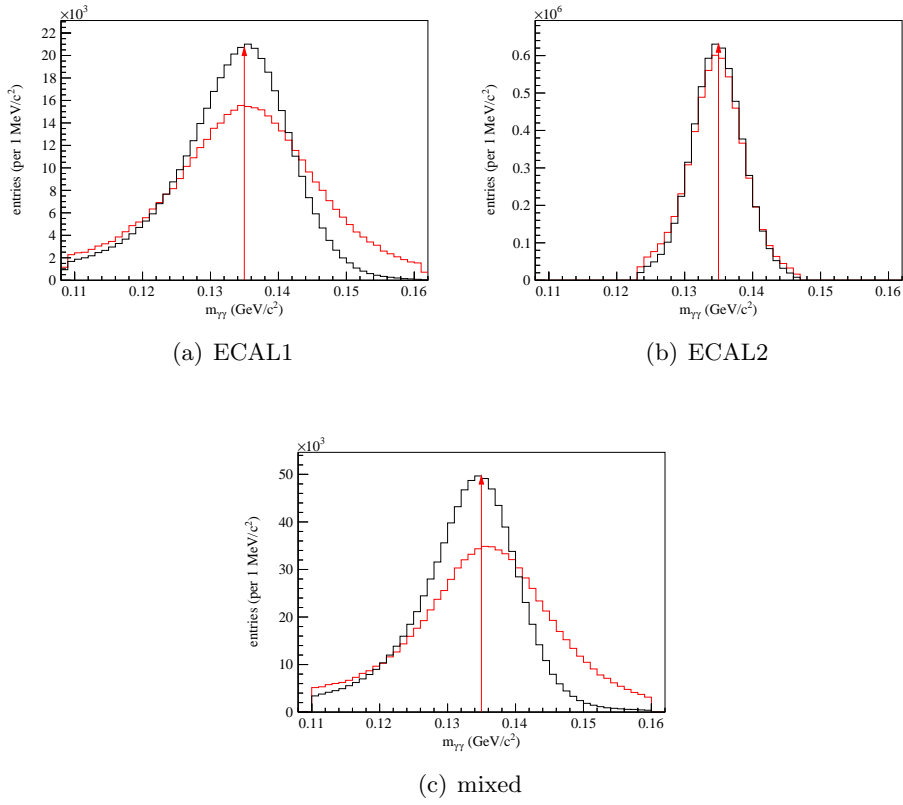


Figure 2.18: Two-photon invariant mass spectra for $\pi^-\pi^0\pi^0$ final states for cases with (a) both photons detected in ECAL1, (b) both photons detected ECAL2, and (c) for the mixed case with one photon in ECAL1, and the other in ECAL2. The mass spectra are zoomed to the π^0 mass region, Monte Carlo data is shown in black, real data in red. The nominal π^0 mass is indicated by the red arrows.

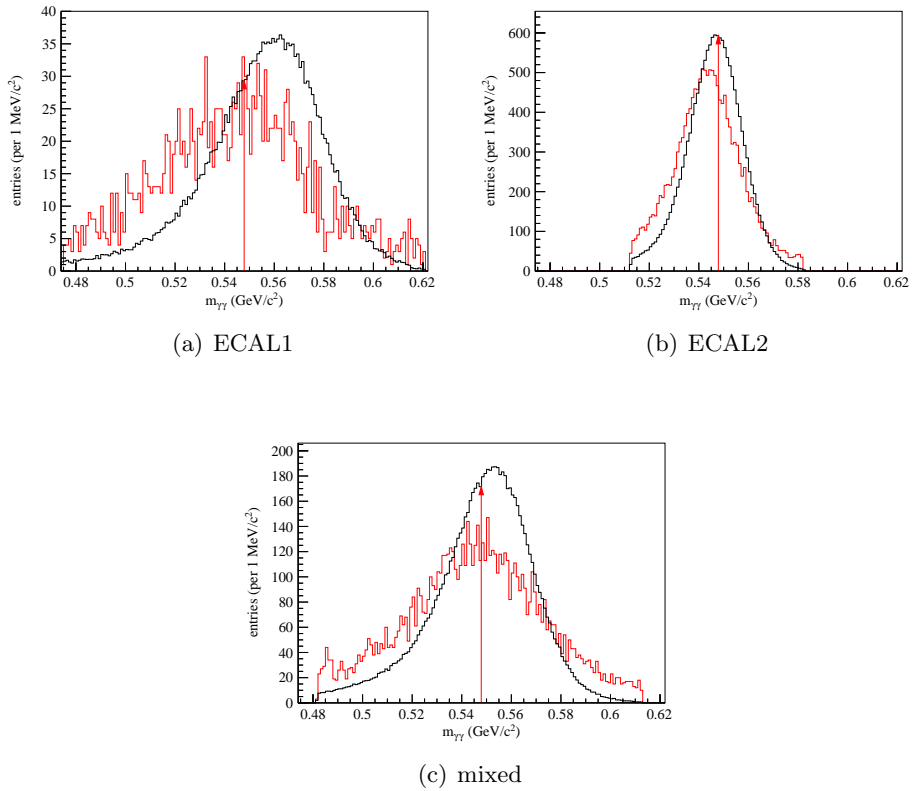


Figure 2.19: Two-photon invariant mass spectra for $\pi^- \eta \eta$ final states for cases with (a) both photons detected in ECAL1, (b) both photons detected in ECAL2, and (c) for the mixed case with one photon in ECAL1, and the other in ECAL2. The mass spectra are zoomed to the η mass region, Monte Carlo data is shown in black, real data in red. The nominal η mass is indicated by the red arrows.

and with a significantly better mass resolution.

Chapter 3

Event Selection

The COMPASS experiment has recorded data with a 190 GeV negative pion beam impinging on a liquid-hydrogen target for six weeks in 2008. Using these data, final states with one π^- plus two π^0 , or two η , respectively, are studied. Only the two-photon decays of the π^0 and η are considered in the following. A series of cuts is applied to the initial data set containing $7.4 \cdot 10^9$ events to select only those events that have the signatures of the two desired final states. The number of events surviving each cut are listed in table 3.1.

3.1 Preselection

The purpose of the preselection is mainly to reduce the size of the data set by removing only uninteresting events. The cuts explained in this section reduce the number of events by more than a factor of 10 from $7.4 \cdot 10^9$ to $6.5 \cdot 10^8$ events. To further reduce the amount of data, only the information relevant for the later analysis is kept.

3.1.1 DT0 Trigger

The diffractive trigger (DT0) has been the main physics trigger for the analyzed data. It selects events where the incoming beam particle reacted with a proton inside the liquid-hydrogen target. The outgoing proton is identified via its energy loss in the two cylindrical layers of the recoil-proton detector (RPD, section 1.1, [2]). The squared four-momentum transfer t to the target (section 3.4.4) has to be larger than about $0.07 \text{ (GeV}/c)^2$ to reach both layers. If t is larger than $4.5 \text{ (GeV}/c)^2$, the recoil proton is leaving the target with angles too small to reach the RPD [39].

The trigger signal is formed by the coincidence of a proton signal in the RPD and the presence of an incoming beam particle. The beam particle is detected by a scintillating fiber detector (FI01X dynode signal) and a scintillator disc (beam counter) upstream of the target. At the same time the two scintillator discs downstream of the second spectrometer magnet and the sandwich detector just downstream of the target are required to have no signal. These veto detectors remove events with non-interacting beam and events with particles outside of

	$\pi^- \pi^0 \pi^0$	$\pi^- \eta \eta$
preselection - part 1		
	number of events	
all events	7 389 600 316	100.0 %
DT0 trigger	5 594 989 610	75.7 %
exactly one primary vertex	4 511 796 725	61.1 %
exactly one outgoing track	2 524 071 421	34.2 %
charge unchanged by vertex fit	2 523 925 264	34.2 %
charge conservation in vertex	2 442 511 364	33.1 %
two or more ECAL showers	1 286 750 904	17.4 %
preselection - part 2		
	number of events	
from preselection	1 286 750 904	100.0 %
four or more ECAL showers	835 904 683	65.0 %
RPD reconstruction	653 563 674	50.8 %
selection of calorimeter clusters		
	number of clusters	
from preselection	5 532 424 006	100.0 %
energy threshold	2 831 816 141	51.2 %
time resolution	2 793 860 445	50.5 %
after both cuts	1 933 026 718	34.9 %
selection of neutral particles		
	number of events	number of events
from preselection - part 2	653 563 674 100.0 %	653 563 674 100.0 %
exactly four ECAL showers	74 353 927 11.4 %	74 353 927 11.4 %
exactly two π^0/η candidates	21 553 043 3.3 %	328 632 0.050 %
after both cuts	7 667 337 1.2 %	67 561 0.010 %
kinematic selection		
	number of events	number of events
from selection of neutral particles	7 667 337 100.0 %	67 561 100.0 %
vertex position	6 961 698 90.8 %	52 763 78.1 %
beam energy	6 008 822 78.4 %	22 213 32.9 %
coplanarity	6 014 344 78.4 %	30 031 44.5 %
t'	5 780 253 75.4 %	47 325 70.0 %
mass range for PWA	6 693 763 87.3 %	62 969 93.2 %
after all cuts	3 604 322 47.0 %	13 157 19.5 %

Table 3.1: Number of events after each cut applied during the event selection for real data.

the spectrometer acceptance. All events used in the analysis have to have been recorded due to the DT0 trigger.

3.1.2 Primary Vertex

Tracks of charged particles are used to reconstruct interaction and decay vertices. In COMPASS, a vertex with an incoming beam particle is called primary vertex. To be considered in the following, each event must have one primary vertex. Events with multiple primary vertices, which might be caused by multiple beam particles entering the experiment at the same time, are discarded. For the analysis only vertices with exactly one outgoing charged particle are interesting. As electric charge is conserved, the outgoing particle needs to have negative charge.

One peculiarity of the vertex fit is, that it can alter the electric charge of a track. More precisely, if the uncertainty of $q/|p|$ from the track fit [1, 2] is large compared to its value, then the vertex fit [1] might achieve a better result when changing the sign of the electric charge. Vertices containing tracks for which the electric charge of the vertex fit does not agree with the electric charge of the track fit are removed.

3.1.3 Photons

To be able to build two π^0 or two η at least four photons are required. As the first step to identify photons, showers in the electromagnetic calorimeters that do not have an associated charged track are selected. This criterion simply selects events with enough photon candidates, it does not yet ensure that the showers are indeed photons.

3.1.4 RPD Reconstruction

The track of the recoil proton is reconstructed from the RPD information [2]. This includes an energy measurement in the outer layer of the detector, and a velocity measurement via the time-of-flight between the inner and outer layer. From the time difference of the signals from the up- and downstream end of the detector, it is also possible to estimate the hit position along the beam axis in either layer, allowing the rough measurement of the scattering angle of the recoil proton and of the vertex position. This vertex position should at least be in the vicinity of the liquid-hydrogen target.

3.2 Calorimeter Information

3.2.1 Energy Thresholds for Photons

To reduce the impact of noise on the π^0 and η signals, showers with a too small energy are removed from the data set. But these showers might also be genuine photons originating from low energetic π^0 or from asymmetric π^0 decays. So

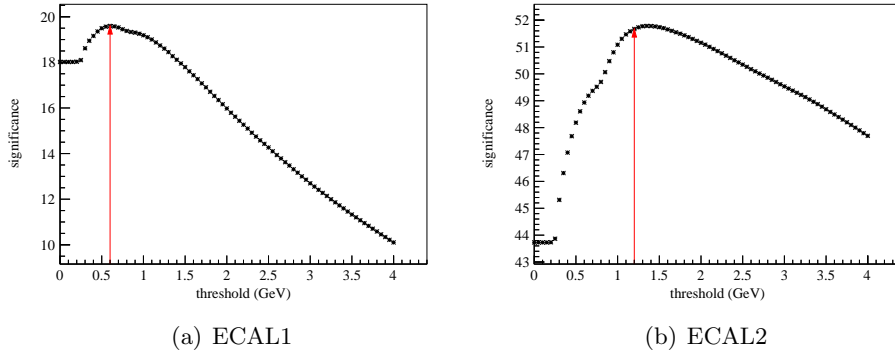


Figure 3.1: Significance of the π^0 mass peak as a function of the applied calorimeter threshold for (a) ECAL1 and (b) ECAL2.

setting the energy threshold too low will harm the acceptance. To optimize the threshold, a significance measure is used as an objective criterion [68]

$$\text{significance} = \frac{\text{signal}}{\sqrt{\text{signal} + \text{background}}} \quad (3.1)$$

The significance of the π^0 mass peak is calculated for various thresholds ranging from 0 to 4 GeV. As the energy range of the two electromagnetic calorimeters is very different, both are treated separately by only looking at those π^0 with both photons in the respective calorimeter. The position and width of the π^0 mass peak are determined from a Gaussian fit (section 2.4.3). The amount of signal is taken from the full integral of the Gaussian, the amount of background from the integral of the background function over a 70 MeV wide mass window around the peak position.

Figure 3.1 shows the significance as a function of the applied threshold. At low thresholds below 0.2 GeV the significance does not change, because here the threshold applied during the reconstruction (section 2.3) already removed the showers. The bumps visible in the spectra are identified with different hardware thresholds caused by, e.g., different amplification settings for outer and inner cells. The threshold applied in this analysis is found by searching for the maximum of the significance for each calorimeter. The thresholds used in the following are 0.6 GeV for ECAL1, and 1.2 GeV for ECAL2.

3.2.2 Time Information

The time information for the showers is used to remove noise and off-time photons. The time resolution of the calorimeters was already shown in fig. 2.12 in section 2.4.2. A 3σ cut on the time of a shower is performed.

3.3 Selection of Neutral Particles

The next step in the event selection is to build candidates for the π^0 or η particles decaying into two photons. Only events with exactly four photons are considered. To construct the Lorentz vectors of the photons it is assumed that they originate from the primary vertex. The Lorentz vectors of each photon pair are summed, and the pair is considered a π^0 candidate if its invariant mass does not differ from the nominal π^0 mass by more than three times the $m_{\gamma\gamma}$ resolution obtained in section 2.4.3. After all possible candidates have been built, they are checked for shared photons. Candidates that share one of their photons with any other candidate are not considered in the following. In the end only two π^0 candidates per event are allowed to remain.

The selection of η for the $\pi^-\eta\eta$ final state is very similar. In addition to building η candidates, also π^0 candidates are formed. It is then checked that none of the photons that are used in a π^0 candidate also contribute to any η candidate. In the end only two η candidates per event are allowed to remain. However, if it were not for the requirement of exactly four photons, any number of π^0 candidates could exist in addition.

Reconstructing the neutral particles reduces the number of events to consider in the analysis from $6.5 \cdot 10^8$ to $7.7 \cdot 10^6$ for the $\pi^-\pi^0\pi^0$ case and to $6.7 \cdot 10^4$ for $\pi^-\eta\eta$.

3.4 Kinematic Selection

Before further usage of the π^0 or η candidates in the analysis, the mass of each π^0 or η candidate is set to the nominal mass by rescaling the energy of the photons. The event selection is then finalized with the cuts discussed in this section. These cuts reduce the number of $\pi^-\pi^0\pi^0$ events to consider in the analysis from $7.7 \cdot 10^6$ after the reconstruction of the neutral particles to $3.6 \cdot 10^6$, and respectively from $6.7 \cdot 10^4$ to $1.3 \cdot 10^4$ for the $\pi^-\eta\eta$ case.

3.4.1 Vertex Position

To ensure an interaction of the beam pion with a free proton, the primary vertex has to be within the volume of the liquid-hydrogen target. The position of the vertex along the beam axis has to lie between -68 cm and -28 cm, the radial distance from the nominal beam axis has to be smaller than 1.5 cm (figs. 3.2 and 3.3).

3.4.2 Beam Momentum

The longitudinal component of the beam momentum is not measured for the hadron beam, but it can be calculated from the information of the outgoing system and the scattering angle between the beam direction and the direction of the final

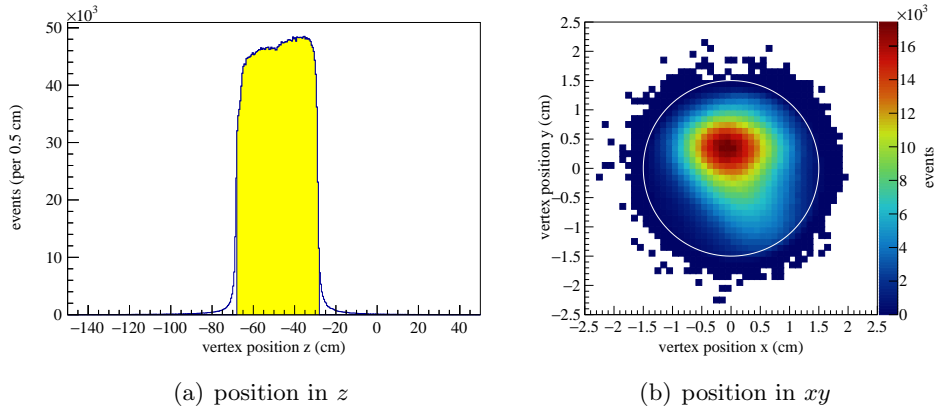


Figure 3.2: Distribution of the position of the interaction vertex for the $\pi^- \pi^0 \pi^0$ final state (a) along the z -direction and (b) in the plane perpendicular to the z -direction. The yellow area in (a) and the white circle in (b) indicate the selected ranges.

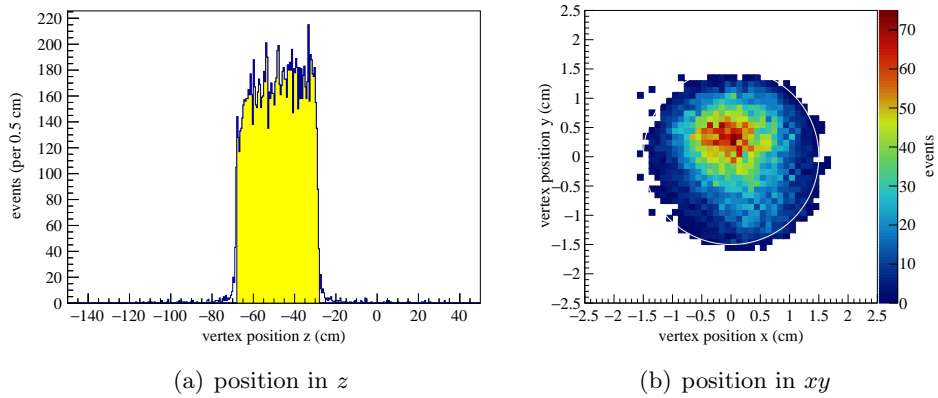


Figure 3.3: Distribution of the position of the interaction vertex for the $\pi^- \eta \eta$ final state (a) along the z -direction and (b) in the plane perpendicular to the z -direction. The yellow area in (a) and the white circle in (b) indicate the selected ranges.

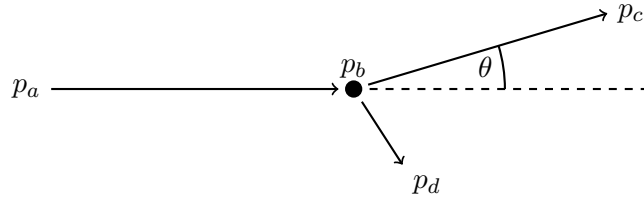


Figure 3.4: Sketch of the reaction of an incoming beam particle p_a with a target particle p_b initially at rest. Particles p_c and p_d are the products of the reaction.

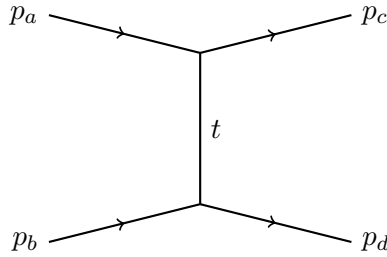


Figure 3.5: Definition of particle momenta and Mandelstam variable t .

state assuming an exclusive measurement. The following information is available (fig. 3.4)

- The **beam particle** is a pion, therefore its mass m_π is known ($p_a^2 = E_a^2 - |\vec{p}_a|^2 = m_\pi^2$). Its direction is precisely measured using the silicon beam telescope.
- The **target particle** is a proton with mass m_p that is assumed to be at rest ($\vec{p}_b = 0$ and $p_b^2 = m_p^2$).
- The **outgoing system** has a fully measured four-vector p_c with $p_c^2 = E_c^2 - |\vec{p}_c|^2 = m_c^2$. p_c is the sum of the measured four-vectors of the final-state particles. With the information on the direction of the beam particle the scattering angle $\theta = \angle(\vec{p}_a, \vec{p}_c)$ is known.
- The **recoil particle** is a proton with mass m_p ($p_d^2 = E_d^2 - |\vec{p}_d|^2 = m_p^2$). In principle the recoil-proton detector gives information on the velocity (via time of flight) and energy (via the energy deposit) of the recoiling proton but with a much worse resolution compared to the variables measured by the spectrometer. Therefore this information will not be used in the following.

The Mandelstam variable t (fig. 3.5) can be written in two ways

$$t = (p_a - p_c)^2 \quad (3.2)$$

$$= m_\pi^2 + m_c^2 - 2p_a p_c \quad (3.3)$$

$$= m_\pi^2 + m_c^2 - 2E_a E_c + 2|\vec{p}_a| |\vec{p}_c| \cos \theta \quad (3.4)$$

and

$$t = (p_d - p_b)^2 \quad (3.5)$$

$$= 2m_p^2 - 2m_p E_d \quad (3.6)$$

$$= 2m_p^2 - 2m_p (E_a + m_p - E_c) \quad (3.7)$$

$$= -2m_p (E_a - E_c) \quad (3.8)$$

avoiding the usage of information on the recoil particle. Combining eqs. (3.4) and (3.8) gives

$$m_\pi^2 + m_c^2 - 2E_a E_c + 2|\vec{p}_a| |\vec{p}_c| \cos \theta = 2m_p (E_c - E_a) \quad (3.9)$$

$$m_\pi^2 + m_c^2 - 2m_p E_c + 2|\vec{p}_a| |\vec{p}_c| \cos \theta = 2E_a (E_c - m_p) \quad (3.10)$$

$$m_\pi^2 + m_c^2 - 2m_p E_c + 2|\vec{p}_a| |\vec{p}_c| \cos \theta = 2\sqrt{m_\pi^2 + |\vec{p}_a|^2} (E_c - m_p) \quad (3.11)$$

Squaring eq. (3.11) and ordering the terms by powers of $|\vec{p}_a|$, one obtains a quadratic equation for $|\vec{p}_a|$

$$\begin{aligned} 0 = & \left(4|\vec{p}_c|^2 \cos^2 \theta - 4(E_c - m_p)^2 \right) |\vec{p}_a|^2 \\ & + 4|\vec{p}_c| \cos \theta (m_\pi^2 + m_c^2 - 2m_p E_c) |\vec{p}_a| \\ & + (m_\pi^2 + m_c^2 - 2m_p E_c)^2 - [2m_\pi (E_c - m_p)]^2 \end{aligned} \quad (3.12)$$

Only the positive solution of the quadratic equation is physically meaningful, so that the beam momentum and finally the beam energy can be calculated.

The Gaussian peak of the beam energy distribution (fig. 3.6) is at 190.6 GeV, and has a width of 2.9 GeV. Events to be considered in the further processing need to have a calculated beam energy that is at maximum three times the width away from the peak position.

3.4.3 Momentum Conservation

The direction of the outgoing system as measured in the spectrometer has to be back to back with respect to the direction of the recoil proton measured by the RPD in the plane transverse to the beam (fig. 3.7). The resolution of this coplanarity is mainly limited by the 12-fold segmentation of the inner ring of the RPD. The angle between the two directions, as measured in the reference system of the incoming beam particle, has to be between $\pi - 0.27$ rad and $\pi + 0.27$ rad.

3.4 Kinematic Selection

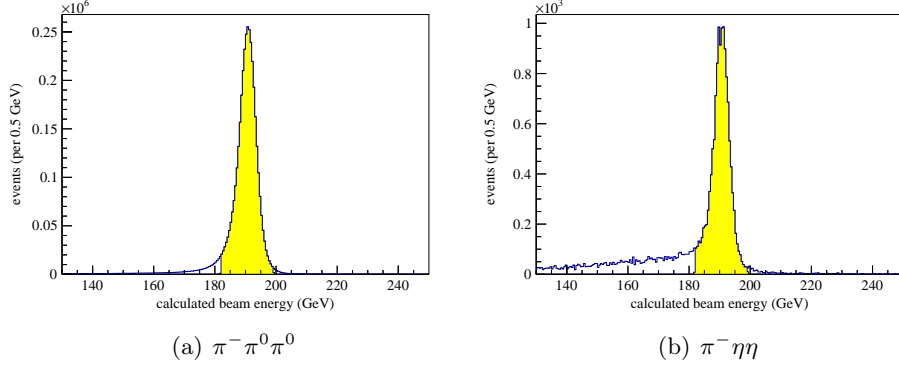


Figure 3.6: Calculated beam energy for (a) the $\pi^- \pi^0 \pi^0$ and (b) the $\pi^- \eta \eta$ final state. The yellow areas indicate the selected ranges.

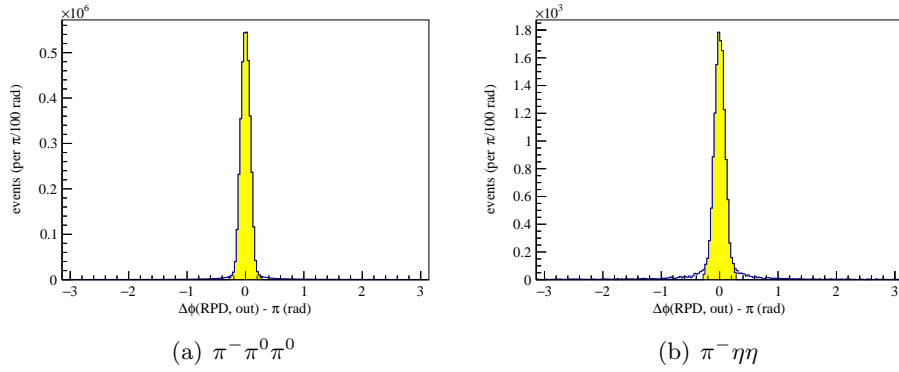


Figure 3.7: Coplanarity of the recoil proton and (a) the $\pi^- \pi^0 \pi^0$ and (b) the $\pi^- \eta \eta$ final state. The yellow areas indicate the selected ranges.

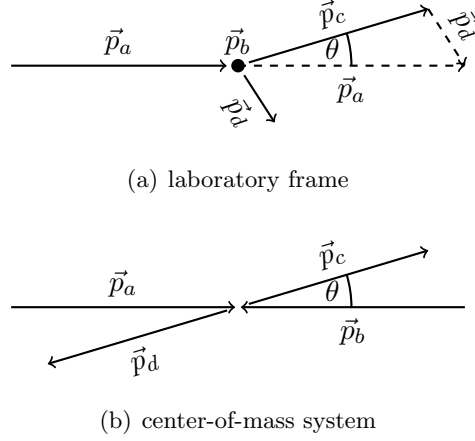


Figure 3.8: Three-momentum conservation of the reaction in (a) the laboratory frame and (b) the center-of-mass system.

3.4.4 Reduced Squared Four-Momentum Transfer t'

The squared four-momentum transfer t to the target is used to characterize the reactions under study. Using the more precisely measured four-momenta of beam and scattered particle, it can be written as

$$t = (p_a - p_c)^2 = m_\pi^2 + m_c^2 - 2E_a E_c + 2|\vec{p}_a| |\vec{p}_c| \cos \theta \quad (3.13)$$

A minimal squared four-momentum transfer $|t|_{\min}$ is required to create a state with mass $m_c \geq m_\pi$. It corresponds to the squared four-momentum transfer for the production of a state with mass m_c at scattering angle $\theta = 0$. Figure 3.8 shows that it is not possible to simply set $\cos \theta = 1$ in eq. (3.13), as changing the scattering angle θ while keeping the magnitude of \vec{p}_c constant would affect the magnitude of \vec{p}_d , which in turn would violate the requirement of having a recoil proton as the energies would not be affected by the rotation. In the center-of-mass system the three-momenta of the outgoing system and the recoil proton are back-to-back with the same magnitude. Changing the scattering angle does not necessitate a change of the magnitude to conserve the total three-momentum. With the kinematic variables in the center-of-mass system $|t|_{\min}$ is given as

$$|t|_{\min} = 2 \left(E_a^{\text{CM}} E_c^{\text{CM}} + |\vec{p}_a|^{\text{CM}} |\vec{p}_c|^{\text{CM}} \right) - m_\pi^2 - m_c^2 \quad (3.14)$$

Finally the reduced squared four-momentum transfer t' is defined as

$$t' = |t| - |t|_{\min} \quad (3.15)$$

While t is a negative number, with this definition, t' is a positive quantity. The analysis is performed in the t' range from 0.1 to 1 $(\text{GeV}/c)^2$ (fig. 3.9).

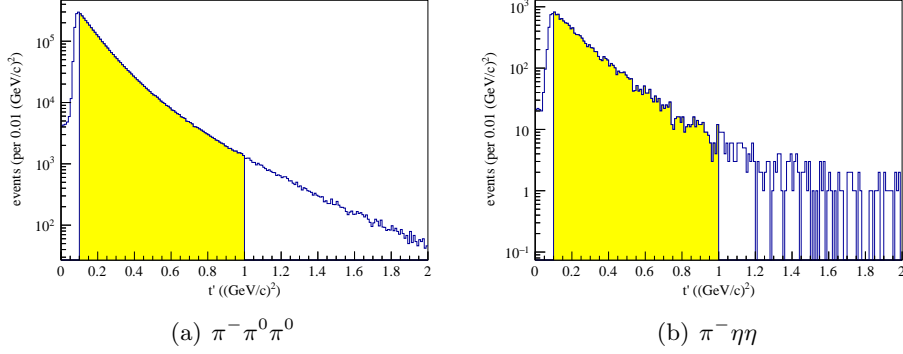


Figure 3.9: Reduced squared four-momentum transfer t' for (a) the $\pi^- \pi^0 \pi^0$ and (b) the $\pi^- \eta \eta$ final state. The yellow areas indicate the selected ranges.

The slope of the t' distribution is related to the production mechanism. Two exponentials are required for a good description of the data. For the $\pi^- \pi^0 \pi^0$ final state one obtains

$$e^{-9.93 (\text{GeV}/c)^{-2} \cdot t'} + 0.0878 \cdot e^{-3.83 (\text{GeV}/c)^{-2} \cdot t'} \quad (3.16)$$

and for the $\pi^- \eta \eta$ final state

$$e^{-7.25 (\text{GeV}/c)^{-2} \cdot t'} + 0.0905 \cdot e^{-3.36 (\text{GeV}/c)^{-2} \cdot t'} \quad (3.17)$$

In both cases the slope of the dominant component has a value consistent with Pomeron exchange.

The $\pi^- \pi^0 \pi^0$ mass spectrum exhibits a pronounced dependance on the selected t' range (fig. 3.10). The relative strength of the shoulder on the low-mass side of the peak at $1.3 \text{ GeV}/c^2$ decreases with increasing t' . At the same time, for higher invariant masses, the spectrum changes only little. Accordingly the t' distribution depends on the mass of the final state (fig. 3.11). While two exponentials are required to describe the total t' spectrum as well as the t' spectrum at low invariant masses of the final state clearly requires two slopes (fig. 3.11(a)), at higher masses, a single exponential seems to be sufficient (fig. 3.11(b)). To minimize the effect of the dependence of the mass spectrum on t' , for the analysis of the $\pi^- \pi^0 \pi^0$ final state, the data set is subdivided into eight non-equidistant t' bins, each containing about the same number of events (table 3.2).

3.4.5 Mass Ranges for Partial-Wave Analysis

The mass ranges selected for the partial-wave analysis (chapters 5 and 6) are $0.5 \text{ GeV}/c^2$ to $2.5 \text{ GeV}/c^2$ for the $\pi^- \pi^0 \pi^0$ channel and $1.25 \text{ GeV}/c^2$ to $4 \text{ GeV}/c^2$ for the $\pi^- \eta \eta$ channel (fig. 3.12).

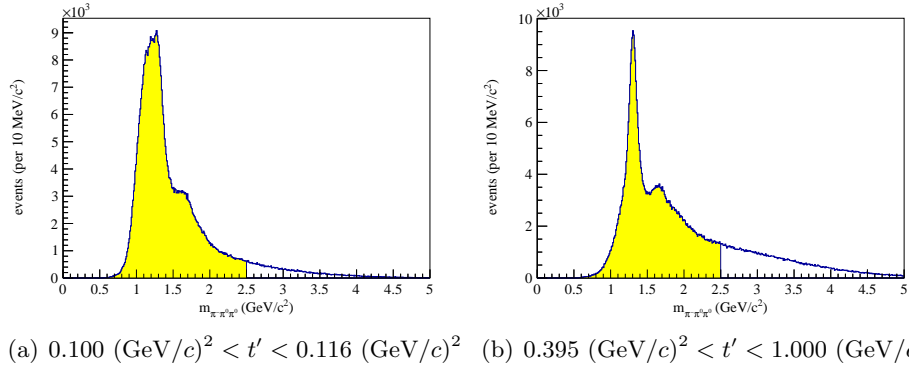


Figure 3.10: Invariant mass of the $\pi^-\pi^0\pi^0$ final state at (a) low and (b) high t' values. The mass spectrum for the t' range from 0.1 to 1.0 $(\text{GeV}/c)^2$ is shown in fig. 3.12(a). The yellow areas indicate the selected mass ranges.

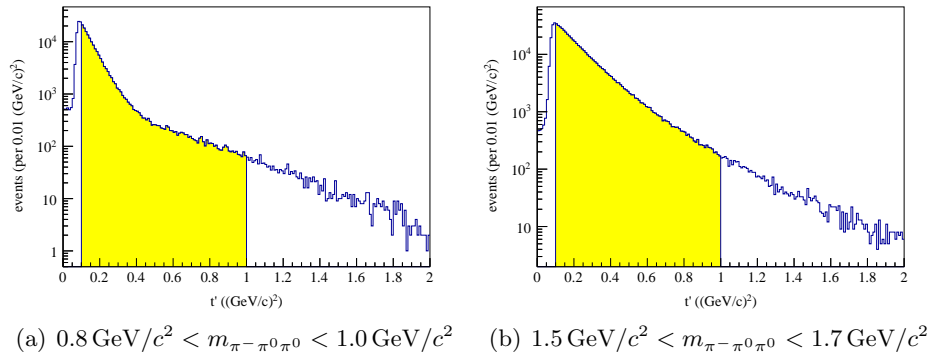
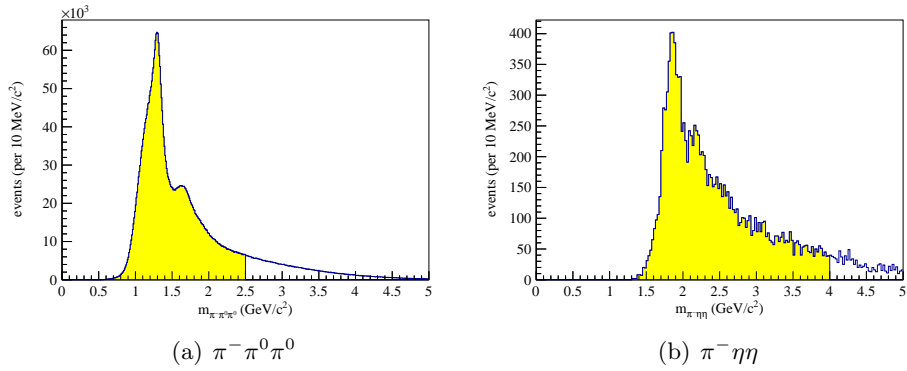


Figure 3.11: Reduced squared four-momentum transfer t' at (a) low and (b) high invariant masses of the final state. The t' distribution for the complete mass range is shown in fig. 3.9(a). The yellow areas indicate the selected ranges.

bin nr.	t' range (GeV/c) ²	number of events
1	0.100 - 0.116	446 584
2	0.116 - 0.136	452 057
3	0.136 - 0.159	454 041
4	0.159 - 0.188	451 267
5	0.188 - 0.227	450 540
6	0.227 - 0.285	448 456
7	0.285 - 0.395	450 010
8	0.395 - 1.000	451 367

Table 3.2: Number of events in the t' bins.Figure 3.12: Invariant mass spectra for (a) the $\pi^- \pi^0 \pi^0$ and (b) the $\pi^- \eta \eta$ final state. The yellow areas indicate the selected ranges.

3.5 Simulation

To evaluate the acceptance of the COMPASS spectrometer, events are generated flat in the phase-space of the final state. These events are then tracked through the spectrometer with a simulation of the response of all detectors, and reconstructed with the same software used for real data. Finally, the reconstructed Monte Carlo events are analyzed with the same cuts as applied for real data.

Vertices for the events are only generated inside the volume of the liquid-hydrogen target. The beam properties including the various correlations between the beam momentum, beam position and beam slope are taken into account [24]. The reduced squared four-momentum transfer t' is simulated in the range from 0.1 to 1.0 $(\text{GeV}/c)^2$ according to the slope parameters extracted for the $\pi^-\pi^0\pi^0$ (eq. (3.16)) and $\pi^-\eta\eta$ final state (eq. (3.17)), respectively. The events are evenly distributed in the mass range used for the partial-wave analysis.

3.5.1 $\pi^-\pi^0\pi^0$ Final State

In total $3 \cdot 10^8$ Monte Carlo events were generated and reconstructed for the $\pi^-\pi^0\pi^0$ final state. The events were analyzed in the same way as real data, the effects of the cuts applied during the selection are listed in table 3.3.

Figure 3.13 compares the number of generated phase-space events with the number of phase-space events accepted by the event selection and the number of real data events. From the $3 \cdot 10^8$ generated events almost $1.4 \cdot 10^7$ are accepted after all cuts. The number of events in the mass bin with the most real data events is similar to the number of Monte Carlo events accepted in that bin. For other mass bins, significantly more accepted Monte Carlo events than real data events are available. From the event counts given before, the average phase-space acceptance is 4.5% for the selected kinematic region. Figure 3.14(a) shows this acceptance as a function of the mass of the final state. The acceptance averaged over the t' bins increases from around 2.5% at low masses to 6% at high masses. The same trend is also visible in the individual t' bins, however, while the acceptance at high masses stays about the same for each t' bins, at lower masses it decreases from almost 3% in the lowest t' bin to slightly less than 2% in the highest t' bin. The larger acceptance towards higher masses can be explained with the larger angles between the outgoing three pions in the laboratory system. This also leads to larger angles of the single photons. As photons with a larger angle will more likely be detected in ECAL1 instead of ECAL2, those photons have to traverse significantly less material, and thus the probability to loose one of these is smaller (section 2.5.1).

The full kinematic information of a three-body final state can be encoded in six variables: the invariant masses of the final state and one two-body subsystem and four angles (section 4.2). One pair of angles is defined in the rest system of the final state (Gottfried-Jackson frame), the other in the rest system of the two-body subsystem (helicity frame). The two-dimensional acceptance distributions in the

	$\pi^- \pi^0 \pi^0$		$\pi^- \eta \eta$	
preselection - part 1				
	number of events		number of events	
all events	300 000 000	100.0 %	11 000 000	100.0 %
DT0 trigger			9 503 573	86.4 %
exactly one primary vertex			8 496 707	77.2 %
exactly one outgoing track			7 158 426	65.1 %
charge unchanged by vertex fit			7 158 393	65.1 %
charge conservation in vertex			7 020 528	63.8 %
two or more ECAL showers	190 357 975	63.5 %	6 983 762	63.5 %
preselection - part 2				
	number of events		number of events	
from preselection	190 357 975	100.0 %	6 983 762	100.0 %
four or more ECAL showers	190 352 183	100.0 %	6 983 517	100.0 %
RPD reconstruction	144 156 155	75.7 %	5 432 178	77.8 %
selection of calorimeter clusters				
	number of clusters		number of clusters	
from preselection - part 2	875 265 270	100.0 %	31 500 862	100.0 %
energy threshold	583 999 516	66.7 %	22 806 116	72.4 %
time resolution	849 676 951	97.1 %	30 741 068	97.6 %
after both cuts	579 430 158	66.2 %	22 656 849	71.9 %
selection of neutral particles				
	number of events		number of events	
from preselection - part 2	144 156 155	100.0 %	5 432 178	100.0 %
exactly four ECAL showers	59 062 548	41.0 %	2 667 018	49.1 %
exactly two π^0/η candidates	19 240 637	13.3 %	660 056	12.2 %
after both cuts	15 633 953	10.8 %	608 407	11.2 %
kinematic selection				
	number of events		number of events	
from selection of neutral particles	15 633 953	100.0 %	608 407	100.0 %
vertex position	14 886 413	95.2 %	584 913	96.1 %
beam energy	14 386 863	92.0 %	579 484	95.2 %
coplanarity	15 123 848	97.3 %	595 863	97.9 %
t'	15 633 953	100.0 %	608 407	100.0 %
mass range for PWA	15 633 953	100.0 %	608 407	100.0 %
after all cuts	13 620 345	87.1 %	551 378	90.6 %

Table 3.3: Number of events after each cut applied during the event selection for Monte Carlo data.

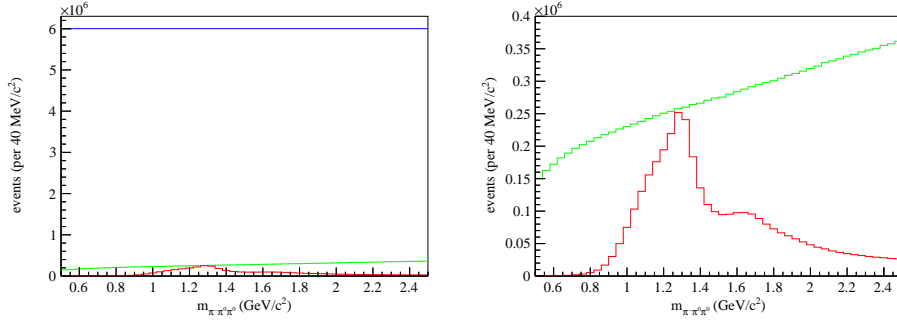


Figure 3.13: Number of events in each mass bin for the generated phase-space Monte Carlo data (blue line), for the accepted Monte Carlo data (green line), and for real data (red line) for the $\pi^-\pi^0\pi^0$ final state. The right plot shows a zoomed view with the accepted Monte Carlo data and real data.

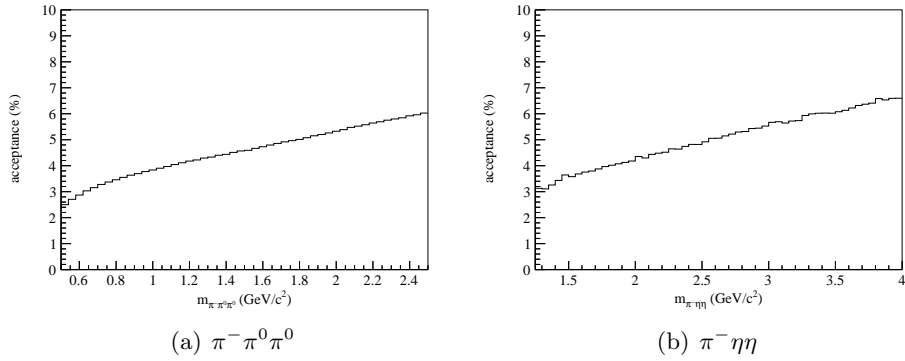


Figure 3.14: Phase-space acceptance as a function of the final state mass for the (a) $\pi^-\pi^0\pi^0$ and (b) $\pi^-\eta\eta$ final state.

angles of each frame for both charge combinations of the two-body subsystem are shown in figs. 3.15 to 3.18. In general, the dependence of the acceptance on the reduced squared four-momentum transfer t' appears to be small, although at low masses a lower acceptance at high values of t' becomes apparent. In contrast to this, there is a strong dependence of the absolute value and the shape of the acceptance distributions on the final-state mass. The acceptance of the charged $\pi^-\pi^0$ two-body subsystem in the Gottfried-Jackson frame (fig. 3.15) prominently shows the most important places of photon losses (section 2.5.1). In particular at higher masses two approximately horizontal bands with lower acceptance are visible. The lower band, containing the point $\cos\theta_{\text{GJ}} \approx -0.5$ at $\phi_{\text{TY}} = 0$, is visible in each bin. It is due to photons absorbed in the light-gas pipe of the RICH. The upper band, containing the point $\cos\theta_{\text{GJ}} \approx +0.5$ at $\phi_{\text{TY}} = 0$, is more pronounced at higher masses, and is caused by the not perfect overlap of the two electromagnetic calorimeters. Also the vertical bands in the acceptance distribution for the helicity frames (figs. 3.16 and 3.18) are caused by the loss of photons in this region.

The resolutions obtained from the simulation are summarized in table 3.4. Only the resolution of the reduced squared four-momentum transfer t' depends strongly on t' . For the three other given variables, the final-state mass is more important. In contrast to the t' resolution, the position resolution of the primary vertex in z -direction is improving with $m_{\pi^-\pi^0\pi^0}$. While the larger scattering angle of the charged pion π^- improves the reconstruction accuracy for the vertex position, it does not improve the t' resolution, which also includes the effect of the larger angles of the π^0 . Apparently the resolution provided by ECAL2 is much better than the one of ECAL1. The worst mass resolution of around $30 \text{ MeV}/c^2$, which is reached for the highest mass bins, also limits the minimal widths of the mass bins chosen for the partial-wave analysis.

3.5.2 $\pi^-\eta\eta$ Final State

In total $1.1 \cdot 10^7$ Monte Carlo events have been generated and reconstructed for the $\pi^-\eta\eta$ final state. As for the $\pi^-\pi^0\pi^0$ final state the Monte Carlo events have been passed through the simulation, reconstruction and event selection described above, the number of events after each selection cut is given in table 3.3.

The comparison of the number of generated phase-space events with the number of accepted Monte Carlo events and the number of real data events is shown in fig. 3.19. Out of the $1.1 \cdot 10^7$ generated events, $5.5 \cdot 10^5$ are accepted resulting in an average phase-space acceptance of 5% in the selected kinematic range (fig. 3.14(b)). The number of accepted Monte Carlo events exceeds the number of real data events by at least a factor of 10 across the analyzed mass range. Therefore the influence of the Monte Carlo on the statistical uncertainty of the result is negligible.

Due to the smaller data sample, the analysis of the spectrometer performance cannot be performed with the same level of detail as for the $\pi^-\pi^0\pi^0$ final state.

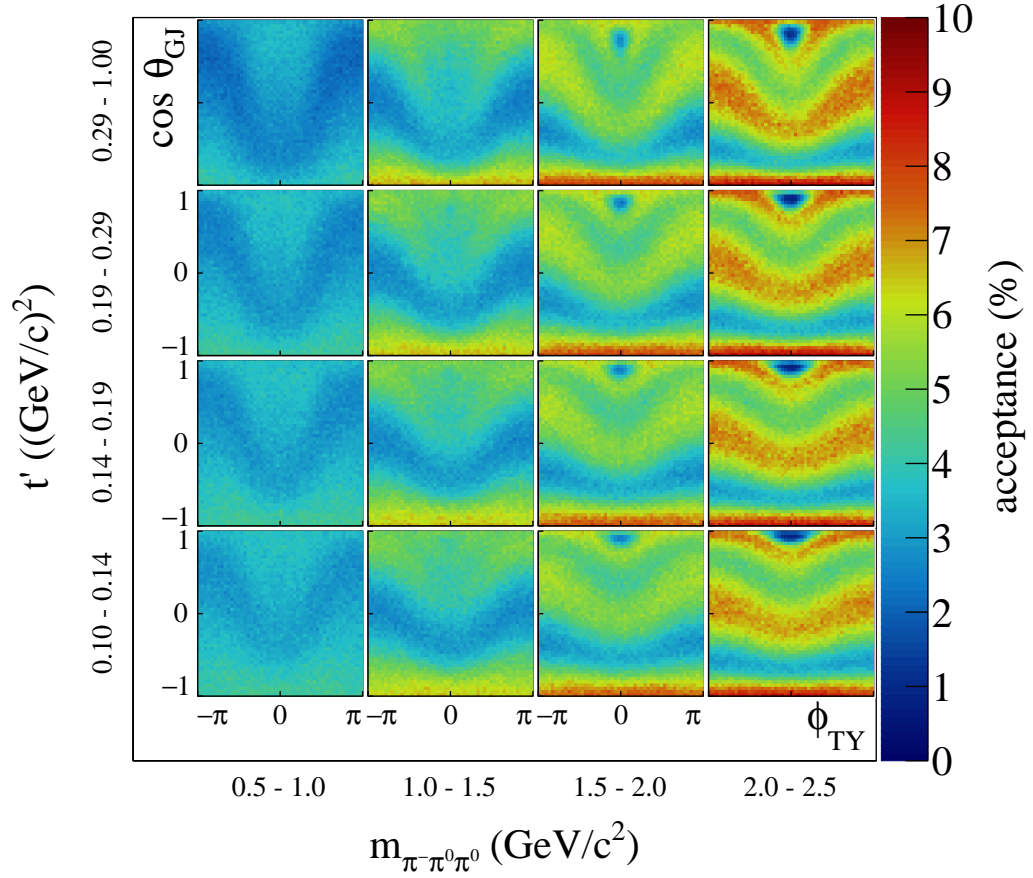


Figure 3.15: Distribution of the phase-space acceptance in the angles of the Gottfried-Jackson frame for bins in the three-pion mass and the reduced squared four-momentum transfer t' for charged $\pi^- \pi^0$ isobars of the $\pi^- \pi^0 \pi^0$ final state.

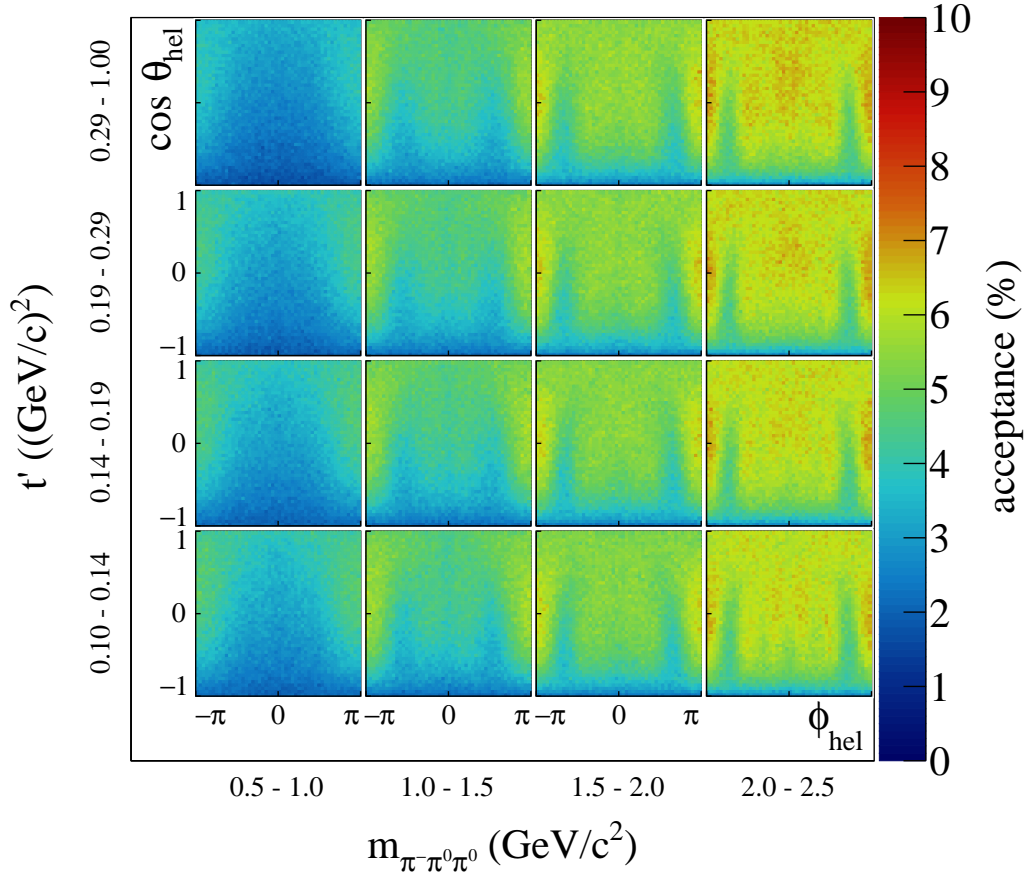


Figure 3.16: Distribution of the phase-space acceptance in the angles of the helicity frame for bins in the three-pion mass and the reduced squared four-momentum transfer t' for charged $\pi^-\pi^0$ isobars of the $\pi^-\pi^0\pi^0$ final state.

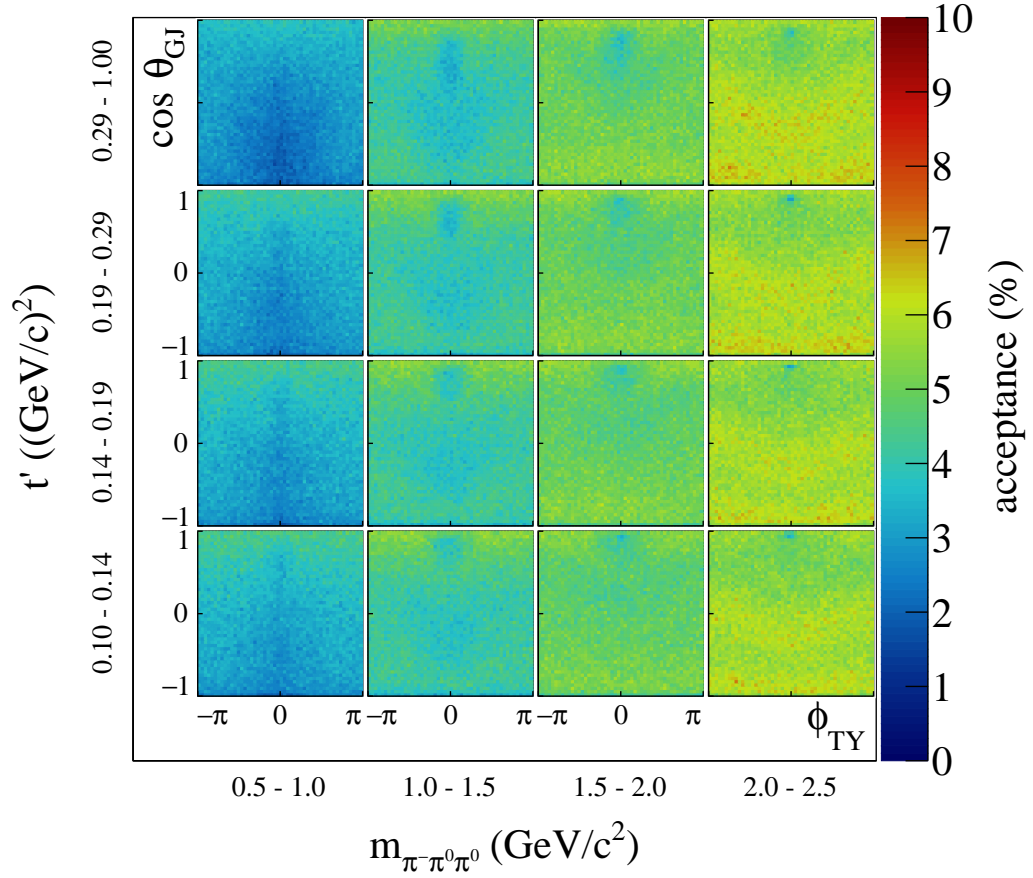


Figure 3.17: Distribution of the phase-space acceptance in the angles of the Gottfried-Jackson frame for bins in the three-pion mass and the reduced squared four-momentum transfer t' for neutral $\pi^0\pi^0$ isobars of the $\pi^-\pi^0\pi^0$ final state.

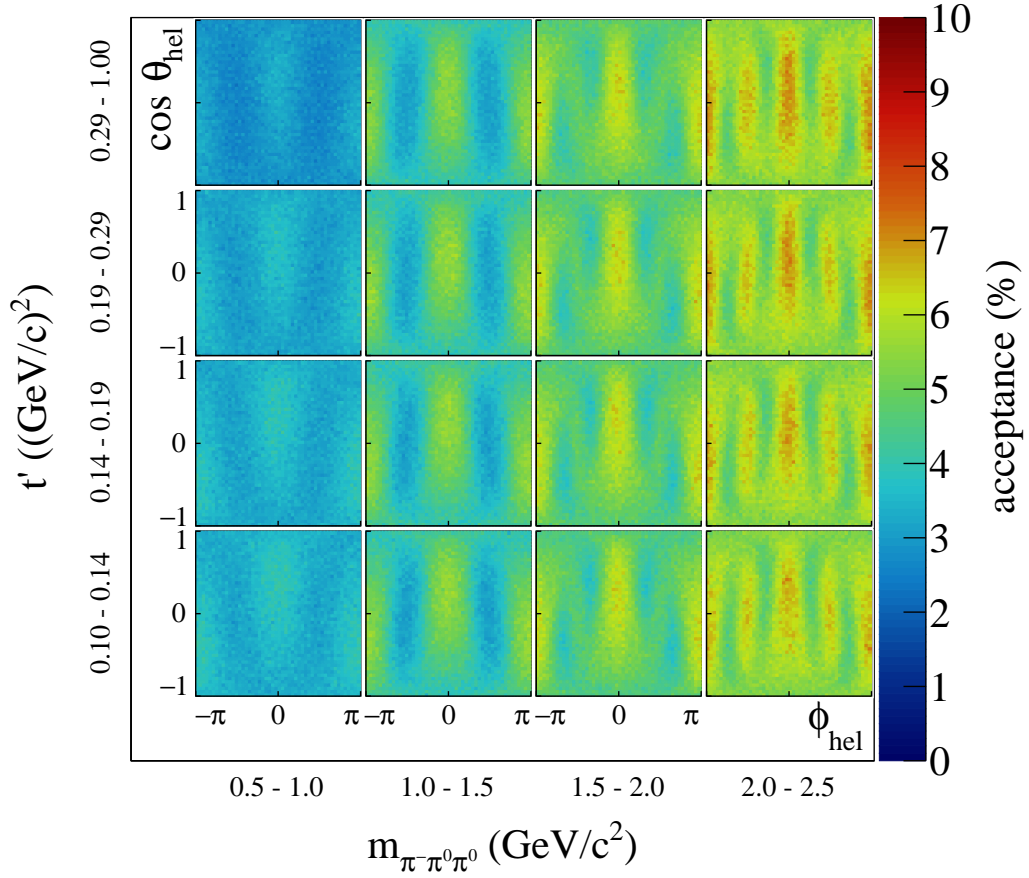


Figure 3.18: Distribution of the phase-space acceptance in the angles of the helicity frame for bins in the three-pion mass and the reduced squared four-momentum transfer t' for neutral $\pi^0\pi^0$ isobar of the $\pi^-\pi^0\pi^0$ final state.

		t' range ((GeV/c) ²)				
		0.10 to 0.14	0.14 to 0.19	0.19 to 0.29	0.29 to 1.00	
$m_{\pi^-\pi^0\pi^0}$ range (GeV/c ²)	0.5 - 1.0	$\delta m_{\pi^-\pi^0\pi^0}$ (MeV/c ²)	10.43	10.40	10.59	10.85
		$\delta t'$ (10^{-3} (GeV/c) ²)	7.98	9.50	11.86	18.04
		δE_{beam} (GeV)	2.56	2.55	2.55	2.53
		δz_{PV} (cm)	2.45	2.36	2.23	2.00
	1.0 - 1.5	$\delta m_{\pi^-\pi^0\pi^0}$ (MeV/c ²)	17.38	17.47	17.57	17.65
		$\delta t'$ (10^{-3} (GeV/c) ²)	9.68	11.45	14.11	21.20
		δE_{beam} (GeV)	2.74	2.72	2.70	2.66
		δz_{PV} (cm)	1.83	1.83	1.80	1.72
	1.5 - 2.0	$\delta m_{\pi^-\pi^0\pi^0}$ (MeV/c ²)	24.90	25.09	25.24	25.34
		$\delta t'$ (10^{-3} (GeV/c) ²)	11.95	14.15	17.39	25.62
		δE_{beam} (GeV)	2.71	2.71	2.70	2.67
		δz_{PV} (cm)	1.52	1.51	1.50	1.46
	2.0 - 2.5	$\delta m_{\pi^-\pi^0\pi^0}$ (MeV/c ²)	32.85	33.22	33.51	33.92
		$\delta t'$ (10^{-3} (GeV/c) ²)	14.92	17.64	21.48	31.14
		δE_{beam} (GeV)	2.68	2.69	2.69	2.70
		δz_{PV} (cm)	1.30	1.31	1.30	1.27

Table 3.4: Absolute resolutions of the three-pion mass $m_{\pi^-\pi^0\pi^0}$, the reduced squared four-momentum transfer t' , the beam energy E_{beam} , and the primary vertex position z_{PV} as obtained by comparing the Monte Carlo truth to the reconstructed value. The resolution is the RMS of the distribution of the residuals.

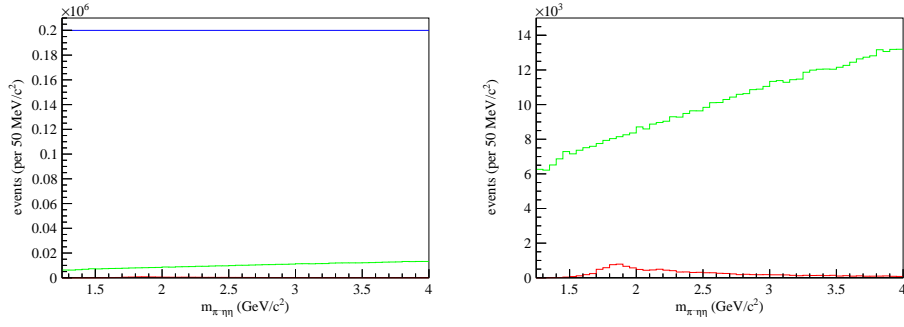


Figure 3.19: Number of events in each mass bin for the generated phase-space Monte Carlo data (blue line), for the accepted Monte Carlo data (green line), and real data (red line). The right plot shows a zoomed view with the accepted Monte Carlo data and real data.

In general the same effects visible for the $\pi^-\pi^0\pi^0$ case also show up in the $\pi^-\eta\eta$ case. However, due to the higher mass of the η , and thus the larger decay angle between the two photons, the effects appear in different kinematic regions (figs. 3.20 and 3.21).

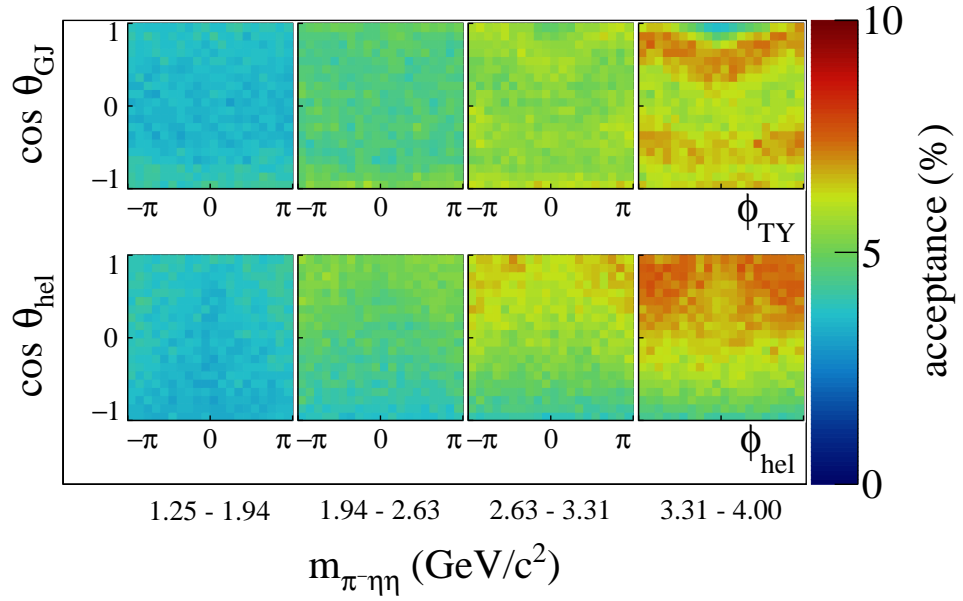


Figure 3.20: Distribution of the phase-space acceptance in the four angles for bins of the final-state mass for charged $\pi^- \eta$ isobars of the $\pi^- \eta \eta$ final state.

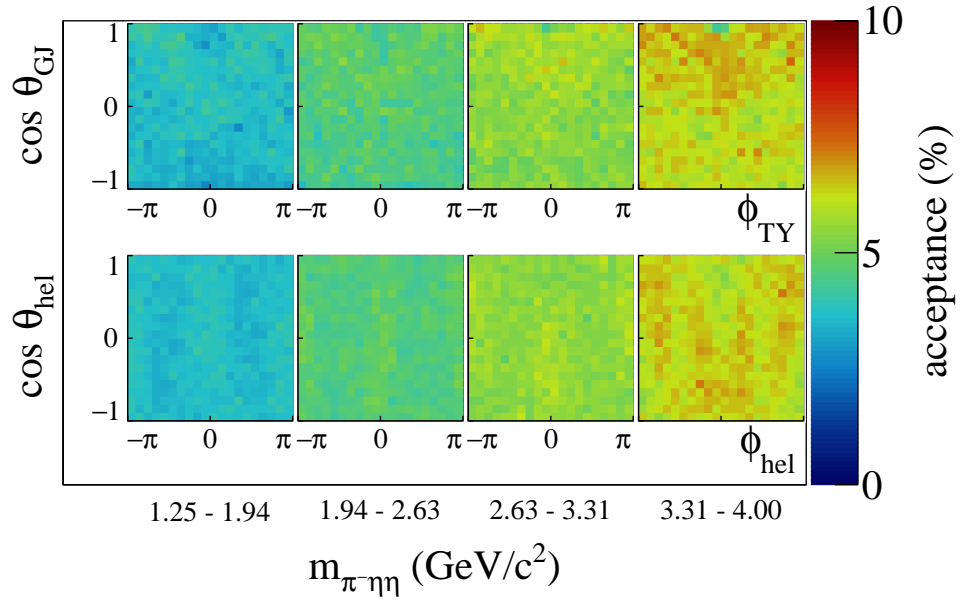


Figure 3.21: Distribution of the phase-space acceptance in the four angles for bins in the final-state mass for neutral $\eta \eta$ isobars of the $\pi^- \eta \eta$ final state.

Chapter 4

Partial-Wave Analysis Method

The analysis method described below follows a two step approach. The first step is the decomposition of the measured data into individual partial waves in bins of the invariant mass of the three-pion system $m_{3\pi}$ and the reduced squared four-momentum transfer t' . This step is independent of resonant structures in the three-pion system, and is performed for each kinematic bin independently. As the dependence on $m_{3\pi}$ and t' does not enter in this step, it is commonly referred to as “mass-independent partial-wave analysis”.

The second step is the description of the $m_{3\pi}$ dependence of the partial waves in terms of resonant and non-resonant structures. This is achieved by fitting mass-dependent functions, like Breit-Wigner amplitudes, or phenomenological functions describing the non-resonant terms, to the results of the mass-independent partial-wave analysis. This resonance-model fit is also called “mass-dependent partial-wave analysis”.

4.1 Cross Section

Considering the production of a single state c , the differential cross section for the reaction $a + b \rightarrow c + d$ with c subsequently decaying to $c \rightarrow 1 + \dots + n$ is given by [65, 33]

$$d\sigma = \frac{1}{4\sqrt{(p_a p_b)^2 - m_a^2 m_b^2}} |\mathcal{M}|^2 d\Phi_{n+1}(p_a + p_b; p_1, \dots, p_n, p_d) \quad (4.1)$$

with the Lorentz-invariant $(n + 1)$ -body phase space element

$$d\Phi_{n+1}(P; p_1, \dots, p_{n+1}) = (2\pi)^4 \prod_{i=1}^{n+1} \frac{d^3 p_i}{(2\pi)^3} \frac{1}{2E_i} \delta^{(4)}\left(P - \sum_{i=1}^{n+1} p_i\right) \quad (4.2)$$

This differential $(n + 1)$ -body phase space can be split into the differential two-body phase space for the intermediate state c and the recoil d , and the differential n -body phase space of the decay of c

$$d\Phi_{n+1}(p_a + p_b; p_1, \dots, p_n, p_d) = d\Phi_2(p_a + p_b; p_c, p_d) \frac{dm_c^2}{2\pi} d\Phi_n(p_c; p_1, \dots, p_n) \quad (4.3)$$

In the overall center-of-mass system the differential two-body phase space $d\Phi_2$ is given by

$$d\Phi_2(p_a + p_b; p_c, p_d) = \frac{1}{(4\pi)^2} \frac{|\vec{p}_c|}{\sqrt{s}} d\cos\theta d\phi \quad (4.4)$$

and the flux factor in the cross-section formula (eq. (4.1)) can be simplified

$$\frac{1}{\sqrt{(p_a p_b)^2 - m_a^2 m_b^2}} = \frac{1}{|\vec{p}_a| \sqrt{s}} \quad (4.5)$$

Substituting $d\cos\theta$ using $dt = -dt' = 2|\vec{p}_a| |\vec{p}_c| d\cos\theta$ and $dm_c^2 = 2m_c \cdot dm_c$, and integrating over $d\phi$, eq. (4.1) can be written as

$$\frac{d\sigma}{dt dm_c} = \frac{1}{(8\pi)^2} \frac{m_c}{|\vec{p}_a|^2 s} |\mathcal{M}|^2 d\Phi_n(p_c; p_1, \dots, p_n) \quad (4.6)$$

It is assumed that the matrix element $\mathcal{M} = \mathcal{M}(a + b \rightarrow 1 + \dots + n + d)$ for this reaction factorizes

$$\mathcal{M}(a + b \rightarrow 1 + \dots + n + d) = \mathcal{M}(a + b \rightarrow c + d) \mathcal{M}(c \rightarrow 1 + \dots + n) \quad (4.7)$$

The first factor describes the production of the system c when the beam particle a scatters elastically off the target b which is recoiled as d . This matrix element is described by the scattering amplitude $\mathcal{A}(s, t; m_c)$ depending on the Mandelstam variables s and t [20, 38]. The second factor in eq. (4.7) describes the decay of the system c to the n -body final state.

Finally, the differential cross section for the production of a single state c is given as given by

$$\frac{d\sigma}{dt dm_c} = \frac{1}{(8\pi)^2} \frac{m_c}{|\vec{p}_a|^2 s} |\mathcal{A}(s, t; m_c) \mathcal{M}(c \rightarrow 1 + \dots + n)|^2 d\Phi_n(p_c; p_1, \dots, p_n) \quad (4.8)$$

In the limit $s \gg m_c \gg t$ the norm of the scattering amplitude $\mathcal{A}(s, t; m_c)$ is given by [38]

$$|\mathcal{A}(s, t; m_c)|^2 \propto F_c(t) \left(\frac{s}{m_c^2} \right)^{2\alpha(t)-1} \quad (4.9)$$

The dependence $F_c(t)$ of the scattering amplitude on the squared four-momentum transfer t can in principle be different for different produced states c . It is typically expressed as a sum of exponentials. The Regge trajectory of the Pomeron is written as $\alpha(t) = \alpha_0 + \alpha' t$ [20].

In the following it is assumed that all states are created with the same dependence on t , so that the cross-section allowing multiple states c is proportional to

$$\frac{d\sigma}{dt dm_c} = \frac{1}{(8\pi)^2} \frac{m_c}{|\vec{p}_a|^2 s} |\mathcal{A}(s, t; m_c)|^2 \mathcal{I}(\tau) d\Phi_n(p_c; p_1, \dots, p_n) \quad (4.10)$$

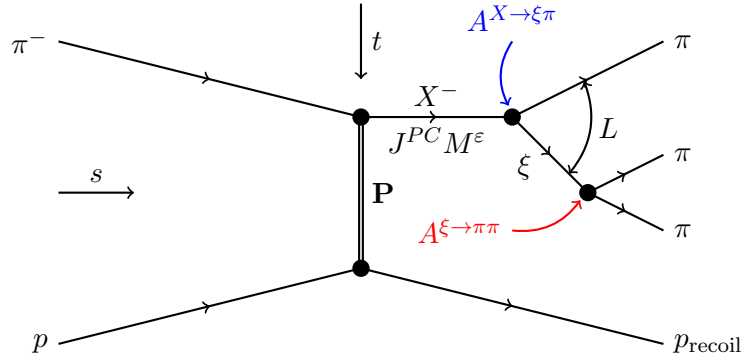


Figure 4.1: Schematic diagram of the three-pion decay of the intermediate state X^- with specific quantum numbers in the isobar model.

with $\mathcal{I}(\tau)$ the total intensity of all partial waves corresponding to the produced states c and their various decay modes into the n -body final state. For a fixed-target experiment with a fixed beam energy, the beam momentum $|p_a|$ and the center-of-mass energy \sqrt{s} are constant. The dependence of the number of events on the invariant mass of the final state m_c (for example $m_{\pi^-\pi^0\pi^0}$) and the reduced squared four-momentum transfer t' have been shown in sections 3.4.4 and 3.4.5. That dependence motivates a binning of the data in these variables. Within each bin all terms in eq. (4.10) except for the partial-wave intensity $\mathcal{I}(\tau)$ are assumed to be constant.

4.2 Decay Amplitudes

The intensity $\mathcal{I}(\tau)$ is assumed to be dominated by resonances. Hence the amplitude of an intermediate state X with specific quantum numbers factorizes into a part describing the production of this state and a second part describing its decay.

The decay amplitude ψ can be calculated using the isobar model [51]. The isobar model assumes that the intermediate state X decays via successive two-body decays into the measured final state (see fig. 4.1 for the three-pion final state). In the helicity formalism [56, 33, 70], each two-body decay of a state ξ with spin J and spin projection M into its daughters ξ_1 and ξ_2 , which have orbital angular momentum L in between, and can be unstable particles themselves, is described by the amplitude

$$\begin{aligned}
 A_{JM}^{\xi \rightarrow \xi_1 \xi_2 L}(\tau) = & \sum_{\lambda_1 = -J_1}^{+J_1} \sum_{\lambda_2 = -J_2}^{+J_2} \left[D_{M(\lambda_1 - \lambda_2)}^J(\phi, \theta, 0) f_{\lambda_1 \lambda_2}^{JL}(m_\xi, m_{\xi_1}, m_{\xi_2}) \right. \\
 & \left. \times A_{J_1 \lambda_1}^{\xi_1 \rightarrow \xi'_1 \xi'_2 L'}(\tau') A_{J_2 \lambda_2}^{\xi_2 \rightarrow \xi''_1 \xi''_2 L''}(\tau'') \right] \quad (4.11)
 \end{aligned}$$

For this amplitude the product of the angular part $D_{M(\lambda_1 - \lambda_2)}^J$, the dynamic part $f_{\lambda_1 \lambda_2}^{JL}$, and the amplitudes of the decays $\xi_1 \rightarrow \xi'_1 \xi'_2$ and $\xi_2 \rightarrow \xi''_1 \xi''_2$ of the daughters is summed up over the various helicity states λ_1 and λ_2 of the daughters. The angular part of the amplitude is described by Wigner D -functions [79]. The amplitudes of the decays of the daughters have the same structure as eq. (4.11). The dynamic part can be written as

$$\begin{aligned}
 f_{\lambda_1 \lambda_2}^{JL}(m_\xi, m_{\xi_1}, m_{\xi_2}) = & \underbrace{\sqrt{2L+1}}_{\text{normalization}} F_L(m_\xi, m_{\xi_1}, m_{\xi_2}) \Delta_\xi(m_\xi, m_{\xi_1}, m_{\xi_2}) \\
 & \times \underbrace{(L \ 0 \ S \ [\lambda_1 - \lambda_2] \ | \ J \ [\lambda_1 - \lambda_2])}_{L\text{-}S \ \text{coupling}} \underbrace{(J_1 \ \lambda_1 \ J_2 \ \lambda_2 \ | \ S \ [\lambda_1 - \lambda_2])}_{\text{spin-spin coupling}} \quad (4.12)
 \end{aligned}$$

The used parameterizations for the angular-momentum barrier factors F_L [26, 52] and for the isobar line shapes Δ_ξ are presented in section 5.1.1. In addition, the dynamic part contains the Clebsch-Gordan coefficient for the coupling of the spins J_1 and J_2 of the daughters to the total intrinsic spin S and the one for the coupling of S with the orbital angular momentum L between the two daughters to J .

The two-body decays are described in right-handed coordinate systems that are rest frames of the decaying state. The coordinate system for the decay of the state X is called Gottfried-Jackson (GJ) frame, the others are so-called helicity frames. The Gottfried-Jackson frame is constructed in the rest system of the state X with the beam direction defining the z_{GJ} axis. The y_{GJ} axis is perpendicular to the production plane ($\vec{y}_{\text{GJ}} \propto \vec{p}_{\text{beam}}^{\text{lab}} \times \vec{p}_X^{\text{lab}}$). In the X rest frame, the two daughters are back to back, so the decay is specified by the polar angle θ_{GJ} and the azimuthal angle (Treiman-Yang angle) ϕ_{TY} of one of the daughters.

For a three-body final state there is only one isobar ξ , and therefore also only one helicity frame to consider. This frame is constructed by boosting from the Gottfried-Jackson frame into the rest system of the isobar ξ . The z_{hel} axis is given by the original direction of ξ , the y_{hel} axis is defined as $\vec{y}_{\text{hel}} \propto \vec{z}_{\text{GJ}} \times \vec{z}_{\text{hel}}$. In the isobar rest system the two pions are back to back, so also the isobar decay is specified by two angles, the polar angle θ_{hel} and the azimuthal angle ϕ_{hel} .

For the three-pion final state the amplitudes eq. (4.11) can be simplified further. A similar argumentation also applies for the $\pi^- \eta \eta$ final state. Only two two-body decay amplitudes have to be considered: $A_{JM}^{X \rightarrow \xi \pi L}(\tau)$ and $A_{J_\xi \lambda}^{\xi \rightarrow \pi \pi L'}(\tau)$. Since pions and eta mesons are spin-less particles, their helicities are equal to 0. Also the total

intrinsic spin S in the decay $\xi \rightarrow \pi\pi$ is equal to 0. Therefore the relative angular momentum L' between the two pions is equal to the spin J_ξ of the isobar. The amplitude for the decay $\xi \rightarrow \pi\pi$ simplifies to

$$A_{J_\xi \lambda}^{\xi \rightarrow \pi\pi J_\xi}(\tau) = \sqrt{2J_\xi + 1} D_{\lambda 0}^{J_\xi}(\phi_{\text{hel}}, \theta_{\text{hel}}, 0) F_{J_\xi}(m_\xi, m_\pi, m_\pi) \Delta_\xi(m_\xi, m_\pi, m_\pi) \quad (4.13)$$

Similarly in the decay $X \rightarrow \xi\pi$, the total spin of the isobar-pion system is given by the spin J_ξ of the isobar. Since the analysis is performed in narrow bins of m_X , no assumption is made on its line-shape amplitude $\Delta_X(m_X, m_\xi, m_\pi)$. It is set to unity

$$A_{JM}^{X \rightarrow \xi\pi L}(\tau) = \sum_{\lambda=-J_\xi}^{+J_\xi} \sqrt{2L+1} D_{M\lambda}^J(\phi_{\text{TY}}, \theta_{\text{GJ}}, 0) (L \ 0 \ J_\xi \ \lambda \mid J \ \lambda) F_L(m_X, m_\xi, m_\pi) A_{J_\xi \lambda}^{\xi \rightarrow \pi\pi J_\xi}(\tau) \quad (4.14)$$

For a fixed three-pion mass m_X , the decay of the state X is fully described by five variables $\tau = (\phi_{\text{TY}}, \theta_{\text{GJ}}, m_\xi, \phi_{\text{hel}}, \theta_{\text{hel}})$.

Parity conservation in the production process is directly taken into account by working in the reflectivity basis [30]. Linear combinations of partial-wave decay amplitudes with opposite signs of the spin-projection quantum number M form new amplitudes with positive M and an additional quantum number, the reflectivity $\varepsilon = \pm 1$. The reflectivity is the eigenvalue of the amplitude with respect to the reflection through the X production plane. In the high-energy limit, the reflectivity corresponds to the naturality of the exchanged particle. With this the decay amplitude can be written as

$$\psi_{JM^\varepsilon}^{X \rightarrow \xi\pi L}(\tau) = c(M) \left[A_{JM}^{X \rightarrow \xi\pi L}(\tau) - \varepsilon P(-1)^{J-M} A_{J,-M}^{X \rightarrow \xi\pi L}(\tau) \right] \quad (4.15)$$

with

$$\varepsilon = \pm 1, \ M \geq 0, \ \text{and} \ c(M) = \begin{cases} 1/\sqrt{2} & \text{for } M > 0 \\ 1/2 & \text{for } M = 0 \end{cases} \quad (4.16)$$

The two π^0 in the $\pi^- \pi^0 \pi^0$ final state, and also the two η in the $\pi^- \eta \eta$ final state, are indistinguishable, hence the amplitude has to be Bose symmetrized

$$\psi_{JM}^{X \rightarrow \xi\pi L}(\tau) = \frac{1}{\sqrt{2}} \left(A_{JM}^{X \rightarrow \xi\pi L}(\tau_{12}) + A_{JM}^{X \rightarrow \xi\pi L}(\tau_{13}) \right) \quad (4.17)$$

In the case of an isobar decaying to $\pi^- \pi^0$ or $\pi^- \eta$, the phase-space variables τ_{12} and τ_{13} correspond to the two possible combinations to form this isobar from the $\pi_1^- \pi_2^0 \pi_3^0$ or $\pi_1^- \eta_2 \eta_3$ final states. In general all five variables differ between the two

combinations. If the isobar decays to $\pi^0\pi^0$ or $\eta\eta$, only the angles in the helicity frame change by a point reflection on the origin of the helicity frame.

Each partial-wave decay amplitude $\psi_{JM^\varepsilon}^{X \rightarrow \xi \pi^L}$ corresponds to a state X with the quantum numbers J and M^ε that is decaying into an isobar ξ and a bachelor pion or eta meson with a relative orbital angular momentum L in between. Below, the decay amplitude will simply be written as ψ_i where i stands for all this information.

4.3 Total Partial-Wave Intensity

The model fitted to the data should reproduce the kinematic distributions observed in data. It is defined by a set of partial-wave decay amplitudes $\{\psi(\tau)\}$ with τ being the five kinematic variables fully describing one event, and the (spin-)density matrix ρ . The intensity for a single event is obtained by summing over all possible combinations of partial waves i and j

$$\mathcal{I}(\tau) = \sum_{i,j}^{N_{\text{waves}}} \psi_j^*(\tau) \rho_{ji} \psi_i(\tau) \quad (4.18)$$

In the reflectivity basis, the spin-density matrix assumes block diagonal form, with one block for each reflectivity [30]

$$\rho = \begin{pmatrix} \rho^+ & 0 \\ 0 & \rho^- \end{pmatrix} \quad (4.19)$$

Therefore partial waves with opposite reflectivities do not interfere. The sum over the two reflectivities is explicitly stated, and the partial wave indices i and j are redefined to reflect this. The intensity for a single event can then be rewritten as

$$\mathcal{I}(\tau) = \sum_{\varepsilon=\pm 1} \sum_{i,j}^{N_{\text{waves}}^\varepsilon} \psi_j^{\varepsilon*}(\tau) \rho_{ji}^\varepsilon \psi_i^\varepsilon(\tau) \quad (4.20)$$

The spin-density sub-matrices ρ^ε are Hermitian, positive-definite matrices. Using the Cholesky decomposition they can be expressed as the product of the Hermitian conjugate of an upper triangle matrix with this upper triangle matrix

$$\rho^\varepsilon = \mathcal{T}^{\varepsilon\dagger} \mathcal{T}^\varepsilon \quad (4.21)$$

with

$$\mathcal{T}^\varepsilon = \begin{pmatrix} T_1^{1\varepsilon} & T_2^{1\varepsilon} & \dots & T_{n-1}^{1\varepsilon} & T_n^{1\varepsilon} \\ 0 & T_2^{2\varepsilon} & \dots & T_{n-1}^{2\varepsilon} & T_n^{2\varepsilon} \\ & & \ddots & & \\ 0 & 0 & \dots & T_{n-1}^{(n-1)\varepsilon} & T_n^{(n-1)\varepsilon} \\ 0 & 0 & \dots & 0 & T_n^{n\varepsilon} \end{pmatrix} \quad (4.22)$$

4.4 Mass-independent Partial-Wave Analysis

where the elements $T_i^{r\epsilon}$ are called transition amplitudes, and the variable r is called the rank. The diagonal elements $T_i^{r\epsilon}$ with $i = r$ are positive and real-valued, while the off-diagonal elements are complex numbers. A particular element of the spin-density matrix is given by

$$\rho_{ji}^\epsilon = \sum_r^{N_{\text{rank}}^\epsilon} T_j^{r\epsilon*} T_i^{r\epsilon} \quad (4.23)$$

With this the intensity for a single event can be rewritten as

$$\mathcal{I}(\tau) = \sum_{\epsilon=\pm 1} \sum_r^{N_{\text{rank}}^\epsilon} \sum_{i,j}^{N_{\text{waves}}^\epsilon} \psi_j^{\epsilon*}(\tau) T_j^{r\epsilon*} T_i^{r\epsilon} \psi_i^\epsilon(\tau) \quad (4.24)$$

$$= \sum_{\epsilon=\pm 1} \sum_r^{N_{\text{rank}}^\epsilon} \left| \sum_i^{N_{\text{waves}}^\epsilon} T_i^{r\epsilon} \psi_i^\epsilon(\tau) \right|^2 \quad (4.25)$$

Finally, an isotropic background wave, called flat wave, is added incoherently, so that

$$\mathcal{I}(\tau) = \sum_{\epsilon=\pm 1} \sum_r^{N_{\text{rank}}^\epsilon} \left| \sum_i^{N_{\text{waves}}^\epsilon} T_i^{r\epsilon} \psi_i^\epsilon(\tau) \right|^2 + T_{\text{flat}}^2 \quad (4.26)$$

4.4 Mass-independent Partial-Wave Analysis

The probability to observe an event e with kinematic variables τ_e is

$$P(\tau_e) = \frac{\mathcal{I}(\tau_e)}{\int d\Phi_n(\tau) \mathcal{I}(\tau) \eta(\tau)} \quad (4.27)$$

where the denominator $\bar{N} = \int d\Phi_n(\tau) \mathcal{I}(\tau) \eta(\tau)$ is the normalization integral of the intensity over the complete phase-space weighted with the acceptance $\eta(\tau)$, which is the number of expected events. The probability depends on the unknown transition amplitudes $T_i^{r\epsilon}$. The level of agreement between data and model is given by the extended likelihood, which includes the Poisson probability to measure N events

$$\mathcal{L} = \frac{e^{-\bar{N}} \bar{N}^N}{N!} \prod_e^N P(\tau_e) \quad (4.28)$$

$$= \frac{e^{-\bar{N}}}{N!} \prod_e^N \mathcal{I}(\tau_e) \quad (4.29)$$

For the maximum-likelihood estimation, usually the negative logarithm of the likelihood is minimized.

$$-\ln \mathcal{L} = \bar{N} + \ln N! - \sum_e^N \ln \mathcal{I}(\tau_e) \quad (4.30)$$

For the minimization, the absolute value of the log-likelihood does not matter. Therefore the constant term $\ln N!$ can be dropped.

$$-\ln \mathcal{L} = - \sum_e^N \ln \mathcal{I}(\tau_e) + \bar{N} \quad (4.31)$$

The expected number of events \bar{N} can be calculated using

$$\begin{aligned} \bar{N} &= \int d\Phi_n(\tau) \mathcal{I}(\tau) \eta(\tau) \quad (4.32) \\ &= \sum_{\varepsilon=\pm 1} \sum_r^{N_{\text{rank}}^\varepsilon} \sum_{i,j}^{N_{\text{waves}}^\varepsilon} T_j^{r\varepsilon*} T_i^{r\varepsilon} \underbrace{\int d\Phi_n(\tau) \psi_j^{\varepsilon*}(\tau) \psi_i^\varepsilon(\tau) \eta(\tau)}_{\mathcal{N}_{ij}^\varepsilon} + T_{\text{flat}}^2 \underbrace{\int d\Phi_n(\tau) \eta(\tau)}_{\mathcal{N}_{\text{flat}}} \end{aligned} \quad (4.33)$$

The appearing normalization integrals $\mathcal{N}_{ij}^\varepsilon$ are independent of the transition amplitudes, and can be pre-calculated ahead of the minimization. The normalization integrals are evaluated using Monte Carlo methods, where the integrals are reduced to a sum over $N_{\text{MC}}^{\text{gen}}$ phase-space events $\{\tau_e^{\text{gen}}\}$ that are generated and passed through the complete detector simulation and reconstruction.

$$\mathcal{N}_{ij}^\varepsilon = \frac{V_{\Phi_n}}{N_{\text{MC}}^{\text{gen}}} \sum_e^{N_{\text{MC}}^{\text{gen}}} \psi_j^{\varepsilon*}(\tau_e^{\text{gen}}) \psi_i^\varepsilon(\tau_e^{\text{gen}}) \eta(\tau_e^{\text{gen}}) \quad (4.34)$$

Here $V_{\Phi_n} = \int d\Phi_n(\tau)$ is the phase-space volume [72]. The acceptance $\eta(\tau_e^{\text{gen}})$ is either 1 or 0 depending on whether the reconstructed MC event passed all selection cuts, or not. With $N_{\text{MC}}^{\text{acc}}$ accepted events $\{\tau_e^{\text{acc}}\}$ eq. (4.34) simplifies to

$$\mathcal{N}_{ij}^\varepsilon = \frac{V_{\Phi_n}}{N_{\text{MC}}^{\text{gen}}} \sum_e^{N_{\text{MC}}^{\text{acc}}} \psi_j^{\varepsilon*}(\tau_e^{\text{acc}}) \psi_i^\varepsilon(\tau_e^{\text{acc}}) \quad (4.35)$$

Similarly, the normalization integral for the flat wave simplifies to

$$\mathcal{N}_{\text{flat}} = V_{\Phi_n} \frac{N_{\text{MC}}^{\text{acc}}}{N_{\text{MC}}^{\text{gen}}} = \mathcal{A} \cdot V_{\Phi_n} \quad (4.36)$$

where \mathcal{A} is the average acceptance of phase-space distributed events. Collecting the normalization integrals and the expression for the intensity eq. (4.26) into the log-likelihood eq. (4.31) gives

$$\begin{aligned}
 -\ln \mathcal{L} = & -\sum_e^N \ln \left(\sum_{\varepsilon=\pm 1} \sum_r^{N_{\text{rank}}^\varepsilon} \left| \sum_i^{N_{\text{waves}}^\varepsilon} T_i^{r\varepsilon} \psi_i^\varepsilon(\tau) \right|^2 + T_{\text{flat}}^2 \right) \\
 & + \sum_{\varepsilon=\pm 1} \sum_r^{N_{\text{rank}}^\varepsilon} \sum_{i,j}^{N_{\text{waves}}^\varepsilon} T_j^{r\varepsilon*} T_i^{r\varepsilon} \mathcal{N}_{ij}^\varepsilon + T_{\text{flat}}^2 \mathcal{N}_{\text{flat}} \quad (4.37)
 \end{aligned}$$

As the phase-space volume V_{Φ_n} is assumed to be constant in the narrow mass bins in m_X used for the mass-independent fit, and as it can only be evaluated numerically, it is removed from the log-likelihood. To this end the phase-space integrals are introduced. They are analogous to the normalization integrals, but do not include the acceptance

$$\mathcal{P}_{ij}^\varepsilon = \int d\Phi_n(\tau) \psi_j^{\varepsilon*}(\tau) \psi_i^\varepsilon(\tau) \quad (4.38)$$

$$= \frac{V_{\Phi_n}}{N_{\text{MC}}^{\text{gen}}} \sum_e^{N_{\text{MC}}^{\text{gen}}} \psi_j^{\varepsilon*}(\tau_e^{\text{gen}}) \psi_i^\varepsilon(\tau_e^{\text{gen}}) \quad (4.39)$$

The phase-space integral for the flat wave is $\mathcal{P}_{\text{flat}} = V_{\Phi_n}$. Not to change the overall log-likelihood function, a couple of variables are replaced at the same time

$$\mathcal{N}_{ij}^\varepsilon \rightarrow \overline{\mathcal{N}}_{ij}^\varepsilon = \mathcal{N}_{ij}^\varepsilon \frac{1}{\sqrt{\mathcal{P}_{ii}^\varepsilon \mathcal{P}_{jj}^\varepsilon}} \quad (4.40)$$

$$T_i^{r\varepsilon} \rightarrow \overline{T}_i^{r\varepsilon} = T_i^{r\varepsilon} \cdot \sqrt{\mathcal{P}_{ii}^\varepsilon} \quad (4.41)$$

$$\psi_i^\varepsilon(\tau_e) \rightarrow \overline{\psi}_i^\varepsilon(\tau_e) = \psi_i^\varepsilon(\tau_e) \frac{\sqrt{V_{\Phi_n}}}{\sqrt{\mathcal{P}_{ii}^\varepsilon}} \quad (4.42)$$

Inserting these replacements into the log-likelihood eq. (4.37) gives

$$\begin{aligned}
 -\ln \mathcal{L} = & -\sum_e^N \ln \left(\frac{1}{V_{\Phi_n}} \sum_{\varepsilon=\pm 1} \sum_r^{N_{\text{rank}}^\varepsilon} \left| \sum_i^{N_{\text{waves}}^\varepsilon} \overline{T}_i^{r\varepsilon} \overline{\psi}_i^\varepsilon(\tau) \right|^2 + \overline{T}_{\text{flat}}^2 \right) \\
 & + \sum_{\varepsilon=\pm 1} \sum_r^{N_{\text{rank}}^\varepsilon} \sum_{i,j}^{N_{\text{waves}}^\varepsilon} \overline{T}_j^{r\varepsilon*} \overline{T}_i^{r\varepsilon} \overline{\mathcal{N}}_{ij}^\varepsilon + \overline{T}_{\text{flat}}^2 \mathcal{A} \quad (4.43)
 \end{aligned}$$

Changing the variable of the maximum-likelihood estimation to $\overline{T}_i^{r\varepsilon}$, this transformation removes the phase-space volume V_{Φ_n} from the normalization part of the log-likelihood. The factor $1/V_{\Phi_n}$ in the sum over the intensities of each event

can be dropped when not considering absolute values of the log-likelihood. In summary, the log-likelihood function that is minimized reads

$$\begin{aligned}
 -\ln \mathcal{L} = & -\sum_e^N \ln \left(\sum_{\varepsilon=\pm 1} \sum_r^{N_{\text{rank}}^\varepsilon} \left| \sum_i^{N_{\text{waves}}^\varepsilon} \overline{T}_i^{r\varepsilon} \overline{\psi}_i^\varepsilon(\tau_e) \right|^2 + \overline{T}_{\text{flat}}^2 \right) \\
 & + \sum_{\varepsilon=\pm 1} \sum_r^{N_{\text{rank}}^\varepsilon} \sum_{i,j}^{N_{\text{waves}}^\varepsilon} \overline{T}_j^{r\varepsilon*} \overline{T}_i^{r\varepsilon} \overline{\mathcal{N}}_{ij}^\varepsilon + \overline{T}_{\text{flat}}^2 \mathcal{A} \quad (4.44)
 \end{aligned}$$

The intensity per event eq. (4.26) with the transformation applied is given as

$$\mathcal{I}(\tau) = \frac{1}{V_{\Phi_n}} \left[\sum_{\varepsilon=\pm 1} \sum_r^{N_{\text{rank}}^\varepsilon} \left| \sum_i^{N_{\text{waves}}^\varepsilon} \overline{T}_i^{r\varepsilon} \overline{\psi}_i^\varepsilon(\tau) \right|^2 + \overline{T}_{\text{flat}}^2 \right] \quad (4.45)$$

This expression still contains the phase-space volume V_{Φ_n} . In contrast the expression to calculate the expected number of events eq. (4.33) with the transformation applied does not contain V_{Φ_n} . It is given as

$$\bar{N} = \sum_{\varepsilon=\pm 1} \sum_r^{N_{\text{rank}}^\varepsilon} \sum_{i,j}^{N_{\text{waves}}^\varepsilon} \overline{T}_j^{r\varepsilon*} \overline{T}_i^{r\varepsilon} \overline{\mathcal{N}}_{ij}^\varepsilon + \overline{T}_{\text{flat}}^2 \mathcal{A} \quad (4.46)$$

4.5 Spin-density matrix

In the initial expression for the intensity (eq. (4.20)) the spin-density matrix ρ_{ij} has been used. Its elements are connected to the transition amplitudes via eq. (4.23). When transforming the transition amplitudes (eq. (4.41)) also the elements of the spin-density matrix are transformed

$$\overline{\rho}_{ij}^\varepsilon = \sum_r^{N_{\text{rank}}^\varepsilon} \overline{T}_j^{r\varepsilon*} \overline{T}_i^{r\varepsilon} \quad (4.47)$$

Using this spin-density matrix, the number of expected events (eq. (4.46)) is written as

$$\bar{N} = \sum_{\varepsilon=\pm 1} \sum_{i,j}^{N_{\text{waves}}^\varepsilon} \overline{\rho}_{ij}^\varepsilon \overline{\mathcal{N}}_{ij}^\varepsilon + \overline{\rho}_{\text{flat}} \mathcal{A} \quad (4.48)$$

Analogously the number of acceptance corrected events is

$$\bar{N}_{\text{corr}} = \int d\Phi_n(\tau) \mathcal{I}(\tau) \quad (4.49)$$

$$= \sum_{\varepsilon=\pm 1} \sum_{i,j}^{N_{\text{waves}}^\varepsilon} \bar{\rho}_{ij}^\varepsilon \bar{\mathcal{P}}_{ij}^\varepsilon + \bar{\rho}_{\text{flat}} \quad (4.50)$$

where

$$\bar{\mathcal{P}}_{ij}^\varepsilon = \frac{\mathcal{P}_{ij}^\varepsilon}{\sqrt{\mathcal{P}_{ii}^\varepsilon \mathcal{P}_{jj}^\varepsilon}} \text{ with } \bar{\mathcal{P}}_{ii}^\varepsilon = 1 \text{ and } \bar{\mathcal{P}}_{ij}^\varepsilon = \bar{\mathcal{P}}_{ji}^{\varepsilon*} \quad (4.51)$$

It can be seen that as a consequence of the transformation of the transition amplitudes (eq. (4.41)) the elements of the spin-density matrix now are given in units of numbers of events. The intensity I_i^ε of a single wave i is given by the corresponding diagonal element of the spin-density matrix

$$I_i^\varepsilon = \bar{\rho}_{ii}^\varepsilon \quad (4.52)$$

The intensity sum of two waves can accordingly be written as

$$I = \bar{\rho}_{ii}^\varepsilon + \bar{\rho}_{jj}^\varepsilon + \bar{\rho}_{ij}^\varepsilon \bar{\mathcal{P}}_{ij}^\varepsilon + \bar{\rho}_{ji}^\varepsilon \bar{\mathcal{P}}_{ji}^\varepsilon \quad (4.53)$$

$$= \bar{\rho}_{ii}^\varepsilon + \bar{\rho}_{jj}^\varepsilon + O_{ij}^\varepsilon \quad (4.54)$$

Here the overlap

$$O_{ij}^\varepsilon = \bar{\rho}_{ij}^\varepsilon \bar{\mathcal{P}}_{ij}^\varepsilon + \bar{\rho}_{ji}^\varepsilon \bar{\mathcal{P}}_{ji}^\varepsilon = \bar{\rho}_{ij}^\varepsilon \bar{\mathcal{P}}_{ij}^\varepsilon + (\bar{\rho}_{ij}^\varepsilon \bar{\mathcal{P}}_{ij}^\varepsilon)^* = 2 \cdot \Re(\bar{\rho}_{ij}^\varepsilon \bar{\mathcal{P}}_{ij}^\varepsilon) \quad (4.55)$$

has been introduced. These expressions are easily generalized for sets of more than two waves.

The interferences between the waves are represented by the off-diagonal elements of the spin-density matrix. Absolute values r_{ij}^ε and phases between two waves φ_{ij}^ε of these elements are defined such that

$$\bar{\rho}_{ij}^\varepsilon = r_{ij}^\varepsilon e^{i\varphi_{ij}^\varepsilon} \quad (4.56)$$

The coherence C_{ij}^ε between two waves is defined as

$$C_{ij}^\varepsilon = \sqrt{\frac{\bar{\rho}_{ij}^\varepsilon \bar{\rho}_{ij}^{\varepsilon*}}{\bar{\rho}_{ii}^\varepsilon \bar{\rho}_{jj}^\varepsilon}} \quad (4.57)$$

For a fit with rank $N_{\text{rank}}^\varepsilon = 1$, the coherence is always one.

Chapter 5

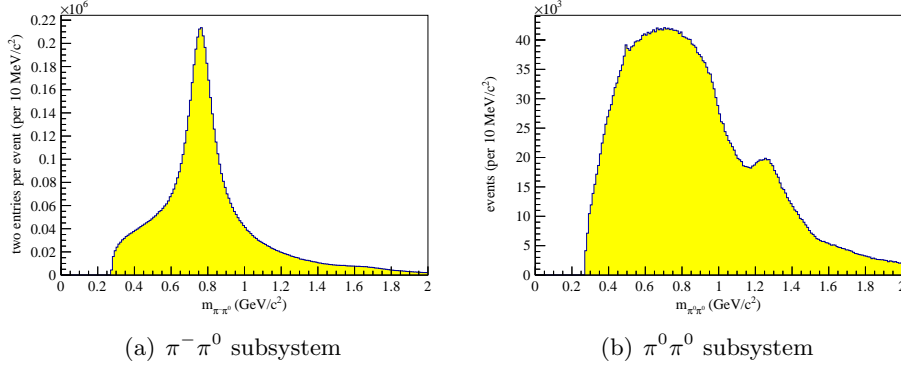
Partial-Wave Analysis of the $\pi^- \pi^0 \pi^0$ Final State

In this chapter, results of the partial-wave analysis of the $\pi^- \pi^0 \pi^0$ final state are shown. The partial-wave analysis of the $\pi^- \eta \eta$ final-state is presented in chapter 6. The model employed for the partial-wave analysis of the $\pi^- \pi^0 \pi^0$ final state is motivated in section 5.1, details of the used parameterizations are given in section 5.1.1. The quality of the partial-wave decomposition is evaluated in section 5.2. The total intensity and the contributions of background waves are presented in section 5.3. Sections 5.4 and 5.5 explain how intensities and phases of individual waves are investigated in sections 5.7 to 5.13. The resonance-model fit is explained in section 5.6, some systematics of this fit are discussed in section 5.14. To conclude, the results for the $\pi^- \pi^0 \pi^0$ final state are compared to those of the $\pi^- \pi^- \pi^+$ final state in section 5.15.

5.1 Fit Model

In eq. (4.18) the total intensity is expanded into a sum over a set of partial waves. Due to computational constraints this set needs to be truncated from a set containing all possible waves to a set containing only the relevant ones. Each wave is defined by a combination of the quantum numbers of the intermediate state X , and the quantum numbers and isobars occurring during its decay (section 4.2). Pomeron exchange is assumed to be the dominant production process, therefore isospin and G -parity I^G of the intermediate state X have to be equal to those of the pion, i.e. $I^G = 1^-$. As the quantum numbers I^G are the same for all waves, they will not be stated explicitly for the waves discussed below.

A first list of isobars to include into the fit model can be created from the invariant mass spectra of the two-pion subsystems of the $\pi^- \pi^0 \pi^0$ final state (fig. 5.1). From peaks and shoulders of the distributions, six important isobars are extracted, namely the ρ (770) and the ρ_3 (1690) in the $\pi^- \pi^0$ subsystem, as well as the f_0 (980), f_0 (1500), f_2 (1270), and a broad $(\pi\pi)_S$ component in the $\pi^0 \pi^0$ subsystem. Isobars decaying to $\pi^0 \pi^0$ have quantum numbers $I_\xi^G = 0^+$, while those decaying to $\pi^- \pi^0$ have $I_\xi^G = 1^+$. As pions are spin-less particles, and therefore the total intrinsic spin S of two pions always is 0, the spin J_ξ of the isobar corresponds to the relative orbital angular momentum L' between the two pions. The G parity of


 Figure 5.1: Invariant masses of the two-pion subsystems of the $\pi^-\pi^0\pi^0$ final state.

the isobar is given by $G_\xi = (-1)^{L+S+I\xi}$. Isobars decaying to $\pi^0\pi^0$ need to fulfill $G_\xi = (-1)^{J\xi} = +1$, and therefore need to have even spin J_ξ . Similarly isobars with an odd spin can only decay to $\pi^-\pi^0$.

Some of these isobars can also be seen in Dalitz plots for two slices of the $\pi^-\pi^0\pi^0$ mass (figs. 5.2 and 5.3). In all three plots the band of the $\rho(770)$ is clearly visible at $m_{\pi^-\pi^0}^2 \approx 0.6$ (GeV/c^2)². In fig. 5.3(b) the $\rho(770)$ can be seen as the diagonal band. In the slice for the higher invariant mass of the three-pion state (fig. 5.3) also the $f_2(1270)$ appears at $m_{\pi^0\pi^0}^2 \approx 1.5$ (GeV/c^2)².

5.1.1 Masses and Parameterisations

The masses of the stable particles and the resonance parameters for the isobars used in the analysis of the $\pi^-\pi^0\pi^0$ and $\pi^-\eta\eta$ final state are summarized in table 5.1. With two exceptions the lineshapes $\Delta_\xi(m)$ of the isobars are parameterized by relativistic Breit-Wigner functions

$$\Delta_\xi(m) = \frac{\Gamma_0 m_0}{m_0^2 - m^2 - i\Gamma(m)m_0} \quad \text{with} \quad \Gamma(m) = \Gamma_0 \frac{m_0}{m} \frac{q F_L^2(q)}{q_0 F_L^2(q_0)} \quad (5.1)$$

with the break-up momentum q (q_0) of a state with mass m (nominal mass m_0) decaying into its two daughters, and the angular-momentum barrier factors $F_L(q)$. The intensity and the Argand diagram are shown exemplarily for the $\rho(770)$ in fig. 5.4.

For the $f_0(980)$ isobar the relativistic Breit-Wigner amplitude is not well suited as the KK decay channel opens close to the resonance mass and distorts the lineshape. For this isobar a Flatté parameterization taking also the KK decay into account is used

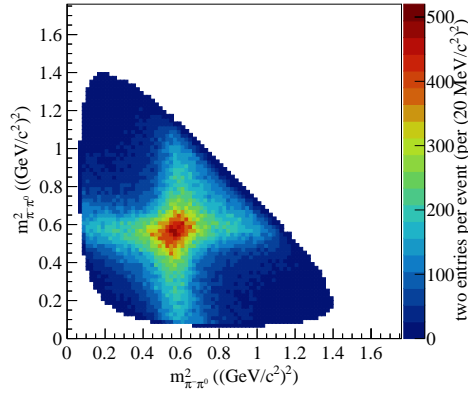


Figure 5.2: Dalitz plot showing the squared invariant masses of one $\pi^-\pi^0$ subsystem versus the other $\pi^-\pi^0$ subsystem for a $20 \text{ MeV}/c^2$ wide mass slice around the mass of the $a_2(1320)$ for the $\pi^-\pi^0\pi^0$ final state ($1.30 < m_{\pi^-\pi^0\pi^0} < 1.32 \text{ GeV}/c^2$).

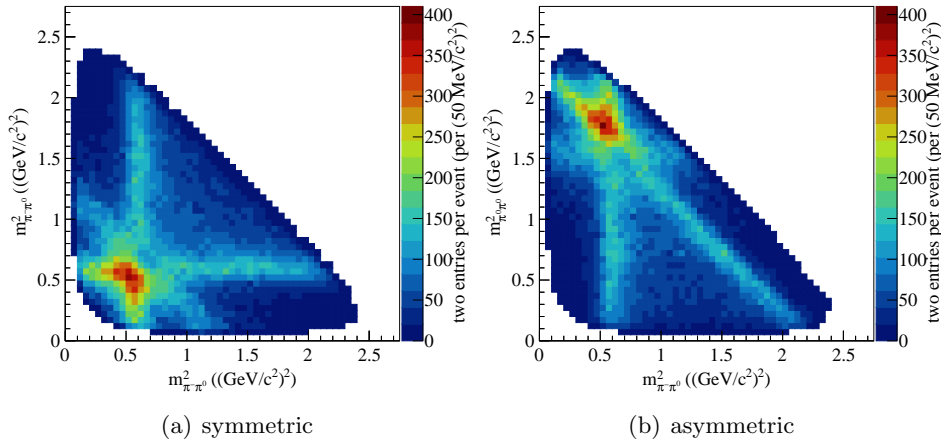


Figure 5.3: Dalitz plots for a $20 \text{ MeV}/c^2$ wide mass slice around the mass of the $\pi_2(1670)$ for the $\pi^-\pi^0\pi^0$ final state ($1.66 < m_{\pi^-\pi^0\pi^0} < 1.68 \text{ GeV}/c^2$). In (a) the squared invariant masses of one $\pi^-\pi^0$ subsystem versus the other $\pi^-\pi^0$ subsystem is shown, in (b) the squared invariant masses of one $\pi^-\pi^0$ subsystem versus the $\pi^0\pi^0$ subsystem is shown.

particle	mass (MeV/c ²)	isobars in $\pi^-\eta\eta$	mass (MeV/c ²)	width (MeV/c ²)	
p^+	938.272	a_0 (980)	993.1	71	
π^-	139.57	a_0 (1450)	1474	265	
π^0	134.977	a_2 (1320)	1318	107	
η	547.3	a_4 (2040)	2014	361	
isobars in $\pi^-\pi^0\pi^0$	mass (MeV/c ²)	width (MeV/c ²)	f_0 (1370)	1350	350
f_0 (1500)	1500	112	f_0 (1500)	1500	112
ρ (770)	769.3	150.2	f_2 (1270)	1275.4	185.1
f_2 (1270)	1275.4	185.1	f_4 (2050)	2034	222
ρ_3 (1690)	1691	161	π_1 (1400)	1354	330

Table 5.1: Particle masses and resonance parameters used for the partial-wave analysis of the $\pi^-\pi^0\pi^0$ and $\pi^-\eta\eta$ final state.

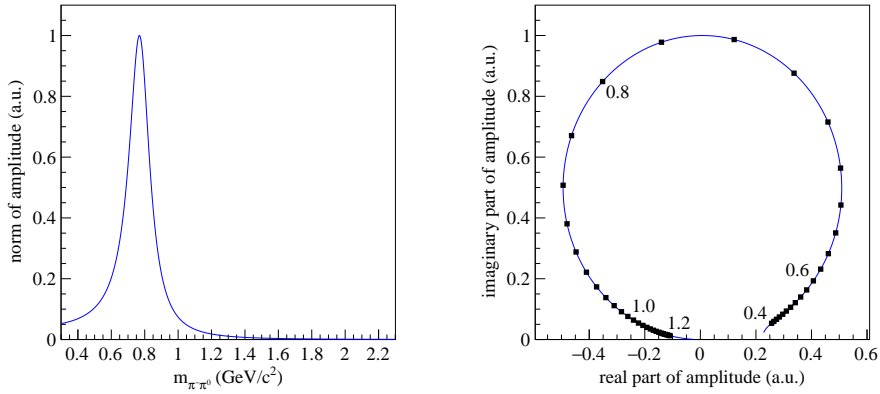


Figure 5.4: Intensity and Argand diagram for the ρ (770) parameterized by a relativistic Breit-Wigner amplitude. The black markers in the Argand diagram indicate equidistant points in mass apart by 20 MeV, the numbers indicate at which two-body mass these points are reached.

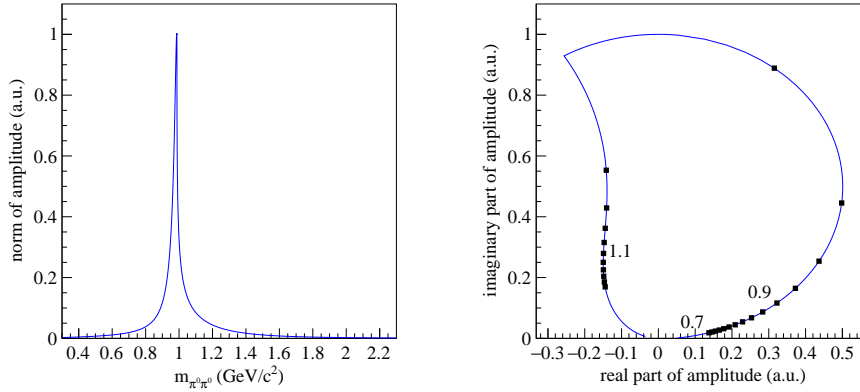


Figure 5.5: Intensity and Argand diagram for the $f_0(980)$ parameterized by a Flatté amplitude [3]. The black markers in the Argand diagram indicate equidistant points in mass apart by 20 MeV, the numbers indicate at which two-body mass these points are reached.

$$\Delta_\xi(m) = \frac{1}{m_0^2 - m^2 - i(g_{\pi\pi}\rho_{\pi\pi} + g_{KK}\rho_{KK})} \quad \text{with } \rho_{\pi\pi} = \frac{2q_{\pi\pi}}{m} \quad \text{and } \rho_{KK} = \frac{2q_{KK}}{m} \quad (5.2)$$

with the break-up momentum $q_{\pi\pi}$ (q_{KK}) of a state with mass m decaying into $\pi\pi$ (KK). The parameters for the $f_0(980)$ have been obtained in [3]

$$m_0 = 0.965 \text{ GeV}/c^2 \quad (5.3)$$

$$g_{\pi\pi} = 0.165 (\text{GeV}/c^2)^2 \quad (5.4)$$

$$g_{KK}/g_{\pi\pi} = 4.21 \quad (5.5)$$

This parameterization is shown in fig. 5.5.

The relativistic Breit-Wigner is also not used for the $(\pi\pi)_S$ amplitude. Here the modified M -solution from [18] is used with the following modifications removing the $f_0(980)$, which is taken into account by separate waves, and the diagonal entries of the M matrix

$$c_{11}^4 = c_{22}^4 = 0 \quad (5.6)$$

$$c_{12}^0 = c_{12}^1 = c_{12}^2 = c_{12}^3 = c_{12}^4 = 0 \quad (5.7)$$

$$a_{12} = 0 \quad (5.8)$$

$$f_1^1 = f_2^1 = 0 \quad (5.9)$$

This parameterization is depicted in fig. 5.6.

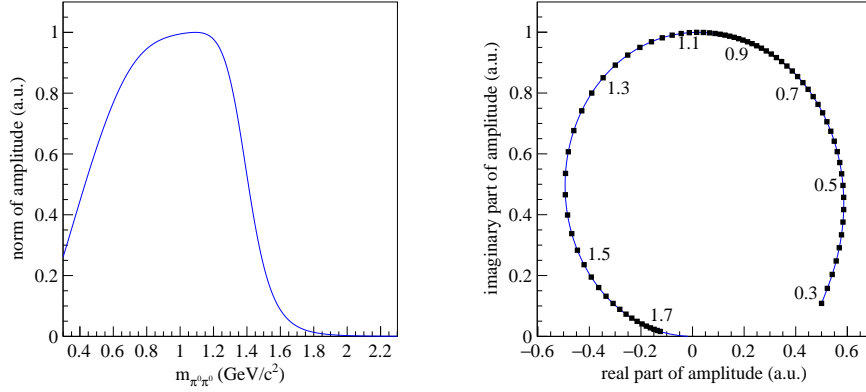


Figure 5.6: Intensity and Argand diagram for the $(\pi\pi)_S$ parameterized by a modified M -solution from [18]. The black markers in the Argand diagram indicate equidistant points in mass apart by 20 MeV, the numbers indicate at which two-body mass these points are reached.

The Blatt-Weisskopf barrier factors $F_L(q)$ [26] are used with the parameterizations given in [52]

$$F_0(q) = 1$$

$$F_1(q) = \sqrt{\frac{2z}{z+1}}$$

$$F_2(q) = \sqrt{\frac{13z^2}{z^2+3z+9}}$$

$$F_3(q) = \sqrt{\frac{277z^3}{z^3+6z^2+45z+225}}$$

$$F_4(q) = \sqrt{\frac{12\,746z^4}{z^4+10z^3+135z^2+1\,575z+11\,025}}$$

$$F_5(q) = \sqrt{\frac{998\,881z^5}{z^5+15z^4+315z^3+6\,300z^2+99\,225z+893\,025}}$$

$$F_6(q) = \sqrt{\frac{118\,394\,977z^6}{z^6+21z^5+630z^4+18\,900z^3+496\,125z^2+9\,823\,275z+108\,056\,025}}$$

with $z = (q/q_R)^2$, where q is the break-up momentum and $q_R = 197.3 \text{ MeV}/c$ the range parameter of the interaction.

5.1.2 Wave Set

Using the six isobars from above, a wave set containing 88 waves had been developed for the $\pi^-\pi^-\pi^+$ final state [50, 11] starting from smaller wave sets of previous analyses [15, 13, 78, 32, 44]. An initial pool of waves with all possible combinations with spin $J \leq 6$, spin projection $M \leq 1$, positive reflectivity $\varepsilon = +1$, and the spin J_ξ of the isobar ranging from 0 to 3 was created. From these about 140 waves, those with a flat intensity spectrum over the complete mass range were removed in an iterative procedure. Some additional waves with spin projection $M = 2$ were added when the corresponding wave with $M = 1$ had a large intensity. Seven waves with negative reflectivity were taken over from the wave sets of previous analyses. To be able to compare the results for the $\pi^-\pi^0\pi^0$ final state presented here with the results for the $\pi^-\pi^-\pi^+$ final state, the same 88 wave set is used (table 5.2). Some of the waves are only used above a mass threshold. If the thresholded waves are used below this threshold, unphysical large destructive interferences between certain waves appear, distorting also the results for other waves. The reason for this is not yet fully understood, it is assumed that the low-mass tails of the isobar amplitudes do not have enough distinguishing power. A more systematic approach using half-Cauchy priors to suppress the intensity in unneeded waves [23] has meanwhile been performed for the $\pi^-\pi^-\pi^+$ final state [40], but suffers from the same problem. This approach in general confirms the wave set used here, removing and adding only waves with small intensities in particular with high spins.

The data are binned into 50 mass bins of $40 \text{ MeV}/c^2$ width, ranging from $0.5 \text{ GeV}/c^2$ to $2.5 \text{ GeV}/c^2$. The bin width is limited by the mass resolution at high masses (section 3.5.1). As the mass spectrum depends on the reduced squared four-momentum transfer t' (fig. 3.10 in section 3.4.4), the data was also binned in this variable. Eight bins were created such that each t' bin, integrated over the analyzed mass range, contains a similar number of events (table 3.2 in section 3.4.4).

A rank-1 fit was performed like for $\pi^-\pi^-\pi^+$. In each of the 400 bins, 100 independent minimizations of the log-likelihood function eq. (4.44) with random start values for the transition amplitudes were performed to find the best fit and to avoid local minima of the log-likelihood surface.

5.2 Verification of Fit Quality

Typical tests to judge the quality of the fit directly by comparing data and the fit result, like the chi-square test, cannot be applied due to the high dimensionality of data. To estimate the quality of the fit and the acceptance corrections, the fit result is used to generate distributions of various kinematic variables, and also their correlations, that can be compared to the distributions obtained from data. At the maximum of the log-likelihood, the expected number of events \bar{N} is close to the number of observed events. Equation (4.32) is rewritten as

Chapter 5 Partial-Wave Analysis of the $\pi^-\pi^0\pi^0$ Final State

wave	threshold (GeV/ c^2)	wave	threshold (GeV/ c^2)
$0^{-+}0^+(\pi\pi)_S \pi S$		$2^{-+}2^+ f_2(1270) \pi D$	
$0^{-+}0^+ f_0(980) \pi S$	1.20	$3^{++}0^+(\pi\pi)_S \pi F$	
$0^{-+}0^+ f_0(1500) \pi S$	1.70	$3^{++}0^+ \rho(770) \pi D$	
$0^{-+}0^+ \rho(770) \pi P$		$3^{++}0^+ \rho(770) \pi G$	
$0^{-+}0^+ f_2(1270) \pi D$		$3^{++}0^+ f_2(1270) \pi P$	0.96
$1^{++}0^+(\pi\pi)_S \pi P$		$3^{++}0^+ \rho_3(1690) \pi S$	1.38
$1^{++}0^+ f_0(980) \pi P$	1.18	$3^{++}0^+ \rho_3(1690) \pi I$	
$1^{++}0^+ \rho(770) \pi S$		$3^{++}1^+(\pi\pi)_S \pi F$	
$1^{++}0^+ \rho(770) \pi D$		$3^{++}1^+ \rho(770) \pi D$	
$1^{++}0^+ f_2(1270) \pi P$	1.22	$3^{++}1^+ \rho(770) \pi G$	
$1^{++}0^+ f_2(1270) \pi F$		$3^{++}1^+ f_2(1270) \pi P$	1.14
$1^{++}0^+ \rho_3(1690) \pi D$		$3^{++}1^+ \rho_3(1690) \pi S$	1.38
$1^{++}0^+ \rho_3(1690) \pi G$		$3^{-+}1^+ \rho(770) \pi F$	
$1^{++}1^+(\pi\pi)_S \pi P$	1.10	$3^{-+}1^+ f_2(1270) \pi D$	1.34
$1^{++}1^+ f_0(980) \pi P$	1.14	$4^{++}1^+ \rho(770) \pi G$	
$1^{++}1^+ \rho(770) \pi S$		$4^{++}1^+ f_2(1270) \pi F$	
$1^{++}1^+ \rho(770) \pi D$		$4^{++}1^+ \rho_3(1690) \pi D$	1.70
$1^{++}1^+ f_2(1270) \pi P$		$4^{++}2^+ \rho(770) \pi G$	
$1^{-+}1^+ \rho(770) \pi P$		$4^{++}2^+ f_2(1270) \pi F$	
$2^{++}1^+ \rho(770) \pi D$		$4^{-+}0^+(\pi\pi)_S \pi G$	1.40
$2^{++}1^+ f_2(1270) \pi P$	1.00	$4^{-+}0^+ \rho(770) \pi F$	
$2^{++}1^+ \rho_3(1690) \pi D$	0.80	$4^{-+}0^+ f_2(1270) \pi D$	
$2^{++}2^+ \rho(770) \pi D$		$4^{-+}0^+ f_2(1270) \pi G$	1.60
$2^{++}2^+ f_2(1270) \pi P$	1.40	$4^{-+}1^+ \rho(770) \pi F$	
$2^{-+}0^+(\pi\pi)_S \pi D$		$4^{-+}1^+ f_2(1270) \pi D$	
$2^{-+}0^+ f_0(980) \pi D$	1.16	$5^{++}0^+(\pi\pi)_S \pi H$	
$2^{-+}0^+ \rho(770) \pi P$		$5^{++}0^+ \rho(770) \pi G$	
$2^{-+}0^+ \rho(770) \pi F$		$5^{++}0^+ f_2(1270) \pi F$	0.98
$2^{-+}0^+ f_2(1270) \pi S$		$5^{++}0^+ f_2(1270) \pi H$	
$2^{-+}0^+ f_2(1270) \pi D$		$5^{++}0^+ \rho_3(1690) \pi D$	1.36
$2^{-+}0^+ f_2(1270) \pi G$		$5^{++}1^+(\pi\pi)_S \pi H$	
$2^{-+}0^+ \rho_3(1690) \pi P$	1.00	$5^{++}1^+ f_2(1270) \pi F$	
$2^{-+}1^+(\pi\pi)_S \pi D$		$6^{++}1^+ \rho(770) \pi I$	
$2^{-+}1^+ \rho(770) \pi P$		$6^{++}1^+ f_2(1270) \pi H$	
$2^{-+}1^+ \rho(770) \pi F$		$6^{-+}0^+(\pi\pi)_S \pi I$	
$2^{-+}1^+ f_2(1270) \pi S$	1.10	$6^{-+}0^+ \rho(770) \pi H$	
$2^{-+}1^+ f_2(1270) \pi D$		$6^{-+}0^+ f_2(1270) \pi G$	
$2^{-+}1^+ \rho_3(1690) \pi P$	1.30	$6^{-+}0^+ \rho_3(1690) \pi F$	
$2^{-+}2^+ \rho(770) \pi P$		$6^{-+}1^+(\pi\pi)_S \pi I$	
$2^{-+}2^+ f_2(1270) \pi S$		$6^{-+}1^+ \rho(770) \pi H$	
$1^{++}1^- \rho(770) \pi S$		$2^{++}0^- f_2(1270) \pi P$	1.18
$1^{-+}0^- \rho(770) \pi P$		$2^{++}1^- f_2(1270) \pi P$	1.30
$1^{-+}1^- \rho(770) \pi P$		$2^{-+}1^- f_2(1270) \pi S$	
$2^{++}0^- \rho(770) \pi D$			

Table 5.2: The 88 waves contained in the wave set from [50, 11]. The flat wave is omitted.

$$\bar{N} = \int d\Phi_n(\tau) \mathcal{I}(\tau) \eta(\tau) \quad (5.10)$$

$$= \frac{V_{\Phi_n}}{N_{\text{MC}}^{\text{gen}}} \sum_e^{N_{\text{MC}}^{\text{acc}}} \mathcal{I}(\tau_e^{\text{acc}}) \quad (5.11)$$

This equation indicates that each accepted Monte Carlo event can be weighted with an individual weight $w(\tau_e^{\text{acc}})$ to get the total number of events. Inserting the total partial-wave intensity eq. (4.45) yields

$$w(\tau_e^{\text{acc}}) = \frac{V_{\Phi_n}}{N_{\text{MC}}^{\text{gen}}} \mathcal{I}(\tau_e^{\text{acc}}) \quad (5.12)$$

$$= \frac{V_{\Phi_n}}{N_{\text{MC}}^{\text{gen}}} \frac{1}{V_{\Phi_n}} \left[\sum_{\varepsilon=\pm 1} \sum_r^{N_{\text{rank}}^\varepsilon} \left| \sum_i^{N_{\text{waves}}^\varepsilon} \bar{T}_i^{r\varepsilon} \bar{\psi}_i^\varepsilon(\tau_e^{\text{acc}}) \right|^2 + \bar{T}_{\text{flat}}^2 \right] \quad (5.13)$$

$$= \frac{1}{N_{\text{MC}}^{\text{gen}}} \left[\sum_{\varepsilon=\pm 1} \sum_r^{N_{\text{rank}}^\varepsilon} \left| \sum_i^{N_{\text{waves}}^\varepsilon} \bar{T}_i^{r\varepsilon} \bar{\psi}_i^\varepsilon(\tau_e^{\text{acc}}) \right|^2 + \bar{T}_{\text{flat}}^2 \right] \quad (5.14)$$

Like the log-likelihood eq. (4.44) the weights do not require an evaluation of the phase-space volume V_{Φ_n} .

The kinematic distributions of a single wave i with reflectivity ε in rank r can be obtained by applying the weight

$$w_i^{r\varepsilon}(\tau_e^{\text{acc}}) = \frac{1}{N_{\text{MC}}^{\text{gen}}} \left| \bar{T}_i^{r\varepsilon} \bar{\psi}_i^\varepsilon(\tau_e^{\text{acc}}) \right|^2 \quad (5.15)$$

As for the elements of the spin-density matrix (section 4.5), it is possible to calculate the weights for any sub-set of waves. These weights could for example be used to find out which parts of the phase space are illuminated by a particular combination of waves.

Histograms are filled with kinematic information calculated from the accepted Monte Carlo events, where each entry is weighted with $w(\tau_e^{\text{acc}})$. These distributions are directly comparable to the corresponding ones from real data. This procedure is called kinematic validation.

By construction, the three-pion invariant mass spectra shown in fig. 5.7 agree perfectly between real data and weighted Monte Carlo. Some differences are seen in the mass spectra of the two-pion subsystems (figs. 5.8 and 5.9) pointing to a non-perfect description of the isobars. In particular in the low-mass region below about $0.6 \text{ GeV}/c^2$ some deviations are visible which might also be caused by the indistinguishability of the isobars by only their low-mass tails. In the highest t' bin a tiny contamination of the $\pi^0\pi^0$ spectrum for real data with K_S^0 can be seen (fig. 5.9(b)), but this should not distort the result.

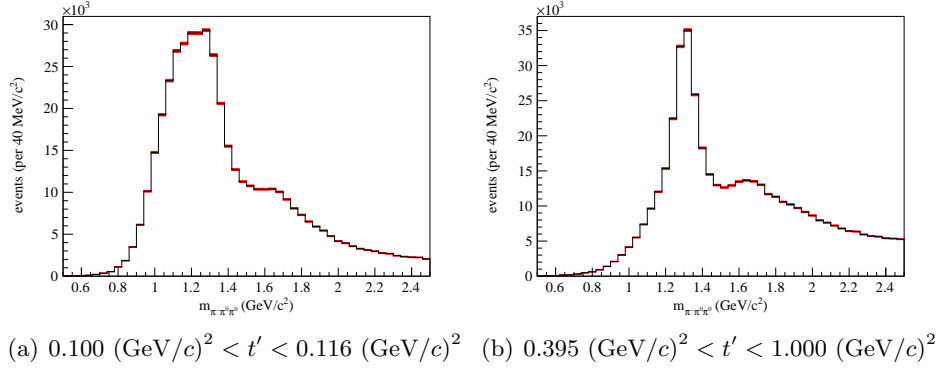


Figure 5.7: Three-pion invariant mass $m_{\pi^-\pi^0\pi^0}$ spectra for (a) the lowest and (b) the highest t' bin. Real data are shown in black, the distribution obtained from weighted Monte Carlo is shown in red.

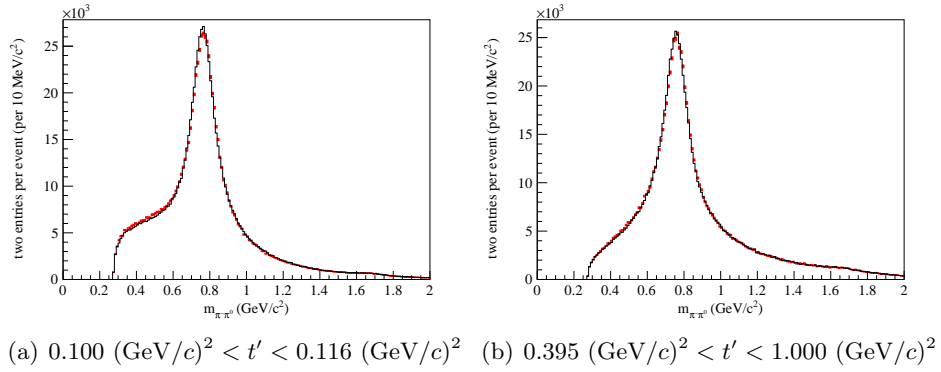


Figure 5.8: Two-pion invariant mass spectra $m_{\pi^-\pi^0}$ for the charged $\pi^-\pi^0$ sub-systems of the three-pion final state for (a) the lowest and (b) the highest t' bin. Real data are shown in black, the distribution obtained from weighted Monte Carlo is shown in red.

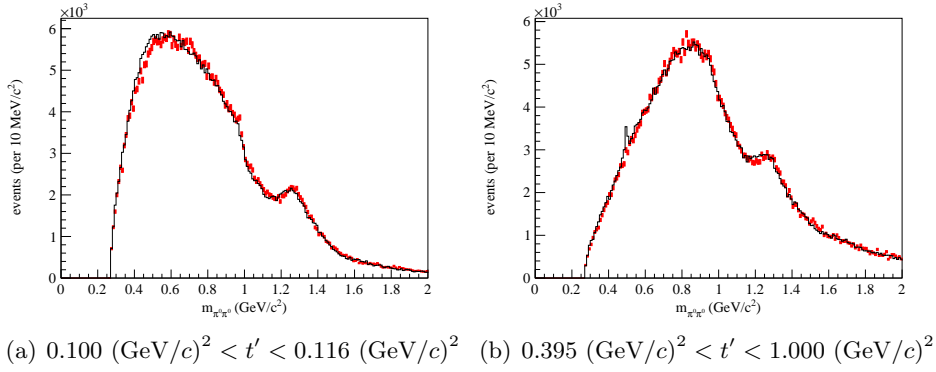


Figure 5.9: Two-pion invariant mass spectra $m_{\pi^0\pi^0}$ for the neutral $\pi^0\pi^0$ subsystems of the three-pion final state for (a) the lowest and (b) the highest t' bin. Real data are shown in black, the distribution obtained from weighted Monte Carlo is shown in red.

A comparison of the angles depending on $m_{\pi^-\pi^0\pi^0}$ and t' is shown in figs. 5.10 and 5.11 for the $\pi^0\pi^0$ system. For the two central mass ranges from 1.02 to 1.98 GeV/c^2 a good agreement between real data and weighted Monte Carlo data is found for the four angles used in the partial-wave analysis. The ratio in the lowest and highest mass range is distorted by the regions with only a few entries, outside these region a good agreement is found.

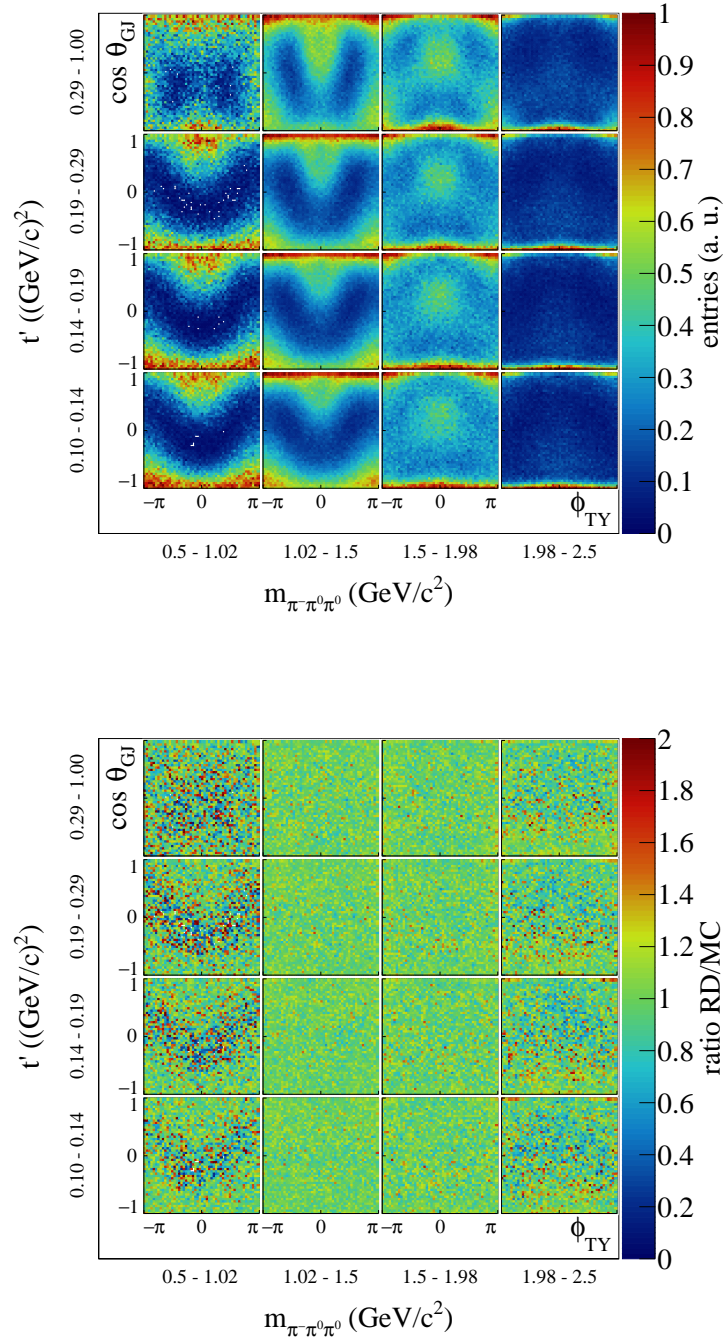


Figure 5.10: Distribution of events in the angles of the Gottfried-Jackson system for neutral isobars for real data, and the ratio of real data over weighted Monte Carlo.

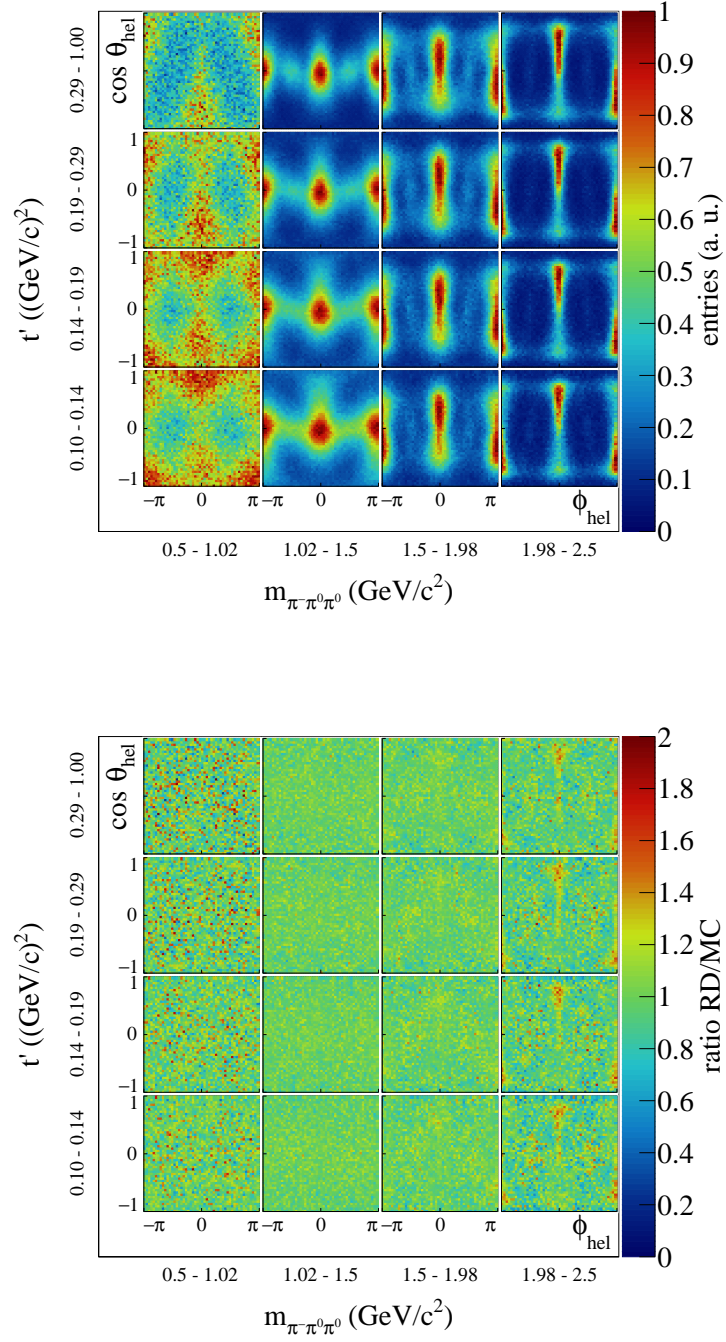


Figure 5.11: Distribution of events in the angles of the helicity frame for neutral isobars for real data, and the ratio of real data over weighted Monte Carlo.

5.3 Total Intensities and Spin Totals

The total intensities of the fit obtained with eq. (4.50) are shown in fig. 5.12. They can be understood as acceptance corrected versions of the mass spectra shown in figs. 3.10 and 3.12(a). The change of the mass spectrum below $1.3 \text{ GeV}/c^2$ with the reduced squared four-momentum transfer t' , which lead to the binning in t' mentioned in section 3.4.4, is also visible in these plots.

Using eq. (4.54) the intensity of a set of waves can be calculated. The intensities for sets of waves containing all waves with the same quantum numbers J^{PC} , M or ε , or a combination thereof, are called spin totals. In these spin totals, interference effects between waves are considered. In contrast to this, the t' -summed intensity is obtained by incoherently summing the results obtained in the eight t' bins.

There are two kinds of waves that are considered to not contain resonant contributions. The first is the flat wave (fig. 5.13). The contribution of the flat wave to the total intensity increases from 0.4% in the lowest t' bin to 3.1% in the highest t' bin. Averaged over all eight t' bins, the contribution of the flat wave is 1%. The second kind of waves are those with negative reflectivity (fig. 5.14). The contribution of the $\varepsilon = -1$ spin totals to the total intensity increases from 1.6% in the lowest t' bin to 3.2% in the highest t' bin. Averaged over all eight t' bins, the contribution is 2%.

Table 5.3 lists the relative contributions of several spin totals to the total intensity in the lowest and the highest t' bin, and averaged over all t' bins. The first set of spin totals are for waves with positive reflectivity that have the same J^{PC} quantum numbers, but differ in the decay chain, i.e. in the isobar or in the relative orbital angular momentum between the isobar and the bachelor pion. Due to interference effects these relative contributions do not sum up to the relative contribution of all waves with positive reflectivity. But, as waves with different reflectivities do not interfere, the sum of the relative contributions of all waves with positive reflectivity, all waves with negative reflectivity, and of the flat wave have to sum up to 100%.

The contributions of the various J^{PC} components with positive reflectivity to the total intensity change quite drastically with t' . The $J^{PC} = 1^{++}$ sector with a_1 -like quantum numbers is dominant in all t' bins. However, its relative contribution to the total intensity decreases from 60%, which is four times larger than the second largest contribution in the lowest t' bin, to 28% in the highest t' bin, which is comparable to the two next smaller contributions. The shape of the $J^{PC} = 1^{++}$, $\varepsilon = +$ spin total (fig. 5.15) suggests that the intensity on the low-mass side of the peak at $1.3 \text{ GeV}/c^2$ in figs. 3.10, 3.12(a) and 5.12 can to a large extent be attributed to the a_1 sector. Accordingly, the position of the peak moves from about $1.1 \text{ GeV}/c^2$ at low t' to $1.3 \text{ GeV}/c^2$ at high t' . Such a behavior is a priori not expected for genuine resonances and suggests a strong interference of the resonant components with possible non-resonant contributions. At the same time the shape of other spin totals, like e.g. the $J^{PC} = 2^{++}$ (a_2 -like, fig. 5.16) or the $J^{PC} = 2^{-+}$ (π_2 -like, fig. 5.17), does not change with t' .

5.3 Total Intensities and Spin Totals

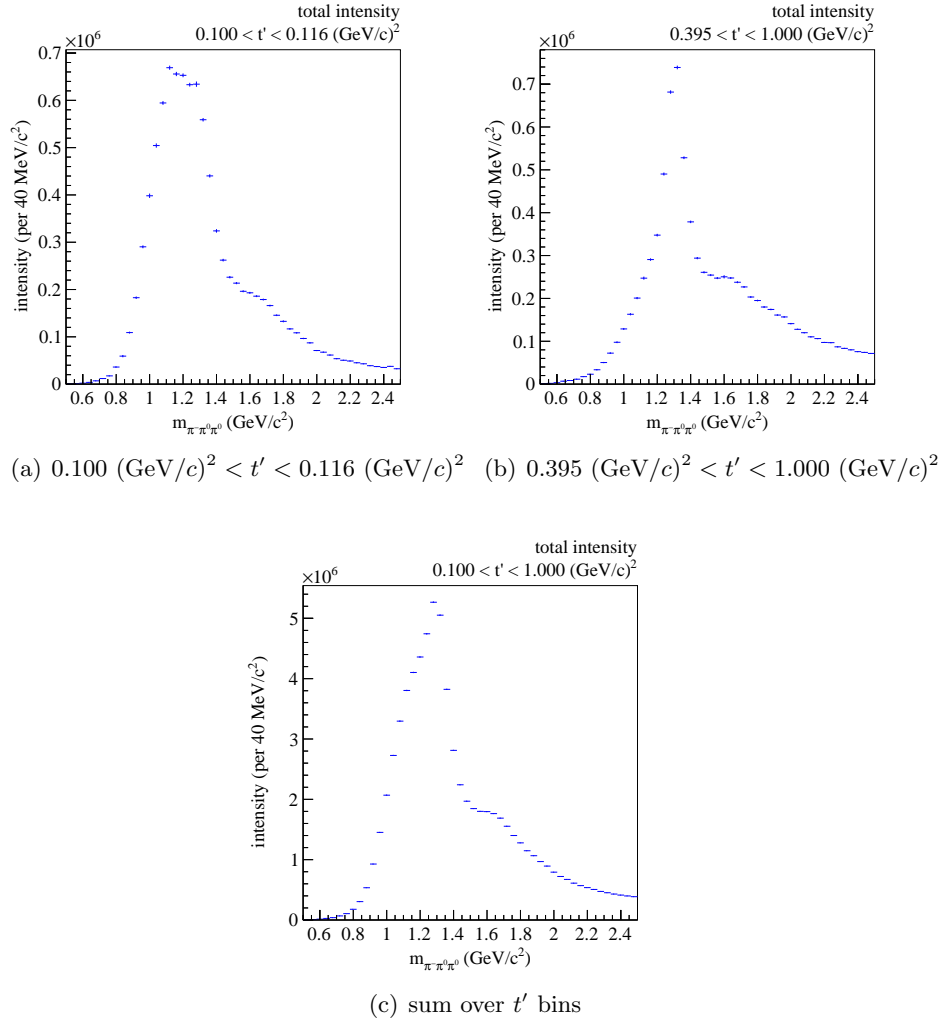


Figure 5.12: Total intensity of the fit in (a) the lowest and (b) the highest t' bin, and (c) the t' -summed total intensity.

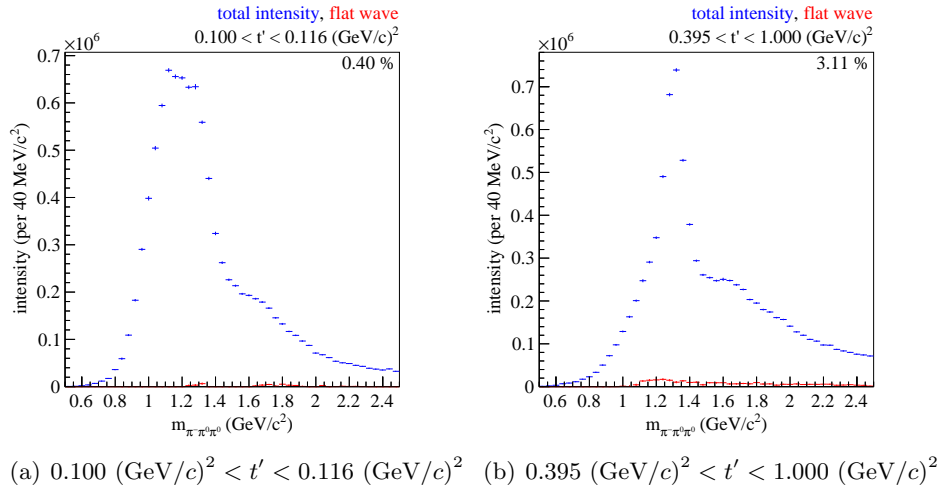


Figure 5.13: Intensity of the flat wave (red markers) compared to the total intensity (blue markers) for (a) the lowest and (b) the highest t' bin. The fraction of the intensity of the flat wave with respect to the total intensity is given in the upper right corner of the plots.

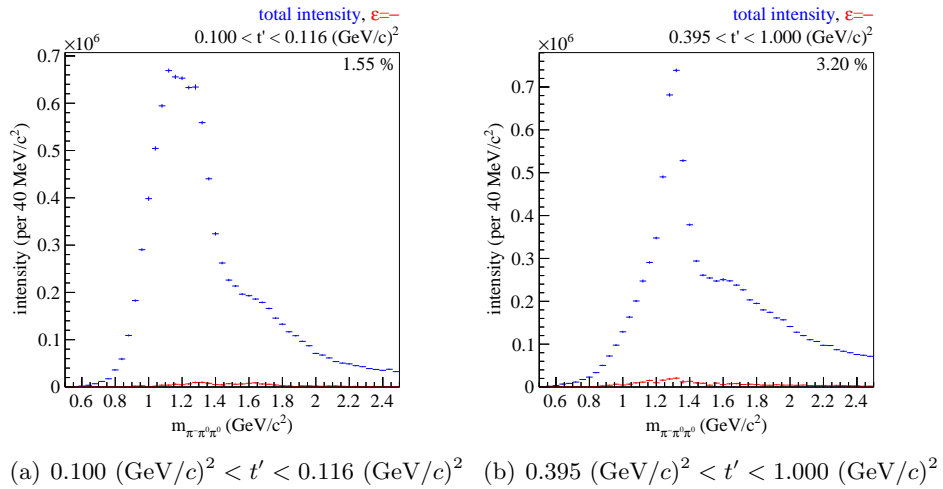


Figure 5.14: Spin total for waves with negative reflectivity (red markers) compared to the total intensity (blue markers) for (a) the lowest and (b) the highest t' bin. The fraction of the spin total for waves with negative reflectivity with respect to the total intensity is given in the upper right corner of the plots.

5.3 Total Intensities and Spin Totals

wave	lowest t' bin	highest t' bin	average over t' bins
$J^{PC} = 0^{-+}, \varepsilon = +$	10.3 %	4.5 %	6.5 %
$J^{PC} = 1^{++}, \varepsilon = +$	60.0 %	27.8 %	49.8 %
$J^{PC} = 1^{-+}, \varepsilon = +$	0.9 %	1.0 %	1.0 %
$J^{PC} = 2^{++}, \varepsilon = +$	4.9 %	23.7 %	11.3 %
$J^{PC} = 2^{-+}, \varepsilon = +$	14.1 %	22.6 %	18.0 %
$J^{PC} = 3^{++}, \varepsilon = +$	3.9 %	5.7 %	4.5 %
$J^{PC} = 3^{-+}, \varepsilon = +$	0.1 %	0.2 %	0.1 %
$J^{PC} = 4^{++}, \varepsilon = +$	0.6 %	1.8 %	1.1 %
$J^{PC} = 4^{-+}, \varepsilon = +$	1.4 %	3.6 %	2.4 %
$J^{PC} = 5^{++}, \varepsilon = +$	0.7 %	0.7 %	0.8 %
$J^{PC} = 6^{++}, \varepsilon = +$	0.1 %	0.2 %	0.1 %
$J^{PC} = 6^{-+}, \varepsilon = +$	1.0 %	1.9 %	1.5 %
positive reflectivity	98.0 %	93.7 %	97.1 %
negative reflectivity	1.6 %	3.2 %	2.0 %
flat	0.4 %	3.1 %	0.9 %

Table 5.3: Relative contributions of spin totals with respect to the total intensity.

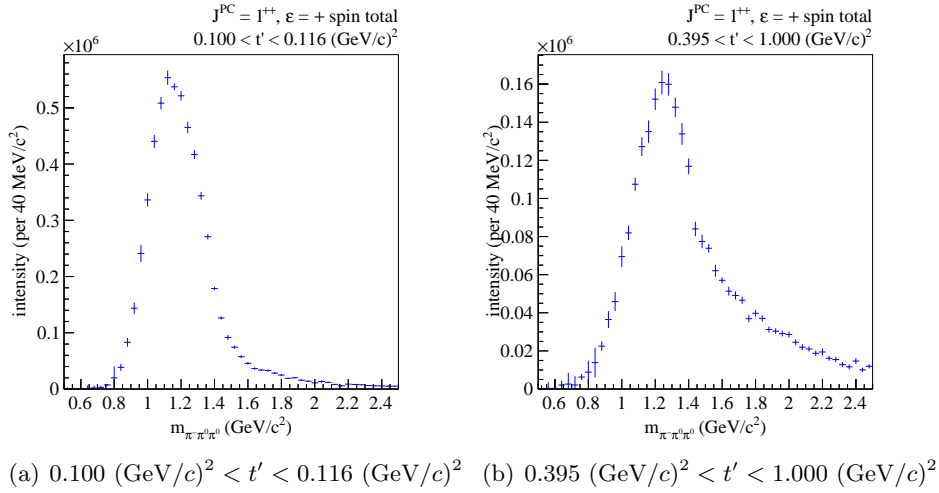
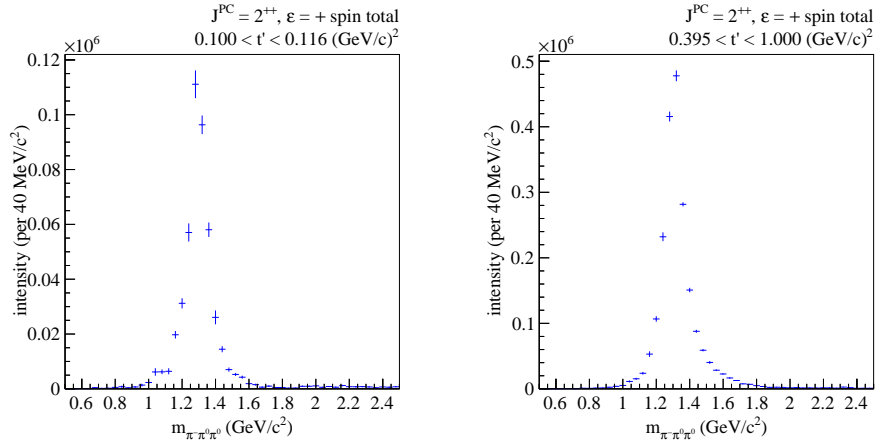
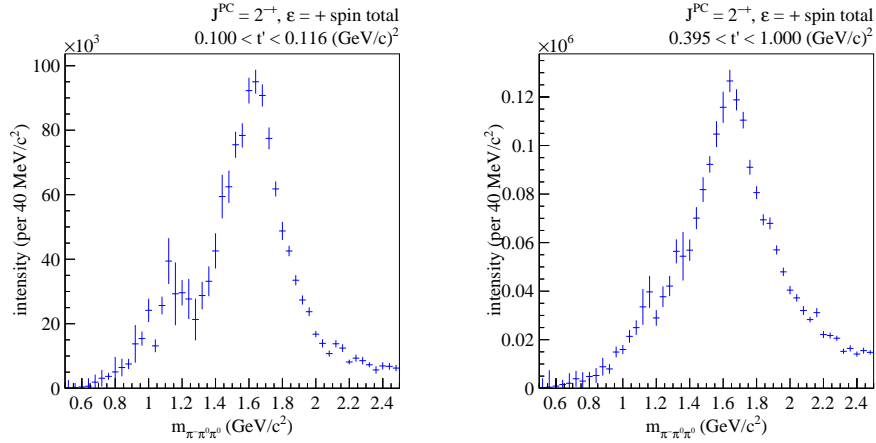


Figure 5.15: Spin total for waves with positive reflectivity and quantum numbers $J^{PC} = 1^{++}$ for (a) the lowest and (b) the highest t' bin.



(a) 0.100 (GeV/c)² < t' < 0.116 (GeV/c)² (b) 0.395 (GeV/c)² < t' < 1.000 (GeV/c)²

Figure 5.16: Spin total for waves with positive reflectivity and quantum numbers $J^{PC} = 2^{++}$ for (a) the lowest and (b) the highest t' bin.



(a) 0.100 (GeV/c)² < t' < 0.116 (GeV/c)² (b) 0.395 (GeV/c)² < t' < 1.000 (GeV/c)²

Figure 5.17: Spin total for waves with positive reflectivity and quantum numbers $J^{PC} = 2^{-+}$ for (a) the lowest and (b) the highest t' bin.

5.4 Individual Partial-Wave Intensities

The intensities of selected individual waves are discussed below (sections 5.7 to 5.13). All waves used in the resonance-model fit (section 5.6) are shown. In addition, for some of these waves the partners with higher spin projection M or with the isospin partners of the isobars are also shown. The three waves with the largest intensities correspond to the wave with the highest intensity in each of the three J^{PC} sectors mentioned above (1^{++} , 2^{++} , 2^{-+}).

The t' dependence of the intensity spectra is studied in mass ranges around well known resonances. For each t' bin the intensity spectrum of a wave is integrated over a certain mass range, and this integral is plotted as a function of the t' bin. The obtained t' -dependent intensity spectra are exemplarily shown in fig. 5.23 for waves with $J^{PC} = 1^{++}$. A χ^2 -fit to the t' -dependent intensity spectra has been performed with the function

$$C \cdot t'^M e^{-b \cdot t'} \quad (5.16)$$

where the slope parameter b and a constant C are optimized such that the integral of the function over each t' bin agrees with the measured intensity in each t' bin. To be insensitive to changes in the production mechanism, the highest t' bin has been excluded from this fit, as it covers a rather large range of the reduced squared four-momentum transfer. The results of these fits are summarized in table 5.4, the corresponding plots can be found in sections 5.7 to 5.13.

5.5 Phases

The presence of a resonance in a specific wave cannot be concluded from the observation of a peak in the intensity spectrum alone, but needs to be confirmed by an accompanying phase motion of 90° at the mass value of the peak, and a phase motion of 180° over the complete mass range from $m = 0$ to $m \rightarrow \infty$ (as can be seen in the Argand diagram of a relativistic Breit-Wigner as shown in fig. 5.4). As absolute phases cannot be measured, the relative phases between two waves have to be studied. A phase difference of 180° is observed only in the ideal case of a resonance in one wave and no resonance in the second wave. If both waves contain the same resonance, their phase difference is constant. If the two waves contain two different resonances with different masses, the resulting phase difference should be visible in the mass region where the two overlap. Selected phase are shown in sections 5.7 to 5.13.

5.6 Resonance-Model Fit

Resonance parameters are extracted in the second step of the partial-wave analysis. The mass-dependence of the spin-density matrix elements, extracted by the mass-independent analysis, is described with a resonance model.

wave	mass range (GeV/ c^2)	slope (GeV/ c) $^{-2}$	χ^2/ndf
Major waves			
$1^{++}0^+ f_2(1270) \pi P$	1.66 - 1.90	6.7 ± 0.6	2.51
$1^{++}0^+ \rho(770) \pi S$	1.10 - 1.30	10.9 ± 0.0	8.45
$1^{++}1^+ \rho(770) \pi S$	1.10 - 1.30	16.1 ± 0.2	1.75
$1^{-+}1^+ \rho(770) \pi P$	1.50 - 1.70	9.7 ± 0.3	1.30
$2^{++}1^+ f_2(1270) \pi P$	1.18 - 1.42	7.6 ± 0.5	3.03
$2^{++}1^+ \rho(770) \pi D$	1.18 - 1.42	8.3 ± 0.1	2.14
$2^{++}2^+ \rho(770) \pi D$	1.18 - 1.42	9.6 ± 0.3	0.98
$2^{-+}0^+ f_2(1270) \pi S$	1.54 - 1.78	8.5 ± 0.1	2.26
$2^{-+}1^+ f_2(1270) \pi S$	1.54 - 1.78	7.4 ± 0.2	2.06
$2^{-+}0^+ f_2(1270) \pi D$	1.78 - 2.02	7.5 ± 0.3	1.02
$2^{-+}0^+ \rho(770) \pi F$	1.54 - 1.78	8.7 ± 0.2	1.70
$2^{-+}0^+ \rho(770) \pi F$	1.78 - 2.02	6.3 ± 0.2	0.74
$4^{++}1^+ f_2(1270) \pi F$	1.86 - 2.06	10.8 ± 0.5	1.13
$4^{++}1^+ \rho(770) \pi G$	1.86 - 2.06	8.9 ± 0.2	0.25
Waves with $f_0(980)$ isobar			
$0^{-+}0^+ f_0(980) \pi S$	1.70 - 1.90	10.8 ± 0.3	0.47
$1^{++}0^+ f_0(980) \pi P$	1.38 - 1.58	11.2 ± 0.7	1.51
$2^{-+}0^+ f_0(980) \pi D$	1.54 - 1.78	6.6 ± 0.7	0.75
$2^{-+}0^+ f_0(980) \pi D$	1.78 - 2.02	6.7 ± 0.6	0.54
Waves with $(\pi\pi)_S$ isobar			
$0^{-+}0^+ (\pi\pi)_S \pi S$	1.10 - 1.30	19.5 ± 0.5	7.13
$0^{-+}0^+ (\pi\pi)_S \pi S$	1.70 - 1.90	12.2 ± 0.3	0.35
$1^{++}0^+ (\pi\pi)_S \pi P$	1.10 - 1.30	13.2 ± 0.2	5.99
$2^{-+}0^+ (\pi\pi)_S \pi D$	1.54 - 1.78	9.6 ± 0.3	1.15

 Table 5.4: Slopes of the t' spectra of various waves.

With the ansatz chosen for the mass-independent fit, the transition amplitudes absorb the factors of the cross-section formula eq. (4.10) that are assumed to be constant within one bin of the invariant mass of the final state m and the reduced squared four-momentum transfer t'

$$\sqrt{\frac{m}{|\vec{p}_a|^2 s}} \mathcal{A}(s, t; m) \quad (5.17)$$

Here $\mathcal{A}(s, t; m)$ is the scattering amplitude for the process $\pi^- + p^+ \rightarrow X^- + p^+$. For a fixed-target experiment with a fixed beam energy the terms $|\vec{p}_a|^2$ and s are constant. The transition amplitudes are parametrized by a sum of model components $A_{i,k}^\varepsilon(m, t'; \zeta_k)$ representing resonant or non-resonant contributions. The strength of each model component is given by a possibly t' -dependent complex-valued coupling $C_{i,k}^{r\varepsilon}(t')$. The index i denotes a wave, while the index k runs over the model components that are used to describe this wave

$$\hat{T}_i^{r\varepsilon}(m, t') = \sqrt{\frac{m}{|\vec{p}_a|^2 s}} \mathcal{A}(s, t; m) \sum_k^{N_{i,\text{comp}}^{r\varepsilon}} C_{i,k}^{r\varepsilon}(t') A_{i,k}^\varepsilon(m, t'; \zeta_k) \quad (5.18)$$

The transition amplitudes $\hat{T}_i^{r\varepsilon}(m, t')$ are functions of the binning variables m and t' . Additional parameters of the mass-dependent amplitudes $A_{i,k}^\varepsilon(m, t'; \zeta_k)$, as for example resonance mass and width, are represented by ζ_k . Applying the same normalization to the transition amplitudes as used in the mass-independent analysis (eq. (4.41) in section 4.4) yields

$$\hat{\bar{T}}_i^{r\varepsilon}(m, t') = \sqrt{\frac{m}{|\vec{p}_a|^2 s}} \mathcal{A}(s, t; m) \sqrt{\mathcal{P}_{ii}^\varepsilon(m)} \sum_k^{N_{i,\text{comp}}^{r\varepsilon}} C_{i,k}^{r\varepsilon}(t') A_{i,k}^\varepsilon(m, t'; \zeta_k) \quad (5.19)$$

With the transition amplitudes the spin-density matrix can be calculated

$$\hat{\rho}_{ij}^\varepsilon(m, t') = \sum_r^{N_{\text{rank}}^\varepsilon} \hat{\bar{T}}_j^{r\varepsilon*}(m, t') \hat{\bar{T}}_i^{r\varepsilon}(m, t') \quad (5.20)$$

$$\begin{aligned} &= \frac{m}{|\vec{p}_a|^2 s} |\mathcal{A}(s, t; m)|^2 \sqrt{\mathcal{P}_{jj}^\varepsilon(m) \mathcal{P}_{ii}^\varepsilon(m)} \\ &\quad \times \left(\sum_k^{N_{j,\text{comp}}^{r\varepsilon}} C_{j,k}^{r\varepsilon}(t') A_{j,k}^\varepsilon(m, t'; \zeta_k) \right)^* \left(\sum_k^{N_{i,\text{comp}}^{r\varepsilon}} C_{i,k}^{r\varepsilon}(t') A_{i,k}^\varepsilon(m, t'; \zeta_k) \right) \end{aligned} \quad (5.21)$$

Five different mass-dependent amplitudes $A_{i,k}^\varepsilon(m, t'; \zeta_k)$ are used, three parameterizations for the resonant contributions and two different parameterizations for

the background terms. The resonant contributions are parameterized with Breit-Wigner amplitudes. The simple constant-width Breit-Wigner is used for most resonant contributions

$$A_{i,k}^\varepsilon(m, t'; m_0, \Gamma_0) = \frac{\Gamma_0 m_0}{m_0^2 - m^2 - i \Gamma_0 m_0} \quad (5.22)$$

Resonant contributions with a large intensity are described by Breit-Wigner functions with a mass-dependent width

$$A_{i,k}^\varepsilon(m, t'; m_0, \Gamma_0) = \frac{\Gamma_0 m_0}{m_0^2 - m^2 - i \Gamma(m) m_0} \quad (5.23)$$

The dynamic width $\Gamma(m)$ can be parameterized in two different ways. The first option is based on a quasi-two-body assumption for the three-body decay and sums the two-body phase-space contributions of the decay channels of the resonance

$$\Gamma(m) = \Gamma_0 \frac{m_0}{m} \sum_c^{N_{\text{chan}}} b_c \frac{q_c F_L^2(q_c)}{q_{0c} F_L^2(q_{0c})} \quad (5.24)$$

This parameterization is used to describe the $a_2(1320)$ in the fit presented below taking into account the branching into $b_1 = 80\% \rho(770)\pi D$ and $b_2 = 20\% \eta\pi^- D$ [65]. The second option uses the three-body phase-space integral over the decay amplitudes

$$\Gamma(m) = \Gamma_0 \sum_c^{N_{\text{chan}}} b_c \frac{\mathcal{P}_{cc}^\varepsilon(m)}{\mathcal{P}_{cc}^\varepsilon(m_0)} \quad (5.25)$$

The phase-space integrals $\mathcal{P}_{cc}^\varepsilon = \int d\Phi_n(\tau) |\psi_c^\varepsilon|^2$ are equal to the ones used in the mass-independent partial-wave analysis (section 4.4 and eq. (4.38)). This parameterization is used to describe the $a_1(1260)$ [27]. Only the branching to $\rho(770)\pi S$ is taken into account. It includes the effect of the finite isobar width and correctly takes sub-threshold behavior into account. For masses far from threshold the two ways to describe the dynamic width become equivalent, as $q \cdot F_L^2(q) \approx m \cdot \mathcal{P}_{cc}^\varepsilon(m)$. For all three different ways to parameterize the Breit-Wigner amplitude, Γ_0 and m_0 are the free parameters.

The parameterizations for the background are based on exponentials of the squared phase-space integral over the decay amplitude. The simple background parameterization is

$$A_{i,k}^\varepsilon(m, t'; c_0) = \exp \left[-c_0 \left(\frac{m \mathcal{P}_{ii}^\varepsilon(m)}{m_n \mathcal{P}_{ii}^\varepsilon(m_n)} \right)^2 \right] \quad (5.26)$$

This formula has only one free parameter c_0 . m_n is an arbitrary mass at which the ratio is normalized, in the following the center of the highest mass bin is used. The t' -dependent background parameterization is

$$\begin{aligned}
A_{i,k}^\varepsilon(m, t'; m_0, c_0, c_1, c_2, c_3) \\
= (m - m_0)^{c_0} \exp\left(- (c_1 + c_2 t' + c_3 t'^2) \left(\frac{m \mathcal{P}_{ii}^\varepsilon(m)}{m_n \mathcal{P}_{ii}^\varepsilon(m_n)}\right)^2\right) \quad (5.27)
\end{aligned}$$

This parameterization contains five free parameters, m_0 , c_0 , c_1 , c_2 , and c_3 . In the following m_0 is fixed to $0.5 \text{ GeV}/c^2$.

To be able to evaluate the elements of the spin-density matrix in eq. (5.21), the scattering amplitude $\mathcal{A}(s, t; m)$ for the production of the intermediate state X , and the phase-space volume $V_{\Phi_3}(m)$ in the phase-space integrals $\mathcal{P}_{ii}^\varepsilon$ need to be calculated. The norm $|\mathcal{A}(s, t; m)|^2$ of the scattering amplitude eq. (4.9) is integrated over the analyzed range of the reduced squared four-momentum transfer t' from 0.1 to 1.0 $(\text{GeV}/c)^2$ using $F_c(t') = \exp[-5 (\text{GeV}/c)^{-2} t']$, $\alpha_0 = 1.1$ and $\alpha' = 0.25 (\text{GeV}/c)^{-2}$ [71] so that

$$|\mathcal{A}(s, t; m)|^2 = \left(\frac{35.8 \text{ GeV}/c^2}{m}\right)^{3.47} - \left(\frac{23.1 \text{ GeV}/c^2}{m}\right)^{3.84} \quad (5.28)$$

The phase-space volume $V_{\Phi_3}(m)$ (fig. 5.18) is evaluated using the methods of reference [57]. It is parameterized as

$$V_{\Phi_3}(m) = 3.25 \cdot 10^{-5} - 1.86 \cdot 10^{-4} m + 2.81 \cdot 10^{-4} m^2 - 6.54 \cdot 10^{-5} m^3 + 1.05 \cdot 10^{-5} m^4 \quad (5.29)$$

for the $\pi^- \pi^0 \pi^0$ final state, and for the $\pi^- \eta \eta$ final state as

$$V_{\Phi_3}(m) = 4.44 \cdot 10^{-4} - 7.87 \cdot 10^{-4} m + 4.08 \cdot 10^{-4} m^2 - 5.55 \cdot 10^{-5} m^3 + 4.41 \cdot 10^{-6} m^4 \quad (5.30)$$

In both cases m needs to be given in units of GeV/c^2 .

These factors are shown exemplarily for the $1^{++}0^+ \rho(770) \pi S$ wave and the $2^{++}1^+ \rho(770) \pi D$ wave in fig. 5.19. The red curves show the product of the norm of the production amplitude with the phase-space volume $m |\mathcal{A}(s, t; m)|^2 V_{\Phi_3}$, which is equal for the two waves. The blue curves represent the phase-space integral $\mathcal{P}_{ii}(m)$ divided by the phase-space volume V_{Φ_3} . The black curves show the full product $m |\mathcal{A}(s, t; m)|^2 \mathcal{P}_{ii}^\varepsilon(m)$ applied onto the diagonal elements of the spin-density matrix corresponding to the two waves.

The coupling constants $\{C_{i,k}^{r\varepsilon}\}$ and the parameters $\{\zeta_k\}$ of the mass-dependent amplitudes are determined using a least-square fit with the χ^2 definition

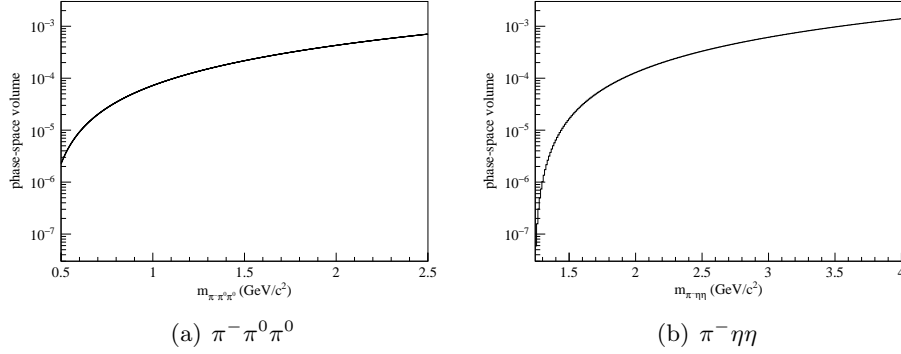


Figure 5.18: Phase-space volume as a function of the final-state mass for (a) the $\pi^-\pi^0\pi^0$ and (b) the $\pi^-\eta\eta$ final state.

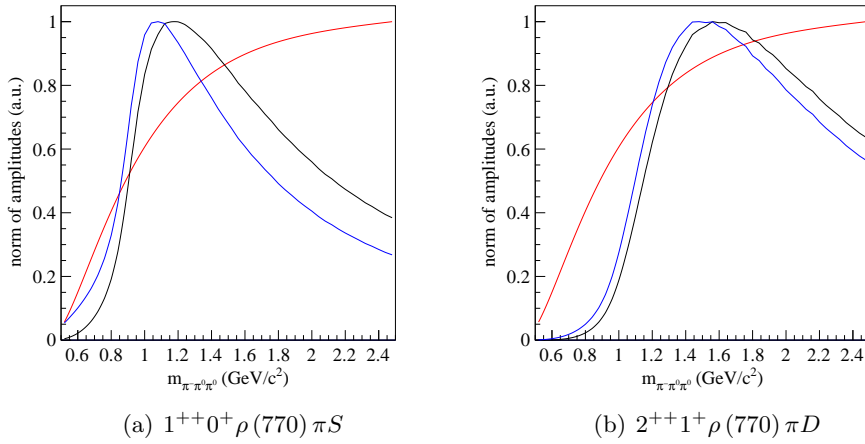


Figure 5.19: Final-state mass dependence of the partial-wave intensity for (a) the $1^{++}0^+\rho(770)\pi S$ and (b) the $2^{++}1^+\rho(770)\pi D$ wave. See text for details.

$$\chi^2 = \sum_m \sum_{t'} \sum_{i,j \geq i}^{N_{\text{waves}}^\varepsilon} \left[\hat{\rho}_{ij}^\varepsilon(m, t') - \bar{\rho}_{ij}^\varepsilon(m, t') \right]^T [\text{Cov}_{ij}(m, t')]^{-1} \left[\hat{\rho}_{ij}^\varepsilon(m, t') - \bar{\rho}_{ij}^\varepsilon(m, t') \right] \quad (5.31)$$

where the covariance matrix $\text{Cov}_{ij}(m, t')$ for one spin-density matrix element has to be calculated from the covariance matrix of the transition amplitudes $\bar{T}_i^{t' \varepsilon}$ from the mass-independent fit.

Of the 88 waves used in the mass-independent fit, 14 waves are selected for the resonance-model fit (table 5.5). The model for the analysis of the $\pi^- \pi^- \pi^+$ final state [75] was used a starting point, the differences are motivated in section 5.14. The resonances are described using Breit-Wigner amplitudes with different parameterizations for the width. With two exceptions constant widths Breit-Wigners (eq. (5.22)) are used. The $a_2(1320)$ is parameterized using a dynamic width assuming a quasi-two-body decay (eq. (5.23) with eq. (5.24)), the $a_1(1260)$ using a dynamic width taking into account the isobar width (eq. (5.23) with eq. (5.25)). Each wave also contains one non-resonant part. The t' -dependent background amplitude of eq. (5.27) is used for the description of the transition amplitudes of the three waves with the highest intensities, $1^{++}0^+ \rho(770) \pi S$, $2^{++}1^+ \rho(770) \pi D$, and $2^{-+}0^+ f_2(1270) \pi S$. Also in two of the smaller waves, the $1^{-+}1^+ \rho(770) \pi P$ and $2^{-+}0^+ \rho(770) \pi F$ waves, the t' -dependent background amplitude is employed. For all the other waves the simple exponential background of eq. (5.26) is used.

The results of the resonance-model fit are summarized in table 5.6. Errors are omitted from this table as the statistical uncertainties are much smaller than the systematic ones. A full treatment of the systematic errors as performed in [75] for the $\pi^- \pi^- \pi^+$ final state has not yet been done for the $\pi^- \pi^0 \pi^0$ final state. Resolution effects from the spectrometer (section 3.5.1), that might have a sizable effect in particular for the widths of narrow resonances, are not unfolded. The results for the individual waves are shown below (sections 5.7 to 5.13), for example in fig. 5.20(a). The red curve corresponds to the t' -summed intensity of the resonance-model fit in that wave. The blue curves show the intensities of the resonant contributions, and the cyan curve that of the non-resonant contribution. Depending on the number of resonances in the wave, there are one to three blue curves. For phases, e.g. in fig. 5.35(a), the red curve shows the resonance-model. In all plots, full curves indicate the fitted mass ranges, and dashed curves the extrapolation of the model over the complete mass range.

wave	mass range (GeV/ c^2)	resonances
$0^-+0^+ f_0(980) \pi S$	1.22 - 2.30	π (1800)
$1^{++}0^+ f_0(980) \pi P$	1.30 - 1.70	a_1 (1420)
$1^{++}0^+ f_2(1270) \pi P$	1.42 - 2.10	a_1 (1260), a_1 (1640)
$1^{++}0^+ \rho(770) \pi S$	0.90 - 2.30	a_1 (1260), a_1 (1640)
$1^-+1^+ \rho(770) \pi P$	0.90 - 1.98	π_1 (1600)
$2^{++}1^+ f_2(1270) \pi P$	1.02 - 1.98	a_2 (1320), a_2 (1700)
$2^{++}1^+ \rho(770) \pi D$	0.90 - 1.98	a_2 (1320), a_2 (1700)
$2^{++}2^+ \rho(770) \pi D$	1.02 - 1.98	a_2 (1320), a_2 (1700)
$2^-+0^+ f_2(1270) \pi S$	1.42 - 2.30	π_2 (1670), π_2 (1880)
$2^-+0^+ f_2(1270) \pi D$	1.62 - 2.30	π_2 (1670), π_2 (1880)
$2^-+0^+ \rho(770) \pi F$	1.22 - 2.10	π_2 (1670), π_2 (1880)
$2^-+1^+ f_2(1270) \pi S$	1.42 - 2.30	π_2 (1670), π_2 (1880)
$4^{++}1^+ f_2(1270) \pi F$	1.26 - 2.30	a_4 (2040)
$4^{++}1^+ \rho(770) \pi G$	1.42 - 2.30	a_4 (2040)

Table 5.5: List of waves used in the resonance-model fit. The waves are only fitted in limited mass ranges. The resonances used to describe each wave are also listed.

resonance	mass (MeV/ c^2)	width (MeV/ c^2)
a_1 (1260)	1293	410
a_1 (1420)	1414	197
a_1 (1640)	1538	713
a_2 (1320)	1313	117
a_2 (1700)	1670	428
a_4 (2040)	1938	362
π (1800)	1793	227
π_1 (1600)	1550	435
π_2 (1670)	1651	256
π_2 (1880)	1886	347

Table 5.6: Resonance parameters extracted by the resonance-model fit. Errors are not given as the statistical uncertainties are much smaller than the systematic ones.

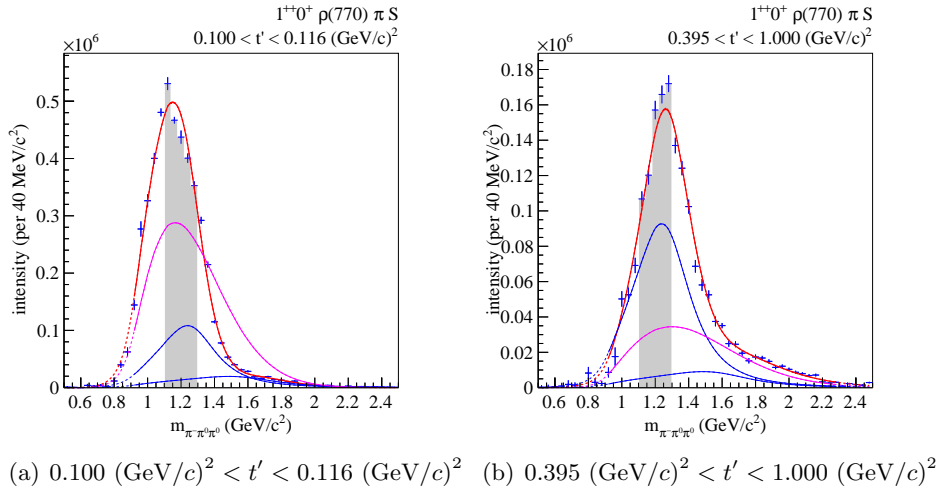


Figure 5.20: Intensities of the $1^{++}0^+\rho(770)\pi S$ wave in (a) the lowest and (b) the highest t' bin. The shaded areas correspond to the regions integrated over for the t' spectra.

5.7 The $J^{PC} = 1^{++}$ Sector

The wave with the overall largest intensity is the $1^{++}0^+\rho(770)\pi S$ wave (figs. 5.20 and 5.21(a)). Averaged over t' it contributes about 41% to the total intensity (51% in the lowest, 20% in the highest t' bin). In this wave the $a_1(1260)$ is expected to appear. Further excited states like the $a_1(1640)$ have been observed by previous experiments, but are not fully established. As this wave dominates the intensity in the $J^{PC} = 1^{++}$ sector, the same features are visible as in fig. 5.15. The shape of the peak structure changes with t' and the position of its maximum moves from $1.1 \text{ GeV}/c^2$ at low t' to $1.3 \text{ GeV}/c^2$ at high t' . At the same time the peak is getting more symmetric towards higher t' . Such a behavior is not expected for a pure resonance, whose shape should not at all depend on t' , but points to a t' -dependent interference of resonant and non-resonant contributions. The $1^{++}1^+\rho(770)\pi S$ wave with spin projection $M = 1$ behaves similarly (fig. 5.21(b)). Only the high-mass shoulder at $1.8 \text{ GeV}/c^2$ is more pronounced in the $M = 1$ wave compared to the one with $M = 0$. The intensity of the $M = 1$ wave is about one order of magnitude smaller than the $M = 0$ wave. This is in agreement with observations made for the $\pi^-\pi^-\pi^+$ final state [11].

A peak at $1.3 \text{ GeV}/c^2$ is also visible for other decay modes with different isobars and different relative orbital angular momenta between the isobar and the bachelor pion. Figure 5.22(a) shows the intensity of the $1^{++}0^+(\pi\pi)_S\pi P$ wave. As already for the $1^{++}1^+\rho(770)\pi S$ wave a shoulder on the high-mass side of the peak is visible.

For the decay via the $f_2(1270)$ isobar ($1^{++}0^+f_2(1270)\pi P$ wave, fig. 5.22(b))

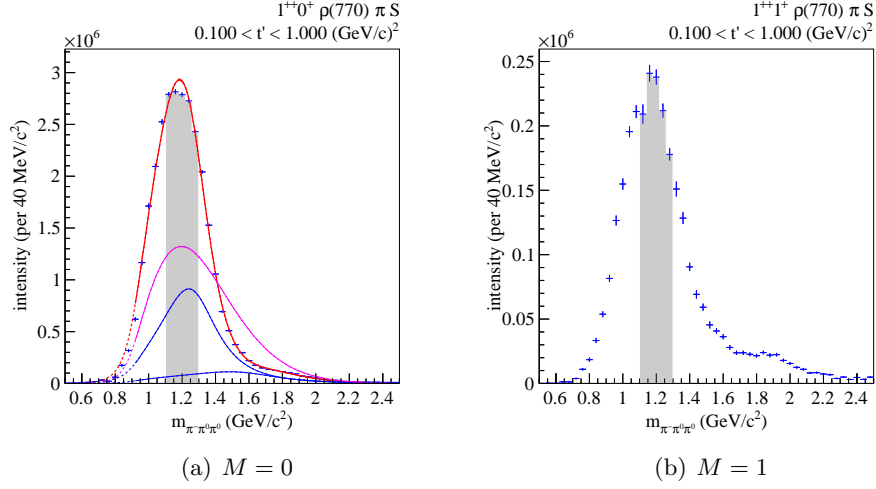


Figure 5.21: t' -summed intensities of the $1^{++}M^+\rho(770)\pi S$ waves with (a) $M = 0$ and (b) $M = 1$. The shaded areas correspond to the regions integrated over for the t' spectra.

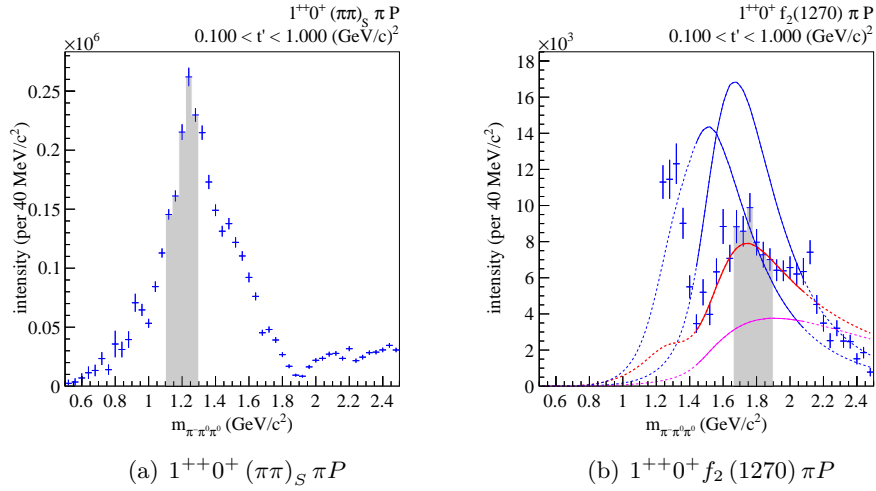


Figure 5.22: t' -summed intensities of $1^{++}0^+$ waves with (a) $(\pi\pi)_S\pi P$ and (b) $f_2(1270)\pi P$ decay modes. The shaded areas correspond to the regions integrated over for the t' spectra.

this high-mass shoulder is even more prominent. Due to the mass threshold of $1.22 \text{ GeV}/c^2$ applied for this wave, the intensity only starts at the position of the peak in the other waves. Basically from the threshold onwards, the intensity decreases with a sharp drop reaching a local minimum around a mass of $1.45 \text{ GeV}/c^2$. The intensity then starts growing again, which might be interpreted as the contribution of a second a_1 resonance at about $1.7 \text{ GeV}/c^2$.

For the analysis of the t' dependence of the partial-wave intensities the intensity spectra are integrated over mass ranges containing the $a_1(1260)$ and $a_1(1640)$. For the $a_1(1260)$, the intensity distribution of the $1^{++}0^+\rho(770)\pi S$, $1^{++}1^+\rho(770)\pi S$, and $1^{++}0^+(\pi\pi)_S\pi P$ waves are integrated for all t' bins between 1.1 and $1.3 \text{ GeV}/c^2$ (fig. 5.23). The slopes of the t' spectra (eq. (5.16)) range from about 11 to $16 (\text{GeV}/c)^{-2}$. This is a bit higher than the around $8 (\text{GeV}/c)^{-2}$ expected for Pomeron exchange, again supporting the idea of important non-resonant contributions. The intensity measured in the $1^{++}0^+f_2(1270)\pi P$ wave is integrated between 1.66 and $1.9 \text{ GeV}/c^2$ where a bump that might correspond to the $a_1(1640)$ is observed. The slope of about $7 (\text{GeV}/c)^{-2}$ supports the interpretation of this bump being caused by a resonant contribution to this wave.

Resonance parameters for two resonances, the $a_1(1260)$ and the $a_1(1640)$, are determined by the resonance-model fit (table 5.6). According to the fit, the $a_1(1260)$ has a mass of $1293 \text{ MeV}/c^2$ and a width of $410 \text{ MeV}/c^2$. The higher-lying state $a_1(1640)$ has a mass of $1538 \text{ MeV}/c^2$ and a width of $713 \text{ MeV}/c^2$.

The resonance-model fit supports the expectation that the $1^{++}0^+\rho(770)\pi S$ wave contains a large non-resonant component that strongly depends on t' (cyan line in fig. 5.20, compared to the resonant contributions in blue). A possible contribution to the non-resonant component in this wave is the Deck effect [36]. It describes a process in which the incoming pion produces a two-pion resonance and a virtual pion, this virtual pion is then made real by scattering off a target. This reaction also produces the three-pion final state, but not via a three-pion resonance. In [28] it is suggested that the Deck effect can describe the intensity and phases observed in the $1^{++}0^+\rho(770)\pi S$ wave to a large extent. This could explain why the components used in the resonance model (section 5.6), which are aimed at resonances in the three-pion state, cannot fully describe the peak region of the $1^{++}0^+\rho(770)\pi S$ wave in figs. 5.20 and 5.21(a).

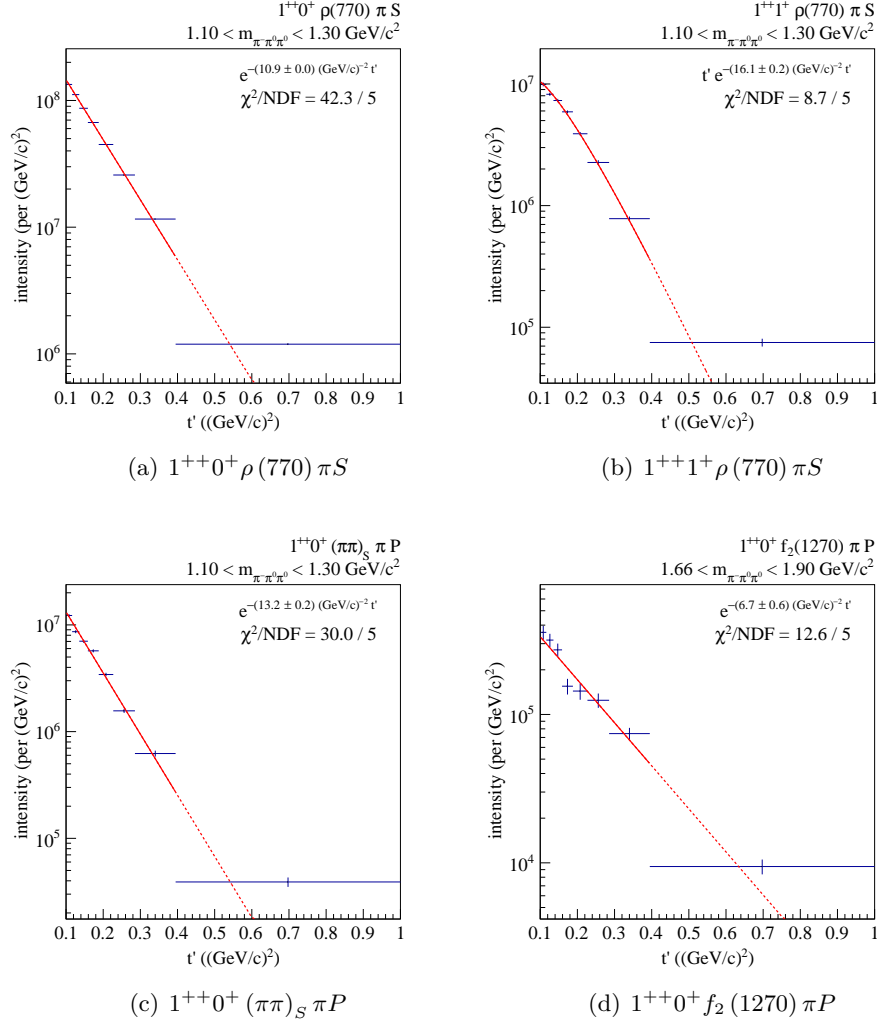


Figure 5.23: t' spectra of (a) the $1^{++}0^+ \rho(770) \pi S$, (b) the $1^{++}1^+ \rho(770) \pi S$, (c) the $1^{++}0^+ (\pi\pi)_S \pi P$, and (d) the $1^{++}0^+ f_2(1270) \pi P$ waves obtained by integrating the respective mass distributions in the ranges highlighted in figs. 5.20 to 5.22. The single-exponential fit is shown with the solid red line, the extrapolation to the whole range is shown by the dashed line.

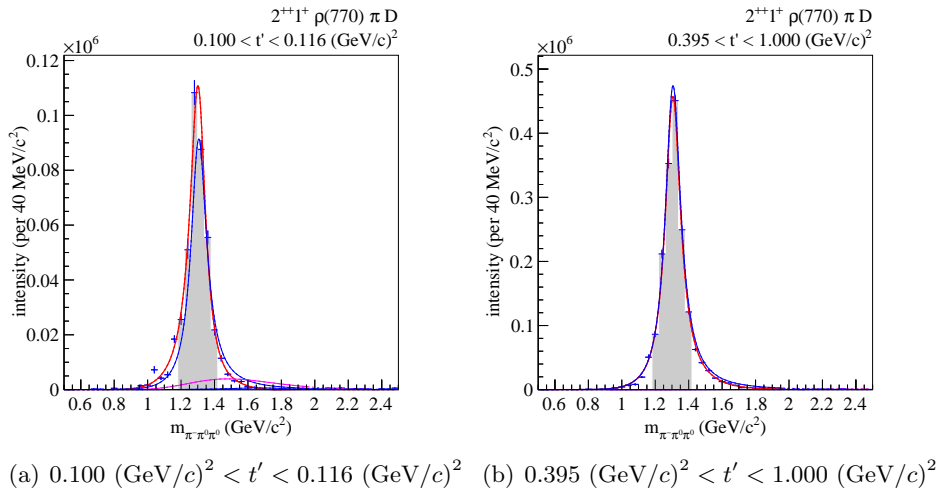


Figure 5.24: Intensities of the $2^{++}1^+\rho(770)\pi D$ wave in (a) the lowest and (b) the highest t' bin. The shaded areas correspond to the regions integrated over for the t' spectra.

5.8 The $J^{PC} = 2^{++}$ Sector

The wave with the overall second largest intensity is the $2^{++}1^+\rho(770)\pi D$ wave (figs. 5.24 and 5.25(a)). Averaged over t' it contributes about 10% of the total intensity (4.3% in the lowest, 20% in the highest t' bin). In this wave the $a_2(1320)$ is expected. Further states like the $a_2(1700)$ have been seen by previous experiments, but are again not well established. The intensity of the $2^{++}1^+\rho(770)\pi D$ wave increases with t' , while at the same time the shape stays constant. When increasing the spin projection from $M = 1$ to $M = 2$ ($2^{++}2^+\rho(770)\pi D$ wave, fig. 5.25(b)) the intensity decreases by about a factor of 25. A similar decrease is found in the $\pi^-\pi^-\pi^+$ and $\pi^-\eta$ final states [11, 10]. The high-mass side of the peak at $1.3 \text{ GeV}/c^2$ falls steeper in the $M = 2$ wave compared to the $M = 1$ wave.

In contrast, the $2^{++}1^+f_2(1270)\pi P$ wave appears to have a steeper low-mass side of the peak at $1.3 \text{ GeV}/c^2$. This might be caused by the phase space, which for the decay via the heavier $f_2(1270)$ isobar opens only at higher masses compared to the $\rho(770)$ isobar. At the high-mass side a shoulder is visible pointing towards an $a_2(1700)$.

The intensity spectra of all three waves are integrated over the $m_{\pi^-\pi^0\pi^+}$ region around the mass of the $a_2(1320)$. The slopes of the resulting t' spectra scatter around the expected value for Pomeron exchange of $8 \text{ (GeV}/c)^{-2}$, which is a strong indication for a clean resonance signal. As expected for a resonance, the t' dependence is similar for the various decay channels.

This is confirmed by the resonance-model fit. The resonant component for the $a_2(1320)$ (eq. (5.23) with eq. (5.24)) is able to describe the intensity spec-

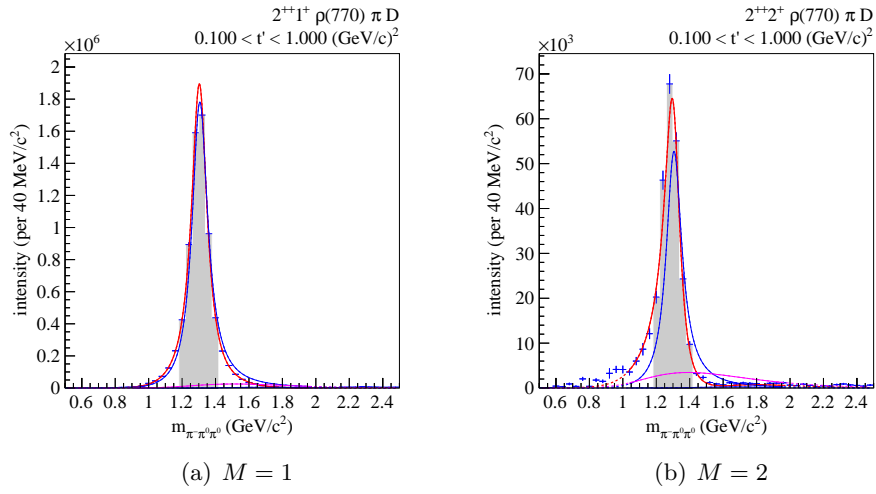


Figure 5.25: t' -summed intensities of the $2^{++}M^+\rho(770)\pi S$ waves with (a) $M = 1$ and (b) $M = 2$. The shaded areas correspond to the regions integrated over for the t' spectra.

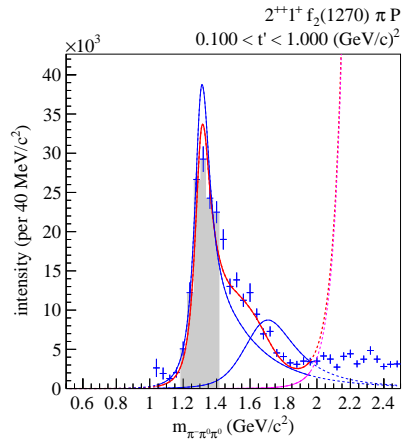


Figure 5.26: t' -summed intensity of the $2^{++}1^+f_2(1270)\pi P$ wave. The shaded area corresponds to the region integrated over for the t' spectrum.

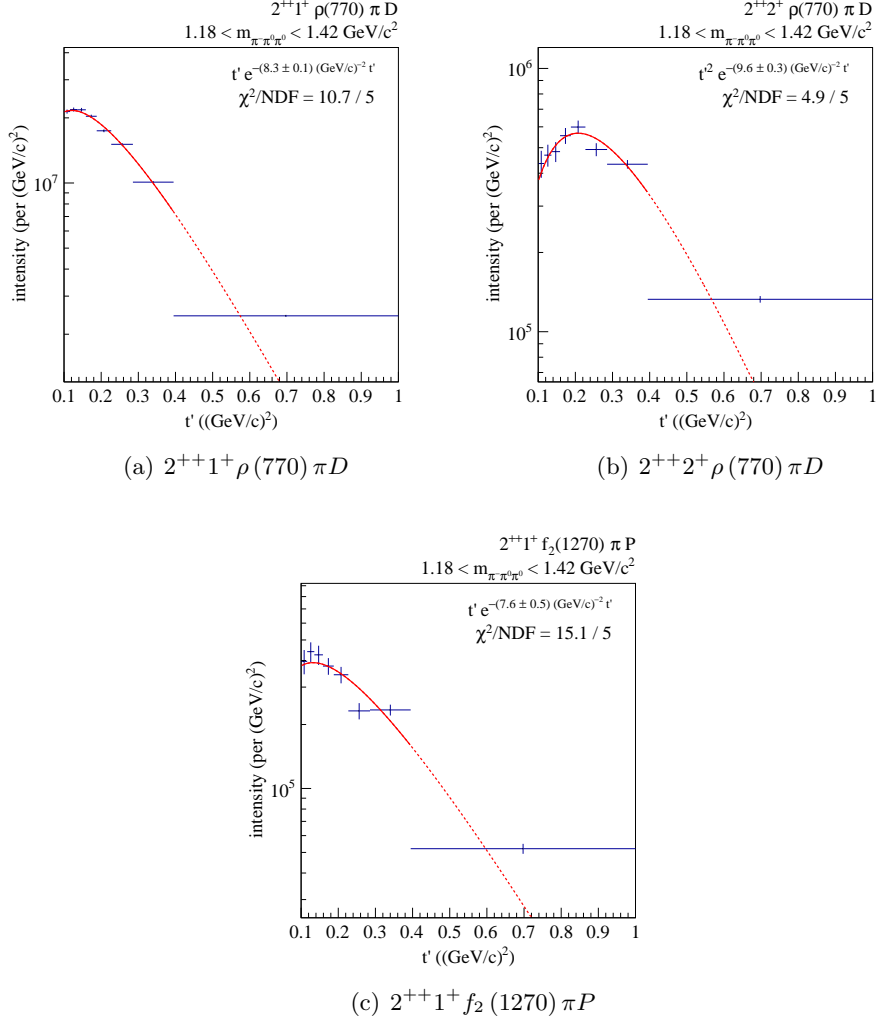


Figure 5.27: t' spectra of (a) the $2^{++}1^+ \rho(770) \pi D$, (b) the $2^{++}2^+ \rho(770) \pi D$, and (c) the $2^{++}1^+ f_2(1270) \pi P$ waves obtained by integrating the respective mass distributions in the ranges highlighted in figs. 5.24 to 5.26. The single-exponential fit is shown with the solid red line, the extrapolation to the whole range is shown by the dashed line.

tra and phases in this mass region basically on its own. The extracted mass of this resonance is $1313 \text{ MeV}/c^2$, its width is $117 \text{ MeV}/c^2$. In the two waves decaying via the $\rho(770)$ isobar the additional $a_2(1700)$ is hardly visible, but in the $2^{++}1^+ f_2(1270) \pi P$ wave it is important to describe the high-mass region. Its mass is $1670 \text{ MeV}/c^2$, the width $428 \text{ MeV}/c^2$. The very clean signal of the $a_2(1320)$ in particular in the $2^{++}1^+ \rho(770) \pi D$ wave also guarantees a stable interferometer against which other resonances can be measured. This is further supported by the very small statistical errors of the Breit-Wigner parameters for the $a_2(1320)$, which are at least an order of magnitude smaller than for the other resonances.

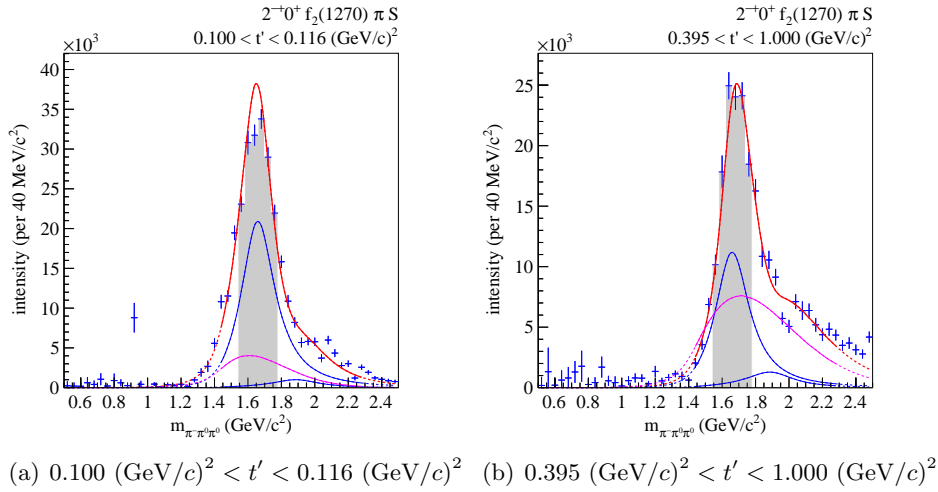


Figure 5.28: Intensities of the $2^{-+}0^{+}f_2(1270)\pi S$ wave in (a) the lowest and (b) the highest t' bin. The shaded areas correspond to the regions integrated over for the t' spectra.

5.9 The $J^{PC} = 2^{-+}$ Sector

The wave with the overall third largest intensity is the $2^{-+}0^{+}f_2(1270)\pi S$ wave (figs. 5.28 and 5.29(a)). Averaged over t' it contributes about 3.4% of the total intensity (3.3% in the lowest, 3.0% in the highest t' bin). In this wave, the $\pi_2(1670)$ and $\pi_2(1880)$ are well-established states. Further states like the $\pi_2(2005)$ have been claimed by previous experiments, but require confirmation. The shape of this wave changes only slightly depending on t' . The $2^{-+}1^{+}f_2(1270)\pi S$ wave with the higher spin projection $M = 1$ (fig. 5.29(b)) is missing the shoulder of the $\pi_2(1670)$ peak at a mass of around $2.1 \text{ GeV}/c^2$ visible in the $M = 0$ wave. Compared to the $M = 0$ wave the intensity of the $M = 1$ wave is reduced by about a factor 6 similar to what is observed in the $\pi^-\pi^-\pi^+$ final state [11].

The intensity spectrum of the wave with a relative orbital angular momentum of $L = 2$ between the isobar and the bachelor pion ($2^{-+}0^{+}f_2(1270)\pi D$ wave, fig. 5.30(a)) has a peak at about $1.8 \text{ GeV}/c^2$ that is shifted by $200 \text{ MeV}/c^2$ towards higher masses compared to the decay with $L = 0$. Also the intensity of the $2^{-+}0^{+}\rho(770)\pi F$ wave (fig. 5.30(b)) exhibits a shoulder at about $1.8 \text{ GeV}/c^2$, which might be attributed to the $\pi_2(1880)$. In contrast, the two waves with a spin-0 isobar ($2^{-+}0^{+}f_0(980)\pi D$ and $2^{-+}0^{+}(\pi\pi)_S\pi D$ waves, fig. 5.31) have a local minimum at that mass. This might be caused by destructive interference of two resonant components.

The intensity spectra of various $J^{PC} = 2^{-+}$ waves feature two bumps. The two best known resonances in this sector are the $\pi_2(1670)$ and $\pi_2(1880)$. The intensity spectra are integrated over the corresponding mass ranges if they show

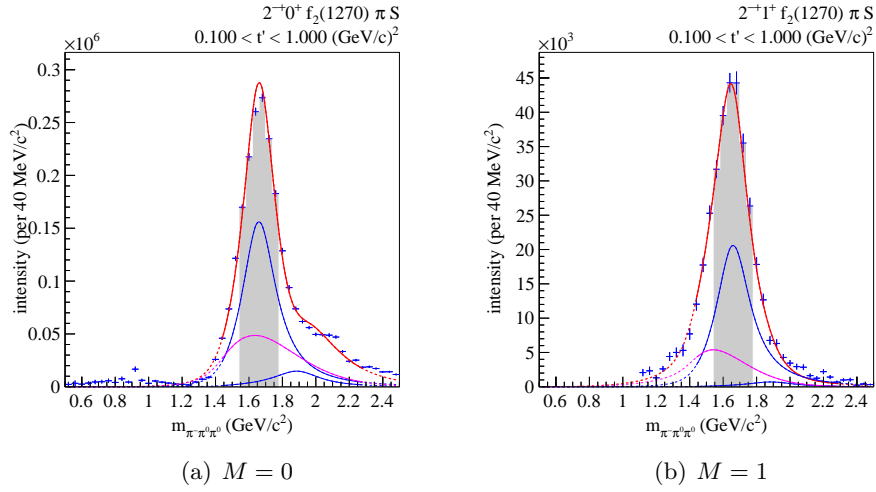


Figure 5.29: t' -summed intensities of the $2^{-+}M^+f_2(1270)\pi S$ wave with (a) $M = 0$ and (b) $M = 1$. The shaded areas correspond to the regions integrated over for the t' spectra.

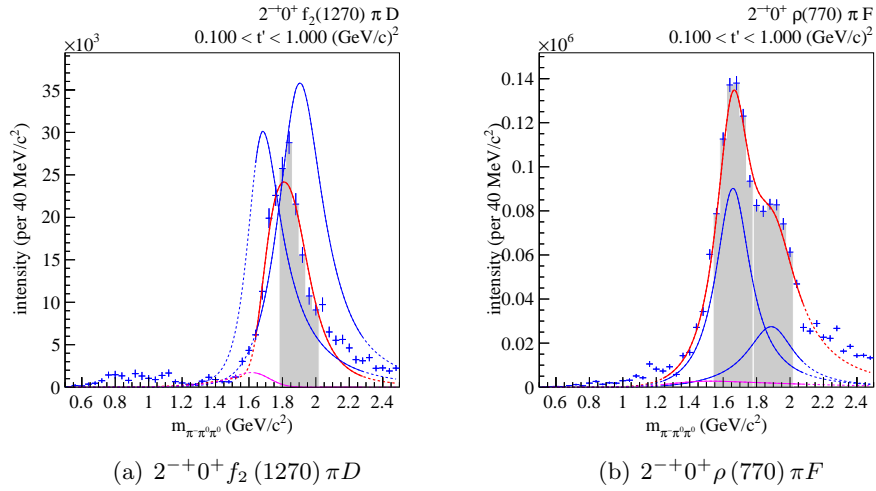


Figure 5.30: t' -summed intensities of $2^{-+}0^+$ waves with (a) $f_2(1270)\pi D$ and (b) $\rho(770)\pi F$. The shaded areas correspond to the regions integrated over for the t' spectra.

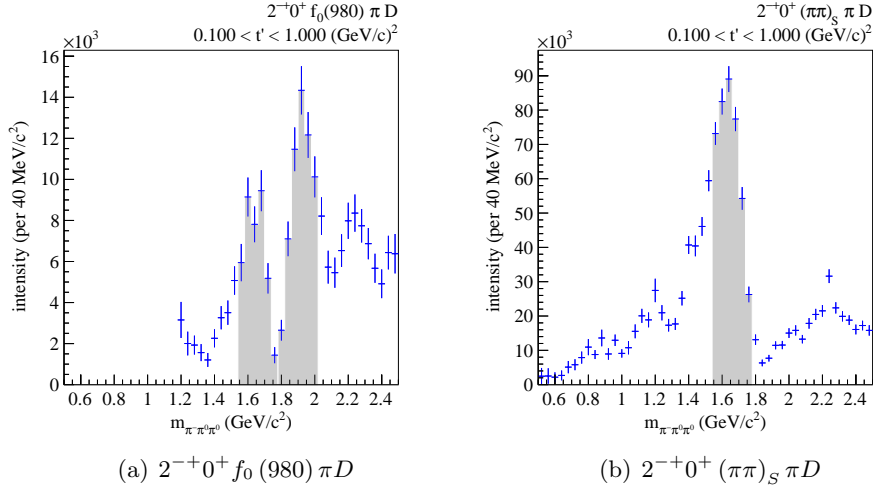


Figure 5.31: t' -summed intensities of $2^{-+}0^{+}$ waves with (a) $f_0(980) \pi S$ and (b) $(\pi\pi)_S \pi S$ decay modes. The shaded areas correspond to the regions integrated over for the t' spectra.

a bump. In all cases the slopes of the t' spectra (figs. 5.32 and 5.33) suggest dominant resonant contributions.

The phase difference between the $1^{++}0^{+} \rho(770) \pi S$ and the $2^{-+}0^{+} f_2(1270) \pi S$ waves is shown for two t' bins in fig. 5.34. At masses below $1 \text{ GeV}/c^2$, the phase cannot be measured reliably due to the small intensity of the $2^{-+}0^{+} f_2(1270) \pi S$ wave. The intermediate mass region from $1 \text{ GeV}/c^2$ to $1.5 \text{ GeV}/c^2$ changes with t' : the slightly decreasing phase motion at low t' becomes a $+180^\circ$ phase motion at high t' . This behavior supports the assumption of a strong non-resonant component in the $1^{++}0^{+} \rho(770) \pi S$ in particular for low values of t' . Above a mass of $1.5 \text{ GeV}/c^2$, the phase motions show similar behavior in both t' regions.

Due to the limited mass range in which the $2^{++}1^{+} \rho(770) \pi D$ wave has a sizable intensity, the phase between this wave and the $2^{-+}0^{+} f_2(1270) \pi S$ wave (fig. 5.35) is only well defined between $1 \text{ GeV}/c^2$ and $1.7 \text{ GeV}/c^2$. Starting from around $1.1 \text{ GeV}/c^2$ the phase is rising, indicating a resonance in the $2^{++}1^{+} \rho(770) \pi D$ wave, the $a_2(1320)$. At higher masses, beyond $1.5 \text{ GeV}/c^2$, the phase starts to decrease again, this can be interpreted as a resonance in the $2^{-+}0^{+} f_2(1270) \pi S$ wave, probably the $\pi_2(1670)$.

The resonance model contains the two previously mentioned resonances in $J^{PC} = 2^{-+}$ waves. The $\pi_2(1670)$ is extracted with a mass of $1651 \text{ MeV}/c^2$ and a width of $256 \text{ MeV}/c^2$, the $\pi_2(1880)$ with a mass of $1886 \text{ MeV}/c^2$ and a width of $347 \text{ MeV}/c^2$ (table 5.6). A third resonance, for example a $\pi_2(2005)$, is not required to describe to data (section 5.14).

The $\pi_2(1880)$ is in principle too close in mass to the $\pi_2(1670)$ to be a radial

Chapter 5 Partial-Wave Analysis of the $\pi^-\pi^0\pi^0$ Final State

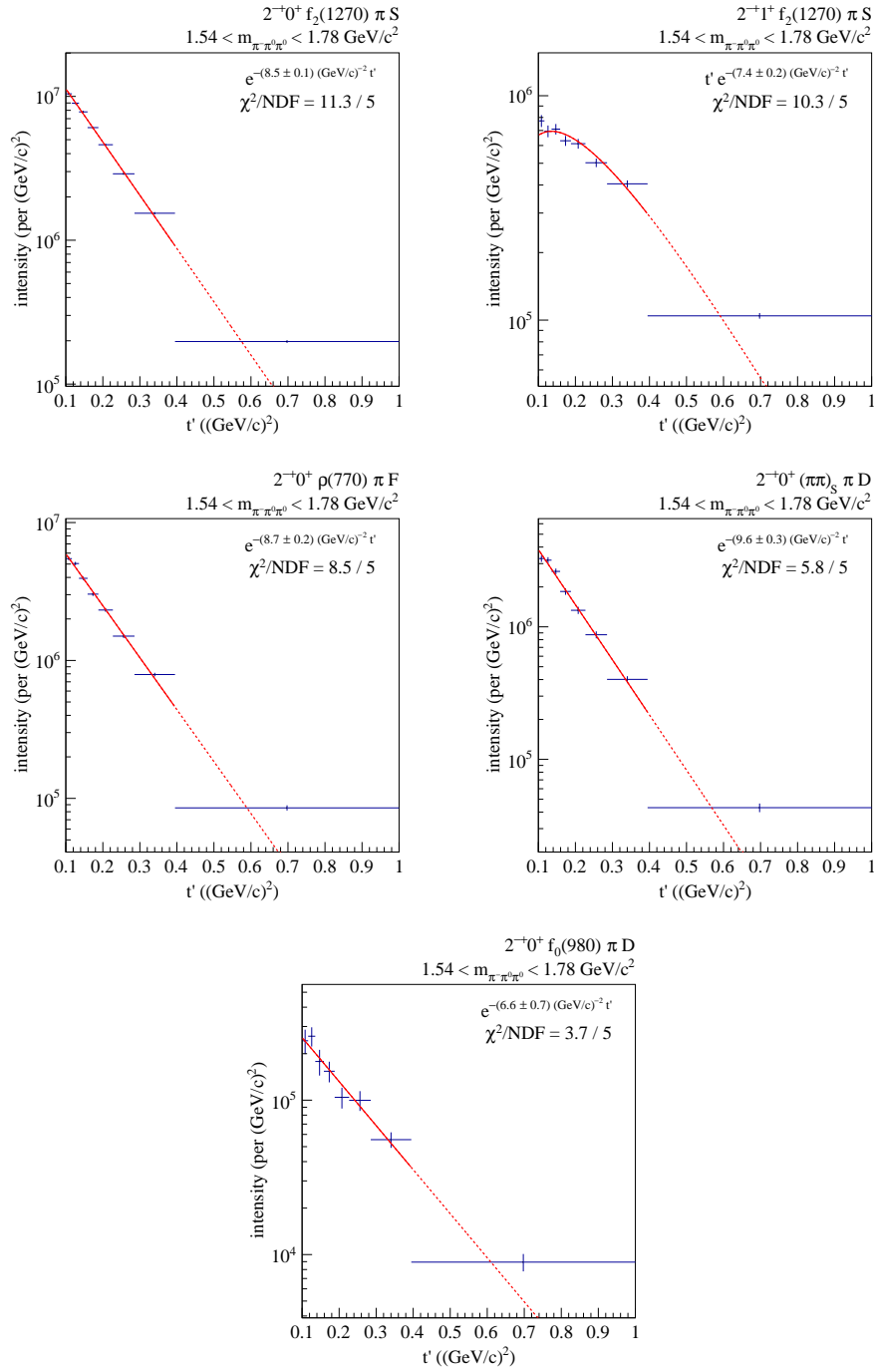


Figure 5.32: t' spectra of the $2^{-+0^+}f_2(1270)\pi S$, the $2^{-+1^+}f_2(1270)\pi S$, the $2^{-+0^+}\rho(770)\pi F$, the $2^{-+0^+}(\pi\pi)_S\pi D$, and the $2^{-+0^+}f_0(980)\pi D$ waves obtained by integrating the respective mass distributions in the ranges highlighted in figs. 5.28, 5.28, 5.30 and 5.31. The single-exponential fit is shown with the solid red line, the extrapolation to the whole range is shown by the dashed line.

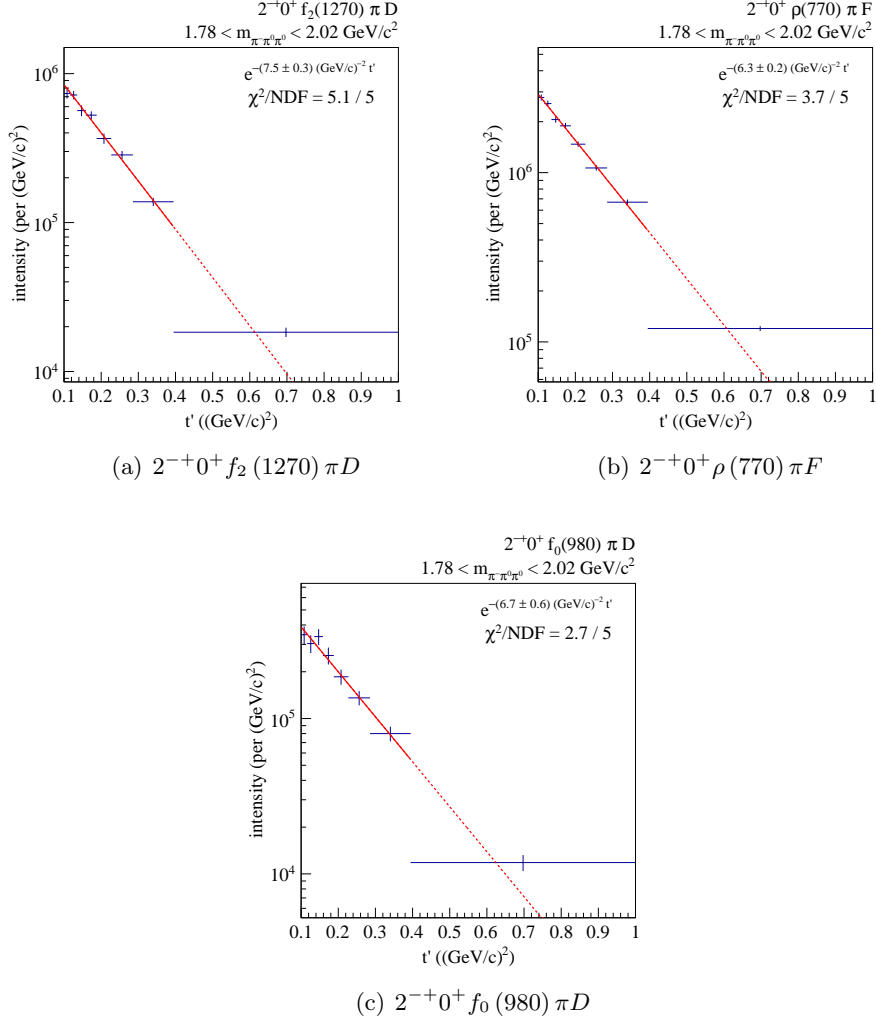
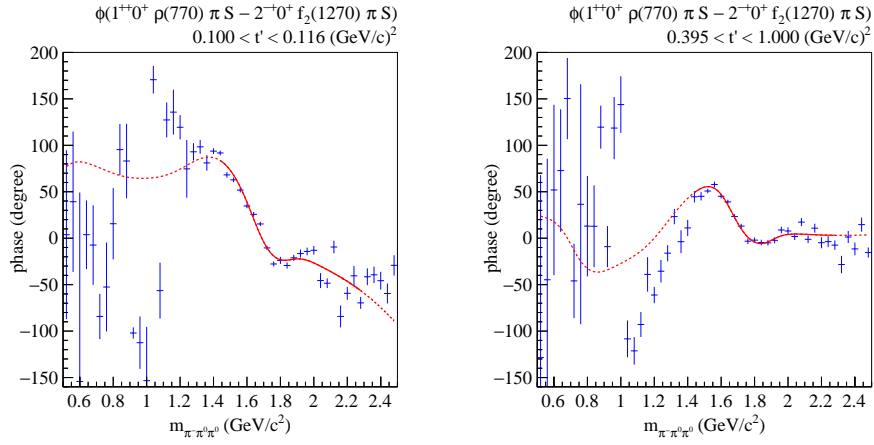
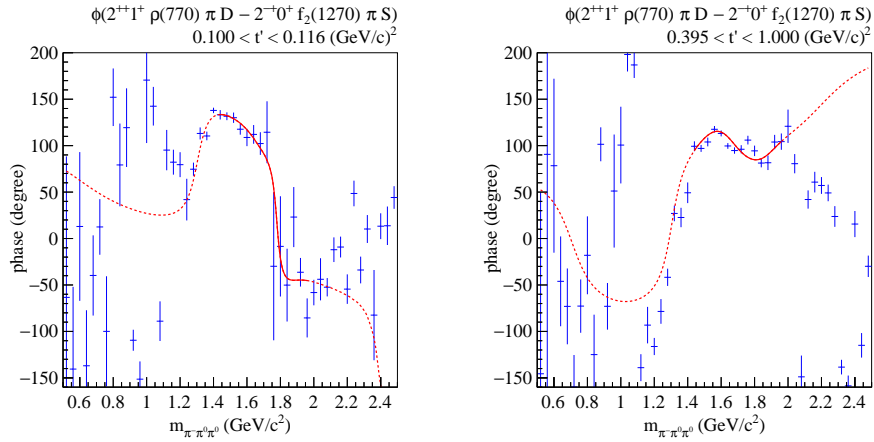


Figure 5.33: t' spectra of (a) the $2^{-+}0^{+} f_2(1270) \pi D$, (b) the $2^{-+}0^{+} \rho(770) \pi F$, and (c) the $2^{-+}0^{+} f_0(980) \pi D$ waves obtained by integrating the respective mass distributions in the ranges highlighted in figs. 5.30 and 5.31. The single-exponential fit is shown with the solid red line, the extrapolation to the whole range is shown by the dashed line.



(a) $0.100 (\text{GeV}/c)^2 < t' < 0.116 (\text{GeV}/c)^2$ (b) $0.395 (\text{GeV}/c)^2 < t' < 1.000 (\text{GeV}/c)^2$

Figure 5.34: Phases of the $1^{++}0^+ \rho(770) \pi S$ with respect to the $2^{-+}0^+ f_2(1270) \pi S$ waves in (a) the lowest and (b) the highest t' bin.



(a) $0.100 (\text{GeV}/c)^2 < t' < 0.116 (\text{GeV}/c)^2$ (b) $0.395 (\text{GeV}/c)^2 < t' < 1.000 (\text{GeV}/c)^2$

Figure 5.35: Phases of the $2^{++}1^+ \rho(770) \pi D$ with respect to the $2^{-+}0^+ f_2(1270) \pi S$ waves in (a) the lowest and (b) the highest t' bin.

excitation of the ground state. It has instead been proposed as a hybrid-meson candidate [58, 19]. The experimentally observed intensity of the $\pi_2(1880)$ found in the $2^{-+}0^+ f_2(1270) \pi D$ wave (fig. 5.30(a)) is stronger than the one for the decay into an S wave (fig. 5.29(a)), while model calculations for the hybrid-meson interpretation predicted the decay via the S wave to be dominant over the one via the D wave [34, 66]. The $\pi_2(1880)$ has also been explained as an interference of the $\pi_2(1670)$ with the Deck effect [43]. This interference is supposed to cause the observed shift of the peak position. But, following this explanation, it would not be expected to observe two peaks in the $2^{-+}0^+ \rho(770) \pi F$ wave (fig. 5.30(b)).

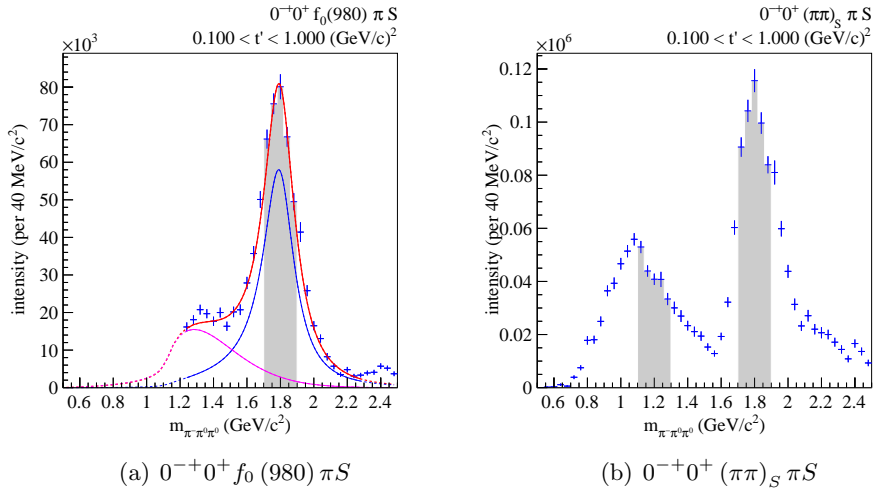


Figure 5.36: t' summed intensities of $0^{-+}0^{+}$ waves with (a) $f_0(980) \pi S$ and (b) $(\pi\pi)_S \pi S$ decay modes. The shaded areas correspond to the regions integrated over for the t' spectra.

5.10 The $J^{PC} = 0^{-+}$ Sector

The sector with the next smaller intensity is the $J^{PC} = 0^{-+}$ sector. With these quantum numbers, the $\pi(1800)$ is well established; further states like the $\pi(1300)$ are still disputed. Figure 5.36 shows the intensity of two waves which both have a peak at $1.8 \text{ GeV}/c^2$. In the $0^{-+}0^{+} f_0(980) \pi S$ wave (fig. 5.36(a)) no further structures can be seen, while for the $0^{-+}0^{+} (\pi\pi)_S \pi S$ wave (fig. 5.36(b)) another bump shows up at about $1 \text{ GeV}/c^2$. It has an odd triangular shape, and is in a mass region where other waves show instabilities.

The t' spectra obtained by integrating the intensity distributions over the mass region of the $\pi(1800)$ (fig. 5.37) have a slope of 11 to 12 $(\text{GeV}/c)^{-2}$. In contrast, the intensity spectrum of the $0^{-+}0^{+} (\pi\pi)_S \pi S$ wave integrated in the $\pi(1300)$ mass region has a slope of almost 20 $(\text{GeV}/c)^{-2}$. This is far from the expected 8 $(\text{GeV}/c)^{-2}$ for Pomeron exchange, and points towards large non-resonant contributions.

The resonance-model fit of the $\pi(1800)$ in the $0^{-+}0^{+} f_0(980) \pi S$ wave finds only a small non-resonant contribution in the mass region around the resonance. The mass of the $\pi(1800)$ is $1793 \text{ MeV}/c^2$, the width is $227 \text{ MeV}/c^2$.

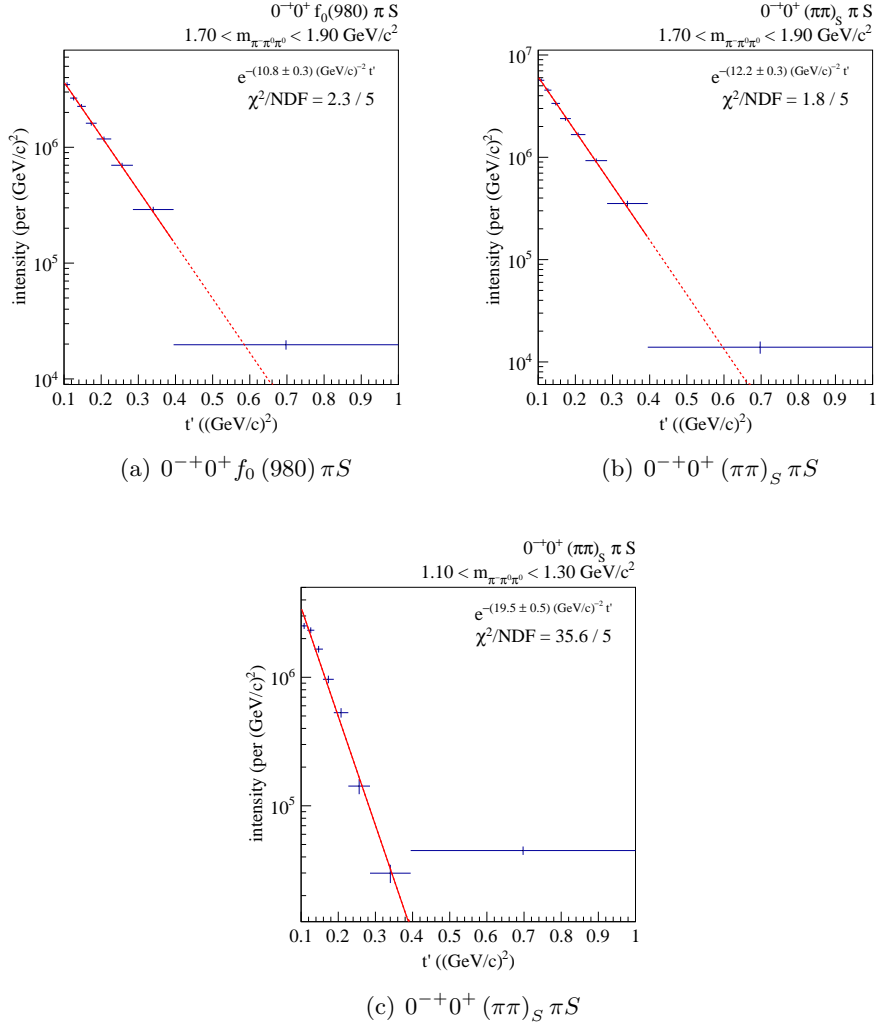


Figure 5.37: t' spectra of (a) the $0^{-+}0^{+} f_0(980) \pi S$ wave, (b) the $0^{-+}0^{+} (\pi\pi)_S \pi S$ wave in the high mass region, and (c) the $0^{-+}0^{+} (\pi\pi)_S \pi S$ wave in the low mass region obtained by integrating the respective mass distributions in the ranges highlighted in fig. 5.36. The single-exponential fit is shown with the solid red line, the extrapolation to the whole range is shown by the dashed line.

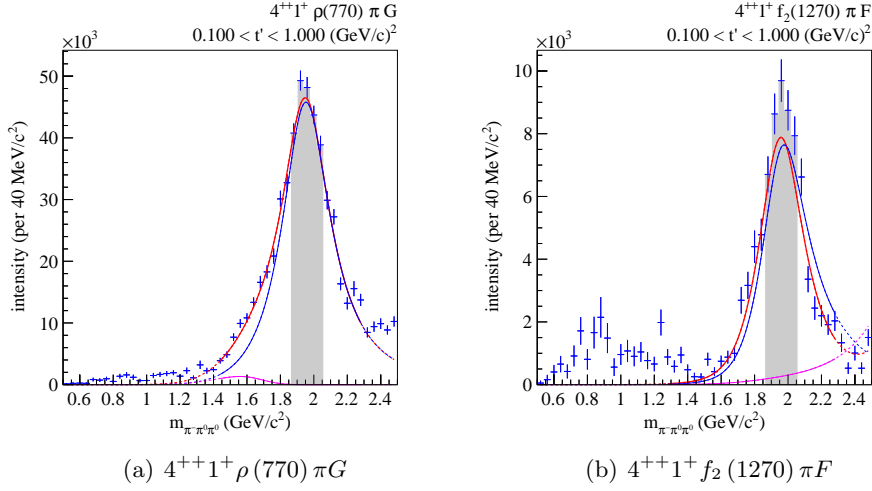


Figure 5.38: t' -summed intensities of $4^{++}1^+$ waves with (a) $\rho(770) \pi G$ and (b) $f_2(1270) \pi S$ decay modes. The shaded areas correspond to the regions integrated over for the t' spectra.

5.11 The $J^{PC} = 4^{++}$ Sector

The waves with $J^{PC} = 4^{++}$ are not the next smaller group by intensity, but in contrast to the 3^{++} , 4^{-+} and 6^{-+} sectors it features a well established resonance, the $a_4(2040)$. The intensities of two 4^{++} waves are shown in fig. 5.38. Both waves indeed exhibit a peak at around $2 \text{ GeV}/c^2$. While for the $4^{++}1^+ f_2(1270) \pi F$ wave (fig. 5.38(b)) this peak is clean, the $4^{++}1^+ \rho(770) \pi G$ wave (fig. 5.38(a)) features a shoulder to the low-mass side.

The t' spectra of the intensities in the $a_4(2040)$ mass region (fig. 5.39) are compatible with production by Pomeron exchange.

The phase between the $4^{++}1^+ \rho(770) \pi G$ and $2^{-+}0^+ f_2(1270) \pi S$ wave (fig. 5.40) is unstable below $1.5 \text{ GeV}/c^2$ due to the low intensity in both waves. Above $1.5 \text{ GeV}/c^2$, the phase motion is similar for all t' bins, first there is a falling phase motion by -50° till $1.8 \text{ GeV}/c^2$, then a rising one by $+75^\circ$. The falling phase motion might be caused by the $\pi_2(1670)$ in the $2^{-+}0^+ f_2(1270) \pi S$, which is then cancelled by the $a_4(2040)$ at higher mass in the $4^{++}1^+ \rho(770) \pi G$ wave.

Also the resonance-model fit finds a clear signal of the $a_4(2040)$ with a mass of $1938 \text{ MeV}/c^2$ and a width of $362 \text{ MeV}/c^2$.

5.11 The $J^{PC} = 4^{++}$ Sector

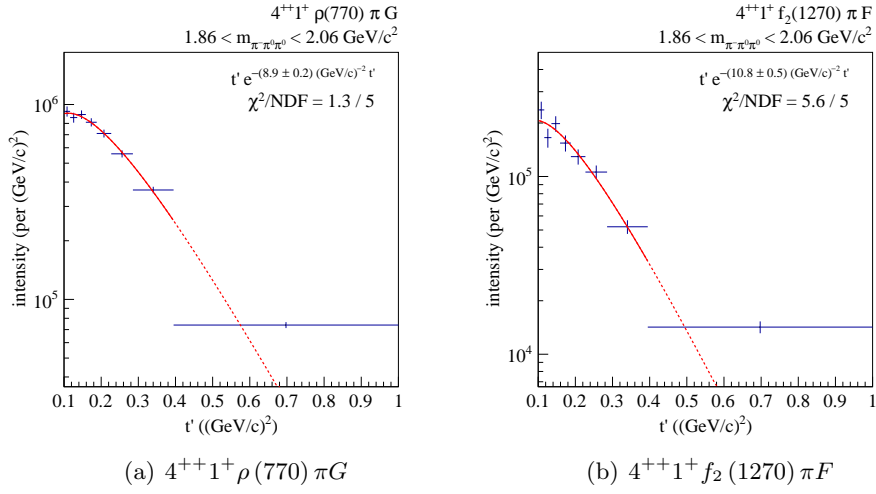


Figure 5.39: t' spectra of (a) the $4^{++}1^+ \rho(770) \pi G$, and (b) the $4^{++}1^+ f_2(1270) \pi F$ waves obtained by integrating the respective mass distributions in the ranges highlighted in fig. 5.38. The single-exponential fit is shown with the solid red line, the extrapolation to the whole range is shown by the dashed line.

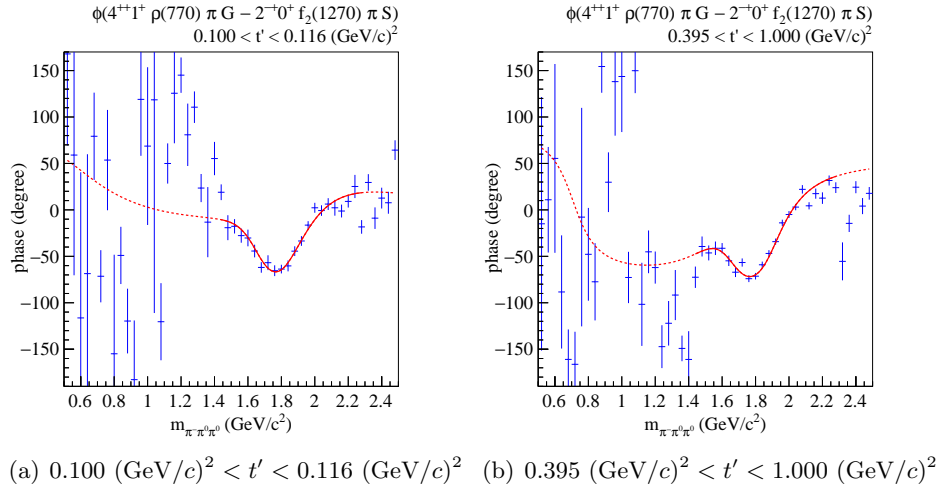


Figure 5.40: Phases of the $4^{++}1^+ \rho(770) \pi G$ with respect to the $2^{-+}0^+ f_2(1270) \pi S$ waves in (a) the lowest and (b) the highest t' bin.

5.12 The $a_1(1420)$

The major new discovery of the partial-wave analysis of the $\pi^-\pi^-\pi^+$ final state is a new axial-vector state, the $a_1(1420)$, seen in the $1^{++}0^+f_0(980)\pi P$ wave [9, 50, 11]. Also in the $\pi^-\pi^0\pi^0$ channel the intensity of this wave shows a peak that is compatible with this resonance (fig. 5.41). However, while the peak is clearly visible for lower t' , it washes out in the highest t' bin.

The resonance nature of the $a_1(1420)$ is derived from several relative phases with respect to waves with well-established resonances. The phase motion between the $1^{++}0^+f_0(980)\pi P$ and the $2^{-+}0^+f_2(1270)\pi S$ wave (fig. 5.42) in the $1.4\text{ GeV}/c^2$ region is even more pronounced in the highest t' bin. Also between the $1^{++}0^+f_0(980)\pi P$ and the $4^{++}1^+\rho(770)\pi G$ wave (fig. 5.43), the phase motion at $1.4\text{ GeV}/c^2$ is clearly seen.

The t' spectrum of the intensity distribution is obtained by integrating over a mass range from 1.38 to $1.58\text{ GeV}/c^2$ (fig. 5.44), it features a slope of $11(\text{GeV}/c)^{-2}$ which is still within the expected range for Pomeron exchange.

Indeed the resonance-model fit describes the intensity with a resonance sitting on top of a non-resonant component. The mass of the resonant component is $1414\text{ MeV}/c^2$, the width is $197\text{ MeV}/c^2$. For the phases of the $1^{++}0^+f_0(980)\pi P$ wave with respect to the $2^{-+}0^+f_2(1270)\pi S$ and $4^{++}1^+\rho(770)\pi G$ waves, the resonance model appears to be jumping down by about 100° in the lowest t' bin at a mass of $1.3\text{ GeV}/c^2$. At this mass, the intensity in the $1^{++}0^+f_0(980)\pi P$ wave is zero, and thus the phase is not well defined. By shifting the phase by -360° for the points below this mass, a smooth transition as for the highest t' bin could be constructed.

Several explanations of the $a_1(1420)$ have been brought forward [64, 77] since the publication of its observation in the $\pi^-\pi^-\pi^+$ final state [9]. As for the $\pi_2(1670)$ and $\pi_2(1880)$, the $a_1(1420)$ has been explained by interference of the $a_1(1260)$ with the Deck effect [21]. While this calculation proposes the experimentally found mass for the $a_1(1420)$, the width is estimated to be about $300\text{ MeV}/c^2$. Also phases are not correctly predicted.

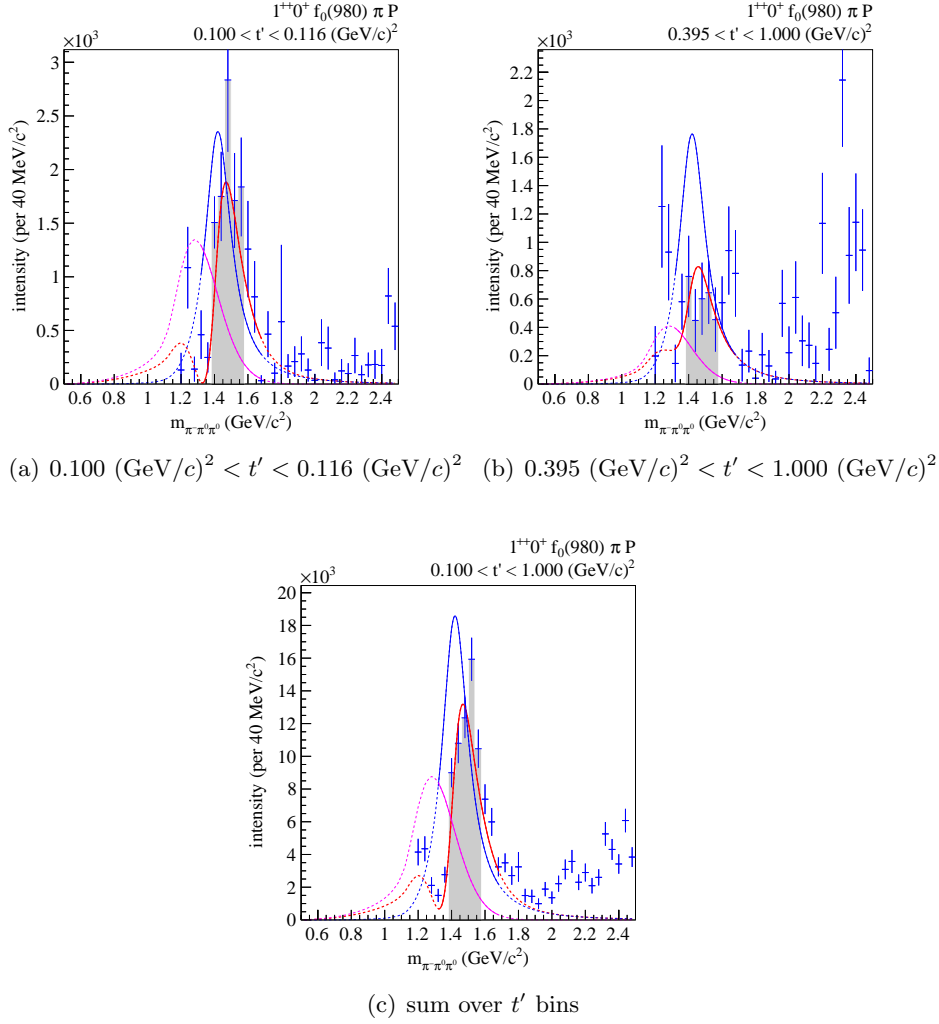


Figure 5.41: Intensity of the $1^{++}0^+ f_0(980) \pi P$ wave in (a) the lowest and (b) the highest t' bin. (c) shows the t' -summed intensity. The shaded areas correspond to the regions integrated over for the t' spectra.

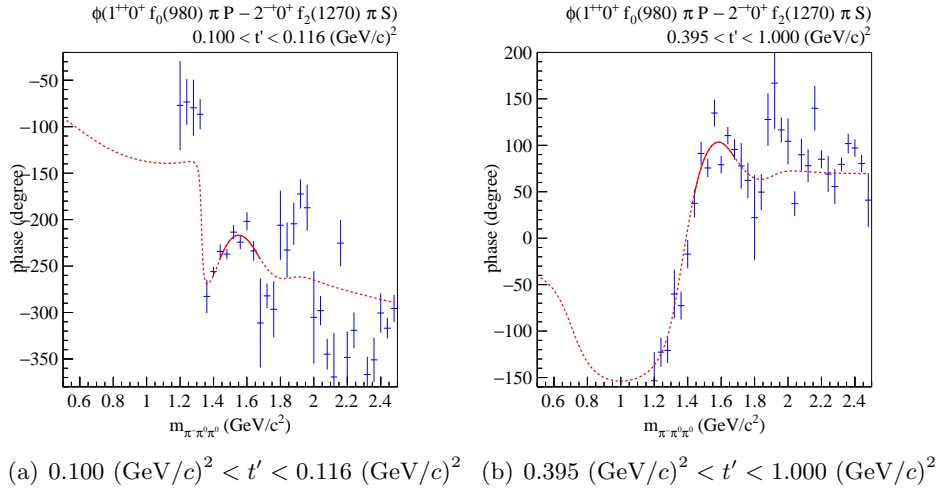


Figure 5.42: Phases of the $1^{++}0^+ f_0(980) \pi P$ with respect to the $2^{-+}0^+ f_2(1270) \pi S$ waves in (a) the lowest and (b) the highest t' bin.

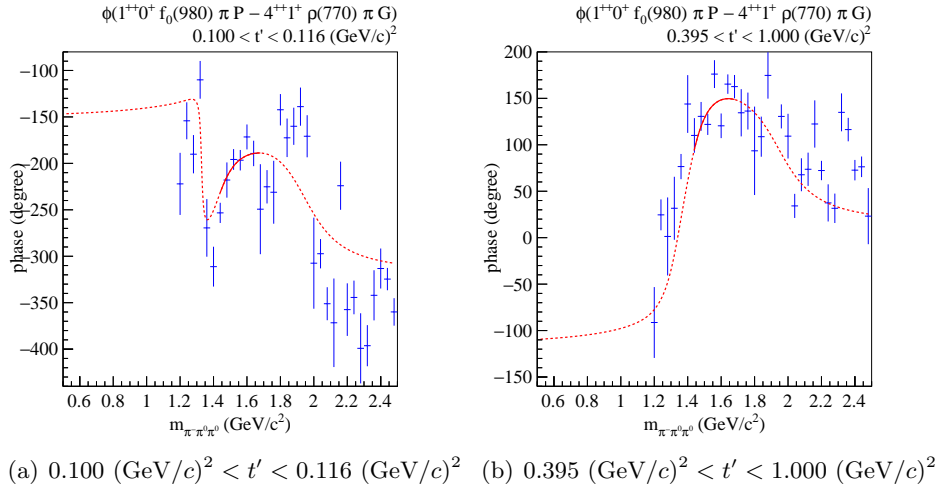


Figure 5.43: Phases of the $1^{++}0^+ f_0(980) \pi P$ with respect to the $4^{++}1^+ \rho(770) \pi G$ waves in (a) the lowest and (b) the highest t' bin.

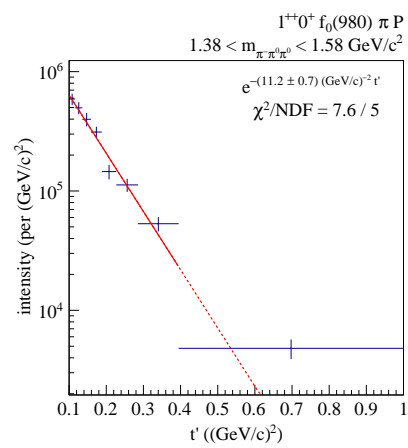


Figure 5.44: t' spectrum of the $1^{++}0^+ f_0(980) \pi P$ wave obtained by integrating the respective mass distributions in the range highlighted in fig. 5.41. The single-exponential fit is shown with the solid red line, the extrapolation to the whole range is shown by the dashed line.

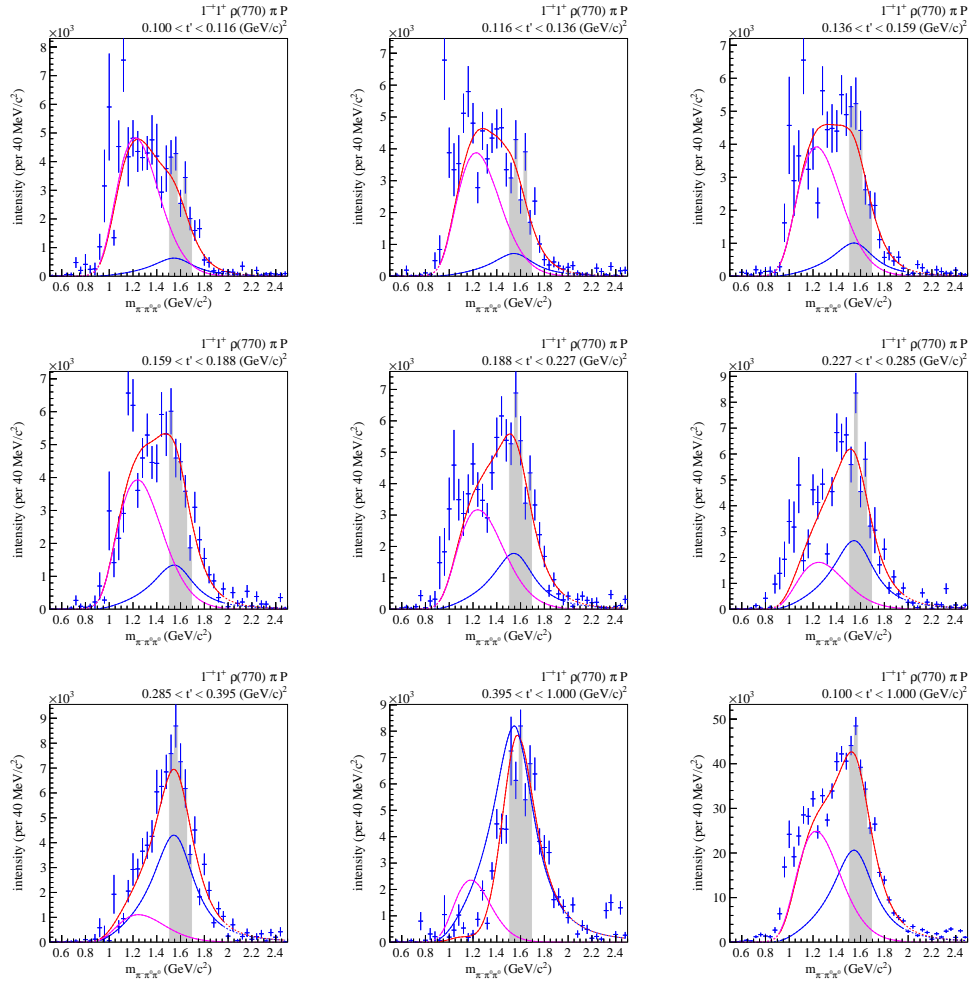


Figure 5.45: Intensities of the $1^{-+}1^{+}\rho(770)\pi P$ wave in each of the eight t' bins, and the t' -summed intensity (bottom right).

5.13 The $\pi_1(1600)$

The intensity of the spin-exotic $1^{-+}1^{+}\rho(770)\pi P$ wave is shown in fig. 5.45. It changes significantly with t' . While for low t' only a $600\text{ MeV}/c^2$ broad bump is visible, towards higher t' , a peak at $1.6\text{ GeV}/c^2$ is developing.

The phase with respect to the $1^{++}0^{+}\rho(770)\pi S$ wave (fig. 5.46) shows a slight phase motion at $1.6\text{ GeV}/c^2$ also for the lowest t' bin. In contrast to that, the phase with respect to the $2^{++}1^{+}\rho(770)\pi D$ wave (fig. 5.47) only moves by about 10° around the resonance position, indicating that resonances in each of the waves cancel each other.

The slope of the t' dependence of the intensity around the $\pi_1(1600)$ (fig. 5.48) is $10(\text{GeV}/c)^{-2}$ which is in agreement with the expectation for Pomeron exchange

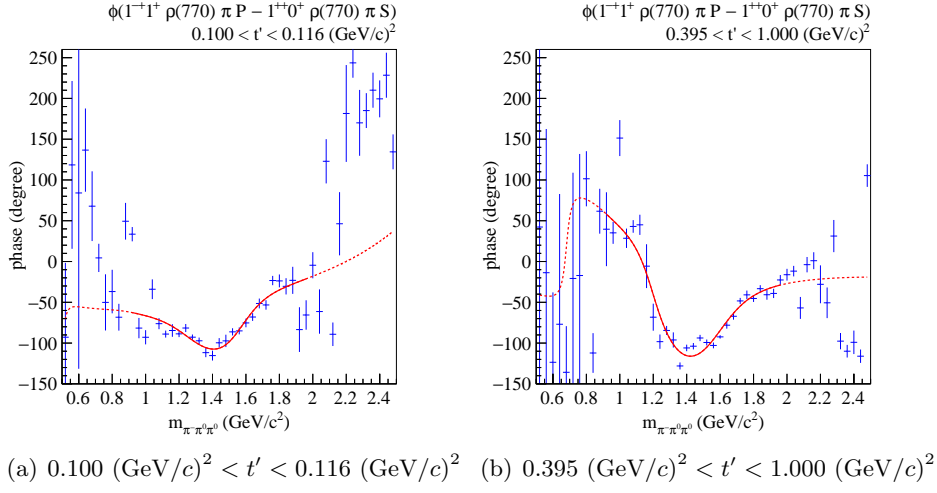


Figure 5.46: Phases of the $1^{-+}1^{+}\rho(770)\pi P$ with respect to the $1^{++}0^{+}\rho(770)\pi S$ waves in (a) the lowest and (b) the highest t' bin.

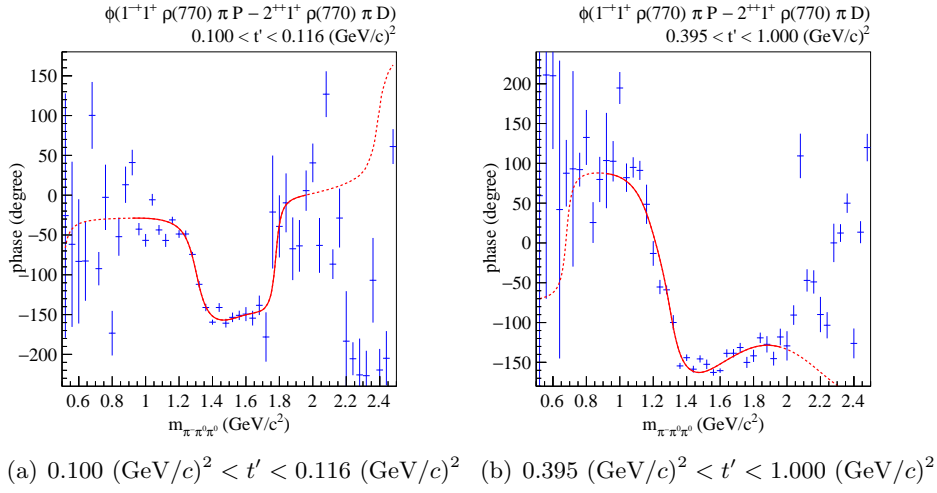


Figure 5.47: Phases of the $1^{-+}1^{+}\rho(770)\pi P$ with respect to the $2^{++}1^{+}\rho(770)\pi D$ waves in (a) the lowest and (b) the highest t' bin.

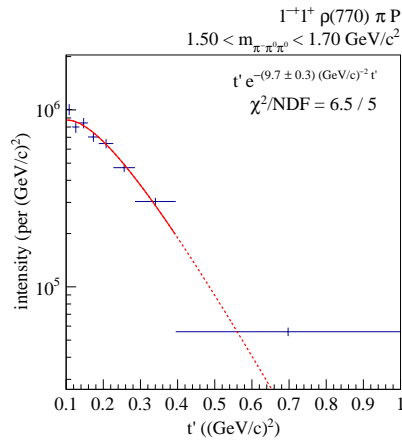


Figure 5.48: t' spectrum of the $1^{-+}1^{+}\rho(770)\pi P$ wave obtained by integrating the respective mass distributions in the range highlighted in fig. 5.45. The single-exponential fit is shown with the solid red line, the extrapolation to the whole range is shown by the dashed line.

in the production process.

The resonance-model fit supports a resonant contribution of a $\pi_1(1600)$ with a mass of $1550 \text{ MeV}/c^2$ and a width of $435 \text{ MeV}/c^2$. The contribution of the resonant contribution to the intensity strongly depends on t' . At low t' it only contributes little, while at high t' it dominates the intensity spectrum.

The non-resonant contribution in this wave is expected to be produced via the Deck effect [36, 37]. For the $\pi^-\pi^-\pi^+$ final-state a Deck model based on results by [35] has been simulated and analyzed in terms of its contributions to the partial waves [50]. It was found that the simulated Deck effect can explain large parts of the non-resonant contribution observed there, and also has the correct dependence on t' . For the $\pi^-\pi^0\pi^0$ final state a similar analysis has recently been started [71].

5.14 Some Systematics of the Resonance-Model Fit

resonance	standard		with branchings		with π_2 (2005)	
	mass	width	mass	width	mass	width
	(MeV/c ²)		(MeV/c ²)		(MeV/c ²)	
a_1 (1260)	1293	410	1382	605	1297	402
a_1 (1420)	1414	197	1413	196	1416	196
a_1 (1640)	1538	713	1341	619	1630	692
a_2 (1320)	1313	117	1314	119	1313	116
a_2 (1700)	1670	428	1671	413	1668	426
a_4 (2040)	1938	362	1954	326	1947	324
π (1800)	1793	227	1789	222	1799	226
π_1 (1600)	1550	435	1539	463	1552	441
π_2 (1670)	1651	256	1643	263	1653	285
π_2 (1880)	1886	347	1864	335	1852	295
π_2 (2005)	—	—	—	—	2065	333

Table 5.7: Resonance parameters extracted by the resonance-model fit for three different resonance models. Errors are not given as the statistical uncertainties are much smaller than the systematic ones.

5.14 Some Systematics of the Resonance-Model Fit

The resonance model presented above (section 5.6) has two major differences compared to the one for the $\pi^-\pi^-\pi^+$ final state [75]. The impact of these differences has been studied, the results are summed up in table 5.7.

The production of a resonance is independent of its decay, thus the t' dependence of the strength of a resonance should not depend on the decay channel. This can be incorporated into the resonance model by factorizing the couplings $C_{j,k}^{r,\varepsilon}(t')$ in eq. (5.21) to one possibly t' -dependent complex-valued coupling of the quantum numbers $J^{PC}M^\varepsilon$ to a resonance, and one complex-valued branching of the resonance to a specify decay channel. As an example, the couplings of the $2^{-+}0^+ f_2(1270)\pi S$ and the $2^{-+}0^+ \rho(770)\pi F$ waves to the $\pi_2(1670)$ can be rewritten as

$$C_{2^{-+}0^+ f_2(1270)\pi S, \pi_2(1670)}^{r,+}(t') = C_{2^{-+}0^+, \pi_2(1670)}^{r,+}(t') B_{\pi_2(1670), f_2(1270)\pi S} \quad (5.32)$$

$$C_{2^{-+}0^+ \rho(770)\pi F, \pi_2(1670)}^{r,+}(t') = C_{2^{-+}0^+, \pi_2(1670)}^{r,+}(t') B_{\pi_2(1670), \rho(770)\pi F} \quad (5.33)$$

The coupling $C_{2^{-+}0^+, \pi_2(1670)}^{r,+}(t')$ is the same in both cases, so that this factorization reduces the number of parameters in the fit when using multiple t' bins. For the resonance-model fit of the $\pi^-\pi^-\pi^+$ final state [75], these branchings have been used.

For the resonance model fit presented in section 5.6, using these branchings reduces the number of fit parameters from 698 to 544. But the additional con-

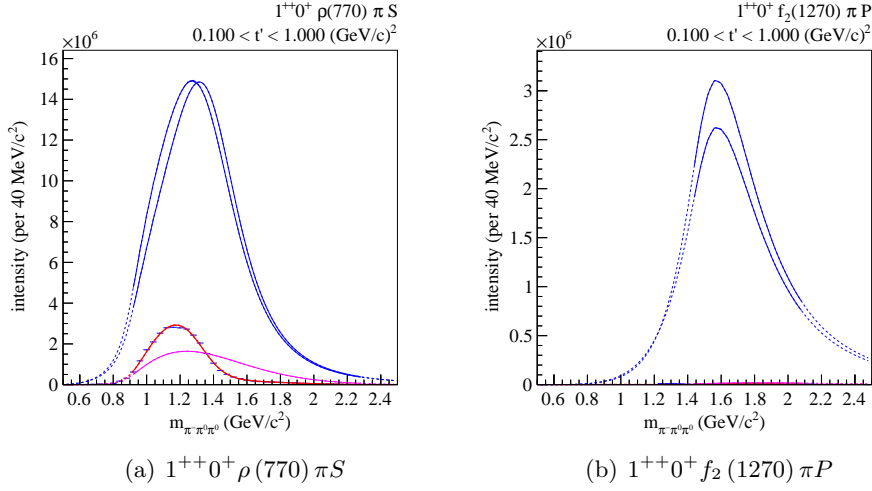


Figure 5.49: t' -summed intensities of $1^{++}0^+$ waves with (a) $\rho(770) \pi S$ and (b) $f_2(1270) \pi P$ decay modes for the resonance-model fit using branchings. The intensities for the fit using only couplings are shown in fig. 5.21(a) for the $\rho(770) \pi S$, and fig. 5.22(b) for the $f_2(1270) \pi P$ decay mode.

straints seem to favor a solution of the resonance-model fit where the $a_1(1260)$ and $a_1(1640)$ resonances in the $1^{++}0^+ \rho(770) \pi S$ and $1^{++}0^+ f_2(1270) \pi P$ waves have similar Breit-Wigner parameters (table 5.7). A strong destructive interference is required to describe the intensity spectra in fig. 5.49. In contrast to the $\pi^-\pi^-\pi^+$ final state using the branchings does not stabilize the resonance-model fit, but causes this unphysical effect. In addition, the Breit-Wigner parameters for the masses of the $\pi_2(1670)$ and the $\pi_2(1880)$ are moved further away from results of previous experiments [65] towards lower values. Therefore the branchings have not been used for the result of the $\pi^-\pi^0\pi^0$ final state.

For a good description of the data, the resonance model for the $\pi^-\pi^-\pi^+$ required a third resonance with $J^{PC} = 2^{-+}$ quantum number, the $\pi_2(2005)$, in addition to the ones listed in table 5.6 [75]. Adding the $\pi_2(2005)$ to the resonance model for the $\pi^-\pi^0\pi^0$ final state, has an effect mostly on the parameters of the other π_2 resonances, but also on the $a_1(1640)$ (table 5.7). The mass of the Breit-Wigner parameterization for the $\pi_2(1880)$ is shifted further away from results of previous experiments [65] and towards lower values by $30 \text{ MeV}/c^2$ compared to the standard resonance model. The background component in the $2^{-+}0^+ \rho(770) \pi F$ wave increases for the extrapolation beyond the fit range, while for the standard resonance model, the intensity of the model follows the points from the mass-independent fit also in this range (fig. 5.50). There is also no visible improvement of the description of data for the extended resonance model. For these reasons the

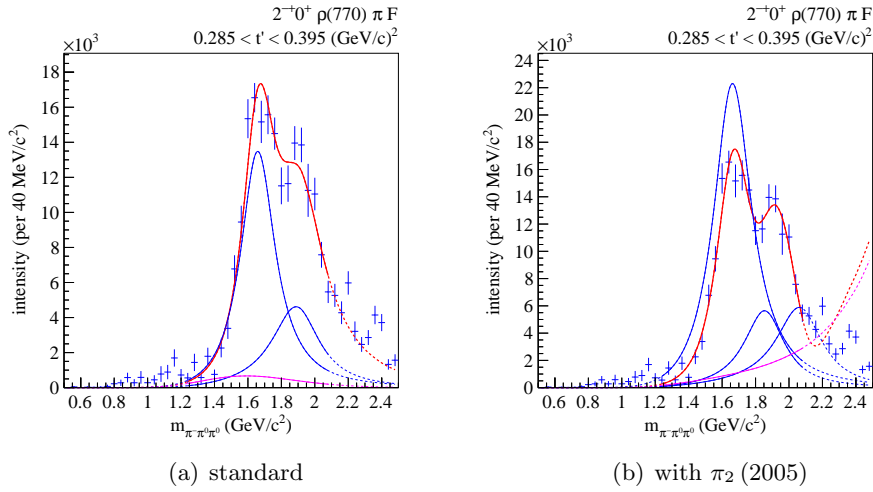


Figure 5.50: Intensity of the $2^{-+}0^{+}\rho(770)\pi F$ wave in the second highest t' bin for (a) the standard resonance model and (b) the resonance model including the $\pi_2(2005)$.

$\pi_2(2005)$ is not included in the resonance model for the $\pi^{-}\pi^{0}\pi^{0}$ final state.

Obviously those two additional resonance models can only be a starting point for a full systematic study of the resonance-model fit, as it was performed for the $\pi^{-}\pi^{-}\pi^{+}$ final state in [75]. So far the two studies indicate that the Breit-Wigner parameters of the $a_2(1320)$, the $a_2(1700)$, the $a_1(1420)$, and the $\pi(1800)$ have a rather small systematic error. In particular for the $a_2(1320)$ and $\pi(1800)$ this is an important message, as those states can be used as stable interferometers. In addition to the studies presented in [75] it might also be interesting to study the dependence of the $a_1(1420)$ parameters on the fitted mass range in the $1^{++}0^{+}f_0(980)\pi P$ wave. To obtain a good description of the intensity for the $\pi^{-}\pi^{0}\pi^{0}$ final state, it was necessary to increase the upper limit of the fit range in the $1^{++}0^{+}f_0(980)\pi P$ wave by 100 MeV/c² compared to the one for the $\pi^{-}\pi^{-}\pi^{+}$ final state. For the $a_1(1420)$ and $\pi_1(1600)$ it might also be useful to extract resonance parameters from single t' bins. The intensity of the $1^{++}0^{+}f_0(980)\pi P$ wave is much stronger at lower t' , while at higher t' it is washed out with larger errors (fig. 5.41). In the $1^{-+}1^{+}\rho(770)\pi P$ wave (fig. 5.45), a clean peak is visible for the highest t' bin, while in the lower t' bins a large non-resonant contribution has to be considered.

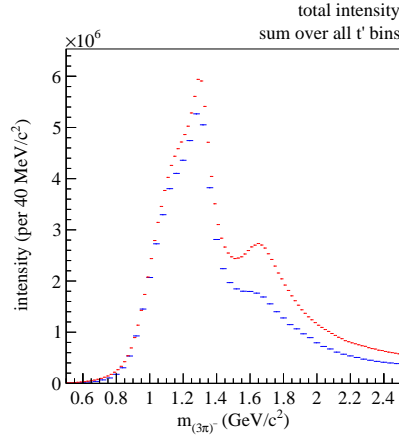


Figure 5.51: t' -summed total intensity for the $\pi^-\pi^0\pi^0$ (blue) and the $\pi^-\pi^-\pi^+$ (red) final states.

5.15 Comparison with the $\pi^-\pi^-\pi^+$ Final State

The $\pi^-\pi^-\pi^+$ final state has also been analyzed in COMPASS [11, 50]. Compared to the $\pi^-\pi^0\pi^0$ channel the data set is 15 times larger and contains about 50 million events. The difference in data-set size is caused by the different acceptances of the two channels. Due to the larger available data set, the $\pi^-\pi^-\pi^+$ channel is analyzed in finer bins of the three-pion mass (20 MeV/ c^2 instead of 40 MeV/ c^2) and the squared four-momentum transfer (11 bins instead of 8). Neglecting details,¹ the intensities of the $\pi^-\pi^-\pi^+$ final state have been scaled up to accommodate the different mass and t' binning by a factor of 1.6 for individual t' bins and a factor of 2 for t' -summed intensities.

In the total intensities (fig. 5.51), it is apparent that the bump around 1.7 GeV/ c^2 is much weaker in the $\pi^-\pi^0\pi^0$ channel compared to the $\pi^-\pi^-\pi^+$ channel. Comparing the $J^{PC} = 2^{-+}$ spin totals (fig. 5.17) and the total intensity (figs. 5.12(a) and 5.12(b)) suggests that the 1.7 GeV/ c^2 mass region has a large contribution from waves with $J^{PC} = 2^{-+}$ quantum numbers, which in turn decay predominantly via the $f_2(1270)$ isobar. Due to isospin symmetry, the decay to isospin-0 isobars are expected to be suppressed by Clebsch-Gordan coefficients in the $\pi^-\pi^0\pi^0$ channel, while waves with isospin 1 should not be affected. This becomes apparent in fig. 5.52(a) which shows the total intensities of waves decaying via $\rho(770)$, which are comparable for the two final states, whereas waves decaying via $f_2(1270)$ (fig. 5.52(b)), have only about half the intensity for the $\pi^-\pi^0\pi^0$ final state.

This observation also holds for individual waves. For the $1^{++}0^+\rho(770)\pi S$ wave

¹The two channels have been analyzed using data from two different productions with slightly different number of events. Also there are still imperfections in the simulation.

5.15 Comparison with the $\pi^-\pi^-\pi^+$ Final State

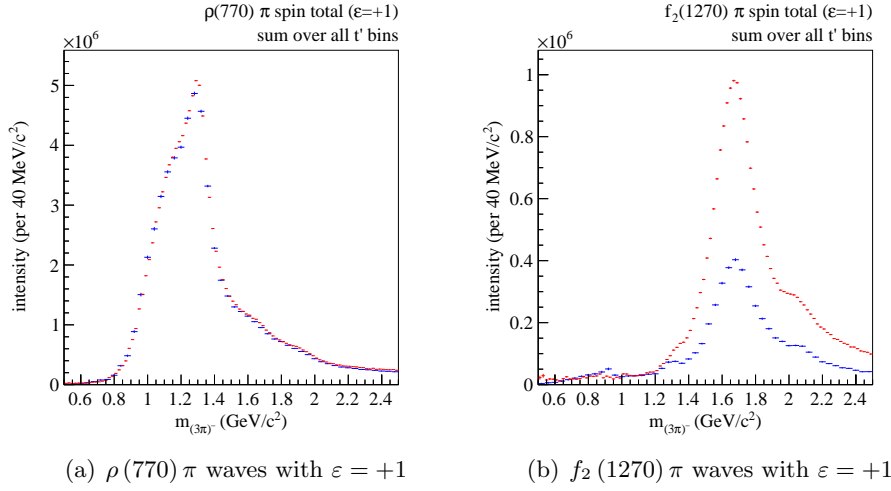


Figure 5.52: t' -summed spin totals of all waves with positive reflectivity with (a) $\rho(770)\pi$ and (b) $f_2(1270)\pi$ decay modes for the $\pi^-\pi^0\pi^0$ (blue) and the $\pi^-\pi^-\pi^+$ (red) final states.

(fig. 5.53(a)), the $2^{++}1^+\rho(770)\pi D$ wave (fig. 5.53(b)), and the $4^{++}1^+\rho(770)\pi G$ wave (fig. 5.53(c)), which all decay via the $\rho(770)$ isobar, the intensities are similar for the two final states. In contrast, for the $0^{-+}0^+f_0(980)\pi S$ (fig. 5.54(a)), and $2^{-+}0^+f_2(1270)\pi S$ (fig. 5.54(b)) waves the intensity of the $\pi^-\pi^0\pi^0$ final state is lower, but the shapes still agree.

The lower intensity for waves with isospin-0 isobars in the $\pi^-\pi^0\pi^0$ final state is also visible in fig. 5.55 for the $1^{++}0^+f_0(980)\pi P$ wave. But the $a_1(1420)$ is at a similar place and has a similar shape in both final states.

For the spin-exotic $1^{-+}1^+\rho(770)\pi P$ wave (fig. 5.56) no effect due to isospin symmetry is expected. But the intensities do not match for individual t' bins. In general, there is at least an agreement of the shape of the intensity distributions for the lower t' bins. For higher t' bins, the intensity found in the two final state clearly differs. While for the $\pi^-\pi^0\pi^0$ final state a peak around $1.6\text{ GeV}/c^2$ is forming, for the $\pi^-\pi^-\pi^+$ final state this remains a broad structure until $t' > 0.5(\text{GeV}/c)^2$.

Those similarities and differences are also visible in the resonance-model fit (see [75] for the $\pi^-\pi^-\pi^+$ final state). The masses for the $a_1(1260)$, the $a_2(1320)$, the $a_4(1938)$, but also the new $a_1(1420)$ are in agreement, the widths in the $\pi^-\pi^0\pi^0$ final state are larger by typically more than 10 to $30\text{ MeV}/c^2$. For the π_2 resonances a better agreement to the results of the $\pi^-\pi^-\pi^+$ final state is found for the resonance-model fit using branchings (section 5.14), while for the $a_1(1640)$ the usage of the $\pi_2(2005)$ would improve the agreement.

The mass of the new $a_1(1420)$ found here for the $\pi^-\pi^0\pi^0$ channel is close to the one found for $\pi^-\pi^-\pi^+$ in [75], but the width is significantly broader. For the higher

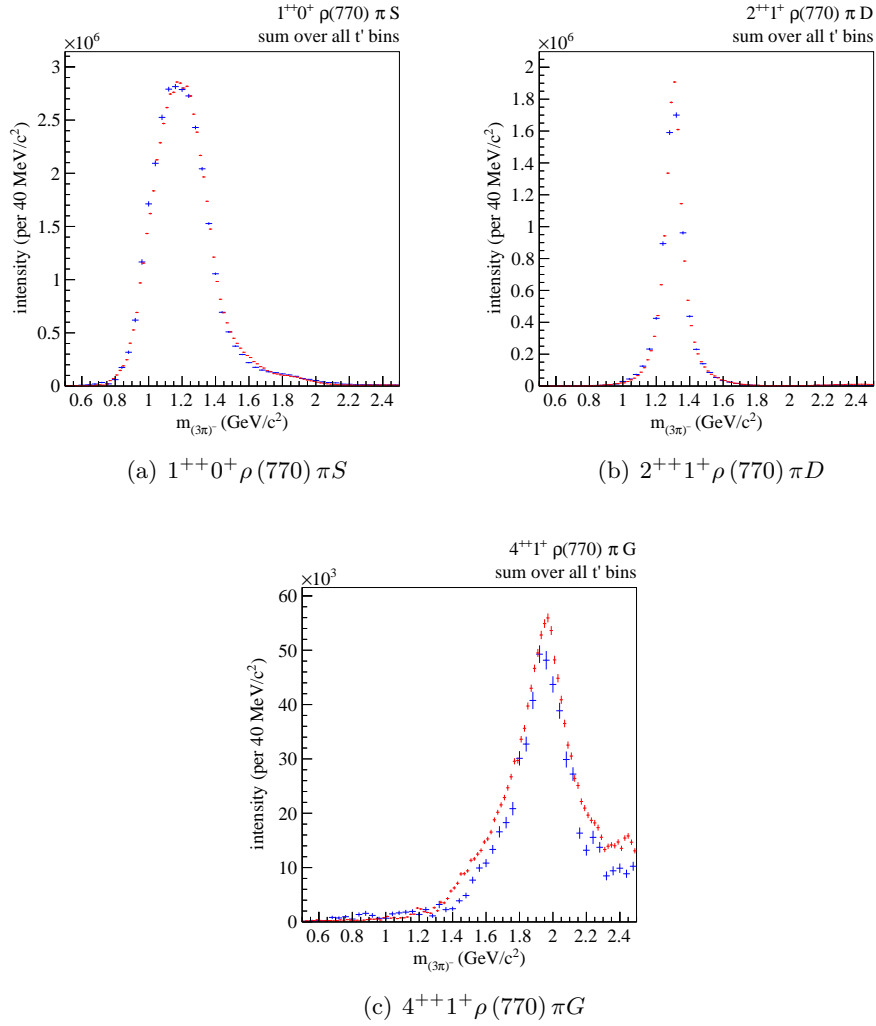


Figure 5.53: t' -summed intensities of (a) the $1^{++}0^+ \rho(770) \pi S$, (b) the $2^{++}1^+ \rho(770) \pi D$, and (c) the $4^{++}1^+ \rho(770) \pi G$ waves for the $\pi^-\pi^0\pi^0$ (blue) and the $\pi^-\pi^-\pi^+$ (red) final states.

5.15 Comparison with the $\pi^-\pi^-\pi^+$ Final State

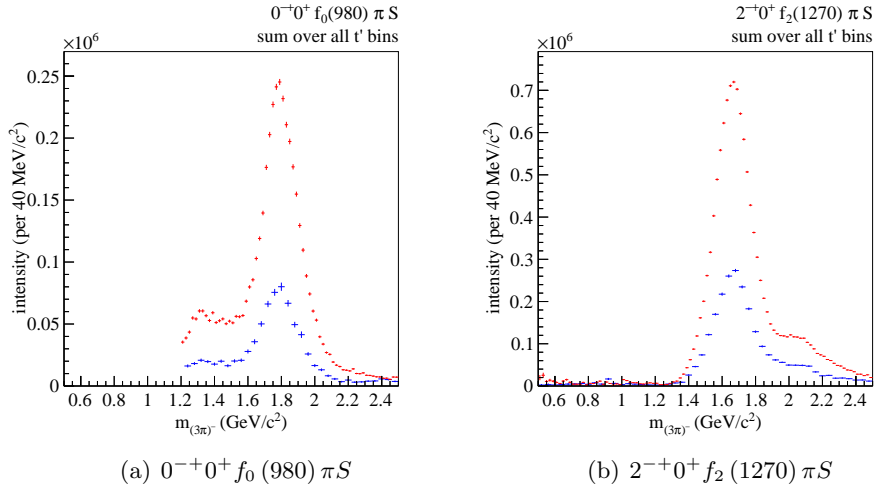


Figure 5.54: t' -summed intensities of (a) the $0^{-+}0^{+} f_0(980) \pi S$, and (b) the $2^{-+}0^{+} f_2(1270) \pi S$ waves for the $\pi^-\pi^0\pi^0$ (blue) and $\pi^-\pi^-\pi^+$ (red) final states.

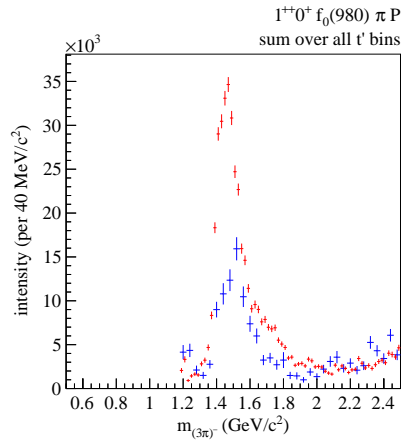


Figure 5.55: t' -summed intensity of the $1^{++}0^{+} f_0(980) \pi P$ wave for the $\pi^-\pi^0\pi^0$ (blue) and the $\pi^-\pi^-\pi^+$ (red) final states.

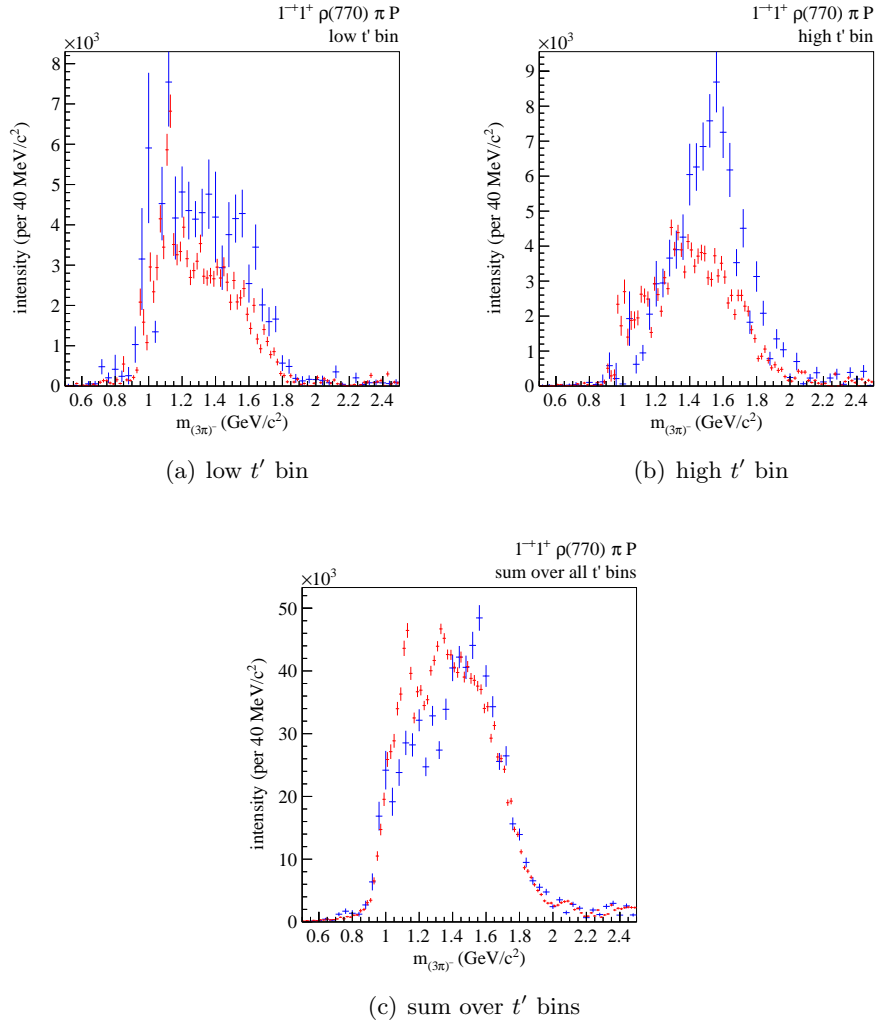


Figure 5.56: Intensities of the $1^-+1^+ \rho(770) \pi P$ wave for $\pi^-\pi^0\pi^0$ (blue) and $\pi^-\pi^-\pi^+$ (red) channels in (a) a low and (b) a high t' bin. (c) shows the t' -summed intensity.

5.15 Comparison with the $\pi^-\pi^-\pi^+$ Final State

t' bins the intensity of the $1^{++}0^+ f_0(980) \pi P$ wave washes out and becomes a broad bump (fig. 5.41(b)), which might affect the width. In this wave the mass range of the resonance-model fit had to be increased to a higher limit of $1.70 \text{ GeV}/c^2$ instead of the $1.60 \text{ GeV}/c^2$ used in the $\pi^-\pi^-\pi^+$ final state as otherwise the non-resonant contribution would have dominated the complete spectrum. Also the behavior of this non-resonant contribution might play a role in this difference.

For the $\pi_1(1600)$ quite different parameters are found. The mass is found to be $50 \text{ MeV}/c^2$ lower in the $\pi^-\pi^0\pi^0$ final state, the width is even $150 \text{ MeV}/c^2$ smaller than in the $\pi^-\pi^-\pi^+$ final state. This is caused by the different behavior of the non-resonant contribution for the two final states. While the intensity in the lowest t' bin look rather similar, at higher t' the peak attributed to the $\pi_1(1600)$ is more clearly visible in the $\pi^-\pi^0\pi^0$ final state. In the $\pi^-\pi^-\pi^+$ final state it becomes that clean only for $t' \geq 0.7 (\text{GeV}/c)^2$. Having several t' bins with a wide object, a broad resonance might better describe the data. More systematic studies of the resonance-model fit, also varying the t' bins used for the fit, are required to resolve this issue.

Chapter 6

Partial-Wave Analysis of the $\pi^- \eta \eta$ Final State

The kinematic selection of the $\pi^- \eta \eta$ final state has been presented in chapter 3. Compared with the $\pi^- \pi^0 \pi^0$ final state, the number of measured events in this final state is much smaller. Also previous experiments have collected only small data samples, but still were able to perform a partial-wave analysis of this final state [45, 14].

6.1 Partial-Wave Analysis using the Wave Set by E852

The $\pi^- \eta \eta$ mass spectrum after event selection is shown in fig. 3.12(b). The mass spectra of the two-particle subsystems (fig. 6.1) suggest to include the a_0 (980) and the a_2 (1320) as isobars in $\pi^- \eta$, as well as the f_0 (1500) in $\eta \eta$. A partial-wave decomposition of the data set has been performed using the model by E852 [45] which uses the aforementioned isobars and consists of only four waves listed in table 6.1.

The COMPASS data were subdivided into 55 mass bins of $50 \text{ MeV}/c^2$ width, ranging from $1.25 \text{ GeV}/c^2$ to $4 \text{ GeV}/c^2$. A rank-1 fit was performed with 100 fit attempts per mass bin. In each mass bin the fit result with the highest likelihood has been selected to create the plots shown below. The lowest three mass bins are omitted in the plots as the fits did not converge.

The total intensity of all partial waves is shown in fig. 6.2. The flat wave shown in comparison contributes nearly 40 % to the total intensity. Performing a rank-2 fit decreases the contribution to the total intensity to about 30 %. This points to some incoherence in the data, that can be resolved by adding a second block of non-interfering transition amplitudes. The incoherence might be caused by the integration over a broad range in the reduced squared four-momentum transfer

wave	wave
$0^-+0^+ a_0(980) \eta S$	$2^-+0^+ a_0(980) \eta D$
$0^-+0^+ f_0(1500) \pi S$	$2^-+0^+ a_2(1320) \eta S$

Table 6.1: Wave set by E852 to analyze the $\pi^- \eta \eta$ final state [45]. The flat wave is omitted.

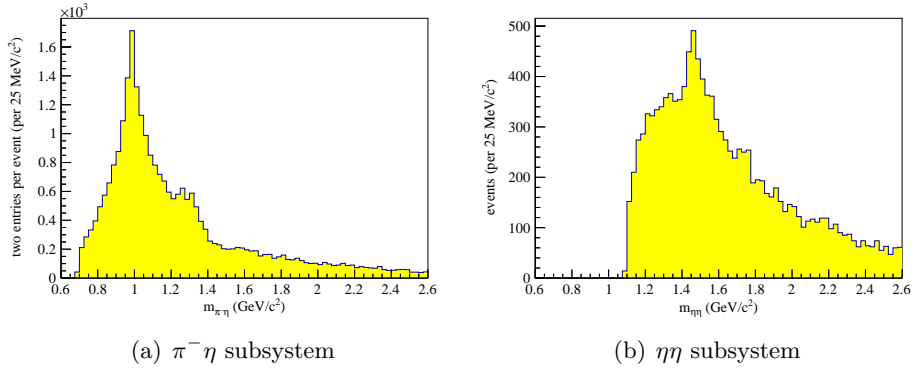


Figure 6.1: Invariant mass spectra for the two-particle subsystems of the $\pi^-\eta\eta$ final state.

t' . In the $\pi^-\pi^0\pi^0$ final state the importance of this binning has been shown in section 3.4.4 and chapter 5, but, due to the limited amount of data, a binning in this variable cannot be done for the $\pi^-\eta\eta$ final state. Even the smaller contribution of the rank-2 fit is still larger than the 5% to 15% observed in [45]. As the rank-2 fit does not reduce the contribution to this level, in the following only the rank-1 fit will be shown. Typically such a large fraction hints to contributions from either non-diffractively produced states, missing waves in the used wave set, or an imperfect isobar description. The comparison of real data with weighted Monte Carlo (section 5.2) does not point to any obvious deficiencies of the model.

The intensities of the individual waves are shown in fig. 6.3. In the two 0^{-+} waves a structure between $1.8\text{ GeV}/c^2$ and $1.9\text{ GeV}/c^2$ is visible, E852 identified this as the $\pi(1800)$ in a mass-dependent fit. The peak of the $2^{-+}0^+a_2(1320)\eta S$ wave at around $1.9\text{ GeV}/c^2$ has been identified by E852 as the hybrid candidate $\pi_2(1880)$. As the bump visible in the $a_0(980)\eta D$ decay mode at around $2.5\text{ GeV}/c^2$ is at the limit of the mass range studied by E852, they do not claim anything in this wave, however, given the huge width, it is questionable whether it is a single resonance.

6.2 Biggest-Conceivable-Model Method

With the E852 wave set, a large contribution of the flat wave to the total intensity is found. To test whether this is caused by missing important waves, the biggest-conceivable-model method (BCM method) [23] was tried. This method was initially developed for the analysis of the $\pi^-\pi^-\pi^-\pi^+\pi^+$ final state, where basically no prior knowledge of the relevant waves is existing. To overcome this situation the likelihood as given in eq. (4.44) is modified by adding a prior

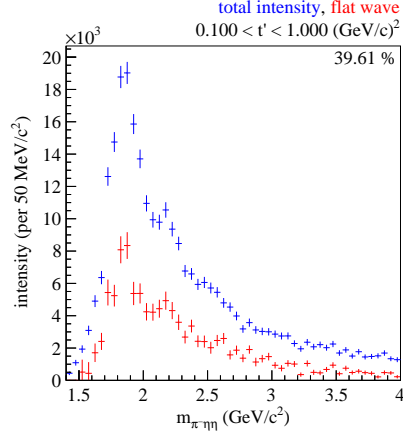


Figure 6.2: Total intensity of all partial waves (blue markers) overlaid with the contribution of the flat wave (red markers).

$$-\ln \mathcal{L}' = -\ln \mathcal{L} - \ln \mathcal{L}_{\text{prior}} \quad (6.1)$$

where the additional term $\mathcal{L}_{\text{prior}}$ is a half-Cauchy prior for the intensities of the individual waves

$$\mathcal{L}_{\text{prior}} = \prod_{\varepsilon=\pm 1} \prod_r^{N_{\text{rank}}^\varepsilon} \prod_i^{N_{\text{waves}}^\varepsilon} \left(1 + \frac{\overline{T}_i^{r\varepsilon*} \overline{T}_i^{r\varepsilon}}{\gamma^2} \right)^{-1} \quad (6.2)$$

where the width parameter γ is fixed to 0.5 in the following. This prior applies a penalty for non-zero intensities. Unless including a wave with some non-zero intensity increases the likelihood significantly, this wave is pushed towards zero.

To select a model, the log-likelihood including the half-Cauchy prior eq. (6.1) is minimized using the biggest-conceivable wave pool in each mass bin individually. The wave pool is constructed with waves having a spin J between 0 and 4 and a spin projection M of either 0 or 1. The angular momentum L between the isobar and the bachelor pion is allowed to be between 0 and 4. The list of allowed isobars is given in table 6.2. The resulting wave pool created for the analysis of the $\pi^- \eta \eta$ final state consists in total of 264 waves, 151 waves with positive and 113 with negative reflectivity ε .

Figure 6.4 shows the partial-wave intensities for two neighboring mass bins. The waves are ordered by their intensities. Contributions from the waves with positive and negative reflectivity and from the flat wave are shown in different colors. Due to the prior there is at least one step drop in the intensity spectra. The waves to the left of the first step are selected for a first, mass bin specific,

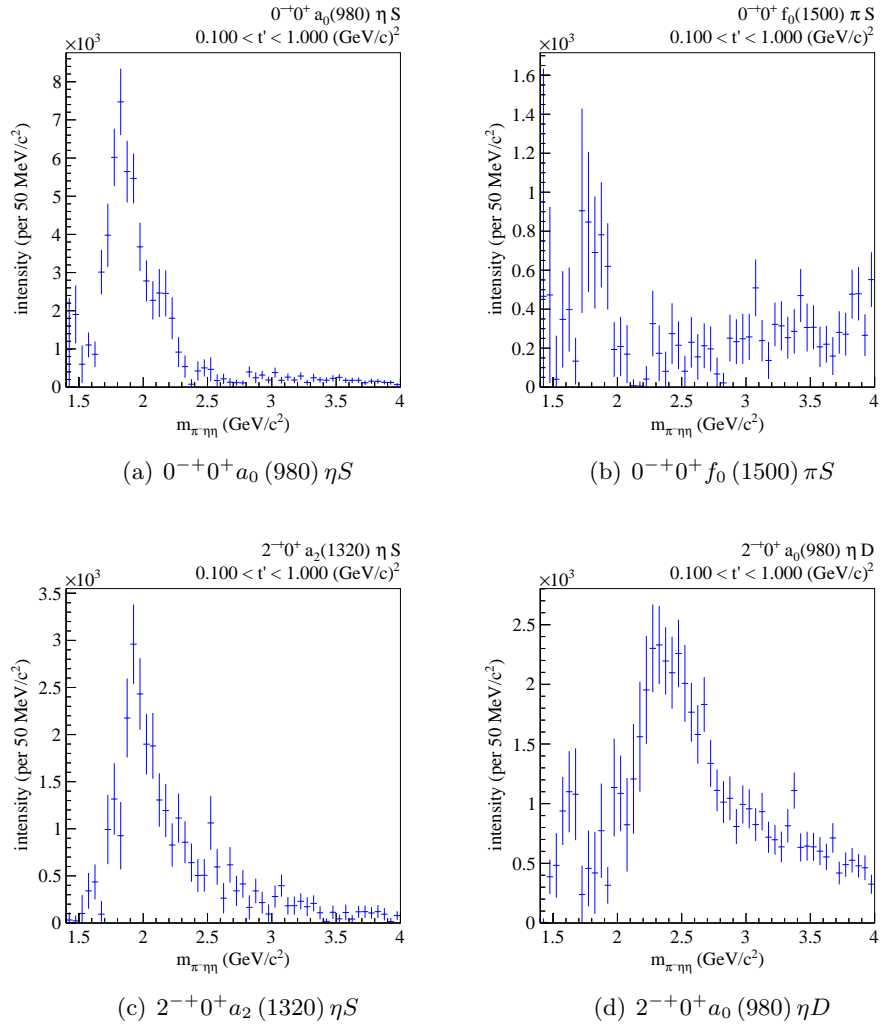


Figure 6.3: Result of the partial-wave fit to the $\pi^-\eta\eta$ final state using the wave set of E852 (table 6.1).

isobar J^{PC}	isobar name
$\pi^- \eta$ isobars	
0^{++}	$a_0(980), a_0(1450)$
2^{++}	$a_2(1320)$
4^{++}	$a_4(2040)$
1^{-+}	$\pi_1(1400)$
$\eta\eta$ isobars	
0^{++}	$f_0(1370), f_0(1500)$
2^{++}	$f_2(1270)$
4^{++}	$f_4(2050)$

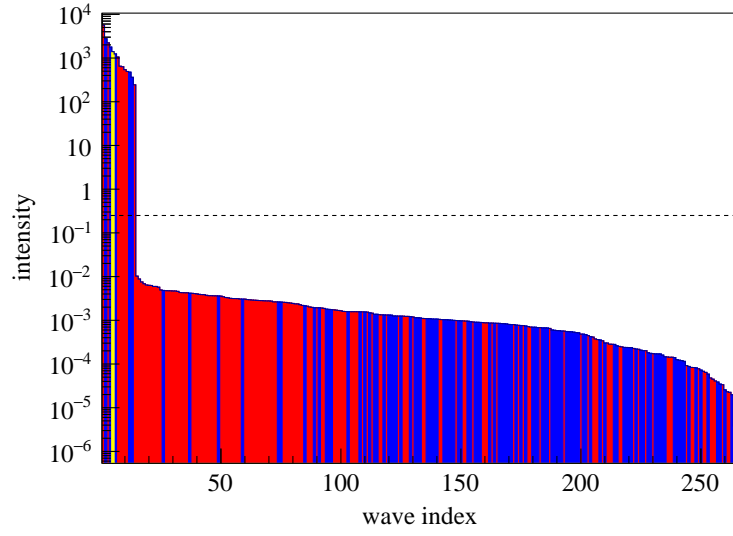
Table 6.2: List of isobars used to generate the wave pool for the analysis of the $\pi^- \eta\eta$ final state with the biggest-conceivable-model method.

wave set. In the lowest six mass bins (from $1.25 \text{ GeV}/c^2$ to $1.55 \text{ GeV}/c^2$) this first step is after just the flat wave, indicating that the events in this mass region can be described by pure three-body phase space. The intensities of the waves with negative reflectivity tend to be small as expected for the dominant Pomeron exchange. In 44 of the 55 mass bins, the waves with negative reflectivity are even completely separated from the other waves by a second step as in fig. 6.4(b). In the remaining mass bins above $1.55 \text{ GeV}/c^2$ the waves with negative reflectivity have low intensities.

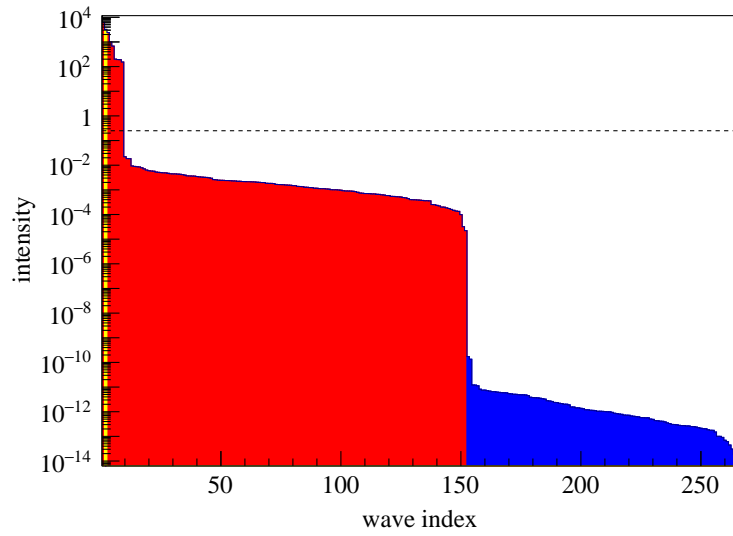
The selection of the model is first performed for each mass bin individually. Of the initial 264 waves 92 are selected in at least one mass bin, 80 of these waves have positive reflectivity and 12 negative reflectivity ε . Figure 6.5 shows in which mass bins each wave is selected. Only 12 waves are selected in ten or more mass bins, more than one third of all waves is selected in only a single mass bin. The number of waves selected in each mass bin is shown in fig. 6.6. For mass bins above $1.7 \text{ GeV}/c^2$ the number of selected waves is basically constant with a slight tendency towards smaller wave set sizes at higher masses. Some pairs of isobars with the same quantum numbers but different masses exist, as for example the $a_0(980)$ and the $a_0(1450)$. Only one of the two waves is typically selected in each mass bin for these cases. There are 55 BCM wave sets for the 55 mass bins. If the standard log-likelihood eq. (4.44) is minimized using the corresponding wave set for each mass bin, the flat wave contributes about 15% of the total intensity. However, the intensities for the individual partial waves are not continuous.

To achieve this, a continuity criterion is applied to select the final wave set. Only waves which are selected in four or more consecutive mass bins by the BCM method are considered. In case of isobar pairs, only the one selected more often is kept. This way the truncated BCM wave set contains twelve waves (table 6.3). Three of the four waves used by E852 (table 6.1) are also found by this method, only the $0^{-+}0^+ f_0(1500) \pi S$ wave is not picked up.

The intensity of the flat wave contributes almost 30% of the total intensity



(a) $1.75 \text{ GeV}/c^2 < m_{\pi^-\eta\eta} < 1.8 \text{ GeV}/c^2$



(b) $1.8 \text{ GeV}/c^2 < m_{\pi^-\eta\eta} < 1.85 \text{ GeV}/c^2$

Figure 6.4: Intensities of all waves for two neighboring mass bins. The waves are sorted by intensity, the wave at index 0 is representing the wave with the largest intensity. Waves with positive reflectivity are drawn in red, waves with negative reflectivity in blue. The flat wave is drawn in yellow. The dashed line indicates the width γ of the half-Cauchy prior.

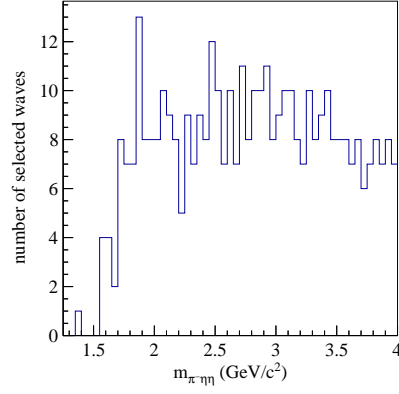


Figure 6.6: Number of waves selected by the BCM method in each mass bin.

wave	wave
$0^-+0^+ a_0$ (980) ηS	$2^-+0^+ f_2$ (1270) πS
$1^{++}0^+ a_0$ (980) ηP	$3^{++}0^+ a_0$ (980) ηF
$1^{++}0^+ f_0$ (1370) πP	$3^{++}0^+ f_0$ (1370) πF
$2^-+0^+ a_0$ (980) ηD	$3^{++}1^+ a_0$ (980) ηF
$2^-+0^+ a_2$ (1320) ηS	$4^-+0^+ a_0$ (980) ηG
$2^-+0^+ f_0$ (1370) πD	$4^-+1^+ a_0$ (980) ηG

Table 6.3: The 12 waves selected for the truncated BCM wave set.

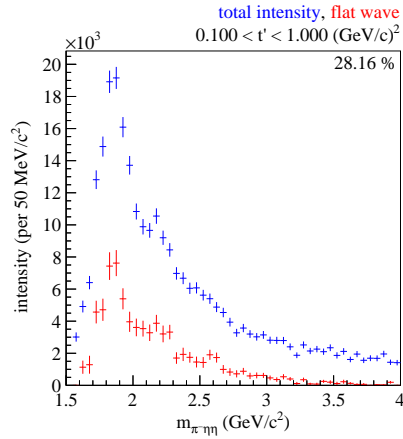


Figure 6.7: Total intensity of all partial waves (blue markers) overlaid with the contribution of the flat wave (red markers) for the truncated BCM wave set.

(fig. 6.7) using the truncated BCM wave set. Looking at individual waves (fig. 6.8), a good agreement between the intensities found with the E852 wave set, the wave sets of the BCM method, and the truncated BCM wave set is only found for the $0^{-+}0^{+}a_0(980)\eta S$ wave (fig. 6.8(a)). The $2^{-+}0^{+}a_2(1320)\eta S$ wave (fig. 6.8(b)) is only selected above $1.85\text{ GeV}/c^2$ by the BCM method, also the truncated BCM wave set has a unstable intensity with large error bars below that mass. For the $2^{-+}0^{+}a_0(980)\eta D$ wave there is a large discrepancy between the E852 and the truncated BCM wave sets. In general, the intensities using the BCM wave set and the truncated BCM wave set agree.

As the $0^{-+}0^{+}a_0(980)\eta S$ and the $2^{-+}0^{+}a_2(1320)\eta S$ are the only waves for which the intensities using the BCM wave set and the truncated BCM wave set agree, a preliminary resonance-model fit should only use those two waves. As the $2^{-+}0^{+}a_2(1320)\eta S$ wave is unstable below $1.85\text{ GeV}/c^2$, but this mass region is where the $0^{-+}0^{+}a_0(980)\eta S$ wave contains most of its intensity there would be little overlap in which the phase information between the two waves could be used. Instead the fit would have to rely on the intensity information of single waves. Therefore a reliable extraction of resonance parameters is unfortunately impossible at the moment.

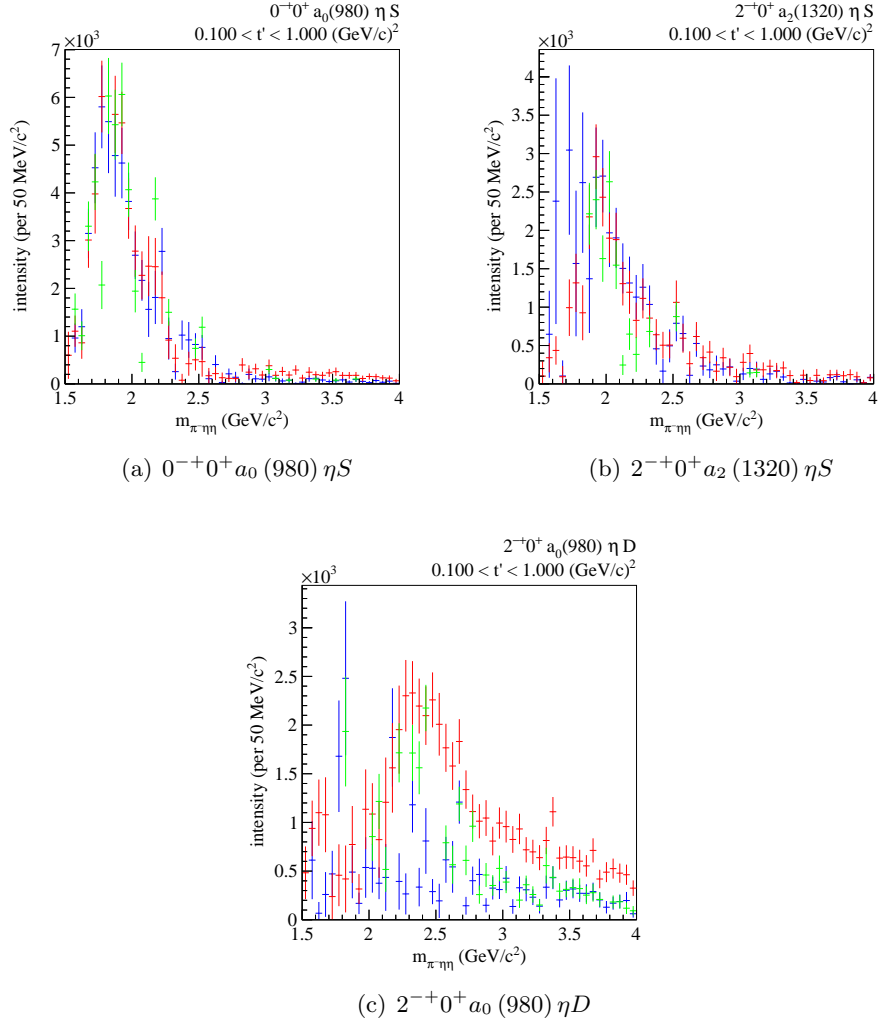


Figure 6.8: Intensities of the three waves the truncated BCM wave set (blue markers) has in common with the wave set by E852 (red markers, same as fig. 6.3). The green markers show the intensities using the BCM wave sets, accordingly green markers are missing if the wave was not selected in that mass bin.

Chapter 7

Conclusions and Outlook

7.1 Electromagnetic Calorimetry

The new implementation of the shower fitting ([60], section 2.3.1) and the corrections applied on top of it (section 2.3.2), improved the π^0 mass resolution for high-energetic π^0 by 25 % [46]. Despite an LED system being used to compensate for fluctuations in the amplification of the calorimeter signals, a time dependence of the π^0 mass was found and corrected (section 2.4.1). With these corrections applied, the $\pi^- \eta \eta$ final state was directly visible for the first time in COMPASS when plotting the invariant mass of one photon pair versus the invariant mass of the other one for $\pi^- \gamma \gamma \gamma \gamma$ events (fig. 2.13).

Using this improved calorimeter information in the kinematic selection (chapter 3), the number of good $\pi^- \pi^0 \pi^0$ candidate events increased by 50 % compared to the previous reconstruction and analysis of the same data set.

So far the new photon reconstruction is only applied for ECAL2. The application for ECAL1 had been prepared [53], but was not applied in a production of the full data set. The π^0 mass resolution of ECAL2 is similar in real data and Monte Carlo, the one of ECAL1 is about a factor of 1.5 worse in real data than for the simulation (section 2.5.2). A successful application of the new algorithm with the necessary corrections could improve this resolution. That way, not only would the agreement between real data and simulation be improved, but also the cuts on the π^0 and η mass could be tightened providing a cleaner selection of the π^0 and η (section 3.3). As about 30 % of the photons of the $\pi^- \eta \eta$ final state hit ECAL1, this might have a sizable effect in particular for the analysis of this channel.

7.2 Partial-Wave Analysis of the $\pi^- \pi^0 \pi^0$ Final State

A partial-wave analysis of the $\pi^- \pi^0 \pi^0$ final state was performed in bins of $m_{\pi^- \pi^0 \pi^0}$ and t' (chapter 5). The additional binning in t' provides a leverage to better separate non-resonant from resonant contributions already with a rank-1 fit. Previous analyses relied on higher-rank fits to achieve this. In each bin the five-dimensional kinematic distributions of the final-state particles were decomposed into 88 partial waves (table 5.2, [50, 11]). Resonance parameters were extracted from a subset of these waves (section 5.6). In general a good agreement with the values from [65] was found for most resonances. In particular the $a_2(1320)$ and $\pi(1800)$ resonances

can provide a reliable interferometer. The π_2 (1670) and the a_4 (2040) resonances are found lighter than in [65], but are consistent with previous COMPASS results [13].

In the $J^{PC} = 2^{-+}$ sector, the partial-wave intensities and phases can be described with only two π_2 resonances. This is in contrast to the analysis of the $\pi^-\pi^-\pi^+$ final state which required a third π_2 , the π_2 (2005), to describe all features of the data [75]. This difference is most obvious in the $2^{-+}0^+\rho(770)\pi F$ wave. In the $\pi^-\pi^0\pi^0$ final state, this particular wave is spoiled by adding the π_2 (2005) (section 5.14 and fig. 5.50). Removing the π_2 (2005) from the fit also moves the mass and width of the π_2 (1670) and π_2 (1880) closer to the values found in [65].

The a_1 (1420) previously observed in the $\pi^-\pi^-\pi^+$ final state [50, 9, 11] is also found in the $1^{++}0^+f_0(980)\pi P$ wave of the $\pi^-\pi^0\pi^0$ final state. With the resonance-model fit a mass consistent with the $\pi^-\pi^-\pi^+$ results is obtained, while the width is larger (section 5.12). This is probably caused by the much smaller data sample for the $\pi^-\pi^0\pi^0$ final state. While the partial-wave intensities of this wave show a clear peak for the lower t' bins, this peak is washed out in the higher t' bins (fig. 5.41).

The behavior of the intensity in the spin-exotic $1^{-+}1^+\rho(770)\pi P$ wave is opposite: A broad bump at low values of t' transforms to a rather clear peak in the highest t' bin (fig. 5.45). A Breit-Wigner has been used to describe the resonant content in this wave (section 5.13). The resulting mass is compatible with the π_1 (1600). While the width is larger than previous COMPASS results obtained from the $\pi^-\pi^-\pi^+$ final state on a lead target [13], its value is within the wide range spanned by previous experiments. The width is also significantly smaller than the one obtained for the π_1 (1600) in the $\pi^-\pi^+\pi^+$ final state on a liquid-hydrogen target [50, 75]. This might be caused by a larger non-resonant contribution in the $\pi^-\pi^-\pi^+$ final state that is not fully separated by the resonance-model fit.

A possible candidate for this non-resonant contribution is non-resonant production of the three-pion final state via the Deck effect [36]. The Deck effects in the $\pi^-\pi^-\pi^+$ and $\pi^-\pi^0\pi^0$ final-states are currently under study [71]. Preliminary results show that including a Deck amplitude into the partial-wave analysis removes the intensity in the low-mass region of fig. 5.45 from the $1^{-+}1^+\rho(770)\pi P$ wave for all t' bins, with only a peak similar to that in the highest t' bin remaining. The Deck effect is also a candidate for the non-resonant contribution in the $1^{++}0^+\rho(770)\pi S$ wave, however, adding the Deck amplitude has no effect on this wave.

A systematic study of the resonance-model fit has only been performed with two additional models so far. For the analysis of the $\pi^-\pi^-\pi^+$ final state a number of models have been worked out [75] that need to be tested for the $\pi^-\pi^0\pi^0$ final state. In addition the dependence of the Breit-Wigner parameters of the a_1 (1420) and π_1 (1600) on the used t' bins should be studied further. In both cases the intensity of the corresponding waves does not feature a clear peak in all t' bins.

The wave set used in the partial-wave analysis was taken over from the analysis

of the $\pi^-\pi^-\pi^+$ final state [50, 11]. This wave set was not created in a fully systematic way, but based on prior knowledge. The creation of a wave set without any prior knowledge is possible with the biggest-conceivable-model method developed in [23] and tested for the $\pi^-\pi^-\pi^+$ final state in [40]. The application of this method to the $\pi^-\pi^0\pi^0$ final state would help to confirm the correctness of this wave set, or provide a better alternative.

7.3 Partial-Wave Analysis of the $\pi^-\eta\eta$ Final State

The partial-wave decomposition of the $\pi^-\eta\eta$ final state (chapter 6) in general seems to be promising to study mesonic resonances in particular at higher masses. A large contribution of the flat wave to the total intensity points to non-diffractively produced states or imperfections in the partial-wave analysis model. To exclude the latter, the biggest-conceivable-model method from [23] has been employed to find a wave set for this final state. But also with this method the large contribution of the flat wave to the total intensity cannot be removed.

A cleaner selection of this final state might be able to reduce the background contributions, but for the moment is limited by the performance of ECAL1 (section 7.1). A better performance of ECAL1 might also lift the severe limit of the analysis due the available amount of real data events. Some additional events might be gained by considering not only the two-photon decay of the η , but also the $\pi^-\pi^+\pi^0$ decay channel. This possibility will be studied in the future.

List of Figures

1.1	Meson spectrum predicted by lattice QCD	2
1.2	COMPASS set-up	5
2.1	Schematic view of ECAL1	8
2.2	Schematic view of gaps in center of ECAL1	8
2.3	Schematic view of ECAL2	9
2.4	Shashlyk blocks	10
2.5	Cumulative shower profiles	12
2.6	Ratio of energy deposit	13
2.7	p/E of electrons in Shashlyk blocks	15
2.8	Distance between shower and track position for electrons	15
2.9	π^0 mass versus run number	17
2.10	π^0 width versus run number	17
2.11	Shower time versus shower energy	18
2.12	Shower time resolution versus shower energy	19
2.13	Mass of two-photon pairs for four-photon events	20
2.14	π^0 mass spectra	21
2.15	η mass spectra	22
2.16	Single-photon acceptance	23
2.17	Position-dependent single-photon acceptance in energy bins	24
2.18	π^0 mass spectra in Monte Carlo	25
2.19	η mass spectra in Monte Carlo	26
3.1	Significance of π^0 mass peak	30
3.2	Vertex position for $\pi^-\pi^0\pi^0$ final state	32
3.3	Vertex position for $\pi^-\eta\eta$ final state	32
3.4	Sketch of the reaction	33
3.5	Particle momenta and Mandelstam variable t	33
3.6	Calculated beam energy	35
3.7	Coplanarity of the recoil proton	35
3.8	Sketch of the reaction with three-momenta	36
3.9	Reduced squared four-momentum transfer t'	37
3.10	Invariant mass spectra in t' bins for $\pi^-\pi^0\pi^0$ final state	38
3.11	t' in mass bins for $\pi^-\pi^0\pi^0$ final state	38
3.12	Invariant mass spectra	39
3.13	Number of Monte Carlo events for $\pi^-\pi^0\pi^0$ final state	42
3.14	Phase-space acceptances	42

List of Figures

3.15	Phase-space acceptance in Gottfried-Jackson frame for $\pi^-\pi^0$ isobar	44
3.16	Phase-space acceptance in helicity frame for $\pi^-\pi^0$ isobar	45
3.17	Phase-space acceptance in Gottfried-Jackson frame for $\pi^0\pi^0$ isobar	46
3.18	Phase-space acceptance in helicity frame for $\pi^0\pi^0$ isobar	47
3.19	Number of Monte Carlo events for $\pi^-\eta\eta$ final state	49
3.20	Phase-space acceptance in angles for $\pi^-\eta$ isobar	50
3.21	Phase-space acceptance in angles for $\eta\eta$ isobar	50
4.1	Schematic of three-pion decay with involved quantum numbers . .	53
5.1	Two-pion mass spectra for the $\pi^-\pi^0\pi^0$ final state	64
5.2	Dalitz plot around the mass of the $a_2(1320)$	65
5.3	Dalitz plots around the mass of the $\pi_2(1670)$	65
5.4	Intensity and Argand diagram for relativistic Breit-Wigner	66
5.5	Intensity and Argand diagram for $f_0(980)$ parameterization	67
5.6	Intensity and Argand diagram for $(\pi\pi)_S$ parameterization	68
5.7	Weighted Monte Carlo: three-pion mass spectra	72
5.8	Weighted Monte Carlo: two-pion mass spectra for $\pi^-\pi^0$ isobar . .	72
5.9	Weighted Monte Carlo: two-pion mass spectra for $\pi^0\pi^0$ isobar . . .	73
5.10	Weighted Monte Carlo: Gottfried-Jackson frame for $\pi^0\pi^0$ isobar .	74
5.11	Weighted Monte Carlo: helicity frame for $\pi^0\pi^0$ isobar	75
5.12	Total intensity	77
5.13	Intensity of flat wave	78
5.14	Spin total for waves with $\varepsilon = -1$	78
5.15	Spin total for waves with $J^{PC} = 1^{++}$ and $\varepsilon = +1$	79
5.16	Spin total for waves with $J^{PC} = 2^{++}$ and $\varepsilon = +1$	80
5.17	Spin total for waves with $J^{PC} = 2^{-+}$ and $\varepsilon = +1$	80
5.18	Phase-space volume	86
5.19	Final-state mass dependence	86
5.20	Intensities of $1^{++}0^+\rho(770)\pi S$ wave	89
5.21	Intensities of $1^{++}0^+\rho(770)\pi S$ and $1^{++}1^+\rho(770)\pi S$ waves	90
5.22	Intensities of $1^{++}0^+(\pi\pi)_S\pi P$ and $1^{++}0^+f_2(1270)\pi P$ waves . . .	90
5.23	t' spectra of $J^{PC} = 1^{++}$ waves	92
5.24	Intensities of $2^{++}1^+\rho(770)\pi D$ wave	93
5.25	Intensities of $2^{++}1^+\rho(770)\pi D$ and $2^{++}2^+\rho(770)\pi D$ wave	94
5.26	Intensities of $2^{++}1^+f_2(1270)\pi P$ wave	94
5.27	t' spectra of $J^{PC} = 2^{++}$ waves	95
5.28	Intensities of $2^{-+}0^+f_2(1270)\pi S$ wave	97
5.29	Intensities of $2^{-+}0^+f_2(1270)\pi S$ and $2^{-+}1^+f_2(1270)\pi S$ waves . .	98
5.30	Intensities of $2^{-+}0^+f_2(1270)\pi D$ and $2^{-+}0^+\rho(770)\pi F$ waves . . .	98
5.31	Intensities of $2^{-+}0^+f_0(980)\pi D$ and $2^{-+}0^+(\pi\pi)_S\pi D$ waves	99
5.32	t' spectra for $J^{PC} = 2^{-+}$ waves I	100
5.33	t' spectra for $J^{PC} = 2^{-+}$ waves II	101
5.34	Phases of $1^{++}0^+\rho(770)\pi S$ wave w.r.t. $2^{-+}0^+f_2(1270)\pi S$ waves .	102

5.35	Phases of $2^{++}1^+\rho(770)\pi D$ wave w.r.t. $2^{-+}0^+f_2(1270)\pi S$ waves	102
5.36	Intensities of $0^{-+}0^+f_0(980)\pi S$ and $0^{-+}0^+(\pi\pi)_S\pi S$ waves	104
5.37	t' spectra of $J^{PC} = 0^{-+}$ waves	105
5.38	Intensities of $4^{++}1^+\rho(770)\pi G$ and $4^{++}1^+f_2(1270)\pi S$ waves	106
5.39	t' spectra of $J^{PC} = 4^{++}$ waves	107
5.40	Phases of $4^{++}1^+\rho(770)\pi G$ wave w.r.t. $2^{-+}0^+f_2(1270)\pi S$ wave	107
5.41	Intensities of $1^{++}0^+f_0(980)\pi P$ wave	109
5.42	Phases of $1^{++}0^+f_0(980)\pi P$ wave w.r.t. $2^{-+}0^+f_2(1270)\pi S$ waves	110
5.43	Phases of $1^{++}0^+f_0(980)\pi P$ wave w.r.t. $4^{++}1^+\rho(770)\pi G$ waves	110
5.44	t' spectrum of $1^{++}0^+f_0(980)\pi P$ wave	111
5.45	Intensities of $1^{-+}1^+\rho(770)\pi P$ wave	112
5.46	Phases of $1^{-+}1^+\rho(770)\pi P$ wave w.r.t. $1^{++}0^+\rho(770)\pi S$ waves	113
5.47	Phases of $1^{-+}1^+\rho(770)\pi P$ wave w.r.t. $2^{++}1^+\rho(770)\pi D$ waves	113
5.48	t' spectrum of $1^{-+}1^+\rho(770)\pi P$ wave	114
5.49	Resonance models: intensities of $1^{++}0^+$ waves	116
5.50	Resonance models: intensities of $2^{-+}0^+\rho(770)\pi F$ wave	117
5.51	$\pi^-\pi^0\pi^0$ and $\pi^-\pi^-\pi^+$: total intensity	118
5.52	$\pi^-\pi^0\pi^0$ and $\pi^-\pi^-\pi^+$: spin totals for waves with $\rho(770)$ or $f_2(1270)$ isobar	119
5.53	$\pi^-\pi^0\pi^0$ and $\pi^-\pi^-\pi^+$: intensities of waves with $\rho(770)$ isobar	120
5.54	$\pi^-\pi^0\pi^0$ and $\pi^-\pi^-\pi^+$: intensities of waves with non- $\rho(770)$ isobars	121
5.55	$\pi^-\pi^0\pi^0$ and $\pi^-\pi^-\pi^+$: intensity of $1^{++}0^+f_0(980)\pi P$ wave	121
5.56	$\pi^-\pi^0\pi^0$ and $\pi^-\pi^-\pi^+$: intensities of $1^{-+}1^+\rho(770)\pi P$ wave	122
6.1	Two-particle mass spectra for the $\pi^-\eta\eta$ final state	126
6.2	Total intensity and intensity of flat wave for E852 wave set	127
6.3	Partial-wave intensities for E852 wave set	128
6.4	Intensities of all waves used in the BCM method	130
6.5	Waves selected by the BCM method	131
6.6	Number of waves selected by the BCM method	132
6.7	Total intensity and intensity of flat wave for truncated BCM method	133
6.8	Partial-wave intensities for truncated BCM method	134

List of Tables

2.1	Mass resolutions for π^0 and η	19
3.1	Number of events during event selection for real data	28
3.2	Number of events in t' bins	39
3.3	Number of events during event selection for Monte Carlo data . . .	41
3.4	Resolutions obtained from simulation	48
5.1	Particle masses and resonance parameters	66
5.2	Wave set for $\pi^-\pi^0\pi^0$ final state	70
5.3	Intensities of spin totals	79
5.4	Slopes of t' spectra	82
5.5	Waves used in the resonance-model fit	88
5.6	Resonance parameters	88
5.7	Resonance parameters for different resonance models	115
6.1	Wave set for $\pi^-\eta\eta$ final state by E852	125
6.2	Isobars used in partial-wave analysis of $\pi^-\eta\eta$ final state	129
6.3	Wave set for $\pi^-\eta\eta$ final state by truncated BCM method	132

Bibliography

- [1] P. Abbon et al. “The COMPASS Experiment at CERN”. In: *Nuclear Instruments and Methods in Physics Research A* 577 (2007), pp. 455–518.
- [2] P. Abbon et al. “The COMPASS setup for physics with hadron beams”. In: *Nuclear Instruments and Methods in Physics Research Section A: Accelerators, Spectrometers, Detectors and Associated Equipment* 779 (2015), pp. 69–115. ISSN: 0168-9002. DOI: <http://dx.doi.org/10.1016/j.nima.2015.01.035>. arXiv: 1410.1797.
- [3] M. Ablikim et al. “Resonances in $J/\psi \rightarrow \phi\pi^+\pi^-$ and ϕK^+K^- ”. In: *Physics Letters B* 607 (2005), pp. 243–253. ISSN: 0370-2693. DOI: <http://dx.doi.org/10.1016/j.physletb.2004.12.041>. URL: <http://www.sciencedirect.com/science/article/pii/S0370269304017265>.
- [4] G.S. Adams et al. “Experimental evidence for hadroproduction of exotic mesons”. In: *Nuclear Physics A* 680 (2001). Quark Nuclear Physics 2000, pp. 335–341. ISSN: 0375-9474. DOI: [http://dx.doi.org/10.1016/S0375-9474\(00\)00439-5](http://dx.doi.org/10.1016/S0375-9474(00)00439-5). URL: <http://www.sciencedirect.com/science/article/pii/S0375947400004395>.
- [5] C. Adolph et al. “First Measurement of Chiral Dynamics in $\pi^-\gamma \rightarrow \pi^-\pi^-\pi^+$ ”. In: *Phys. Rev. Lett.* 108 (19 May 2012), p. 192001. DOI: 10.1103/PhysRevLett.108.192001. arXiv: 1111.5954.
- [6] C. Adolph et al. “Measurement of radiative widths of $a_2(1320)$ and $\pi_2(1670)$ ”. In: *The European Physical Journal A* 50.4, 79 (2014). ISSN: 1434-6001. DOI: 10.1140/epja/i2014-14079-8. arXiv: 1403.2644.
- [7] C. Adolph et al. “Measurement of the Charged-Pion Polarizability”. In: *Phys. Rev. Lett.* 114 (6 Feb. 2015), p. 062002. DOI: 10.1103/PhysRevLett.114.062002. arXiv: 1405.6377.
- [8] C. Adolph et al. “Measurement of the cross section for high- p_T hadron production in the scattering of 160-GeV/ c muons off nucleons”. In: *Phys. Rev. D* 88 (9 Nov. 2013), p. 091101. DOI: 10.1103/PhysRevD.88.091101. arXiv: 1207.2022.
- [9] C. Adolph et al. “Observation of a New Narrow Axial-Vector Meson $a_1(1420)$ ”. In: *Phys. Rev. Lett.* 115 (8 Aug. 2015), p. 082001. DOI: 10.1103/PhysRevLett.115.082001. arXiv: 1501.05732.

Bibliography

- [10] C. Adolph et al. “Odd and even partial waves of $\eta\pi^-$ and $\eta'\pi^-$ in $\pi^-p \rightarrow \eta^{(\prime)}\pi^-p$ at 191 GeV/c”. In: *Physics Letters B* 740 (2015), pp. 303–311. ISSN: 0370-2693. DOI: <http://dx.doi.org/10.1016/j.physletb.2014.11.058>. arXiv: 1408.4405.
- [11] C. Adolph et al. “Resonance Production and $\pi\pi$ S-wave in $\pi^- + p \rightarrow \pi^- \pi^- \pi^+ + p_{\text{recoil}}$ at 190 GeV/c”. In: *Phys. Rev. D* (2015). arXiv: 1509.00992. Forthcoming.
- [12] D. Alde et al. “Evidence for a 1^{-+} exotic meson”. In: *Physics Letters B* 205.2 (1988), pp. 397–400. ISSN: 0370-2693. DOI: [http://dx.doi.org/10.1016/0370-2693\(88\)91686-3](http://dx.doi.org/10.1016/0370-2693(88)91686-3). URL: <http://www.sciencedirect.com/science/article/pii/0370269388916863>.
- [13] M. G. Alekseev et al. “Observation of a $J^{PC} = 1^{-+}$ Exotic Resonance in Diffractive Dissociation of 190 GeV/c into $\pi^- \pi^- \pi^+$ ”. In: *Phys. Rev. Lett.* 104 (24 June 2010), p. 241803. DOI: 10.1103/PhysRevLett.104.241803. arXiv: 0910.5842.
- [14] D.V. Amelin et al. “Investigation of the diffractive reaction $\pi^- a \rightarrow \eta\eta\pi^- a$ at an incident p_{π^-} momentum of 37 GeV/c”. In: *Physics of Atomic Nuclei* 59.6 (1996), pp. 976–981.
- [15] D.V Amelin et al. “Study of resonance production in diffractive reaction $\pi^- A \rightarrow \pi^+ \pi^- \pi^- A$ ”. In: *Physics Letters B* 356.4 (1995), pp. 595–600. ISSN: 0370-2693. DOI: [http://dx.doi.org/10.1016/0370-2693\(95\)00864-H](http://dx.doi.org/10.1016/0370-2693(95)00864-H). URL: <http://www.sciencedirect.com/science/article/pii/037026939500864H>.
- [16] P. Astbury et al. “Measurement of deep inelastic Compton scattering of high energy photons”. In: *Physics Letters B* 152.5 (1985), pp. 419–427. ISSN: 0370-2693. DOI: [http://dx.doi.org/10.1016/0370-2693\(85\)90521-0](http://dx.doi.org/10.1016/0370-2693(85)90521-0). URL: <http://www.sciencedirect.com/science/article/pii/0370269385905210>.
- [17] H. W. Atherton et al. *Precise Measurements of Particle Production by 400-GeV/c Protons on Beryllium Targets*. 1980.
- [18] K. L. Au, D. Morgan, and M. R. Pennington. “Meson dynamics beyond the quark model: Study of final-state interactions”. In: *Phys. Rev. D* 35 (5 Mar. 1987), pp. 1633–1664. DOI: 10.1103/PhysRevD.35.1633. URL: <http://link.aps.org/doi/10.1103/PhysRevD.35.1633>.
- [19] T. Barnes et al. “Higher quarkonia”. In: *Phys. Rev. D* 55 (7 Apr. 1997), pp. 4157–4188. DOI: 10.1103/PhysRevD.55.4157. URL: <http://link.aps.org/doi/10.1103/PhysRevD.55.4157>.
- [20] Vincenzo Barone and Enrico Predazzi. *High-Energy Particle Diffraction*. Springer-Verlag Berlin Heidelberg, 2002.

- [21] Jean-Louis Basdevant and Edmond L. Berger. “Peak Locations and Relative Phase of Different Decay Modes of the a_1 Axial Vector Resonance in Diffractive Production”. In: *Phys. Rev. Lett.* 114 (19 May 2015), p. 192001. DOI: 10.1103/PhysRevLett.114.192001. URL: <http://link.aps.org/doi/10.1103/PhysRevLett.114.192001>.
- [22] G.M. Beladidze et al. “Study of $\pi^- N \rightarrow \eta\pi^- N$ and $\pi^- N \rightarrow \eta'\pi^- N$ reactions at 37 GeV/c”. In: *Physics Letters B* 313.1 (1993), pp. 276–282. ISSN: 0370-2693. DOI: [http://dx.doi.org/10.1016/0370-2693\(93\)91224-B](http://dx.doi.org/10.1016/0370-2693(93)91224-B). URL: <http://www.sciencedirect.com/science/article/pii/037026939391224B>.
- [23] K.A. Bicker. “Model Selection for and Partial-Wave Analysis of a Five-Pion Final State at the COMPASS Experiment at CERN”. PhD thesis. Technische Universität München, 2016.
- [24] K.A. Bicker. “Yet Another Beamfile for COMPASS”. http://wwwcompass.cern.ch/compass/software/analysis/transparencies/2013/am_130711/bicker_Yet-Another-Beamfile-for-COMPASS_2013-07-11.pdf.
- [25] F. Binon et al. “Hodoscope multiphoton spectrometer GAMS-2000”. In: *Nuclear Instruments and Methods in Physics Research Section A: Accelerators, Spectrometers, Detectors and Associated Equipment* 248.1 (1986), pp. 86–102. ISSN: 0168-9002. DOI: [http://dx.doi.org/10.1016/0168-9002\(86\)90501-2](http://dx.doi.org/10.1016/0168-9002(86)90501-2). URL: <http://www.sciencedirect.com/science/article/pii/0168900286905012>.
- [26] J. Blatt and V. Weisskopf. *Theoretical Nuclear Physics*. 1952.
- [27] M.G. Bowler. “The $\{A1\}$ revisited”. In: *Physics Letters B* 182.3 - 4 (1986), pp. 400–404. ISSN: 0370-2693. DOI: [http://dx.doi.org/10.1016/0370-2693\(86\)90116-4](http://dx.doi.org/10.1016/0370-2693(86)90116-4). URL: <http://www.sciencedirect.com/science/article/pii/0370269386901164>.
- [28] M.G. Bowler et al. “Diffraction dissociation, the deck mechanism and diffractive resonance production”. In: *Nuclear Physics B* 97.2 (1975), pp. 227–255. ISSN: 0550-3213. DOI: [http://dx.doi.org/10.1016/0550-3213\(75\)90033-4](http://dx.doi.org/10.1016/0550-3213(75)90033-4). URL: <http://www.sciencedirect.com/science/article/pii/0550321375900334>.
- [29] R. Brun and F. Rademakers. “ROOT, an object oriented data analysis framework”. In: *Nucl. Instr. and Meth. A* 389 (1997). <http://root.cern.ch>, p. 81.
- [30] S. U. Chung and T. L. Trueman. “Positivity conditions on the spin density matrix: A simple parametrization”. In: *Phys. Rev. D* 11 (3 Feb. 1975), pp. 633–646. DOI: 10.1103/PhysRevD.11.633. URL: <http://link.aps.org/doi/10.1103/PhysRevD.11.633>.

Bibliography

- [31] S. U. Chung et al. “Evidence for exotic $J^{PC}=1^{-+}$ meson production in the reaction $\pi^{-} \vec{p} \rightarrow \eta\pi^{-}p$ at $18\text{GeV}/c$ ”. In: *Phys. Rev. D* 60 (9 Oct. 1999), p. 092001. DOI: 10.1103/PhysRevD.60.092001. URL: <http://link.aps.org/doi/10.1103/PhysRevD.60.092001>.
- [32] S. U. Chung et al. “Exotic and $q\bar{q}$ resonances in the $\pi^{+}\pi^{-}\pi^{-}$ system produced in $\pi^{-}p$ collisions at $18\text{GeV}/c$ ”. In: *Phys. Rev. D* 65 (7 Mar. 2002), p. 072001. DOI: 10.1103/PhysRevD.65.072001. URL: <http://link.aps.org/doi/10.1103/PhysRevD.65.072001>.
- [33] S.U. Chung. *Spin Formalisms*. 1971.
- [34] Frank E. Close and Philip R. Page. “The production and decay of hybrid mesons by flux-tube breaking”. In: *Nuclear Physics B* 443.1 - 2 (1995), pp. 233–254. ISSN: 0550-3213. DOI: [http://dx.doi.org/10.1016/0550-3213\(95\)00085-7](http://dx.doi.org/10.1016/0550-3213(95)00085-7). URL: <http://www.sciencedirect.com/science/article/pii/0550321395000857>.
- [35] C. Daum et al. “Diffractive production of 3π states at 63 and 94 GeV”. In: *Nuclear Physics B* 182.3 (1981), pp. 269–336. ISSN: 0550-3213. DOI: [http://dx.doi.org/10.1016/0550-3213\(81\)90123-1](http://dx.doi.org/10.1016/0550-3213(81)90123-1). URL: <http://www.sciencedirect.com/science/article/pii/0550321381901231>.
- [36] Robert T. Deck. “Kinematical Interpretation of the First $\pi-p$ Resonance”. In: *Phys. Rev. Lett.* 13 (5 Aug. 1964), pp. 169–173. DOI: 10.1103/PhysRevLett.13.169. URL: <http://link.aps.org/doi/10.1103/PhysRevLett.13.169>.
- [37] Alexander Donnachie and Philip R. Page. “Interpretation of experimental J^{PC} exotic signals”. In: *Phys. Rev. D* 58 (11 Oct. 1998), p. 114012. DOI: 10.1103/PhysRevD.58.114012. URL: <http://link.aps.org/doi/10.1103/PhysRevD.58.114012>.
- [38] Sandy Donnachie et al. *Pomeron Physics and QCD*. Cambridge Monographs on Particle Physics, Nuclear Physics and Cosmology. Cambridge University Press, 2005.
- [39] Christian Dreisbach. “Study of elastic $\pi^{-}p$ scattering at COMPASS”. Masters thesis. Technische Universität München, Dec. 2014.
- [40] Oliver Johann Drotleff. “Model Selection for Partial-Wave Analysis of $\pi^{-} + p \rightarrow \pi^{-}\pi^{+}\pi^{-} + p$ at the COMPASS Experiment at CERN”. https://wwwcompass.cern.ch/compass/publications/theses/2015_dpl_drotleff.pdf. Diploma thesis. Technische Universität München, 2015.
- [41] Jozef J. Dudek, Robert G. Edwards, and Christopher E. Thomas. “Energy dependence of the ρ resonance in $\pi\pi$ elastic scattering from lattice QCD”. In: *Phys. Rev. D* 87 (3 Feb. 2013), p. 034505. DOI: 10.1103/PhysRevD.87.034505. URL: <http://link.aps.org/doi/10.1103/PhysRevD.87.034505>.

- [42] Jozef J. Dudek et al. “Toward the excited isoscalar meson spectrum from lattice QCD”. In: *Phys. Rev. D* 88 (9 Nov. 2013), p. 094505. DOI: 10.1103/PhysRevD.88.094505. URL: <http://link.aps.org/doi/10.1103/PhysRevD.88.094505>.
- [43] Jozef Dudek and Adam Szczepaniak. “The Deck effect in $\pi N \rightarrow \pi\pi\pi N$ ”. In: *AIP Conference Proceedings* 814.1 (2006), pp. 587–591. DOI: <http://dx.doi.org/10.1063/1.2176547>. URL: <http://scitation.aip.org/content/aip/proceeding/aipcp/10.1063/1.2176547>.
- [44] A. R. Dzierba et al. “Partial wave analysis of the $\pi^-\pi^-\pi^+$ and $\pi^-\pi^0\pi^0$ systems and the search for a $J^{PC} = 1^{-+}$ meson”. In: *Phys. Rev. D* 73 (7 Apr. 2006), p. 072001. DOI: 10.1103/PhysRevD.73.072001. URL: <http://link.aps.org/doi/10.1103/PhysRevD.73.072001>.
- [45] P. Eugenio et al. “Observation of the $\pi(1800)$ and $\pi_2(1880)$ mesons in decay”. In: *Physics Letters B* 660.5 (2008), pp. 466–470.
- [46] J.M. Friedrich. Private communications.
- [47] Murray Gell-Mann. “Symmetries of Baryons and Mesons”. In: *Phys. Rev.* 125 (3 Feb. 1962), pp. 1067–1084. DOI: 10.1103/PhysRev.125.1067. URL: <http://link.aps.org/doi/10.1103/PhysRev.125.1067>.
- [48] S. Gerassimov. Private communications.
- [49] Stefanie Grabmüller. “Cryogenic Silicon Detectors and Analysis of Primakoff Contributions to the Reaction $\pi^- \text{Pb} \rightarrow \pi^- \pi^- \pi^+ \text{Pb}$ at COMPASS”. PhD thesis. Technische Universität München, Sept. 2012.
- [50] F. Haas. “Two-Dimensional Partial-Wave Analysis of Exclusive 190 GeV $\pi^- p$ Scattering into the $\pi^- \pi^- \pi^+$ Final-State at COMPASS (CERN)”. PhD thesis. Technische Universität München, 2014.
- [51] David J. Herndon, Paul Söding, and Roger J. Cashmore. “Generalized isobar model formalism”. In: *Phys. Rev. D* 11 (11 June 1975), pp. 3165–3182. DOI: 10.1103/PhysRevD.11.3165. URL: <http://link.aps.org/doi/10.1103/PhysRevD.11.3165>.
- [52] Frank von Hippel and C. Quigg. “Centrifugal-Barrier Effects in Resonance Partial Decay Widths, Shapes, and Production Amplitudes”. In: *Phys. Rev. D* 5 (3 Feb. 1972), pp. 624–638. DOI: 10.1103/PhysRevD.5.624. URL: <http://link.aps.org/doi/10.1103/PhysRevD.5.624>.
- [53] Ferdinand Hitzler. “Schauer Charakterisierung in den elektromagnetischen Kalorimetern bei COMPASS (CERN)”. Bachelor thesis. Technische Universität München, July 2011.
- [54] Christian Höppner. “First Measurement of the Cross Section for the Production of Hadrons with High Transverse Momenta at COMPASS, and Developments for Particle Tracking in High-Rate Experiments”. PhD thesis. Technische Universität München, Jan. 2012.

Bibliography

- [55] Matthias Johannes Huber. “Construction of COMPASS PixelGEM detectors”. Bachelor thesis. Technische Universität München, July 2012.
- [56] M. Jacob and G.C. Wick. “On the general theory of collisions for particles with spin”. In: *Annals of Physics* 7.4 (1959), pp. 404–428. ISSN: 0003-4916. DOI: [http://dx.doi.org/10.1016/0003-4916\(59\)90051-X](http://dx.doi.org/10.1016/0003-4916(59)90051-X). URL: <http://www.sciencedirect.com/science/article/pii/000349165990051X>.
- [57] F. James. *Monte Carlo Phase Space*. 1968.
- [58] Eberhard Klempt and Alexander Zaitsev. “Glueballs, hybrids, multiquarks: Experimental facts versus {QCD} inspired concepts”. In: *Physics Reports* 454.1 - 4 (2007), pp. 1–202. ISSN: 0370-1573. DOI: <http://dx.doi.org/10.1016/j.physrep.2007.07.006>. URL: <http://www.sciencedirect.com/science/article/pii/S0370157307003560>.
- [59] A. Lednev. “Shashlik shower profile”. <http://wwwcompass.cern.ch/compass/notes/2012-4/2012-4.pdf>.
- [60] A.A. Lednev. “Electron shower transverse profile measurement”. In: *Nuclear Instruments and Methods in Physics Research Section A: Accelerators, Spectrometers, Detectors and Associated Equipment* 366.2 - 3 (1995), pp. 292–297. ISSN: 0168-9002. DOI: [http://dx.doi.org/10.1016/0168-9002\(95\)00717-2](http://dx.doi.org/10.1016/0168-9002(95)00717-2). URL: <http://www.sciencedirect.com/science/article/pii/0168900295007172>.
- [61] A.A. Lednev. “Shower separation program for ECAL2”. <http://wwwcompass.cern.ch/compass/notes/2009-7/2009-7.pdf>.
- [62] Alexander B. Mann et al. “The universal sampling ADC readout system of the COMPASS experiment”. In: *IEEE Nucl.Sci.Symp.Conf.Rec.* 2009 (2009), pp. 2225–2228. DOI: 10.1109/NSSMIC.2009.5402077.
- [63] C.A. Meyer and E.S. Swanson. “Hybrid mesons”. In: *Progress in Particle and Nuclear Physics* 82 (2015), pp. 21–58. ISSN: 0146-6410. DOI: <http://dx.doi.org/10.1016/j.pnpnp.2015.03.001>. URL: <http://www.sciencedirect.com/science/article/pii/S0146641015000162>.
- [64] M. Mikhasenko, B. Ketzer, and A. Sarantsev. “Nature of the $a_1(1420)$ ”. In: *Phys. Rev. D* 91 (9 May 2015), p. 094015. DOI: 10.1103/PhysRevD.91.094015. URL: <http://link.aps.org/doi/10.1103/PhysRevD.91.094015>.
- [65] K.A. Olive and Particle Data Group. “Review of Particle Physics”. In: *Chinese Physics C* 38.9 (2014), p. 090001. URL: <http://stacks.iop.org/1674-1137/38/i=9/a=090001>.
- [66] Philip R. Page, Eric S. Swanson, and Adam P. Szczepaniak. “Hybrid meson decay phenomenology”. In: *Phys. Rev. D* 59 (3 Jan. 1999), p. 034016. DOI: 10.1103/PhysRevD.59.034016. URL: <http://link.aps.org/doi/10.1103/PhysRevD.59.034016>.

- [67] Michael R Pennington. “Evolving images of the proton: hadron physics over the past 40 years”. In: *Journal of Physics G: Nuclear and Particle Physics* 43.5 (2016), p. 054001. URL: <http://stacks.iop.org/0954-3899/43/i=5/a=054001>.
- [68] S. Pflüger. “Investigations of the Light Meson Spectrum with COMPASS using Final States containing Neutral Particles”. http://wwwcompass.cern.ch/compass/publications/theses/2011_dpl_pflueger.pdf.
- [69] V. Polyakov. Private communications.
- [70] Jeffrey D. Richman. “An Experimenter’s Guide to the Helicity Formalism”. In: (1984).
- [71] D.I. Ryabchikov. Private communications.
- [72] Tobias Schlüter. “The $\pi^- \eta$ and $\pi^- \eta'$ Systems in Exclusive 190 GeV $\pi^- p$ Reactions at COMPASS (CERN)”. PhD thesis. Ludwig-Maximilians-Universität München, June 2012.
- [73] T. Schlüter et al. “Large-area sandwich veto detector with {WLS} fibre readout for hadron spectroscopy at {COMPASS}”. In: *Nuclear Instruments and Methods in Physics Research Section A: Accelerators, Spectrometers, Detectors and Associated Equipment* 654.1 (2011), pp. 219–224. ISSN: 0168-9002. DOI: <http://dx.doi.org/10.1016/j.nima.2011.05.069>. URL: <http://www.sciencedirect.com/science/article/pii/S0168900211010552>.
- [74] Michael Tasiar. “Performance Studies for the COMPASS PixelGEM Tracking Detectors and Development of a Modular Test Bench for GEM Detectors”. Diploma thesis. Technische Universität München, Nov. 2011.
- [75] Stefan Wallner. “Extraction of Resonance Parameters of Light Meson Resonances in the Charged Three-Pion Final State at the COMPASS Experiment (CERN)”. https://wwwcompass.cern.ch/compass/publications/theses/2015_dpl_wallner.pdf. MA thesis. Technische Universität München, 2015.
- [76] Stefan Wallner. “Performance enhancement in the simulation of the electromagnetic calorimeters of COMPASS”. Bachelor thesis. Technische Universität München, Aug. 2013.
- [77] Zhi-Gang Wang. “Light axial-vector tetraquark state candidate: $a_1(1420)$ ”. In: (). arXiv: 1401.1134.
- [78] Quirin Weitzel. “Precision Meson Spectroscopy: Diffractive Production at COMPASS and Development of a GEM-based TPC for PANDA”. <http://nbn-resolving.de/urn/resolver.pl?urn:nbn:de:bvb:91-diss-20080801-668430-1-0>. PhD thesis. Technische Universität München, 2008.
- [79] Eugen Wigner. *Gruppentheorie und ihre Anwendung auf die Quantenmechanik der Atomspektren*. Vieweg+Teubner Verlag, 1931.

Bibliography

- [80] A. Zaitsev et al. “Study of exotic resonances in diffractive reactions”. In: *Nuclear Physics A* 675 (2000). Proceedings of the 8suth International Conference, pp. 155–160. ISSN: 0375-9474. DOI: [http://dx.doi.org/10.1016/S0375-9474\(00\)00238-4](http://dx.doi.org/10.1016/S0375-9474(00)00238-4). URL: <http://www.sciencedirect.com/science/article/pii/S0375947400002384>.

Own contributions

My work on the new reconstruction for the electromagnetic calorimeters was based on the shower profiles from [60] and Anatoli Lednev's FORTRAN code for ECAL2 in COMPASS. In an initial study of his code I found several issues, which lead to the decision to rewrite the code from scratch in C++. While studying the performance of the new code I noticed that the shower profiles were not sufficient to determine the position with the required precision, but that there was a systematic shift depending on the position of the showers in the cell. Another systematic effect was found with the dependence of the energy deposit on the position of a shower caused by the Shashlyk structure. Recognizing and correcting for these effects finally vastly improved the photon reconstruction. For ECAL2, the π^0 mass resolution is improved by 25%. To be on par with real data, I also had to create calibrations for the shower profiles and corrections of the shower parameters for Monte Carlo data. The improvement of the photon reconstruction was an important cornerstone for the measurement of the pion polarizability in pion Compton scattering (published in [7]).

In the course of the work on the photon reconstruction I supervised a bachelor thesis [53] studying the possibility to use the same reconstruction algorithm also for ECAL1. Another bachelor thesis [76] concentrated on extending the usage of GFLASH previously made available for ECAL2 by Tobias Schlüter [72] to improve the simulation speed also for ECAL1.

For the first production of real data from 2008 that was using my reconstruction, and which was used in this thesis, I was responsible to ensure all detector calibrations and reconstruction options were available and adequate. Due to the many changes with respect to previous productions, the event selection had to be revised completely. The selection cuts of previous analyses could only be used as rough guidelines. This event selection was crosschecked by Tobias Weisrock. For the acceptance corrections applied in the partial-wave analysis I took care of the simulation and reconstruction of 300 million phase-space events. Such a large number of Monte Carlo events had never before been created for a single analysis. I used the ROOTPWA package to perform the partial-wave analysis. I contributed a fixed normalization for the weighted Monte Carlo such that real data and weighted Monte Carlo plots no longer needed to be scaled. The partial-wave analysis was crosschecked by Dmitry Ryabchikov, and presented on several national and international conferences. To perform the resonance-model fit, I extended the fitter included in ROOTPWA to work for multiple t' bins and added the resonance and backgrounds amplitudes used for the analysis of the $\pi^-\pi^-\pi^+$ final state.

Own contributions

For the Monte Carlo studies of the analyses performed by Christian Höppner [54] (published in [8]) and Stefanie Grabmüller [49] (published in [5, 6]) I updated the original versions of the COMPASS reconstruction software used for the production of the respective real data to work on more recent systems. These modifications had to be done very carefully, as the outcome of the reconstruction should not be affected.

For four COMPASS beam times, from 2009 to 2012, I was responsible for the 22 GEM and four to six PixelGEM detectors in the experiment. This included the commissioning of the detectors before each run, taking care of the necessary calibrations, and preliminary performance studies to make sure the detectors performed as expected. These studies have later been performed in more detail and with extended scope in a diploma thesis [74] and a bachelor thesis [55], which I partially supervised. I also improved the reconstruction of the spatial information from the data of the GEM and PixelGEM detectors, and the stability of `gemMonitor`, the tool that is used for debugging and calibrating the GEM, PixelGEM and silicon detectors. Before the Primakoff run in 2012, I led the production of four new PixelGEM detectors in a team with Bernhard Ketzer, Florian Haas, Alexander Austregesilo and two technical students.

Acknowledgements

First of all, I would like to thank Prof. Stephan Paul for giving me the opportunity to over the years work on many different topics of which only a small part could be presented in this document, I am grateful for having been able to spent time learning so many different things. I really enjoyed working in his group.

My sincerest thanks to Jan Friedrich, for his encouragement while developing the new ECAL reconstruction, Boris Grube, for his support while performing the partial-wave analysis presented in this thesis, and Bernhard Ketzer. Without their patient and continuous help this thesis would not have been accomplished.

I gratefully acknowledge fruitful discussions concerning the analysis part of this thesis with my colleagues Alex Austregesilo, Charly Bicker, Florian Haas, Stefan Huber, Fabian Krinner, and Dmitry Ryabchikov. For the more technical parts of my work I was always inspired by Markus Ball, Felix Böhmer, Sverre Dørheim, Steffi Grabmüller, Christian Höppner, Igor Konorov, Alexander Mann, Thiemo Nagel, Sebastian Neubert, and Maxence Vandenbroucke.

Of the many people not yet mentioned I particularly have to thank the students who did (parts of) their bachelor, master, or diploma theses under my supervision: Michael Tasiar, Matthias Huber, and Christian Dreisbach for working with me on the PixelGEM project; Ferdinand Hitzler and Stefan Wallner who worked on the reconstruction and simulation of electromagnetic calorimeters; Michael Leeb who helped to prepare the data productions on which my reconstruction of the electromagnetic calorimeters were tested. Also my office mates Florian Goslich, Markus Krämer, Johannes Rauch, and Julian Taylor deserve to be mentioned here.

Of course such a long work covering so many aspects would never be possible without my non-scientific colleagues and co-workers. In particular I thank Martin Aigner, for always being able to help on short notice with whatever we brought to his workshop, and the secretary of our group Karin Frank, for taking care of all the things concerning money.

Obviously I enjoyed working with many more people, of which I could not name everybody. Thanks go out to everybody involved at E18. I enjoyed being part of a group with such a broad spectrum of research areas.